INTERNATIONAL THEORY, RESEARCH AND REVIEWS IN

SCIENCE AND MATHEMATICS

October 2023

EDITOR

PROF. DR. HASAN AKGÜL

SERÜVEN YAYINEVİ

Genel Yayın Yönetmeni / Editor in Chief • C. Cansın Selin Temana

Kapak & İç Tasarım / Cover & Interior Design • Serüven Yayınevi

Birinci Basım / First Edition • © Ekim 2023

ISBN • 978-625-6760-10-3

Serüven Yayınevi / Serüven Publishing
Türkiye Adres / Turkey Address: Kızılay Mah. Fevzi Çakmak 1. Sokak
Ümit Apt No: 22/A Çankaya/ANKARA
Telefon / Phone: 05437675765
web: www.seruvenyayinevi.com
e-mail: seruvenyayinevi@gmail.com

Baskı & Cilt / Printing & Volume
Sertifika / Certificate No: 47083

INTERNATIONAL THEORY, RESEARCH AND REVIEWS IN SCIENCE AND MATHEMATICS

OCTOBER 2023

Editor

Prof. Dr. Hasan AKGÜL

CONTENTS

Chapter 1

STRUCTURAL, ELECTRONIC, ELASTIC, AND VIBRATIONAL PROPERTIES OF THE CHALCOPYRITE SEMICONDUCTOR $ZnSiP_2$

İrem ÖNER ALP[1]

Yasemin ÖZTEKİN ÇİFTCİ[2]

1 İrem ÖNER ALP, Asst. Prof. Dr., Department of Physics, Sciences Faculty, Gazi University, Ankara, TURKEY iremoner@gazi.edu.tr (ORCID: 0000-00026937-7864)

2 Yasemin ÖZTEKİN ÇİFTCİ, Prof. Dr., Department of Physics, Sciences Faculty, Gazi University, Ankara, TURKEY yasemin@gazi.edu.tr (ORCID: 0000-0003-1796-0270)

1. INTRODUCTION

The opportunity to utilize chalcopyrite compounds as source materials for visible and infrared light emitting diodes, photodetectors, infrared generation, and optical parametric oscillator fabrication has aroused the interest of the researchers. These substances are therefore ideal candidates for a wide range of technological applications (Wang et al., 2018; Basalaev, Gordienko, & Poplavnoi, 2005; Rashkeev, Limpijumnong, & Lambrecht, 1999; Scholl & Tang, 1973). If this single crystal is transparent within a broad wavelength interval and of high quality, then the physical and chemical properties resulting from its anisotropic structure allow it to play a significant role in nonlinear optics (Hu, Han, Fang, & Mao, 2023; Taguida et al., 2023; Yu et al., 2012; Jackson, Ohmer, & LeClair, 1997). Such that, quantum electronics and high-power optical frequency conversion in the near- and mid-infrared regions are specifically promising fields. Moreover, they represent the highest nonlinear susceptibility with sufficient birefringence. They are thus regarded as convenient materials for efficient second harmonic generation and phase matching (Kumar & Tripathy, 2014). Besides, chalcopyrite derivatives doped with Mn ions carry a great potential for spintronics owing to their ferromagnetic characteristics at room temperature (Taychour, Zriouel, & Drissi, 2018; Naveh & Kronik, 2006; Medvedkin et al., 2000).

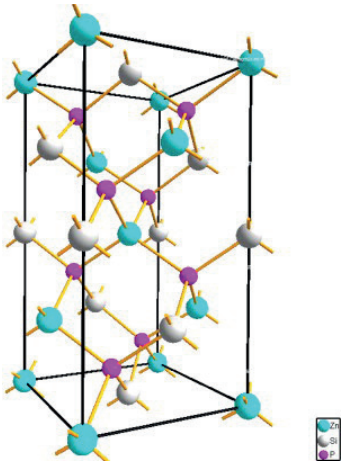

Element	x	y	z	Wyckoff
Zn	0.0	0.0	0.0	4a
Si	0.0	0.0	0.5	4b
P	u	0.25	0.125	8d

Note. u = 0.2691, (the experimental value reported in Abrahams & Bernstein, 1970).

Figure 1. The unit cell of the I-42d phase of $ZnSiP_2$ compound (Peña-Pedraza, López-Rivera, Martin, Delgado, & Power, 2012, p.1467) and the related atomic positions.

Ternary diamond-like $A^{II}B^{IV}C^{V}_2$ semiconductors crystallize in the chalcopyrite structure with a tetragonal phase (Shay & Wernick, 2013) at ambient conditions and they have the same isoelectronic configuration with the well-

known III-V binary compounds. One of these systems, $ZnSiP_2$ was synthesized with structural parameters of a = 5.399 Å and c = 10.435 Å by Abrahams and Bernstein (1970). Subsequently, Deus and Schneider (1983) measured these lattice constant values as a = 5.4001 Å and c = 10.4359 Å. The chalcopyrite $ZnSiP_2$ is classified under the I-42d (D^{12}_{2d} or tI16) nonsymmorphic space group (s.g. no. 122) and comprises of four formula units per unit cell as can be seen in Fig. 1 (Kumar & Tripathy, 2014; Peña-Pedraza, López-Rivera, Martin, Delgado, & Power, 2012). The geometric configuration is derived from a close-packed cubic stacking of phosphorus atoms, wherein half of the tetrahedral positions are orderly occupied by two cations, zinc and silicon atoms. The present arrangement entails the linkage of two zinc (Zn) and two silicon (Si) to a single phosphorus (P), while four P are bonded to a cation (Peña-Pedraza, 2012).

$ZnSiP_2$ has been the subject of much theoretical (Bennacer et al., 2018; Zhang, 2017; Martinez et al., 2015; Tripathy & Kumar, 2014; Ullah et al., 2014; Verma, Sharma, Bhandari, Sarkar, & Jindal, 2012; Chiker, Kebbab, Miloua, & Benramdane, 2011; Kumar, Shrivastava, Banerji, & Dhirhe, 2009; Chiker et al., 2004; Neumann, 2004; Reddy et al., 2000) and applied (Madelung, Rössler, & Schulz, 2000; Goodman, 1991; Mackinnon, 1985; Ambrazevičius, Babonas, & Šileika, 1979; Oshcherin, 1979; Shay, Tell, Buehler, & Wernick, 1973; Vaipolin, 1973) research for many years. In the meantime, Basalaev et al. (2018) implemented advanced ab-initio computation methods to describe ternary semiconductor compounds within a discussion of the electronic properties of $MgSiP_2$, $ZnSiP_2$, and $CdSiP_2$. Kumar and Tripathy (2014) used the plane wave pseudo-potential method within density functional theory (DFT) to investigate the structural, electronic, and elastic properties of chalcopyrite $ZnSiP_2$, as well as its optical characteristics. Peña-Pedraza et al. (2012) previously presented the characterization of $ZnSiP_2$ using Raman spectroscopy and single-crystal X-ray diffraction. The structural, elastic, electronic, and chemical bonding properties of the crystal were analyzed through plane wave pseudo-potential total energy computations, with a focus on the impact of pressure (Arab, Ali Sahraoui, Haddadi, & Louail, 2012). According to this research on the physical properties of $ZnSiP_2$, the chalcopyrite phase remains stable up to 35 GPa and it has been reported in literature that this material exhibits a structural phase transition to a rocksalt Fm-3m form (s.g. no:225) under pressure (Yuan et al., 2021; Bhadram et al., 2017; Tahri, Ouahrani, & Pilmé, 2017; Ouahrani, 2013).

The present paper covers extensively the physical nature of $ZnSiP_2$ via first-principles calculations based on density functional theory. The adequacy of the employed theoretical approach was assessed in light of experimental references. Moreover, the tetragonal distortion, a defining characteristic of chalcopyrite compounds, and its relation with the elastic properties were addressed. Meanwhile, the lattice, electronic, and phonon behavior were examined and the findings were presented systematically.

2. METHOD AND COMPUTATION

This study was performed to comprehend the peculiar physical nature of the $ZnSiP_2$ compound. For this purpose, the Fm-3m and I-42d phases were constructed using the Vienna ab initio simulation package (VASP) (Kresse & Furthmüller, 1996), a widely preferred software, and the pseudo potential projector augmented wave (PAW) method was employed within the generalized gradient approximation of Perdew, Burke, and Ernzerhof (1996) (GGA-PBE). The wave functions were expanded in a plane-wave basis set with a cutoff energy of 650 eV. Pseudo-atomic calculations were considered for Zn: [Ar] $3d^{10}4s^2$, P: [Ne] $3s^2$ $3p^3$, and Si: [Kr] $4d^{10}$ $5s^2$ $5p^2$, and numerical integration in the Brillouin zone was carried out by the Monkhorst-Pack scheme. The k-point meshes were set for the Fm-3m and I-42d phases as 12x12x12 and 11x11x6, respectively. The forces exerted on the atoms and the energy difference between two consecutive iterations in an atomic relaxation loop were specified as less than 10^8 eV per unit cell and 10^6 eV/Å, respectively. The stress-strain method was chosen to derive the mechanical parameters from the estimated elastic constants, and the PHONOPY code (Togo, 2023) considering supercell approximations was utilized to examine the vibrational properties. Ultimately, the dielectric function components were computed by carrying out the Kramers-Kronig transformation.

3. RESULTS AND DISCUSSION

3.1. Structural Properties

The Murnaghan equation of state was used to optimize unit cell volume of $ZnSiP_2$ crystal for the B1 (Fm-3m) and chalcopyrite (I-42d) structures. The equilibrium lattice constants, bulk modulus, and its pressure derivative corresponding to the minimum total energy were computed at different volumes for each, and consequently, the stability comparison is depicted in Figure 2 utilizing the energy versus volume graph. Evidently, I-42d is more stable than Fm-3m. The optimized values of the parameters mentioned above were derived from the minima of the plotted curves, and presented in Table 1 along with other theoretical and experimental results.

The lattice constant and bulk modulus (B_0) of Fm-3m are slightly smaller by 0.03% and 0.58%, respectively, than the closest result obtained using the same approach within another simulation package. However, the lattice constants a, c and the B_0 value of I-42d are 0.23%, 0.73%, and 4.30% higher, respectively, compared to the nearest experimental reference. The discrepancy directions of this output data are consistent with the GGA-PBE method.

Table 1

Calculated equilibrium lattice constants, bulk modulus (B_0), and the pressure derivative of bulk modulus (B_0') with the other theoretical and experimental results for $ZnSiP_2$

Phase	Reference	a (Å)	c (Å)	B_0 (GPa)	B_0' (GPa)
	Theoretical				
Fm-3m	This Study (GGA-PBE/VASP)	6.2162		81.8	4.57
	Arab et al., 2012 (GGA-PW91/VASP)	6.2000		83.0	4.45
	Ouahrani, 2013 (GGA-PBE/WIEN2k)	6.2178		82.28	4.54
I-42d	This Study (GGA-PBE/VASP)	5.4196	10.5294	82.4	4.31
	Arab et al., 2012 (GGA-PW91/VASP)	5.4000	10.5000	86.29	4.16
	Ouahrani, 2013 (GGA-PBE/WIEN2k)	5.4294	10.5330	84.28	4.42
	Kumar & Tripathy, 2014 (LDA/CASTEP)	5.398	10.435	79.30	4.770
	Bennacer et al., 2018 (LDA/WIEN2k)	5.407	10.451	100.360	4.979
	Tahri et al., 2017 (GGA/VASP)	5.42	10.53	85.35	
	Reddy et al., 2000 (Empirical Approximation)			81.93	
	Experimental				
	Basalaev et al., 2005	5.399	10.437		
	Abrahams & Bernstein, 1970	5.399	10.435		
	Deus & Schneider, 1983	5.4001	10.4359		
	Peña-Pedraza et al., 2012	5.4072	10.4539		
	Madelung, 2000	5.400	10.438		
	Vaipolin, 1973	5.399	10.436		
	Oshcherin, 1979			79	

Bennacer et al., conversely, obtained more accurate a and c parameters but quite overestimated B_0 and B_0' by LDA potential described in WIEN2k program package (Bennacer et al., 2018). The calculated minimum energy (E_0) values are -15.53 eV and -18.76 eV and cohesive energy (E_{coh}) values per one formula unit are -1.74 eV and 1.49 eV for Fm-3m and I-42d, respectively. Herein, the positive E_{coh} value indicates the phase stability of I-42d, whereas the opposite is the case for Fm-3m.

In order to identify the disorder in a 2x2x2 supercell, Tahri et al. (2017) carried out a theoretical investigation of distorted Fm-3m at low pressure and rather ordered Fm-3m at high pressure, and the relevant parameters were presented. Furthermore, Yuan et al. (2021) obtained the bulk modulus and pressure derivative of the bulk modulus of $ZnSiP_2$ at ambient pressure fitting the experimental results by the third order Birch-Murnaghan equation of state. Now, let us focus back on Figure 2 indicating a phase transition from I-42d to Fm-3m.

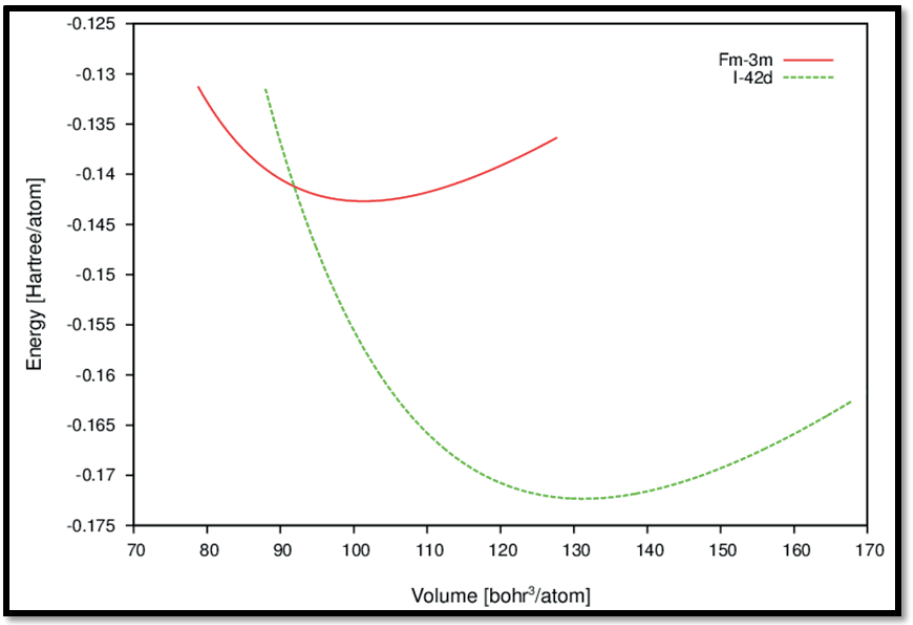

Figure 2. The energy vs volume graph of $ZnSiP_2$ compound.

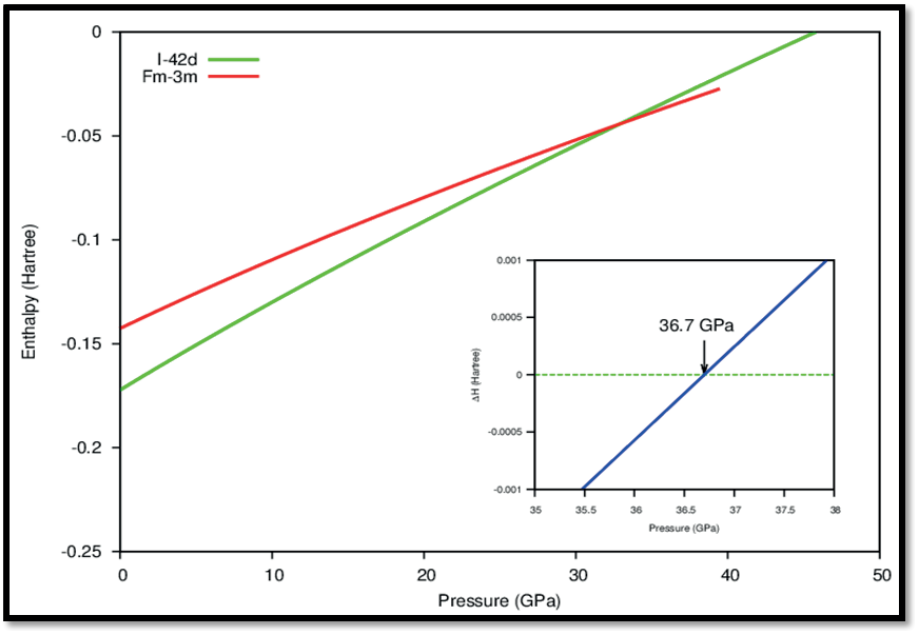

Figure 3. The enthalpy vs pressure graph of $ZnSiP_2$ compound.

Determination of the Gibbs free energy at 0 K allows one to compute the transition pressure (P_t), referring to the point of intersection between the related enthalpy changes (ΔH) - pressure (P) curves of the two phases. By considering Figure 3, which shows the enthalpy dependence on pressure for both, Pt was found to be 36.7 GPa through ΔH - P lines given in the inset. The other papers reported the P_t value in the range of 23.23-35 GPa (Ouahrani, 2013; Tahri et al., 2017; Bhadram et al., 2017). Besides, Yuan et al. stated that the phase transition for $ZnSiP_2$ had been experimentally observed to occur at 23.3 GPa and continued till 36.7 GPa (Yuan et al., 2021) which is in complete agreement with our finding.

3.2. Electronic Properties

Discussing the electronic properties of $ZnSiP_2$ is a crucial step to analyze its optical characteristics in terms of practical requirements. Within this framework, the band structure along the high symmetry directions in the first Brillouin zone and the partial density of states (PDOS) for I-42d and Fm-3m were calculated. The corresponding graphs are displayed in Figure 4 with the Fermi energy level (E_f) positioned at 0 eV. The absence of an energy band gap (E_g) during the E_f line in Figure 4 confirms the metallic character of Fm-3m, whereas I-42d exhibits a semiconducting behavior with a direct band gap of 1.3 eV at the Γ point.

In previous studies, theoretical E_g values obtained from different potential approaches vary between 1.12 eV and 1.42 eV (Basalaev et al., 2005; Rashkeev et al., 1999; Kumar & Tripathy, 2014; Taychour et al., 2019; Chiker et al., 2004; Chiker et al., 2011; Tripathy & Kumar, 2014; Arab et al., 2012), and the present E_g falls within this range. However, the experimental results vary from 2.01 eV to 2.07 eV (Shay et al., 1973; MacKinnon, 1985; Goodman, 1991; Ambrazevičius et al., 1979; Yuan et al., 2021), and Martinez et al. (2015) calculated this value to be 2.075 eV at room temperature. Since the GGA-PBE method typically underestimates the band range, the significant disparity can be minimized by employing mBJ exchange potential as in the studies of Bennacer et al. (2018) and Ouahrani (2013) (E_g is 2.07 eV and 1.881 eV, respectively) or directly the scissor correction method, which fits E_g to the experimental result (Tripathy & Kumar, 2014). Another paper reported a band gap of 1.98 eV (Ullah et al., 2014) utilizing the measured lattice parameters via the EV-GGA scheme implemented in the WIEN2k software.

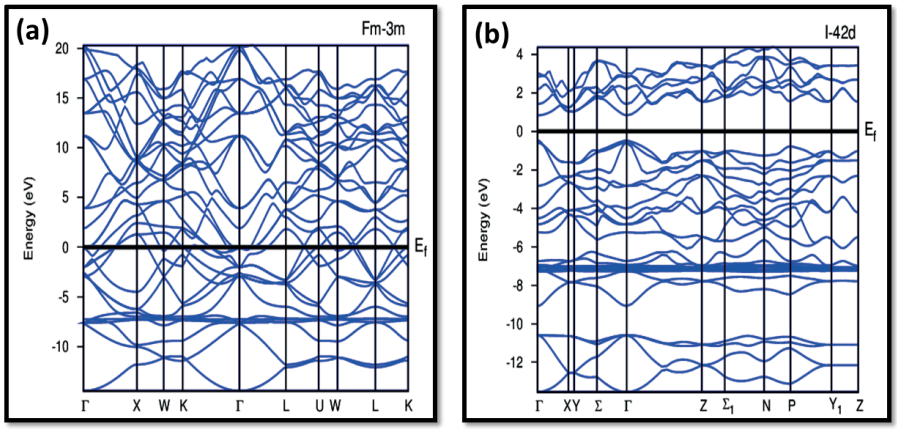

Figure 4. The electronic band structures of the (a) Fm-3m and (b) I-42d phases of $ZnSiP_2$, respectively.

The bonding nature of $ZnSiP_2$ (Zn: $[Ar]3d^{10}\ 4s^2$, P: $[Ne]3s^2\ 3p^3$ and Si: $[Kr]4d^{10}\ 5s^2\ 5p^2$) in the Fm-3m and I-42d phases was also clarified with the PDOSs in Figure 5. The maximum peaks of each are mainly caused by the Zn-3d atom, while the contributions of the P-3s and Si-5s atoms are almost negligible. In the conduction band region of PDOSs, an overlap is observed between some certain peaks arising from the P-3p and Si-5p states. This reveals the hybridization between the atoms of P and Si, thereby the covalent bonding in $ZnSiP_2$. Moreover, the conduction band form of the total DOSs is superimposed by the P-3p states.

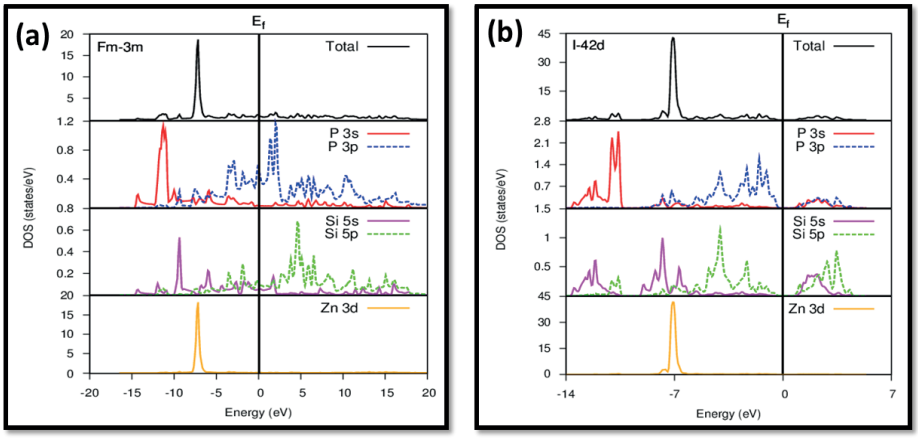

Figure 5. Total and partial density of states of the (a) Fm-3m and (b) I-42d phases of $ZnSiP_2$, respectively.

3.3. Elastic Properties

Elastic constants are essential parameters of crystals that enable the determination of their elasticity, mechanical stability, and stiffness. Furthermore, examination of the associated quantities are required to comprehend the chemical bonding and material cohesion. Hence, primarily in this step, the second-order elastic constants (C_{ij}) of $ZnSiP_2$ were obtained using the "stress-strain" relations, and the computed values of zero-pressure C_{ij} for Fm-3m and I-42d are listed in Table 2.

Table 2

Calculated elastic constants (C_{ij}, GPa) of $ZnSiP_2$ and other theoretical references

Phase	Stability	Reference	C_{11}	C_{12}	C_{13}	C_{33}	C_{44}	C_{66}
Fm-3m	YES	This study	60.28	101.82			11.64	
		Arab et al., 2012	27.32	115.15			-1.031	
I-42d	NO	This study	138.73	57.72	62.10	133.56	94.50	92.12
		Arab et al., 2012	136.68	54.79	60.79	133.11	71.91	69.63
		Kumar & Tripathy, 2014	118.93	39.96	38.17	105.42	54.75	48.77
		Tahri et al., 2017	135.71	57.10	63.26	129.52	69.34	66.20
		Verma et al., 2012	90.9	56.8	54.0	85.2	31.2	28.4
		Neumann et al., 2004	96	57	54	84	32	32

The Born stability criteria for the cubic and tetragonal phases are as follows:

$$\begin{aligned} &(C_{11}-C_{12}>0)\,;\,(C_{11}+C_{12}>0)\,;\,(C_{44}>0) \text{ and} \\ &(C_{11}, C_{33}, C_{44}, C_{66}>0)\,;\,(C_{11}>|C_{12}|)\,;\,(C_{11}C_{33}>(C_{13})^2)\,; \\ &(C_{11}+C_{12})\,C_{33}>2(C_{13})^2, \end{aligned} \tag{1}$$

respectively. Contrary to the mechanical instability of the Fm-3m phase, I-42d is mechanically stable through the data provided in Table 2 and the Born criteria. Therefore, I-42d is addressed after this stage of the research.

The I-42d phase is more resistant to compression than shear since C_{11} and C_{33} are much larger, and the ratios of C_{11}/C_{33}, C_{12}/C_{13}, and C_{44}/C_{66} were calculated to be 1.039, 0.929, and 1.026, respectively. That means the resistance to both compression and shear stress differs slightly depending on the directions in which the related forces are exerted. Therewithal, the aforementioned values of ~1 indicate a pseudo-cubic elastic response characterized by a small elastic anisotropy. This case in the chalcopyrite $ZnSiP_2$ is caused by the loss of the central positions of P atoms within the tetrahedron moving towards one of the cations; thus, two distinct bond lengths are formed as $d_{Zn\text{-}P}$ and $d_{Si\text{-}P}$. The degree of anisotropy can be given by the tetragonal distortion of c/2a = 0.97, which is expected to be 1 when the cation-anion distances are equal (Neumann et al., 2004; Zhang, 2017; Bhadram et al., 2017).

As can be seen in Table 2, the C_{ij} values reported by Verma et al. (2012) are compatible with those of Neumann et al. (2004) which are based on the rigid ion model. Verma et al. additionally took into acount a normalization factor and the ion charge theory. On the other hand, a marked difference from our findings is noticed due to the fact that this method does not consider the long-distance interactions underestimating C_{ij} (Neumann et al., 2004).

Table 3

Calculated shear modulus (G), Young modulus (E), Poisson ratio (ν), B/G ratio (via obtained B from elastic constants), Debye temperature (Θ_D), and longitudinal, transverse, and mean sound velocity (v_l, v_t, and v_m) of $ZnSiP_2$ and other theoretical references

Phase	Reference	G (GPa)	E (GPa)	ν	B/G	Θ_D (K)	v_l (m/s)	v_t (m/s)	v_m (m/s)
I-42d	This study	65.3	156.4	0.20	1.318	541.5	7203	4424	4882
	Ambrazevičius et al., 1979	55.45	136.4	0.23	1.556				
	Verma et al., 2012	48.598	110.45						
	Kumar & Tripathy, 2014		111.71	0.208					
	Kumar et al., 2009					444.79			
	Tripathy & Kumar, 2014					354.58			

The fundamental mechanical parameters of stable I-42d were derived from the obtained elastic constants via the Voigt-Reuss-Hill approximation (Hill, 1952), and are presented in Table 3 along with the other theoretical results. Despite having varying values, the references tend to give similar estimations of mechanical properties. The shear modulus (G) is smaller than the bulk modulus obtained from the elastic constants (B), implying less resistivity of $ZnSiP_2$ to shear in comparison with volume compression as also mentioned in the previous paragraphs. The steepness of the stress-strain line depicting the behavior of a material under tension is referred to as the Young modulus (E), which is a measure of stiffness. Herein, the high E value lies in the band between the stiffness of titanium and steel (Daalkhaijav, 2018). The calculated Poisson ratio (below the upper limit for noncentral forces $\nu = 0.25$) predicts a covalent bonding in the material, thereby confirming PDOS analysis in the section of *Electronic Properties*. Besides, the Pugh criterion relates to the plastic character that follows the elastic boundary of the stress-strain curve, and I-42d has a brittle nature since the *B/G* ratio is less than 1.75 (Arab et al., 2012). And last, the Debye temperature (Θ_D) is defined as the temperature of the highest frequency phonon mode. Θ_D was found to be 541.5 K in the present study, exceeding the value of 402 K for graphite (Tohei, Kuwabara, Oba, & Tanaka, 2006), and it suggests greater stiffness of $ZnSiP_2$. This material also requires more energy to activate all phonon modes, therefore, we expect the formation of high-frequency optical phonons. Aside from that, the longitudinal, transverse, and mean sound velocities are listed in Table 3.

3.4. Vibrational Properties

Many physical properties of solids, such as specific heat, thermal expansion, heat conduction, and electron-phonon interaction, depend on their vibrational properties. In this respect, the phonon band structure will provide much key information. The force constant matrices and phonon frequencies for $ZnSiP_2$ in I-42d phase were computed using superlattice approximation within the PHONOPY code. Subsequently, the phonon dispersion relation was obtained by the VASP package. The 2×2×2 super cell of 64 atoms was used for calculations in high symmetry directions and corresponding phonon dispersion curves are plotted in Figure 6.

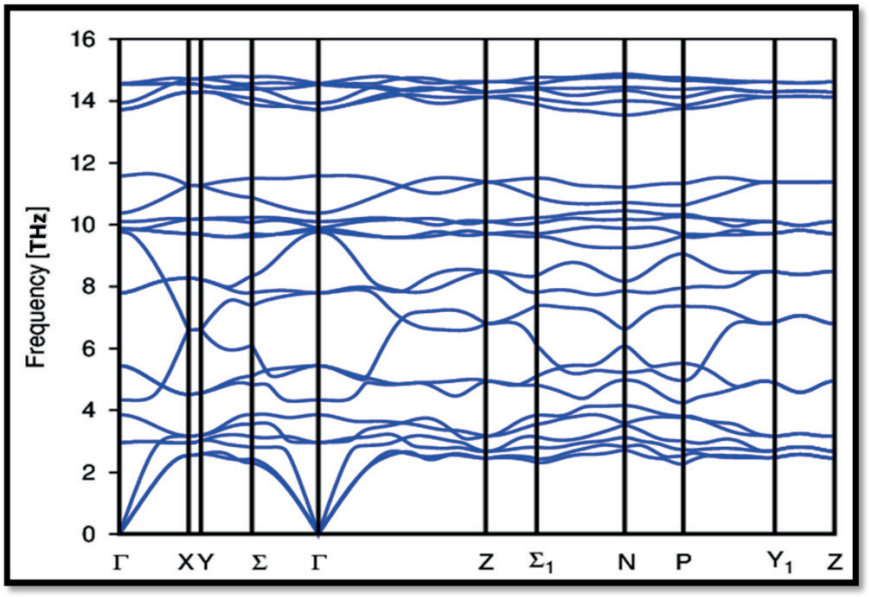

Figure 6. The phonon dispersion curves for the I-42d phase of $ZnSiP_2$.

The unit cell of I-42d has 8 atoms, including 2 Zn, 2 Si, and 4 P. Each atom can move in three distinct direction, giving the system a total of 24 degrees of freedom. It equals to the number of branches in the phonon graph, and the number of acoustic modes in which atoms always vibrate in phase is three, while the remaining 21 are optical modes. The transversal acoustic (TA) and some optical modes are almost degenerate along more symmetrical directions in the Brillouin zone. There is no gap between the acoustic and optical branches, leading to high-frequency oscillation (as the calculated Θ_D value predict in the previous section) for $ZnSiP_2$ due to the strong interaction these two modes have with one another (Xu et al., 2021). The absence of the negative phonon frequencies for any wave vector strongly supports the dynamical stability of this compound.

4. CONCLUSION

First-principles calculations based on density functional theory were used to study the structural, electronic, elastic, and vibrational properties of $ZnSiP_2$. The rocksalt Fm-3m and chalcopyrite I-42d phases were discussed in detail to comprehend the physical behavior of this material. Compared to the experimental result, GGA-PBE provided a reasonably accurate estimation of the bulk modulus; however, this method quite overestimated the lattice parameters due to the anisotropy along the z-axis. I-42d (a = 5.4196 Å and c = 10.5294 Å) was determined to be more energetically stable than Fm-3m (a = 6.2162 Å) according to the energy versus volume graph. The transition pressure (P_t) from Fm-3m to I-42d was found to be ~37 GPa, which is consistent with the observed upper limit of phase transition for $ZnSiP_2$. I-42d was predicted to be mechanically stable, contrary to Fm-3m, via the Born criteria, including elastic constant relations. The PDOS and Poisson ratio (ν) analyses suggested covalent bonding in the I-42d phase of $ZnSiP_2$. There are no negative phonon frequencies, indicating dynamical stability. The modes oscillate at high frequency, requiring more energy to get activated, pointing out the stiff and brittle nature of $ZnSiP_2$, which is also confirmed with elastic parameters. Fm-3m is metallic, possessing no gap around Fermi level, whereas I-42d has a semiconducting character with a band gap of 1.3 eV. This finding is significantly below the measurements, therefore it should be noted that the scissor correction method or TB-mBJ approach may be a great solution to obtain realistic electronic character, and thus related physical features can be stated more correctly.

REFERENCES

Abrahams, S. C., & Bernstein, J. L. (1970). Crystal Structure of Luminescent ZnSiP2. *The Journal of Chemical Physics*, *52*(11), 5607–5613. https://doi.org/10.1063/1.1672831

Ambrazevičius, G., Babonas, G., & Šileika, A. (1979). Reflectance spectra of CdSiP2 and ZnSiP2. *Physica Status Solidi (B)*, *95*(2), 643–647. https://doi.org/10.1002/pssb.2220950238

Arab, F., Ali Sahraoui, F., Haddadi, K., & Louail, L. (2012). Ab initio investigations of structural, elastic and electronic properties of ZnSiP2: Pressure effect. *Computational Materials Science*, *65*, 520–527. https://doi.org/10.1016/j.commatsci.2012.08.012

Basalaev, Y. M., Gordienko, A. B., & Poplavnoi, A. S. (2005). Electronic Structure of Triple Phosphides MgSiP2, ZnSiP2, and CdSiP2. *Russian Physics Journal*, *48*(1), 78–83. https://doi.org/10.1007/s11182-005-0087-0

Bennacer, H., Boukortt, A., Meskine, S., Hadjab, M., Ziane, M. I., & Zaoui, A. (2018). First principles investigation of optoelectronic properties of ZnXP2 (X = Si, Ge) lattice matched with silicon for tandem solar cells applications using the mBJ exchange potential. *Optik*, *159*, 229–244. https://doi.org/10.1016/j.ijleo.2018.01.079

Bhadram, V. S., Krishna, L., Toberer, E. S., Hrubiak, R., Greenberg, E., Prakapenka, V. B., & Strobel, T. A. (2017). Pressure-induced structural transition in chalcopyrite ZnSiP2. *Applied Physics Letters*, *110*(18), 1–5. https://doi.org/10.1063/1.4981889

Chiker, F., Abbar, B., Bresson, S., Khelifa, B., Mathieu, C., & Tadjer, A. (2004). The reflectivity spectra of ZnXP2 (X=Si, Ge, and Sn) compounds. *Journal of Solid State Chemistry*, *177*(11), 3859–3867. https://doi.org/10.1016/j.jssc.2004.07.020

Chiker, F., Kebbab, Z., Miloua, R., & Benramdane, N. (2011). Birefringence of optically uni-axial ternary semiconductors. *Solid State Communications*, *151*(21), 1568–1573. https://doi.org/10.1016/j.ssc.2011.07.026

Daalkhaijav, U. (2018). *Rheological Techniques in Characterization and Aiding in the Modification of Soft Matter*. (Doctoral dissertation, p. 15). Oregon State University, Oregon, USA. (Figure 1.2.(a) Scale of Young's modulus (E) values of common materials and refs in). Retrieved from

https://www.researchgate.net/publication/325593461_Rheological_Techniques_in_Characterization_and_Aiding_in_the_Modification_of_Soft_Matter

Deus, P., & Schneider, H. A. (1983). Thermal Expansion of the Diamond-Like Semiconducting Compound ZnSiP2, within the Temperature Range 20 to 300 K. *Physica Status Solidi (A)*, *79*(2), 411–415. https://doi.org/10.1002/pssa.2210790211

Goodman, C. H. L. (1991). Semiconductor and non-linear optical materials. *Semiconductor Science and Technology*, *6*(8), 725–729. https://doi.org/10.1088/0268-1242/6/8/001

Hill, R. (1952). The Elastic Behaviour of a Crystalline Aggregate. *Proceedings of the Physical Society. Section A*, *65*(5), 349–354. https://doi.org/10.1088/0370-1298/65/5/307

Hu, C. L., Han, Y. X., Fang, Z., & Mao, J. G. (2023). Zn2BS3Br: An Infrared Nonlinear Optical Material with Significant Dual-Property Enhancements Designed through a Template Grafting Strategy. *Chemistry of Materials*, *35*(6), 2647–2654. https://doi.org/10.1021/acs.chemmater.3c00262

Jackson, A., Ohmer, M., & LeClair, S. (1997). Relationship of the second order nonlinear optical coefficient to energy gap in inorganic non-centrosymmetric crystals. *Infrared Physics & Technology*, *38*(4), 233–244. https://doi.org/10.1016/s1350-4495(97)00017-0

Kresse, G., & Furthmüller, J. (1996). Efficient iterative schemes forab initiototal-energy calculations using a plane-wave basis set. *Physical Review B*, *54*(16), 11169–11186. https://doi.org/10.1103/physrevb.54.11169

Kumar, V., & Tripathy, S. (2014). First-principle calculations of the electronic, optical and elastic properties of ZnSiP2 semiconductor. *Journal of Alloys and Compounds*, *582*, 101–107. https://doi.org/10.1016/j.jallcom.2013.08.025

Kumar, V., Shrivastava, A., Banerji, R., & Dhirhe, D. (2009). Debye temperature and melting point of ternary chalcopyrite semiconductors. *Solid State Communications*, *149*(25–26), 1008–1011. https://doi.org/10.1016/j.ssc.2009.04.003

Mackinnon, A. (1985). II-IV-V2 Compounds - Structure and Energy Gaps. In O. Madelung (Ed.), *Landolt-Börnstein - Numerical Data and Functional Relationships in Science and Technology - New Series Group III: Semiconductors / Physics of Ternary Compounds* (Vol. 17h, p. 69): Springer-Verlag.

Madelung, O., Rössler, U., & Schulz, M. (Eds.). (2000). Zinc silicon phosphide (ZnSiP2) crystal structure, lattice parameters, thermal expansion, Debye temperature, melting point, hardness. In *Landolt-Börnstein-Group III: Condensed Matter / Ternary Compounds - Organic Semiconductors* (Vol. 41E, p. 417): Springer-Verlag. https://doi.org/10.1007/10717201_417

Martinez, A. D., Ortiz, B. R., Johnson, N. E., Baranowski, L. L., Krishna, L., Choi, S., . . . Tamboli, A. C. (2015). Development of ZnSiP2 for Si-Based Tandem Solar Cells. *IEEE Journal of Photovoltaics*, *5*(1), 17–21. https://doi.org/10.1109/jphotov.2014.2362305

Medvedkin, G. A., Takayuki Ishibashi, T. I., Takao Nishi, T. N., Koji Hayata, K. H., Yoichi Hasegawa, Y. H., & Katsuaki Sato, K. S. (2000). Room Temperature Ferromagnetism in Novel Diluted Magnetic Semiconductor Cd1-xMnxGeP2. *Japanese Journal of Applied Physics*, *39*(10A), L949–L951. https://doi.org/10.1143/jjap.39.l949

Naveh, D., & Kronik, L. (2006). Spin-polarized electronic structure of Mn–IV–V2 chalcopyrites. *Physica Status Solidi (B)*, *243*(9), 2159–2163. https://doi.org/10.1002/pssb.200666806

Neumann, H. (2004). Lattice dynamics and related properties of AIBIII and AIIBIV

compounds, I. Elastic constants. *Crystal Research and Technology*, *39*(11), 939–958. https://doi.org/10.1002/crat.200410280

Oshcherin, B. N. (1979). On surface energy and compressibility of $A^2B^4C_2^5$ semiconducting compounds. *Physica Status Solidi (A)*, *51*(2), K175–K179. https://doi.org/10.1002/pssa.2210510261

Ouahrani, T. (2013). Chemical and physical insight on the local properties of the phosphides XSiP2 (X = Be, Mg, Cd, Zn and Hg) under pressure: from first principles calculations. *The European Physical Journal B*, *86*(9), 1–11. https://doi.org/10.1140/epjb/e2013-40415-6

Peña-Pedraza, H., López-Rivera, S., Martin, J., Delgado, J., & Power, C. (2012). Crystal and phonon structure of ZnSiP2, a II-IV-V2 semiconducting compound. *Materials Science and Engineering: B*, *177*(16), 1465–1469. https://doi.org/10.1016/j.mseb.2011.12.046

Perdew, J. P., Burke, K., & Ernzerhof, M. (1996). Generalized Gradient Approximation Made Simple. *Physical Review Letters*, *77*(18), 3865–3868. https://doi.org/10.1103/physrevlett.77.3865

Rashkeev, S. N., Limpijumnong, S., & Lambrecht, W. R. L. (1999). Second-harmonic generation and birefringence of some ternary pnictide semiconductors. *Physical Review B*, *59*(4), 2737–2748. https://doi.org/10.1103/physrevb.59.2737

Reddy, R., Nazeer Ahammed, Y., Rama Gopal, K., Abdul Azeem, P., Rao, T., & Mallikarjuna Reddy, P. (2000). Optical electronegativity, bulk modulus and electronic polarizability of materials. *Optical Materials*, *14*(4), 355–358. https://doi.org/10.1016/s0925-3467(00)00004-5

Scholl, & Tang. (1973). Nonlinear Optical Properties of II-IV-V2 Semiconductors. *Physical Review B*, *8*(10), 4607–4611. https://doi.org/10.1103/physrevb.8.4607

Shay, J. L., & Wernick, J. H. (2013). *Ternary Chalcopyrite Semiconductors: Growth, Electronic Properties, and Applications: International Series of Monographs in the Science of the Solid State* (Vol. 7): Pergamon.

Shay, J. L., Tell, B., Buehler, E., & Wernick, J. H. (1973). Band Structure of ZnGeP2and ZnSiP2— Ternary Compounds with Pseudodirect Energy Gaps. *Physical Review Letters*, *30*(20), 983–986. https://doi.org/10.1103/physrevlett.30.983

Taguida, N., Benlamari, S., Meradji, H., Chouahda, Z., Ghemid, S., Gasmi, M., . . . Bin-Omran, S. (2023). First-principles investigations of physical properties of CdXP2 (X = Si, Ge, and Sn) ternary chalcopyrite. *Indian Journal of Physics*, 1–14. https://doi.org/10.1007/s12648-023-02725-9

Tahri, K., Ouahrani, T., & Pilmé, J. (2017). Understanding phase transition in the ZnSiP2 chalcopyrite, a quantum chemical topology study. *Theoretical Chemistry Accounts*, *136*(10), 1–9. https://doi.org/10.1007/s00214-017-2159-y

Taychour, B., Zriouel, S., & Drissi, L. B. (2018). Half Metallic Ferromagnetic Character in ZnXP2 (X = Ge, Si) Chalcopyrites Doped with Mn. *Journal of Superconductivity and Novel Magnetism*, *32*(5), 1333–1339. https://doi.org/10.1007/s10948-018-4820-7

Togo, A. (2023). First-principles Phonon Calculations with Phonopy and Phono3py. *Journal of the Physical Society of Japan*, *92*(1), 1–21. https://doi.org/10.7566/jpsj.92.012001

Tohei, T., Kuwabara, A., Oba, F., & Tanaka, I. (2006). Debye temperature and stiffness of carbon and boron nitride polymorphs from first principles calculations. *Physical Review B*, *73*(6), 1–7. https://doi.org/10.1103/physrevb.73.064304

Tripathy, S. K., & Kumar, V. (2014). Density functional theory studies of electronic and thermal properties of znsip semiconductor. *International Journal of Electronics Signals and Systems*, *3*(3), 165–168. https://doi.org/10.47893/ijess.2014.1160

Ullah, S., Murtaza, G., Khenata, R., Reshak, A., Hayat, S., & Bin Omran, S. (2014). Towards from indirect to direct band gap and optical properties of XYP2 (X=Zn, Cd; Y=Si, Ge, Sn). *Physica B: Condensed Matter*, *441*, 94–99. https://doi.org/10.1016/j.physb.2014.02.021

Vaipolin, A. A. (1973). Specific Defects in the Structure of $A^2B^4C_2^5$ Compounds. *Fizika Tverdogo Tela*, *15*(5), 1430–1435.

Verma, A., Sharma, S., Bhandari, R., Sarkar, B., & Jindal, V. (2012). Elastic properties of chalcopyrite structured solids. *Materials Chemistry and Physics*, *132*(2–3), 416–420. https://doi.org/10.1016/j.matchemphys.2011.11.047

Wang, Y., Zhao, K. J., Tao, D. P., Zhai, F. G., Yang, H. B., & Zhang, Z. Q. (2018). Application of pyrite and chalcopyrite as sensor electrode for amperometric detection and measurement of hydrogen peroxide. *RSC Advances*, *8*(9), 5013–5019. https://doi.org/10.1039/c7ra13628e

Xu, Z., Luo, B., Siu, Z. B., Chen, Y., Huang, J., Li, Y., . . . Jalil, M. B. (2021). Phonon spectrum and electronic structures of WTe2: A first-principles calculation. *Physics Letters A*, *389*, 127081:1-5. https://doi.org/10.1016/j.physleta.2020.127081

Yu, Y., Zhao, B., Zhu, S., Gao, T., Hou, H., & He, Z. (2012). Ab initio study of the linear and nonlinear optical properties of chalcopyrite CdGeAs2. *Journal of Solid State Chemistry*, *185*, 264–270. https://doi.org/10.1016/j.jssc.2011.10.014

Yuan, Y., Zhu, X., Zhou, Y., Chen, X., An, C., Zhou, Y., . . . Yang, Z. (2021). Pressure-engineered optical properties and emergent superconductivity in chalcopyrite semiconductor ZnSiP2. *NPG Asia Materials*, *13*(1), 1–7. https://doi.org/10.1038/s41427-021-00285-0

Zhang, Y. (2017). Bandgap nature of chalcopyrite ZnXP2 (X = Si, Ge, Sn). *Computational Materials Science*, *133*, 152–158. https://doi.org/10.1016/j.commatsci.2017.03.016

Chapter 2

MARS WATER LOSS

E. Nihal ERCAN[1]

1 Prof. Dr., Boğaziçi University, Physics Department

INTRODUCTION

Mars is a dry and freezing planet with a thin atmosphere and low atmospheric pressure. It seems that the planet cannot satisfy the conditions for continuity of life today. Yet, studies show that the red planet once had an enormous amount of water which as we know is the key ingredient for a habitable environment. It is suggested that life may have arisen on Mars when it was wetter and perhaps it still continues. Even though these were all just wrong assumptions, research in this field is really important since Mars once showed Earth-like conditions and could be a place for human colonization in the future.

Studies on the Martian surface, geology, chemical compounds, weather, and atmosphere have been going on for a long time. The existence of past and present water on Mars is an area that continues at full speed. Mars lost most of its water. The remaining water is mostly in the form of ice or vapor in the atmosphere because of Mars' low atmospheric pressure and freezingly cold temperature. There are various theories among scientists about how this enormous amount of water disappeared throughout the centuries.

One of the theories is that water may be trapped beneath the surface and stored as mineral structures. It is thought that trapped water can cover the surface of the planet from 100m to 1000m. Also, it is suggested from Mars Express data that Mars has liquid water as a saltwater lake under the ice. Besides this, the other opinion is that water escaped to space. In the upper atmosphere of Mars, vapor separated as hydrogen and oxygen molecules, and lighter hydrogen was lost into space. This leakage can be observed today and new evidence shows that its rate is affected by seasons and dust storms. Overall, these theories should be held together to understand the mechanism behind when, where, and how Mars lost its water.

MISSIONS OF WATER ON MARS

The Mars missions show that Mars's surface is covered with dry riverbeds, flood plains, gullies, channels, valley networks, and formations caused by rainfall or severe flooding. It suggests that Martian geology was affected by the presence of water in its evolution. Also, a huge amount of underground ice has been detected. Besides these findings, rocks and minerals which can be formed due to a water presence were detected. This evidence and much more support that billions of years ago, Mars had enough water to cover one-fifth of its surface.

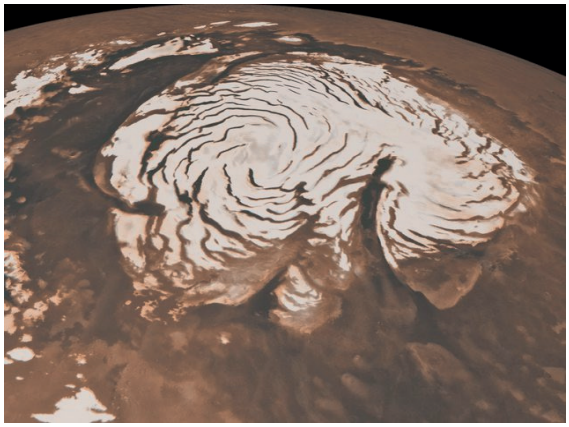

Figure 1. North polar region of Mars. Credit: NASA

The Mariner program lasted between 1962 and 1973. It was a mission that was held by NASA to search Mars, Mercury, and Venus. It was developed in NASA's Jet Propulsion Lab (JPL). It consists of ten different projects. Mariner 3, Mariner 4, Mariner 6, Mariner 7, Mariner 8, Mariner 9 studied Mars. The third and the eighth ones did not succeed in their missions.

Mariner 9 was launched in 1971 and successfully orbited Mars. It took over seven thousand photos till October 1972. It collected data from Mars's surface and atmosphere.

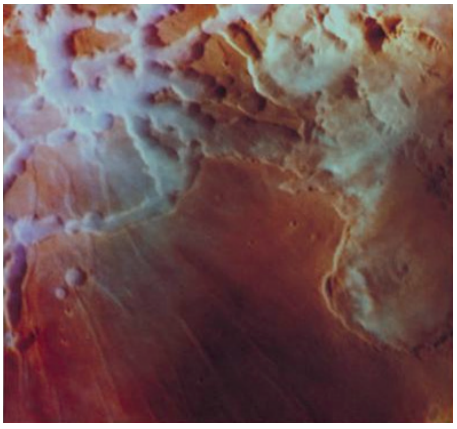

Figure 2. Martian riverbeds and craters captured during Mariner 9 mission. Credit: NASA

By findings such as dry river beds, canyons, water erosion, and water deposition from Mariner 9, evidence has been found to conclude that Mars had water once.

In 1975, NASA started *Viking program*. It consisted of Viking 1 and Viking 2 probes which consisted of two parts: one was the orbiter to photograph from orbit and the lander to surface research. Mars' surface and atmosphere have been studied successfully. Also, it searched for life signals on Mars. Unfortunately, no evidence of life has been found from this mission. Findings gave important evidence of water on Mars.

Figure 3) Viking Mosaic of Ravi Vallis. Credit:NASA

In many areas, river valleys were detected that showed floods of water traveling thousands of kilometers splitted through dams, carved deep valleys, and eroded grooves into bedrock. Evidence on rainfall were found as branched valley networks in the southern hemisphere and volcanoes flanks which

look like they were submitted to rain once. And some other results of the Viking program beside these, showed that enormous amounts of water once existed on Mars and suggest that it still contains some part of these water in the present.

Another Mars mission was *Mars Global Surveyor* which was held by the Jet Propulsion Laboratory of NASA. It launched in 1996 and the mission continued until 2007. It has studied the surface, interior and atmosphere of Mars. Mission showed that Mars has weather patterns and dust storms that are repeating in the same location and at the same time of the year.

Mars Global Surveyor studied mineral composition too by its Thermal Emission Spectrometer. TES found evidence on water in ancient times of the planet. Gullies and debris flows created by liquid water were found which were thought to be occured recent times.

Some channels in Nanedi Valleys and Nirgal Vallis were found that displayed inner channels. Also, presence of liquid water observed in some craters photos.

Mars Pathfinder which landed on Mars in 1997 studied Mars temperature and pressure. It found that

Mars is too cold and has very low-pressure water to occur in liquid or ice form.

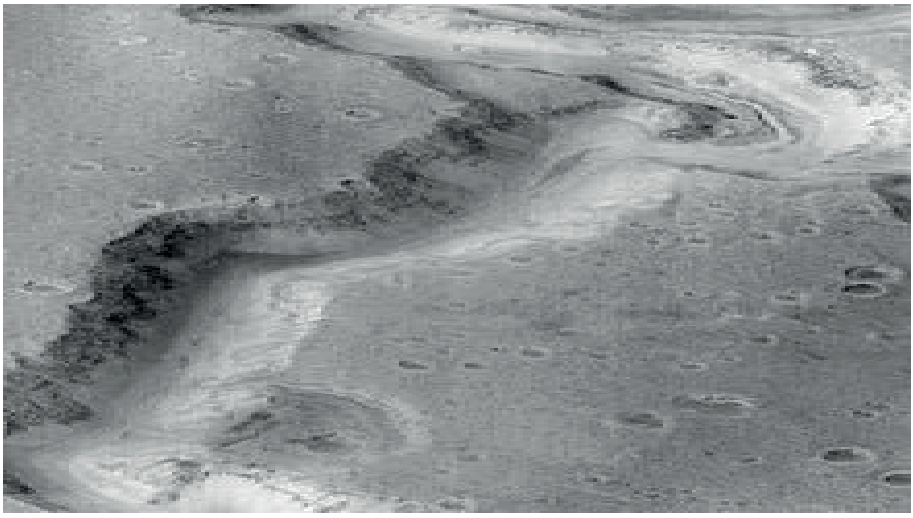

Figure 4) Inner challis observed in Nanedi Valles. Credit: NASA

NASA launched *2001 Mars Odyssey* in 2001 to map the chemical elements and minerals on the surface of Mars. The mission was extended and is still continuing today. It made it possible to receive the most detailed map of Mars so far.

Images that were sent by the Odyssey confirm great amounts of water flowed across the Martian surface; deltas, branching valleys, and layers caused by under lakes are detected. Most importantly enormous amounts of buried water were found just beneath the surface of polar regions.

Mars Express is ESA's Mars orbiter mission which arrived on the planet in 2003. The mission is still going on today. It is found that under the south pole, there is possibly subsurface water. Also, it discovered minerals that should have occurred by water presence.

Spirit and *Opportunity* were NASA's Mars exploration rovers that landed on different sites of Mars in 2004. Both of them studied the rocks and soils to find evidence of past Mars water. As a result, they found clues that Mars' environment was wetter and could be habitable in the past.

Mars Reconnaissance Orbiter (MRO) was launched in 2005 by NASA to study the geology and climate of Mars. The MRO is still in the orbit of Mars and maintains its mission. HİRISE is the camera of the orbiter that took high-resolution images helping study the planet properly.

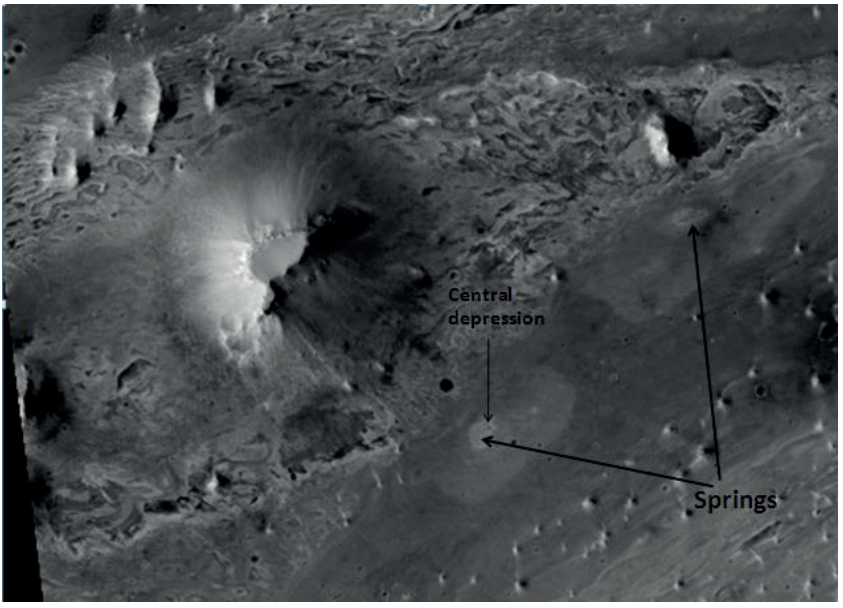

Figure 5) Springs in Vernal Crater. Credit: NASA

By radar measurements, it is found that the north polar ice cap has 821,000 cubic kilometers of ice water. Also, new craters that contain pure ice water have been detected. These waters sublimate after they are exposed. In 2011, it was detected that salty water was flowing on the surface or subsurface of Mars. In addition to these hot springs that keep the signs of life for many years and chlorine that can be residue of lakes which could be habitable places were found. It is a great opportunity to search for microbial life.

The presence of water ice was confirmed by the *Phoenix* lander in 2008. Various chemicals were detected and scientists thought that when they mix with water, the freezing point could become lower. Also, snow and clouds that are composed of water ice were observed. It is confirmed that in the past the climate was wetter and warmer.

Figure 6) Photo from Phoenix showing water ice on the Martian surface. Credit: NASA

NASA's *Curiosity* rover is designed to explore the Gale crater on Mars. It found persistent liquid water existed in the past. Besides this, it was detected that much of the Martian atmosphere lost occurring to space through the top of it. The chemicals that were present in the past have the right components to provide drinkable water.

MARS WATER LOSS:

According to the results of scientists' research, there were enormous water resources on Mars billions of years ago. Unfortunately, this water couldn't hold onto the planet up to today. Mars lost most of its water and nowadays some amounts of water can be detected. The existence of water on Mars is in different forms. There is water in the poles in the ice form and maybe there is liquid water under the ice layers. Also, water exists in the Martian atmosphere as a vapor form.

Water has been escaping from Mars' upper atmosphere for billions of years. This leakage is an ongoing situation today. The escape happens when the vapor situated in the lower atmosphere rises to the upper atmosphere and splits into its atoms. Sunlight breaks the bounds in the water molecule and two hydrogen and one oxygen atoms are released. Hydrogen atoms with enough energy to beat Mars' gravitation then leave the atmosphere and are lost in space.

Observations show that water escape does not display a steady pattern. The escape rate changes from time to time. It is detected by NASA's MAVEN

mission and ESA's Mars Express that the Mars-Sun distance that affects the Mars weather and climate and also dust storms happening on the planet have an impact on hydrogen escape.

The measurement obtained from the SPICAM instrument of Mars Express highlights how vapor distributions change over altitude. Water vapor changing between 0 and 100 km over eight Martian years was evaluated by Anna Fedorova and colleagues.

When Mars is in the closest distance to the Sun which is 249 million km, vapor can exist up to 60 km. Otherwise, when the planet gets close to the Sun at most 207 million km, vapor altitude reaches 90 km. The temperature rising led to vapor and not to freeze. That is why the speed of escape is higher in warmer seasons.

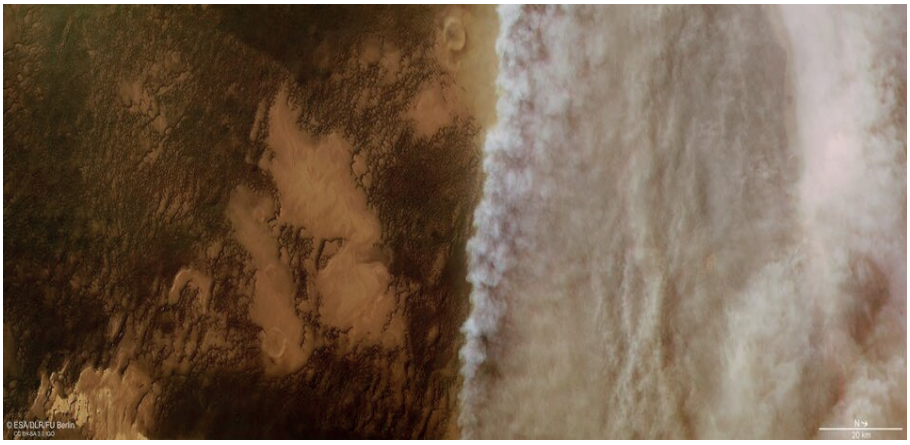

Figure 7) Dust storm on Mars. Credit: NASA

When global dust storms are seen on the planet, the atmosphere becomes warmer. In the measured dust storms time, it is seen that vapor reaches higher altitudes up to 80 km. Jean-Yves Chaufray and his colleagues' study on hydrogen density in the upper atmosphere of Mars supports the idea that global dust storms increase the escape rate of hydrogen.

Even though these studies reveal a mechanism of water loss, they cannot satisfy the calculations completely. According to the findings, a water layer two meters deep escapes to space every year. But, the loss of water at about four billion years is much more than this observation. According to this, water should be trapped underground or in the past escaped faster than calculated today.

CONCLUSION

Mars is an exciting planet for humankind. Even though it is not known if the planet once provided a home for living and it seems that it is not a habitable place today, there is still hope for human colonization in the future. Studies show that once the planet was covered with water and sustained Earth-like conditions. Exploring the planet's past and future characteristics will give us important insights.

The Mars missions that were carried out for a long time examined Mars' geology, weather, atmosphere, and mineral compounds. The results of these missions give a lot of evidence that enormous amounts of water covered the Martian surface billions of years ago. Deltas, river valleys, channels, chemicals that occurred as a result of water presence, and much more were detected.

Nowadays, we can only witness the leftovers of these waters. Mars seems to have lost most of its water and still continues to lose. A part of the present water is in the form of ice located at the poles since the planet is extremely cold. Some studies detected liquid water under the ice cubes. Also, water is present as vapor in the atmosphere and it leaks to space from there.

When water vapor located in the lower atmosphere travels to the upper part, vapor splits into its molecules as two hydrogen and an oxygen atom. Hydrogen atoms then leave the atmosphere and escape to space. This process is happening at an unstable speed at different times of the year.

When Mars is located nearest to the Sun, vapor reaches up to 90 km, and when it is at the farthest point the altitude becomes 60 km. Also, the times when global dust storms are seen on the planet, the Vapor altitude again increases to 80 km. It can be said that the higher the altitude for vapor, the higher the escape from the atmosphere. The calculated escape in a year is the two-meter-deep Martian layer.

These measurements are highly considerable but do not cover all of the water loss for the about four billion-year history of Mars. Therefore, we can reach the conclusion that a large amount of water is trapped beneath the surface or water escaped faster in the past. Studies on Mars are not finished yet, they continue rapidly. We still have many more features to learn about the red planet. Therefore, further observational results will help us to understand all missing points in the near future.

I would like to thank Fatmanur Ertuğrul, one of my undergraduate students for her assistance in preparing this short review.

REFERENCES

"Chronology of Discoveries of Water on Mars." https://en.wikipedia.org/wiki/Chronology_of_discoveries_of_water_on_Mars

"Mars Curiosity Rover." https://mars.nasa.gov/msl/mission/science/results/

"Mars Express and the Story of Water on Mars." https://www.esa.int/Science_Exploration/Space_Science/Mars_Express/Mars_Express_and_the_story_of_water_on_Mars

"Mars Global Surveyor." https://en.wikipedia.org/wiki/Mars_Global_Surveyor

"Mars Global Surveyor." https://mars.nasa.gov/mars-exploration/missions/mars-global-surveyor/

"Mars is leaking water into space during dust storms and warmer seasons." https://www.space.com/mars-water-escapes-to-space-in-dust-storms

"Mars Odyssey Orbiter." https://mars.nasa.gov/odyssey/

"Mars water loss shaped by seasons and storms." https://www.esa.int/Science_Exploration/Space_Science/Mars_Express/Mars_water_loss_shaped_by_seasons_and_storms

"NASA's MAVEN Mission Observes Ups and Downs of Water Escape from Mars." https://www.nasa.gov/feature/goddard/2016/maven-observes-ups-and-downs-of-water-escape-from-mars

"Phoenix (spacecraft)." https://en.wikipedia.org/wiki/Phoenix_(spacecraft)

"Phoenix Mars Mission." http://phoenix.lpl.arizona.edu/mars151.php

"Viking 1 & 2." https://mars.nasa.gov/mars-exploration/missions/viking-1-2/

"Viking Program." https://en.wikipedia.org/wiki/Viking_program

"Water on Mars." https://en.wikipedia.org/wiki/Water_on_Mars#Mars_Reconnaissance_Orbiter

"Water on Mars: discovery of three buried lakes intrigues scientists." https://www.nature.com/articles/d41586-020-02751-1

"Water on Mars: The Story So Far." https://astrobiology.nasa.gov/news/water-on-mars-the-story-so-far/

"What happened to Mars's water? New study suggests most was trapped in underground rocks." https://www.abc.net.au/news/science/2021-03-17/mars-water-oceans-crust-atmosphere-space-ice-minerals/13253028

Fedorova, A., Montmessin, F., Korablev, O., Lefèvre, F., Trokhimovskiy, A., & Bertaux, J. L. (2021). Multi-annual monitoring of the water vapor vertical distribution on Mars by SPICAM on Mars Express. Journal of Geophysical Research: Planets, 126, e2020JE006616.

J.-Y. Chaufray, (2021). "Study of the hydrogen escape rate at Mars during Martian ye-

ars 28 and 29 from comparisons between SPICAM/Mars express observations and GCM-LMD simulations". Icarus, Vol. 353

Squyres, S. W. "The History of Water on Mars". Annual Review of Earth and Planetary Sciences, Vol. 12,

Chapter 3

REACTION OF GUANIDINE AND THEIR DERIVATIVES: ALDEHYDE, KETONE, CHALCONE, ASIT AND-KETOESTER

Nurcan BERBER[1]

1 Vocational School of Health Services, Çanakkale Onsekiz Mart University, Terzioğlu Campus, 17100, Çanakkale / TURKEY, nberber@comu.edu.tr
https://orcid.org/0000-0002-1595-585X

1. Introduction

Guanidines are small nitrogen-rich organic compounds. Guanidine (carbamidine) and its derivatives can be presented simultaneously as aminal (−C(NR_2) (NR_2)−) and imine (-C=NH) (Figur 1) [1]. Due to the aminal functional group of guanidine, it acts as an N-nucleophile in alkylation and acylation. It is also known that guanidine has a strong base (pKb = 0.4) property due to the resonance stabilization [1-3]. strong nucleophilic properties. The imine function is responsible for the strong nucleophilic properties [4]. Due to these groups, their derivatives are used in many fields like medicine [5,6], as a catalyst in plastic synthesis [7], explosive industry [8].

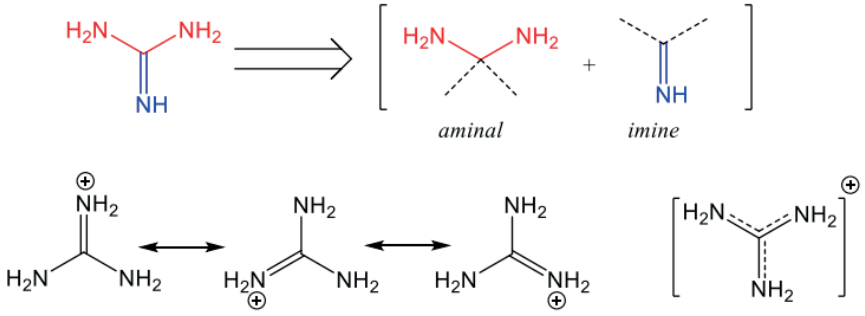

Figure 1. Guanidine structure and resonance structures of its protonated form

Guanidine (carbamidine) and its derivatives are involved in the structure of important biological molecules such as arginine. (amino acid), agmatine (neurotransmitter), creatine (muscular energy intermediate), guanine (purine bases of DNA and RNA), and also in several natural alkaloids like, for example, tetrodotoxin and saxitoxin [9,10].

Aminoguanidine (Pimagedine, AG) is a hydrazine derivative that reduces glycation. It is a scavenger of reactive carbonyl groups, thus being antioxidant agent protecting various cells and tissues from oxidative stress. [11,12]. Also, AG and its derivatives also showed multiple anti-inflammatory properties [13-15]. Some bioactive AG and 1,3-diaminoguanidine derivatives give in Figure 2 [16].

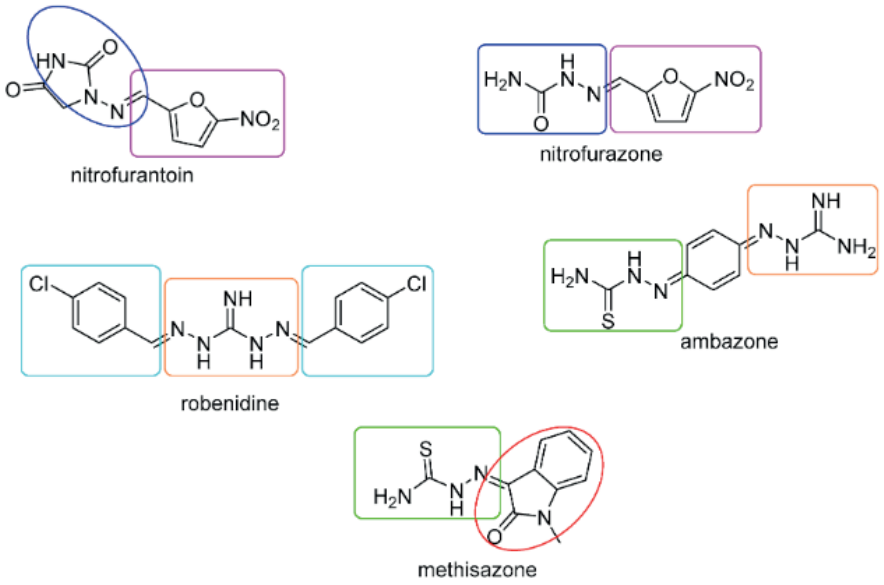

Figure 2. Structure of some bioactive aminoguanidine derivatives

2. Reaction of Guanidine and Its Derivatives with Various Compounds

2.1. Reaction with Aldehyde and Ketone

The reaction of benzaldehyde or acetophenone (1) with 1,3-diaminoguanidine hydrogen chloride to afford robenidine analogues (3), (Scheme 1) [17].

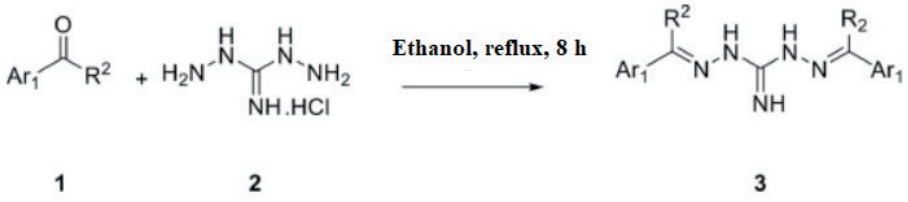

Scheme 1. Synthesis of aminoguanidine derivatives from aldehydes and ketones

2.2. Reaction with Chalcone

Based on chalcone scaffold react with aminoguanidine to give the corresponding guanidines via either a step by step or one-pot procedure [18]. Fukumoto et al. [19] by reaction of chalcones and aminoguanidine in hydrochloric acid, yields of 70–80% (Scheme 2).

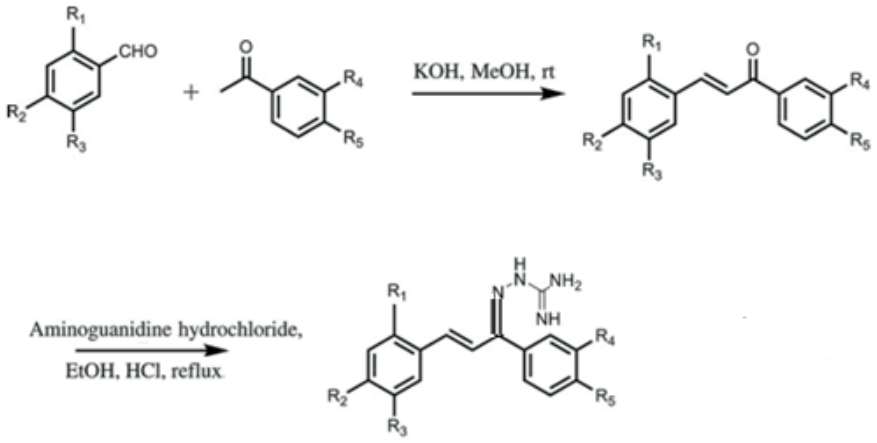

Scheme 2. Synthesis of aminoguanidine derivatives from chalcone scaffold

Similarly, Asiri et al. [20] in acidic medium, Yousif et al. [21] in basic medium carried out the synthesis of guanidine derivatives through the chalcone structure.

2.3. Reaction of Aminoguanidine and β-keto Carboxylates

In condensation of aminoguanidine and β-ketocarboxylates, product pyrimidinone derivative (I) is formed under base catalysis, while product pyrazole derivative (II) is formed under acid catalysis and aminocrotonoate (III) is formed under sodium carbonate (Scheme 3) [22].

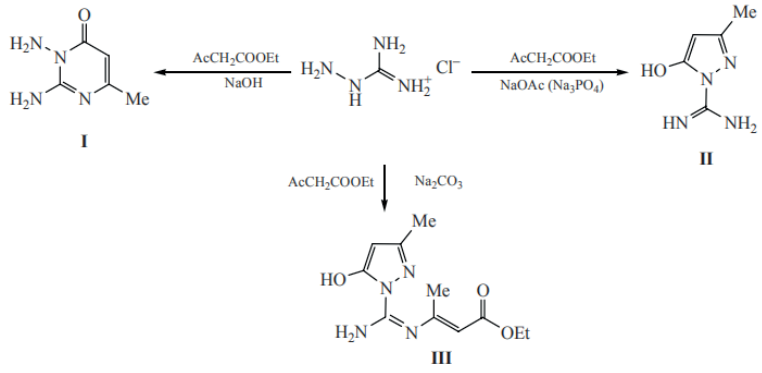

Scheme 3. Condensation of aminoguanidine and β-ketocarboxylates

2.4 Thiazole Ring Formation from Aminoguanidine

Thiazoles conjugated with different heterocyclic ring systems have an significant role because of their pharmacological properties [23,24]. Titus et al. [23] synthesized various 4-hydrazinothiazoles with four-component route (aminoguanidine, carbonyl compounds, α-haloketones, isothiocyanates) under mild reaction conditions, good yield. In this study, The sequential four-component pathway involving masking of binucleophilicaminoguanidine (1) with a carbonyl compound (2), followed by condensation of isothiocyanate (3), and lastly base-catalyzed cyclization with α-haloketones (4) yielded the heavily substituted 4-hydrazinothiazoles (5a-g) (Scheme 4).

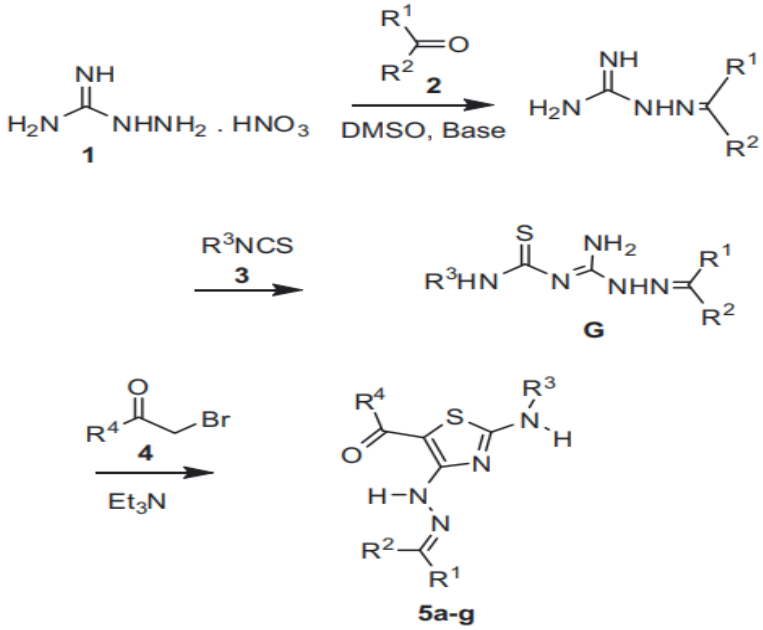

Scheme 4. The synthetic way for thiazole compounds (5a–g)

Similarly, Holla et al. [25] and Manivel et al. [26] reported synthesis of some new thiazole compounds containing hydrazone derivatives.

2.5. Triazole Ring Formation from Aminoguanidine

Generally, triazoles are produced from aminoguanidine by acylation, or interaction with isothiocyanates, cyanates, or carbodiirnides [27]. Ding et al. [28] synthesized triazole derivatives and studied their anti-epileptic activities (Scheme 5).

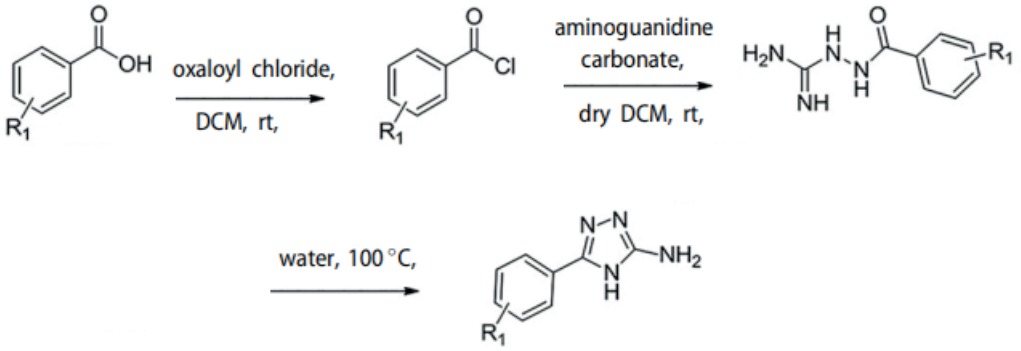

Scheme 5. The synthetic way for triazole from aminoguanidine

The triazole ring can also be easily prepared by reacting aminoguanidine and oxalic acid. [29]. Also, 3-amino-1H-1,2,4-triazoles has achieved through condensation followed by cyclization of a mixture of aminoguanidine bicarbonate and the appropriate organic acid (Scheme 6) [30].

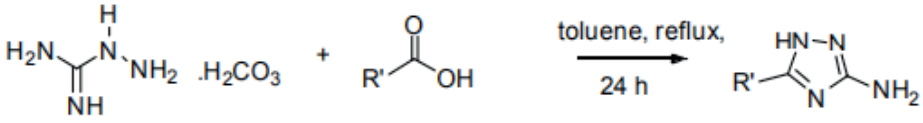

Scheme 6. Synthetic approach used to obtain the triazole ring from aminoguanidine

2.6. Pyrazoles and Pyrazolones Ring Formation from Aminoguanidine

Pyrazolones and pyrazolidinones are well-known heterocycles coumpounds with important biological properties. Pyrazoles have two endocyclic bonds and possess aromatic and tautomeric properties, while Pyrazolones also have two double bonds, one of which is attached to an exocyclic oxygen atom [31]. There are many synthesis methods of Pyrazoles. For example, Pizzuti et al.were synthesized of pyrazole ring by two different ways, Classical synthesis and Ultrasound-promoted. They reported a eco-friendly and mild synthesis protocol for new pyrazole derivatives under ultrasonic irradiation (Scheme 7) [32]. Also, Brasil et al. synthesized pyrazole in the same way in 2016 [33]. Also, Zupancic et al. [34] achieved of pyrazole by the classical synthesis method.

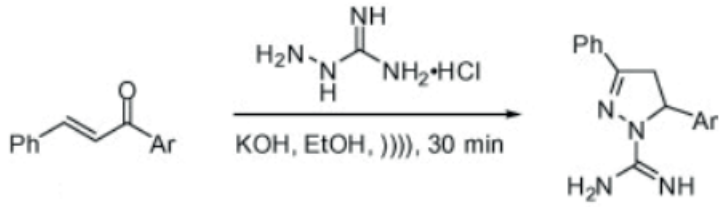

Scheme 7. Synthesis of new pyrazoles under ultrasonic irradiation

On the other hand, pyrazolones ring has a special importance due to its significant characteristic, chemical and biological features [35,37]. Classical method for the synthesis of pyrazolones is condensation reaction of hydrazines and β-ketoester. (Scheme 8) [38].

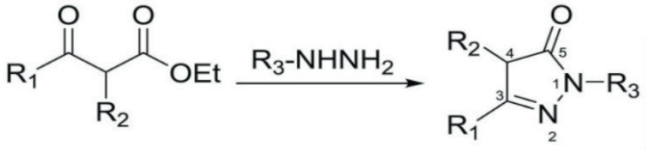

Scheme 8. Synthesis of pyrazolone ring

2.7. **Pyrimidines Ring Formation from Aminoguanidine**

Pyrimidine amine derivatives with two nitrogen atoms in the aromatic ring and a substituted amino outside have shown antibacterial and antiviral activities. Zhang et al. [39] synthesis and characterized pyrimidine amine derivatives containing bicyclic monoterpene moiety and evaluated their antimicrobial activity (Scheme 9). Starting from aldehyde-ketone condensation reaction and in the presence of sodium methoxide or potassium tert-butoxide, a pinanyl ketene intermediates were synthesized. Cyclization of [40] with guanidine hydrochloride produced Pinanyl pyrimidines [41].

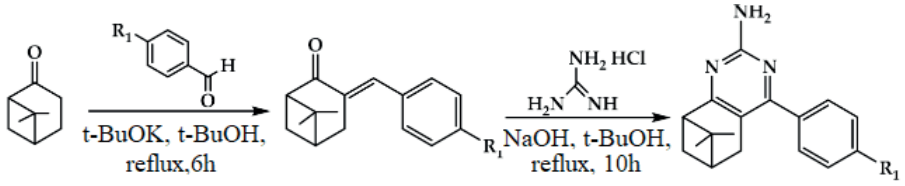

Scheme 9. Synthesis of pyrimidine ring from guanidine

Qomi et al. synthesized new tricyclic pyrimidine derivatives (PFBZDs) using an enaminone-based approach (Scheme 10) [42].

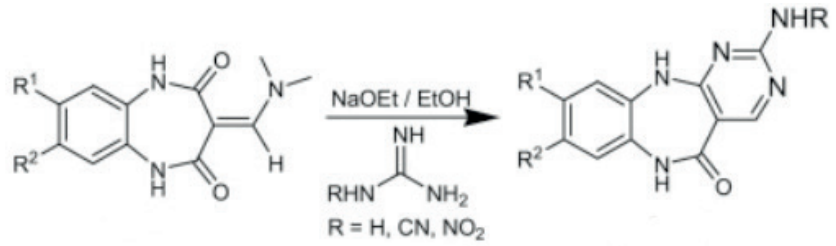

Scheme 10. The synthesis of tricyclic pyrimidine derivatives (PFBZD)

Shipanova et al. described a novel fluorescent pyrimidine formed from the Maillard reaction (Scheme 11). Arginine is a derivative of guanidine [43].

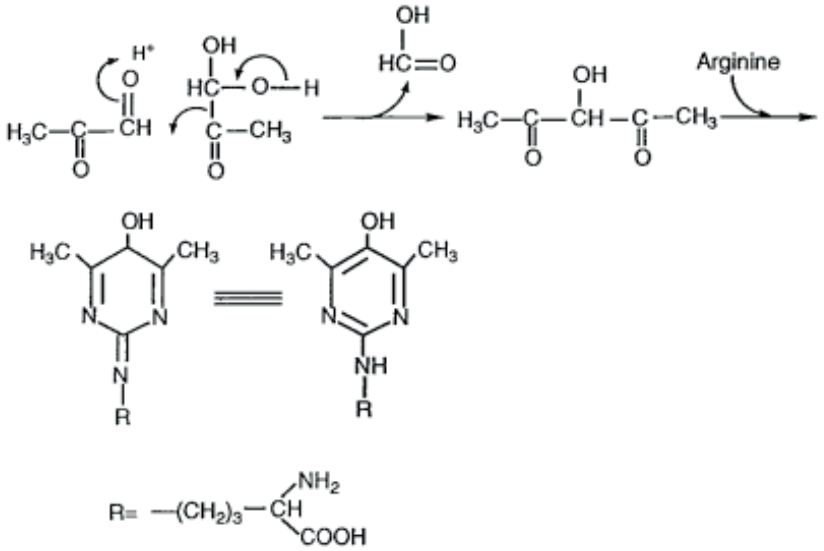

Scheme 11. The Mailard reaction of methylglyoxal with N-a-t-BOC-arginine

2.8. Tetrazoles Ring Formation from Aminoguanidine

Tetrazoles have five-membered ring, containing four nitrogen atoms and one carbon atom [44]. They are also very important among heterocyclic compounds. Kumar et al. reported to have been synthesized a series of tetrazoles that were synthesized by diazotization of amino-guanidine bicarbonate using nitric acid and sodium nitrate to yield guanylazide (Scheme 12) [45].

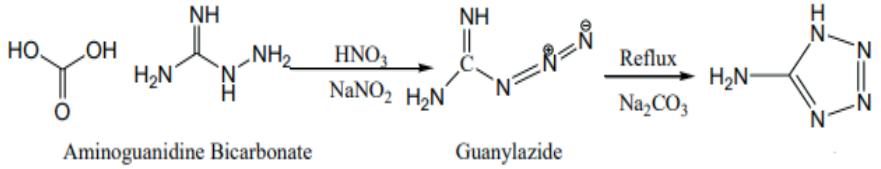

Scheme 12. The synthesis of tetrazole ring from aminoguanidine bicarbonate

Ziviagin et al. reported the Azole-Assembly Alignment (A3): a concise three step ring-forming synthesis ligates 1,2,3-triazole, 1,2,4-triazole and tetrazole to selectively give polydentate nitrogen rich ligand systems (Scheme 13) [46]. Also, et al. described studies on tetrazoles and their complexes [47].

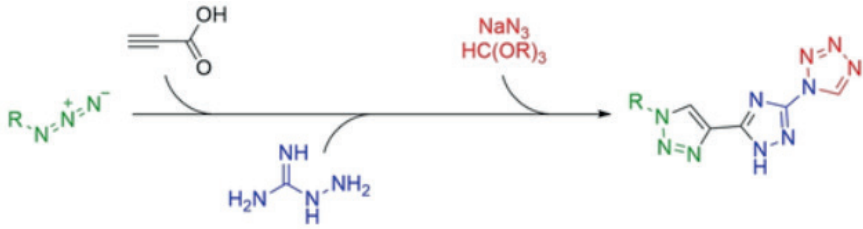

Scheme 13. The synthesis of amino-1,2,4-triazoles.tetrazole ring

3. Conclusion

This review focused onreactions of guanidine and its derivatives and the synthesis of heterocyclic nitrogen-containing compounds. The development of heterocyclic compounds containing nitrogen has an important place in medicine, because of its wide pharmacological activity. In line with the literature studies, it has been seen that guanides and their derivatives are used in the synthesis of the most important heterocyclic nitrogenous compounds (thiazole, triazole, pyrazoles and pyrazolones, etc.) due to their high nitrogen content and positive heat. It has been observed that the syntheses carried out with guanidine and its derivatives were carried out in high yields in mild conditions. This review will encourage further research in the field of chemical reactivity and synthetic methods of guanidine and its derivatives.

REFERENCES

[1] Ishikawa, T. (2010). Guanidine chemistry. Chemical and Pharmaceutical Bulletin, 58(12), 1555-1564.

[2] Berlinck, R. G., & Romminger, S. (2016). The chemistry and biology of guanidine natural products. Natural Product Reports, 33(3), 456-490.

[3] Gund, P. (1972). Guanidine, trimethylenemethane, and" Y-delocalization." Can acyclic compounds have" aromatic" stability?. Journal of Chemical Education, 49(2), 100.

[4] Gomes, A. R., Varela, C. L., Pires, A. S., Tavares-da-Silva, E. J., & Roleira, F. M. (2023). Synthetic and natural guanidine derivatives as antitumor and antimicrobial agents: A review. Bioorganic Chemistry, 106600.

[5] Thomas, S. J., Balónová, B., Cinatl Jr, J., Wass, M. N., Serpell, C. J., Blight, B. A., & Michaelis, M. (2020). Thiourea and Guanidine Compounds and Their Iridium Complexes in Drug-Resistant Cancer Cell Lines: Structure-Activity Relationships and Direct Luminescent Imaging. ChemMedChem, 15(4), 349-353.

[6] Esam, Z., Akhavan, M., Lotfi, M., Pourmand, S., & Bekhradnia, A. (2023). In silico investigation of the therapeutic and prophylactic potential of medicinal substances bearing guanidine moieties against COVID-19. Chemical Papers, 77(2), 1129-1148.

[7] Fuchs, M., Walbeck, M., Jagla, E., Hoffmann, A., & Herres-Pawlis, S. (2022). Guanidine Carboxy Zinc Complexes for the Chemical Recycling of Renewable Polyesters. ChemPlusChem, 87(5), e202200029.

[8] Smith, G. B. L., Sabetta, V. J., & Steinbach Jr, O. F. (1931). Quantitative Study of the Preparations of Guanidine Nitrate and Nitroguanidine. Industrial & Engineering Chemistry, 23(10), 1124-1129.

[9] Kim, S. H., Semenya, D., & Castagnolo, D. (2021). Antimicrobial drugs bearing guanidine moieties: A review. European Journal of Medicinal Chemistry, 216, 113293.

[10] Raczyńska, E. D., Cyrański, M. K., Gutowski, M., Rak, J., Gal, J. F., Maria, P. C., ... & Duczmal, K. (2003). Consequences of proton transfer in guanidine. Journal of physical organic chemistry, 16(2), 91-106.

[11] Lieber, E., & Smith, G. B. L. (1939). The Chemistry of Aminoguanidine and Related Substances. Chemical Reviews, 25(2), 213-271.,

[12] Thornalley, P. J. (2003). Use of aminoguanidine (Pimagedine) to prevent the formation of advanced glycation endproducts. Archives of biochemistry and biophysics, 419(1), 31-40.

[13] Ma, Y., Song, X., Ma, T., Li, Y., Bai, H., Zhang, Z., ... & Gao, L. (2020). Aminoguanidine inhibits IL-1β-induced protein expression of iNOS and COX-2 by blocking the NF-κB signaling pathway in rat articular chondrocytes. Experimental

and Therapeutic Medicine, 20(3), 2623-2630.

[14] Wu, J., Ma, S., Zhang, T. Y., Wei, Z. Y., Wang, H. M., Guo, F. Y., ... & Piao, H. R. (2019). Synthesis and biological evaluation of ursolic acid derivatives containing an aminoguanidine moiety. Medicinal Chemistry Research, 28, 959-973.

[15] Wei, Z. Y., Chi, K. Q., Yu, Z. K., Liu, H. Y., Sun, L. P., Zheng, C. J., & Piao, H. R. (2016). Synthesis and biological evaluation of chalcone derivatives containing aminoguanidine or acylhydrazone moieties. Bioorganic & medicinal chemistry letters, 26(24), 5920-5925.

[16] Krátký, M., Štěpánková, Š., Konečná, K., Svrčková, K., Maixnerová, J., Švarcová, M., ... & Vinšová, J. (2021). Novel Aminoguanidine Hydrazone analogues: from potential antimicrobial agents to potent cholinesterase inhibitors. Pharmaceuticals, 14(12), 1229.

[17] Tapera, M., Kekeçmuhammed, H., Sahin, K., Krishna, V. S., Lherbet, C., Homberset, H., ... & Sarıpınar, E. (2022). Synthesis, characterization, anti-tuberculosis activity and molecular modeling studies of thiourea derivatives bearing aminoguanidine moiety. Journal of Molecular Structure, 1270, 133899.

[18] Zhuang, Q., Han, H., Wang, S., Tu, S., & Rong, L. (2009). Efficient and facile three-component reaction for the synthesis of 2-amine-4, 6-diarylpyrimidine under solvent-free conditions. Synthetic Communications®, 39(3), 516-522.,

[19] Qian, Y., Zhang, H. J., Lv, P. C., & Zhu, H. L. (2010). Synthesis, molecular modeling and biological evaluation of guanidine derivatives as novel antitubulin agents. Bioorganic & medicinal chemistry, 18(23), 8218-8225.

[20] Asiri, A. M., & Khan, S. A. (2011). Synthesis and anti-bacterial activities of a bis-chalcone derived from thiophene and its bis-cyclized products. Molecules, 16(1), 523-531.

[21] Yousif, O. A., Mahdi, M. F., & Raauf, A. M. (2019). Design, synthesis, preliminary pharmacological evaluation, molecular docking and ADME studies of some new pyrazoline, isoxazoline and pyrimidine derivatives bearing nabumetone moiety targeting cyclooxygenase enzyme. Journal of Contemporary Medical Sciences, 5(1).

[22] Erkin, A. V., & Krutikov, V. I. (2009). Formation, structure and heterocyclization of aminoguanidine and ethyl acetoacetate condensation products. Russian Journal of General Chemistry, 79, 1204-1209.

[23] Titus, S., & Sreejalekshmi, K. G. (2014). One-pot four-component synthesis of 4-hydrazinothiazoles: novel scaffolds for drug discovery. Tetrahedron Letters, 55(40), 5465-5467.

[24] Guo, J., Xie, Z., Ruan, W., Tang, Q., Qiao, D., & Zhu, W. (2023). Thiazole-based analogs as potential antibacterial agents against methicillin-resistant Staphylococcus aureus (MRSA) and their SAR elucidation. European Journal of Medicinal Chemistry, 115689.

[25] Holla, B. S., Malini, K. V., Rao, B. S., Sarojini, B. K., & Kumari, N. S. (2003). Sy-

nthesis of some new 2, 4-disubstituted thiazoles as possible antibacterial and anti-inflammatory agents. European Journal of Medicinal Chemistry, 38(3), 313-318.

[26] Manivel, P., & Khan, F. N. (2009). Synthesis of some new 2, 4-disubstituted hydrazinothiazoles and 2, 5-disubstituted thiazolidinones. Phosphorus, Sulfur, and Silicon, 184(11), 2910-2922.

[27] Kurzer, F., & Godfrey, L. E. A. (1963). Syntheses of heterocyclic compounds from aminoguanidine. Angewandte Chemie International Edition in English, 2(8), 459-476.

[28] Ding, J., Cao, F. D., Geng, Y. R., Tian, Y., Li, P., Li, X. F., & Huang, L. J. (2019). Synthesis and in vitro anti-epileptic activities of novel [1, 2, 4]-triazolo [1, 5-a] pyrimidin-7 (4H)-one derivatives. Journal of Asian natural products research, 21(12), 1190-1204.

[29] O'Connell, G. J. (1994). The enzymatic synthesis of nucleoside analogues (Doctoral dissertation, University of Warwick).

[30] Boechat, N., Pinheiro, L. C., Santos-Filho, O. A., & Silva, I. C. (2011). Design and synthesis of new N-(5-trifluoromethyl)-1 H-1, 2, 4-triazol-3-yl benzenesulfonamides as possible antimalarial prototypes. Molecules, 16(9), 8083-8097.

[31] Johnson, M., Younglove, B., Lee, L., LeBlanc, R., Holt Jr, H., Hills, P., ... & Lee, M. (2007). Design, synthesis, and biological testing of pyrazoline derivatives of combretastatin-A4. Bioorganic & medicinal chemistry letters, 17(21), 5897-5901.

[32] Pizzuti, L., Martins, P. L., Ribeiro, B. A., Quina, F. H., Pinto, E., Flores, A. F., ... & Pereira, C. M. (2010). Efficient sonochemical synthesis of novel 3, 5-diaryl-4, 5-dihydro-1H-pyrazole-1-carboximidamides. Ultrasonics Sonochemistry, 17(1), 34-37.

[33] Brasil, S. R., Capiotto, A. C., Faoro, E., Pizzuti, L., Back, D. F., & Flores, A. F. Synthesis of bis (hydrazinecarboximidamides) by condensation of aminoguanidine with in situ generated 1, 2-diketones.

[34] Zupančič, S., Svete, J., & Stanovnik, B. (2008). Transformations of Dialkyl Acetone-1, 3-dicarboxylates via Their Dimethylaminomethylidene Derivatives Into 1-substituted 4-ethoxycarbonyl-5-(ethoxycarbonylmethyl) pyrazoles, 7-amino-2-ethoxycarbonyl-1H, 2H-pyrazolo [2, 3-c] pyrimidin-5-one, 4-hydroxypyridin-2 (1H)-ones and 6-substituted 3-benzoylamino-2, 5-dioxo-5, 6-dihydro-2H-pyrano [3, 2-c] pyridine-8-carboxylates. Acta Chimica Slovenica, 55(4).

[35] Khidre, R. E., Mohamed, H. A., & ABDELWAHAB, B. F. (2013). Advances in the chemistry of pyrazolopyrazoles. Turkish Journal of Chemistry, 37(1), 1-35.

[36] Al-Afaleq, E. I., & Abubshait, S. A. (2001). Heterocyclic o-Aminonitriles: Preparation of Pyrazolo [3, 4-d]-pyrimidines with Modification of the Substituents at the 1-Position. Molecules, 6(7), 621-638.

[37] Kakiuchi, Y., Sasaki, N., Satoh-Masuoka, M., Murofushi, H., & Murakami-Muro-

fushi, K. (2004). A novel pyrazolone, 4, 4-dichloro-1-(2, 4-dichlorophenyl)-3-methyl-5-pyrazolone, as a potent catalytic inhibitor of human telomerase. Biochemical and biophysical research communications, 320(4), 1351-1358.

[38] Zhao, Z., Dai, X., Li, C., Wang, X., Tian, J., Feng, Y., ... & Zheng, X. (2020). Pyrazolone structural motif in medicinal chemistry: Retrospect and prospect. European Journal of Medicinal Chemistry, 186, 111893.

[39] Zhang, M., Wang, Y., Wang, S., & Wu, H. (2022). Synthesis and biological evaluation of novel pyrimidine amine derivatives bearing bicyclic monoterpene moieties. Molecules, 27(22), 8104.

[40] Hurtová, M., Káňová, K., Dobiasová, S., Holasová, K., Čáková, D., Hoang, L., ... & Valentová, K. (2022). Selectively Halogenated Flavonolignans Preparation and Antibacterial Activity. International Journal of Molecular Sciences, 23(23), 15121.

[41] Nimma, R., Kumar, A., Gani, Z., Gahlawat, A., Dilawari, R., Rohilla, R. K., ... & Raje, C. I. (2023). Characterization of the enzymatic and multifunctional properties of Acinetobacter baumannii erythrose-4-phosphate dehydrogenase (E4PDH). Microbial Pathogenesis, 175, 105992.

[42] Qomi, H. R., & Habibi, A. (2017). Synthesis of a novel functionalized tricyclic pyrimidine-fused 1, 5-benzodiazepine library. Tetrahedron, 73(21), 2991-3001.

[43] Shipanova, I. N., Glomb, M. A., & Nagaraj, R. H. (1997). Protein modification by methylglyoxal: chemical nature and synthetic mechanism of a major fluorescent adduct. Archives of biochemistry and biophysics, 344(1), 29-36.

[44] Matyáš, R., Pachman, J., Matyáš, R., & Pachman, J. (2013). Tetrazoles. Primary Explosives, 187-226.

[45] Kumar, K. R., Nuthakki, V. K., & Reddy, C. N. (2014). Synthesis, Characterization and biological evaluation of tetrazole derivatives. Indo Am. J. Pharm. Res., 4(11).

[46] Zviagin, E., Saraev, V., Sysoiev, D., Klepetářová, B., Mazur, M., Zhelavskyi, O., ... & Chebanov, V. (2021). Synthesis of 1-(3-(1-substituted-1, 2, 3-triazol-4-yl)-1, 2, 4-triazol-5-yl)-tetrazoles by Sequential Assembly of Azole Fragments. ChemistrySelect, 6(45), 12890-12894.

[47] Nasrollahzadeh, M., Sajjadi, M., Ghafuri, H., Bidgoli, N. S. S., Pombeiro, A. J., & Hazra, S. (2021). Platinum and palladium complexes with tetrazole ligands: Synthesis, structure and applications. *Coordination Chemistry Reviews*, *446*, 214132.

Chapter 4

EFFECTS OF *Sternbergia lutea* (L.) (ALLIACEAE, AMARYLLIDOIDEAE) METHANOL EXTRACT ON TOTAL HEMOCYTE COUNT AND HEMOCYTE VIABILITY OF *Galleria mellonella* (L.) (LEPIDOPTERA: PYRALIDAE)

Ata ESKİN[1]

1 Assistant Professor Dr, ORCID: 0000-0002-7953-654X, Avanos Vocational School of Fine Arts, Crop Animal Production Department, Nevşehir Hacı Bektaş Veli University, Avanos, Nevşehir.

Introduction

In scientific research, *Sternbergia* species with alkaloid content have been found to have antioxidative, anti-inflammatory, and anti-diabetic characteristics. Because of the alkaloids it contains, the species *Sternbergia lutea* (L.) Ker Gawl.exSpreng has a variety of pharmacological effects (Iscan et al. 2017). It is known that alkaloids such as hippeastrine, tazettine, galanthamine, hippamine, sternbergine, lycorine, galanthin, and lutessine have been isolated from *S. lutea* (Baygar, 2010). Studies are showing that lycorine, a toxic chemical and also an alkaloid, triggers cell death in *Triconomas vaginalis* (Giordani et al. 2011). Additionally, its poisonous and anthelmintic properties have been established in earlier research (Atay et al. 2021).

One of the most dangerous species is *Galleria mellonella* (L.) (Lepidoptera: Pyralidae), which causes tunneling on the honeycomb and results in severe losses in apiculture (Eskin, 2023). *G. mellonella* is an insect model organism that is commonly used to research the effects of human diseases and various pesticides, hormones, and other substances on the immune system (Kaya et al. (2021).

Hemocytes play a central role in immune defenses, They play a variety of roles in insect physiology. They play a role in humoral and cell immune responses. They are involved in the phagocytic, encapsulation, nodulatory, and coagulatory processes. They, also play a role in nutrient metabolism, synthesis, and storage (Moyetta et al. 2021). They respond very quickly to the effects of diverse biotic and abiotic stimuli (Hillyer and Pass 2020).

The number of hemocytes in the hemolymph reveals changes in the insects' immune system (Souza Saraiva et al. 2019). Total hemocyte counts (THCs) are calculated by applying diluted hemolymph to a Neubauer hemocytometer (Silva et al. 2002). THCs offer a helpful method of analyzing the animal's state of health (Babile Jasmine et al. 2018). In some invertebrates, THC is a measure that can be utilized as a stress indicator (Rivaie et al. 2023). Botanical extracts can affect insects' cellular immune systems by interfering with normal hemocyte function. This results in cellular immunity being reduced and lower levels of insect defense (Ramírez-Zamora et al. 2020).

Comparatively to other solvents, methanol is more efficient at obtaining phenolic, flavonoid, and alkaloid chemicals (Habibian et al. 2020). It is a versatile solvent that can draw both polar and non-polar substances to it (Mahasuari et al. 2020). To selectively staining dead tissues or cells, trypan blue is a dye that has been used extensively (Tran et al. 2011). The dye is kept out of alive cells with intact membranes, but it can get inside and concentrate in dead cells with compromised membranes, turning the cells a dark blue color (Chan et al. 2020).

The act of feeding a person or animal against their will is known as force feeding. The force-feeding technique involves injecting a living thing's body against its will with the calories, protein, macro- and micro-elements, and vitamins that it needs. Studies on toxicity frequently employ this technique (Ramarao et al. 2012; Eskin et al. 2021).

This study aims to assess the acute toxic effects of *S. lutea* methanol extract obtained from the underground section of the plant on THCs and hemocyte viability of *G. mellonella* by a force-feeding assay for 24 h after the force-feeding treatment with trypan blue dye. Although there are some studies that show that *S. candida* methanolic extract acts as an acetylcholine inhibitor in studies with different organs of the plant (Haznedaroğlu and Gökçe, 2014), the usefulness of *S. lutea* extract on invertebrate immunity has never been investigated before. Therefore, determining the toxic effects of *S. lutea* on the hemocytes of *G. mellonella*, which is accepted as a model experimental organism, is very important in terms of laying the scientific basis for the studies to be carried out on this topic.

Insects

The larval culture used in the study was established in the Plant and Animal Production Laboratory at Nevşehir Hacı Bektaş Veli University, Turkey (temperature: 27±2 °C; relative humidity: 60 ± 5%). For larval culture continuity, it was carried out by laying eggs of adult insects in jars filled with honeycomb containing 1 liter glass jar with perforated mouths. When the larvae hatched from the obtained eggs reached a weight of 0.16-0.20 grams, they were taken from the jars to the experimental containers to be used in the experiment (Eskin, 2023).

Plant Materials and Extract Preparation

In 2020, the collection of *S. lutea* was conducted within the Gülağzı neighborhood of Menteşe, located within the Muğla province of Turkey. The plant sample was subsequently identified by the botanist, Dr. Olcay Ceylan. It was deposited within the Muğla Sıtkı Koçman University Herbarium (MSKUH), which was assigned the herbarium number OC.2119 (Atay et al. 2021).

A rotary evaporator (Heidolph-Laborota Natural Products and Biotechnology 404011) operating at 50 °C was used to remove the solvent from the filtrate that was obtained. Then, lyophilization (Thermo Savant) was used to remove the water from the extract. The extracts obtained were stored at -20°C (Atay et. al. 2021; Turan & Mammadov, 2021).

The plant's underground (tuber) components were dried separately. The sample, which weighed 10 g, received 100 mL of methanol after the dried plants were chopped into small pieces. Each sample was kept in a shaking incubator at 55 °C for 6 hours (Atay et al. 2021).

By filtering the mixture through the Whatman filter paper, the residue and extraction mixture were separated. For the second and third times, the same conditions were maintained while additional methanol was added and filtered (Atay et al. 2021).

Bioassays with Force-Feeding Treatment

Lethal concentration 50 (LC_{50}) values of *S. lutea* methanol extract (Figure 1) for force-fed *G. mellonella* larvae after 24 h the treatments have been described by us before (Eskin, 2023). According to LC_{50} value of *S. lutea* methanol extract (464.77 µg/10 µl), (10, 25, 50, 100 µg/10 µl) sublethal *S. lutea* methanol extract doses were determined as experimental (treated) doses for all *G. mellonella* studies.

The *S. lutea* methanol extract homogenization was provided with a bath-type sonicator for 15 min. at 35°C. For bioassays, larvae (180 ± 20 mg) were force-fed with different homogenized *S. lutea* methanol extract doses (10, 25, 50, 100µg/10 µl). Each of these doses formed the experimental groups of the study. All doses of the plant extract were prepared with distilled water containing 3% (dimethyl sulfoxide-DMSO).

The control group received only 10 µL of distilled water containing 3% DMSO. These studies were performed using a microfine insulin syringe (29 gauge) (Figure 2). Then, force-feeded, each larva was placed in perforated plastic boxes (20 ml). After 24h, THC and dead hemocytes percentages were calculated for determine the effects of *S. lutea* methanol extract on *G. mellonella* hemocytes (Table 1). Both experimental and control tests were performed with a total of 15 larvae for each dose and control group.

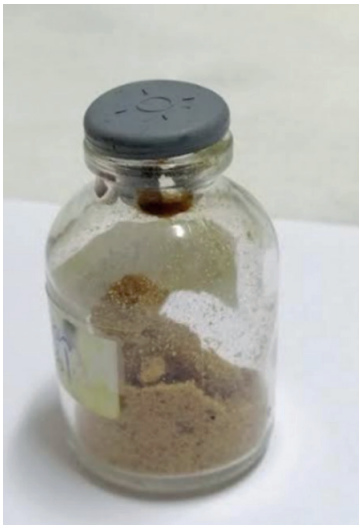

Figure 1. S. lutea methanol extract.

Figure 2. Administration of 10 µl distilled water to G. mellonella larva with forced-feeding method (Eskin and Öztürk, 2022).

Total Hemocyte Counts (THC) in Optical Microscope and Determination of The Dead Hemocytes Percentages

The prior method was used to determine the THCs in the hemolymph (Eskin, 2022). The density of the diluted hemocyte suspension was measured using a Neubauer hemocytometer after 5 µl of hemocyte suspension had been diluted 10 times in 45 µl PBS l of PBS. Hemocytes were counted by using (Swift SW380T, China) microscope. The following formula was used to determine the number of hemocytes per cubic millimeter (1 mm^3) in hemolymph:

Hemocyte number/ml = number of cells counted in big square x dilution factor (10) x 10^4 (Teramoto and Tanaka 2004; Tojo et al., 2000) (Table 1). Trypan blue-stained hemocyte nuclei were thought to be dead, while unstains nuclei were thought to be alive (Uzuner 2018) (Eskin 2022) (Figure 3), and the percentage of dead cells calculated with using THCs (Table 1).

Statistical Analysis

Using IBM-SPSS (Version 20.0), the mean number of hemocytes in *G. mellonella* was estimated. To ascertain whether there were differences between the groups in the parameters that did not have a normal distribution, the nonparametric Kruskal Wallis test was used. The differences between the groups were ascertained using the Mann Whitney U tests.

Following square root arcsine transformation, a one-way ANOVA and Tukey test were run on the data to distinguish between concentrations as percentage values of alive and dead hemocytes. A baseline confidence level of 0.05 was used for all statistical analyses.

Results

The microscope images of the dead cells (a1., a2.) and alive cells (b1., b2.) are given in Figure 3 below.

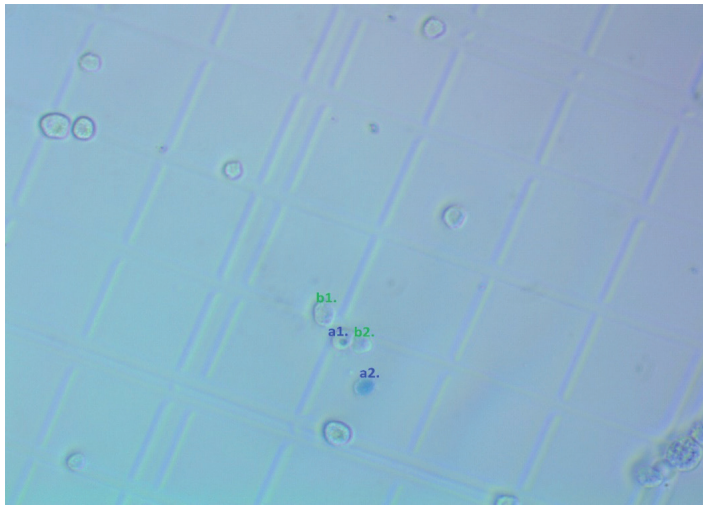

Figure 3. Microscope images of the dead cells (a1., a2.) and alive cells (b1., b2.) on Neuber haemocytometer. The effects of S. lutea methanol extract on THC and hemocyte viability of G. mellonella are given in (Table 1).

Table 1. Effects of Sternbergia lutea methanol extract on THC and hemocyte viability of Galleria mellonella x10^6 within the following 24 h of the treatment

Doses of plant extract (µg/10µl)	Min.- Max.	The number of hemocytes / ml (Mean ± SE)	Percentages of dead hemocytes (%)
0 (distilled water with 3% DMSO).	5.3-34.0	13.83 ± 1.90^b	5.63^a
10	7.0-34.3	20.71 ± 2.09^c	5.31^a
25	4.7-19	9.34 ± 0.96^{ab}	7.27^a
50	2.2-9.8	6.14 ± 0.51^a	7.60^a
100	3.6-28.8	10.53 ± 1.51^b	16.32^b

The obtained data showed that the THC of larvae exposed to 10 µg/10 µl *S. lutea* methanolic extract resulted in a significant increase compared to the control group (Kruskal Wallis, Mann Whitney U Test, $P<0.05$, $P=0.01$) (Table

1). Again, compared to the control group, THCs of the 50 µg/10 µl group was found to **decrease** in 24h significantly ($p<0.05$) (Table 1). The percentage of death cells increased from 5% to 16% after 24 h in 100/10 µl compared to the control group. This increase was statistically significant (Tukey Test, $P<0.05$, $df=4$, $F=8.165$, $P=0.00$) (Table **1**).

Discussion

A promising in vivo model insect called *G. mellonella* is employed in microbiological, medicinal, and pharmaceutical studies (Bugyna et al. 2023). At the same time, it is an important pest in terms of beekeeping and the damage it causes to honeycombs (Eskin, 2022).

Botanical pesticides are effective in controlling a variety of agricultural pests, affordable, easily biodegradable, have a variety of mechanisms of action, are readily available in their sources, and are not hazardous to non-target organisms (Lengai et al. 2020). This study is important both in terms of contributing to the literature to determine the biopesticidal properties of the plant, and in terms of determining its potential toxic effects on living things by testing it on a model organism (*G. mellonella*).

In this context, results showed that increasing doses of the plant extract caused significant changes in the insect's immune system (Table 1). Depending on the increasing doses, the increase in the number of dead hemocytes occurred at a significant level (Table 1). Changes in the THCs are used as a physiological marker in toxicological studies, in the evaluation of the effects of pollutants (Arslan, 2022). In our study, when compared with the control group, significant increases and decreases in the total hemocyte count observed at low and high doses indicate that the THCs parameter is a good indicator.

In a study conducted with *S. fischeriana,* the alkaloid extract of the plant showed a cytotoxic effect according to the Brine Shrimp toxicity analysis. Also, it has been determined that it causes chromosomal abnormalities on *Allium cepa,* and the number of abnormally dividing cells increases depending on the same plant (Baygar, 2010). Similarly, the reason for the significant decrease in THC at 50 µg/10 µl extract dose and the increase in the percentage of dead hemocytes at the 50 µg/10 µl extract dose may be the alkaloids found in the *S. lutea* plant extract (Table 1).

In another study, water extract prepared from and aerial parts of *S. lutea* showed significant cytotoxic activity on brine shrimp (*Artemia salina* Leach.) (Kaya et al. 2010). In the same study, cytotoxic effects; it has been emphasized that it may be caused by lycorine alkaloid, phenolic acid, and flavonoids found in the extract of *S. lutea*. The reason for the cytotoxic effects seen in our study may be due to these biochemical active substances (Table 1) (Kaya et al. 2010).

When evaluated in terms of cytotoxicity, our study was compatible with the literature in this sense.

Within the scope of the immunotoxic effects of *S.lutea* on *G.mellonella*, it will be useful to study the effects of the insect on hemocyte types, apoptotic and necrotic indices, and hemolymph antioxidant enzyme levels in order to understand the toxic effects of the extract in more detail.

Finally, we think that the results of our study will be beneficial in terms of providing data to scientists working on botanical extracts and their toxic effects on living things.

Acknowledgements

Thanks to the Prof. Dr. Ramazan Mammadov (Muğla Sıtkı Koçman University) who sent us the *Sternbergia* extract.

REFERENCES

Arslan, P. (2022) Determinations of the effects of cyfluthrin on the hemocytes parameters of freshwater mussel (*Unio delicatus*). *Ege Journal of Fisheries and Aquatic Sciences*, *39*(1), 39-45. Doi: 10.12714/egejfas.39.1.06.

Atay, M. Ö., Ardıl, B., Alper, M., & Ceylan, O. (2021) Determination of toxic and anthelmintic activities of *Ornithogalum nutans* L., *Sternbergia lutea* (L.) Ker-gawl. ex Spreng. and *Allium stylosum* O. Schwarz. *Natural Products and Biotechnology*, *1*(1), 38-48.

Babile Jasmine, J., Annalakshmi, T., Mabel Parimala S. and Xavier Innocent B (2018) Identification and classification of hemocytes from the fresh water prawn, *Caridina weberi. International Journal of Research and Analytical Reviews (IJRAR), 5* (4), 406-410.

Baygar, T. (2010) *Sternbergia fischeriana* (Herbert) Rupr. Alkaloidlerinin Kimyasal Analizi ve Biyolojik Aktivitelerinin Belirlenmesi. İstanbul Üniversitesi Fen Bilimleri Enstitüsü, Yüksek Lisans Tezi.

Bugyna, L., Kendra, S. and Bujdáková, H., (2023) *Galleria mellonella*—A Model for the Study of aPDT—Prospects and Drawbacks. *Microorganisms, 11*(6), p.1455. Doi: https://doi.org/10.3390/microorganisms11061455.

Chan, L. L. Y., Rice, W. L., & Qiu, J. (2020) Observation and quantification of the morphological effect of trypan blue rupturing dead or dying cells. *PLoS One, 15*(1), e0227950. Doi: https://doi.org/10.1371/journal.pone.0227950.

De Souza Saraiva, A., Soares, M., & Pestana, L. (2019) Toxicity of microbial insecticides toward the non-target freshwater insect *Chironomus xanthus*. *Pest Management Science, 76*(3), 1164-1172. Doi: https://doi.org/10.1002/ps.5629.

Eskin, A. N., Öztürk, Ş., & Eskin, A. (2021) The effects of magnetic iron oxide nanoparticles (Fe3O4) on some biological aspects of *Galleria mellonella* L. (Lepidoptera: Pyralidae). *Celal Bayar University Journal of Science, 17*(3), 319-324. Doi: https://doi.org/10.18466/cbayarfbe.920637.

Eskin, A. (2022). Effects of silicon dioxide nanoparticles (SiO2 NPs) on total hemocyte count and hemocyte viability of *Galleria mellonella*. *International Journal of Tropical Insect Science, 42*(3), 2617-2623. Doi: https://doi.org/10.1007/s42690-022-00790-x.

Eskin, A. N., and Ş. Öztürk (2022). Demir oksit nanopartiküllerinin *Galleria mellonella* (L.) (Lepidoptera: Pyralidae)'nın biyolojisine ve hemositlerine etkisi. Yüksek Lisans Tezi. Nevşehir Hacı Bektaş Veli Üniversitesi.

Eskin, A. (2023) Determination of the lethal concentratıons of *Sternbergia lutea* (L.) (Alliaceae, Amaryllidoideae) methanol extract on *Gallerıa mellonella* larvae (L.) (Lepidoptera: Pyralidae*). Karadeniz 12th International Conference on Applied Sciences* - March 3- 5, 2023 – Rize, 16.

Giordani, R. B., de Brum Vieira, P., Weizenmann, M., Rosemberg, D. B., Souza, A.

P., Bonorino, C., ... & Tasca, T. (2011) Lycorine induces cell death in the amitochondriate parasite, *Trichomonas vaginalis*, via an alternative non-apoptotic death pathway. *Phytochemistry, 72*(7), 645-650. Doi: https://doi.org/10.1016/j.phytochem.2011.01.023.

Habibian, M., Sadeghi, G., & Karimi, A. (2020) Phytochemicals and antioxidant properties of solvent extracts from purslane (*Portulaca oleracea* L.): a preliminary study. *Food Science and Engineering*, 1-12. Doi: https://doi.org/10.37256/fse.11202046.

Haznedaroglu, M., & Gokce, G. (2014) Comparison of anti-acetylcholinesterase activity of bulb and leaf extracts of *Sternbergia candida* Mathew & T. Baytop. *Acta Biologica Hungarica, 65*(4), 396-404. Doi: https://doi.org/10.1556/ABiol.65.2014.4.4.

Hillyer, J. F. & Pass, G. (2020) The insect circulatory system: Structure, function, and evolution. *Annu. Rev. Entomol. 65,* 121–143. Doi: https://doi.org/10.1146/annurev-ento-011019-025003.

IBM-SPSS Statistics for Windows. 2011. Version 20.0. Elsevier, London, UK. IBM Corp. Released. Armonk, NY: IBM Corp.

Iscan, S.G., Sarialtin, Y.S., Yazgan, A., Yılmaz, S.B., Agca, C.A., Çoban T. (2017). The antioxidant, anti-inflammatory andantidiabetic activities of *Sternbergia lutea ssp. lutea* and *Sternbergia lutea* ssp. *sicula. Toxicology Letters*, 8. Doi: http://dx.doi.org/10.1016/j.toxlet.2017.07.247.

Kaya, G.İ., Sarıkaya, B., Çiçek, D. and Somer, N.Ü. (2010). In vitro cytotoxic activity of *Sternbergia sicula*, *S. lutea* and *Pancratium maritimum* Extracts. *Hacettepe University Journal of the Faculty of Pharmacy, (1)*, pp.41-48.

Kaya, S., Akkuş, G., Türkdoğan, S., & Gündüz, B. (2021) Influence of *Helichrysum arenarium* on hemocyte-mediated immune responses and phenoloxidase enzyme activity of model organism *Galleria mellonella* (L.). *International Journal of Tropical Insect Science*, 1-8. Doi: https://doi.org/10.1007/s42690-021-00432-8.

Lengai, G.M., Muthomi, J.W. and Mbega, E.R. (2020). Phytochemical activity and role of botanical pesticides in pest management for sustainable agricultural crop production. *Scientific African,* 7, p.e00239. Doi: https://doi.org/10.1016/j.sciaf.2019.e00239.

Mahasuari, N. P. S., Paramita, N. L. P. V., & Putra, A. G. R. Y. (2020) Effect of methanol concentration as a solvent on total phenolic and flavonoid content of beluntas leaf extract (*Pulchea indica* L.). *Journal of Pharmaceutical Science and Application, 2*(2), 77. Doi: https://doi.org/10.24843/JPSA.2020.v02.i02.p05.

Moyetta, N. R., Ramos, F. O., Leyria, J., Canavoso, L. E., & Fruttero, L. L. (2021) Morphological and ultrastructural characterization of hemocytes in an insect model, the hematophagous *Dipetalogaster maxima* (Hemiptera: Reduviidae). *Insects, 12*(7), 640. Doi: https://doi.org/10.3390/insects12070640.

Ramarao N, Nielsen-Leroux C, Lereclus D. (2012) The insect *Galleria mellonella* as a powerful infection model to investigate bacterial pathogenesis. *Journal of Visu-*

alized Experiments, 70: 4392.

Ramírez-Zamora, J., Salinas-Sánchez, D. O., Figueroa-Brito, R., Ramos-López, M. Á., Castañeda-Espinoza, J. D., & Flores-Macías, A. (2020) Botanical extracts from *Dodonaea viscosa* (Sapindales: Sapindaceae) reduce hemocyte counts from *Spodoptera exigua* (Lepidoptera: Noctuidae) with potential insecticidal synergism with *Isaria fumosorosea* (Hypocreales: Cordycipitaceae). *Biocontrol Science and Technology, 30*(12), 1365-1376. Doi: https://doi.org/10.1080/09583157.2020.1826903.

Rivaie, A. R., Adiputra, Y. T., Setyawan, A., & Putro, D. H. (2023) Effect of different diets on growth performance, a physiological response, and behavior of spiny lobster *Panulirus homarus* (Linnaeus, 1758). *Jurnal Kelautan Tropis, 26*(2), 301-314. Doi: https://doi.org/10.14710/jkt.v26i2.17656.

Silva, J. E. B., Boleli, I. C., & Simões, Z. L. P. (2002) Hemocyte types and total and differential counts in unparasitized and parasitized *Anastrepha obliqua* (Diptera, Tephritidae) larvae. *Brazilian Journal of Biology, 62*, 689-699. Doi: https://doi.org/10.1590/S1519-69842002000400017.

Teramoto T, Tanaka T (2004) Mechanism of reduction in the number of the circulating hemocytes in the *Pseudaletia separata* host parasitized by Cotesia kariyai. *Journal of Insect Physiology 50*, 1103–1111. https://10.1016/j.jinsphys.2004.08.005.

Tojo S, Naganuma F, Arakawa K ve Yokoo S (2000) Involvement of both granular cells and plasmatocytes in phagocytic reactions in the Greater Wax Moth, *Galleria mellonella*. Journal of *Insect Physiology, 46*, 1129-1135. PMID:10817839.

Tran, S. L., Puhar, A., Ngo-Camus, M., & Ramarao, N. (2011) Trypan blue dye enters viable cells incubated with the pore-forming toxin HlyII of *Bacillus cereus*. *PloS one, 6*(9), e22876. Doi: https://doi.org/10.1371/journal.pone.0022876.

Turan, M., & Mammadov, R. (2021) Evaluation of the toxicity activity of bioactive compounds of some geophytes against brine shrimp (*Artemia salina* l.). *Acta Aquatica Turcica, 17*(2),195-201. Doi: https://doi.org/10.22392/actaquatr.791297.

Uzuner, Ç.S. (2018) Development of a direct trypan blue exclusion method to detect cell viability of adherent cells into ELISA plates selcen. *Celal Bayar University Journal of Science 1*(1), 99-104. https:// 10.18466/cbayarfbe.372192.

Chapter 5

HERMITE–HADAMARD INEQUALITIES FOR HARMONIC (S,P)–FUNCTIONS

Serap ÖZCAN[1]

1 Kırklareli University, Faculty of Arts and Sciences, Department of Mathematics, Kırklareli, TURKEY, ORCID ID: https://orcid.org/0000-0001-6496-5088

1. Introduction

A function $\Omega: J \subseteq \mathbb{R} \to \mathbb{R}$ is called convex on I, if

$$\Omega(\lambda\varkappa + (1-\lambda)z) \leq \lambda\Omega(\varkappa) + (1-\lambda)\Omega(z)$$

for all $\varkappa, z \in J$ and $\lambda \in [0,1]$.

The theory of convexity is a fundamental aspect in various domains. Several studies have demonstrated that many of the results obtained concerning these inequalities are direct outcomes of the applications of convex functions. The Hermite–Hadamard inequality stands as one of the most reknowned. This inequality is expressed as follows (see, [1-3]):

Theorem 1.1. Suppose $\Omega: J \subseteq \mathbb{R} \to \mathbb{R}$ is a convex function and $r, k \in J$ with $r < k$. Then the inequality

$$\Omega\left(\frac{r+k}{2}\right) \leq \frac{1}{k-r}\int_r^k \Omega(\varkappa)d\varkappa \leq \frac{\Omega(r)+\Omega(k)}{2}$$

holds.

The Hermite–Hadamard inequality can be viewed as an enhancement of the concept of convexity. In recent times, several generalizations and extensions have been explored for classical convexity. Additionally, numerous investigations have been dedicated to establishing new bounds for both the left and right–hand sides of the Hermite–Hadamard inequality. For some illustrative instances, please refer the monographs [2–23].

In [24], İşcan introduced the class of harmonically convex functions and investigated the Hermite–Hadamard inequality for this class of functions:

Definition 1.2. Let $J \subset (0,\infty)$ be a real interval. A function $\Omega: J \to \mathbb{R}$ is called harmonic convex, if

$$\Omega\left(\frac{\varkappa z}{\lambda\varkappa + (1-\lambda)z}\right) = \lambda\Omega(z) + (1-\lambda)\Omega(\varkappa)$$

for all $\varkappa, z \in J$ and $\lambda \in [0,1]$.

Theorem 1.3. Suppose $J \subset (0,\infty) \to \mathbb{R}$ is harmonic convex and $r, k \in J$ with $r < k$. If $\Omega \in L[r,k]$, then

$$\Omega\left(\frac{2rk}{r+k}\right) \leq \frac{rk}{k-r}\int_r^k \frac{\Omega(x)}{x^2}dx \leq \frac{\Omega(r)+\Omega(k)}{2}.$$

In [25], classes of harmonic s–convex functions and harmonic P–functions are introduced and integral inequalities of Hermite–Hadamard type for these classes of functions are established as follows:

Definition 1.4. Let $s \in (0,1]$. Suppose $J \subseteq \mathbb{R} \setminus \{0\}$ is a real interval. A function $\Omega: J \subseteq (0,\infty) \to \mathbb{R}$ is called harmonic s–convex, if

$$\Omega\left(\frac{\varkappa z}{\lambda\varkappa + (1-\lambda)z}\right) \leq \lambda^s\Omega(z) + (1-\lambda)^s\Omega(\varkappa),$$

for every $\varkappa, z \in J,\ \lambda \in [0,1]$.

Theorem 1.5. Let $\Omega: J \subset (0,\infty) \to \mathbb{R}$ be a harmonic s–convex function and $r, k \in J$ with $r < k$. If $\Omega \in L[r,k]$, then

$$2^{s-1}\Omega\left(\frac{2rk}{r+k}\right) \leq \frac{rk}{k-r}\int_r^k \frac{\Omega(\varkappa)}{\varkappa^2}d\varkappa \leq \frac{\Omega(r)+\Omega(k)}{s+1}.$$

Definition 1.6. A function $\Omega: J \subset (0,\infty) \to \mathbb{R}$ \$ is called harmonic P–function, if

$$\Omega\left(\frac{\varkappa z}{\lambda\varkappa + (1-\lambda)z}\right) = \Omega(\varkappa) + \Omega(z)$$

for every $\varkappa, z \in J$ and $\lambda \in [0,1]$.

Theorem 1.7. Let $\Omega: J \subset (0,\infty) \to \mathbb{R}$ be a harmonic P–function and $r, k \in J$ with $r < k$. If $\Omega \in L[r,k]$, then

$$\Omega\left(\frac{2rk}{r+k}\right) \leq \frac{2rk}{k-r}\int_r^k \frac{\Omega(\varkappa)}{\varkappa^2}d\varkappa \leq 2(\Omega(r)+\Omega(k)).$$

Numerous research efforts have been devoted to extending the concept of harmonic convex functions and deriving their Hermite–Hadamard type inequalities. For recent investigations concerning Hermite–Hadamard type inequalities, you can consult the monographs [24–31].

In [32], Numan and İşcan introduced the concept of (s,P)–function as follows:

Definition 1.8. Let $s \in (0,1]$. A function $\Omega: J \subset \mathbb{R} \to \mathbb{R}$ is called (s,P)-function, if

$$\Omega(\lambda\varkappa + (1-\lambda)z) \leq (\lambda^s + (1-\lambda)^s)(\Omega(\varkappa) + \Omega(z)),$$

for all $\varkappa, z \in J,\ \lambda \in [0,1]$.

Definition 1.9. [33] Let Ω and ζ be two functions. If

$$\big(\Omega(\varkappa) - \Omega(z)\big)\big(\zeta(\varkappa) - \zeta(z)\big) \geq 0$$

holds for every $\varkappa, z \in \mathbb{R}$, then Ω and ζ are called similarly ordered mappings.

In [24], İşcan gave the following lemma:

Lemma 1.10. Let $\Omega: J \subseteq \mathbb{R} \setminus \{0\} \to \mathbb{R}$ be a differentiable mapping on J^0, $r, k \in J$ with $r < k$, and $\Omega' \in L[r,k]$, then

$$\frac{\Omega(r)+\Omega(k)}{2} - \frac{rk}{k-r}\int_r^k \frac{\Omega(\varkappa)}{\varkappa^2}\,d\varkappa = \frac{rk(k-r)}{2}\int_0^1 \frac{1-2\lambda}{(\lambda k + (1-\lambda)r)^2}\,\Omega'\left(\frac{rk}{\lambda k + (1-\lambda)r}\right)d\lambda.$$

Several investigations have indicated that numerous findings in the field of inequality theory are closely linked to the theory of convex functions.

The renowned Hölder inequality is recognized for its fundamental significance across various realms of pure and applied sciences. It also holds notable relevance in the realm of convex functions theory and plays a crucial role in numerous branches of applied mathematics. Similarly, the power–mean integral inequality stands out as one of the most well-known inequalities with applications in the context of convex functions.

In [34], Hölder integral inequality is given as follows:

Theorem 1.11. Let $p > 1$ and $1/p + 1/q = 1$. If the real functions Ω and ζ are defined on $[r,k]$ and if $|\Omega|^p$ and $|\zeta|^q$ are integrable on $[r,k]$, then

$$\int_r^k |\Omega(\varkappa)\zeta(\varkappa)|d\varkappa \leq \left(\int_r^k |\Omega(\varkappa)|^p d\varkappa\right)^{\frac{1}{p}} \left(\int_r^k |\zeta(\varkappa)|^q d\varkappa\right)^{\frac{1}{q}},$$

inequality holds if and only if $A|\Omega(\varkappa)|^p = B|\zeta(\varkappa)|^q$ almost everywhere, where A and B are constants.

An alternative form of the Hölder integral inequality, known as the Power–mean integral inequality, is stated as follows:

Theorem 1.12. Let $q \geq 1$. If the real functions Ω and ζ are defined on $[r, k]$ and if $|\Omega|$, $|\Omega||\zeta|^q$ are integrable on $[r, k]$, then

$$\int_r^k |\Omega(\varkappa)\zeta(\varkappa)|d\varkappa \leq \left(\int_r^k |\Omega(\varkappa)|d\varkappa\right)^{1-\frac{1}{q}} \left(\int_r^k |\Omega(\varkappa)||\zeta(\varkappa)|^q d\varkappa\right)^{\frac{1}{q}}.$$

2. Harmonic (s, P)–Functions and Related Inequalities

Definition 2.1. A function $\Omega: J \subset (0, \infty) \to R$ is said to be harmonic (s, P)–function, if

$$\Omega\left(\frac{\varkappa z}{\lambda\varkappa + (1-\lambda)z}\right) \leq (\lambda^s + (1-\lambda)^s)(\Omega(\varkappa) + \Omega(z)),$$

for all $\varkappa, z \in J$, $\lambda \in [0,1]$ and for some fixed $s \in (0,1]$.

Now, let's revisit the following specific functions.

The gamma function is defined as follows:

$$\Gamma(\varkappa) = \int_0^{+\infty} e^{-\varkappa}\lambda^{\varkappa-1}d\lambda,\ \varkappa > 0.$$

The beta function is defined as follows:

$$\beta(\varkappa, y) = \int_0^1 (1-\lambda)^{y-1}\lambda^{x-1}d\lambda,\ \varkappa > 0, y > 0,$$

$$\beta(\varkappa, y) = \frac{\Gamma(\varkappa)\Gamma(y)}{\Gamma(\varkappa + y)}.$$

The hypergeometric function is defined as follows:

$$ {}_2F_1(\varkappa, y; c; z) = \frac{1}{\beta(y, c-y)} \int_0^1 \lambda^{y-1}(1-\lambda)^{c-y-1}(1-z\lambda)^{-\varkappa} d\lambda, $$
$$ |z| < 1,\ c > y > 0. $$

Theorem 2.2. Let $\Omega: J \subset (0,\infty) \to \mathbb{R}$ be a differentiable mapping on J^0 such that $\Omega' \in L[r,k]$, where $r, k \in J^0$ with $r < k$. If $|\Omega'|^q$ is harmonic (s,P)–function on $[r,k]$ for some fixed $s \in (0,1], q \geq 1$, then

$$ \left| \frac{\Omega(r)+\Omega(k)}{2} - \frac{rk}{k-r} \int_r^k \frac{\Omega(\varkappa)}{\varkappa^2} d\varkappa \right| $$

$$ \leq \frac{rk(k-r)}{2} \kappa_1^{1-\frac{1}{q}}(r,k) \left[\left(\kappa_2(s;r,k) + \kappa_3(s;r,k) \right) \left(|\Omega'(r)|^q + |\Omega'(k)|^q \right) \right]^{\frac{1}{q}}, $$

where

$$ \kappa_1(r,k) = k^{-2} \left({}_2F_1\left(2,2;3;1-\frac{r}{k}\right) - {}_2F_1\left(2,1;2;1-\frac{r}{k}\right) + \frac{1}{2}\, {}_2F_1\left(2,1;3;\frac{1}{2}\left(1-\frac{r}{k}\right)\right) \right), $$

$$ \kappa_2(s;r,k) = k^{-2} \left(\frac{2}{2+\mathrm{s}}\, {}_2F_1\left(2,2+\mathrm{s};3+\mathrm{s};1-\frac{r}{k}\right) - \frac{1}{1+s}\, {}_2F_1\left(2,1+s;2+s;1-\frac{r}{k}\right) + \frac{1}{2^s(1+s)(2+s)}\, {}_2F_1\left(2,1+\mathrm{s};3+\mathrm{s};\frac{1}{2}\left(1-\frac{r}{k}\right)\right) \right), $$

$$ \kappa_3(s;r,k) = k^{-2} \left(\frac{2}{(1+\mathrm{s})(2+s)}\, {}_2F_1\left(2,2;3+\mathrm{s};1-\frac{r}{k}\right) - \frac{1}{1+\mathrm{s}}\, {}_2F_1\left(2,1;2+\mathrm{s};1-\frac{r}{k}\right) + \frac{1}{2}\, {}_2F_1\left(2,1;3;\frac{1}{2}\left(1-\frac{r}{k}\right)\right) \right). $$

Proof. Let $A_\lambda = \lambda r + (1-\lambda)k$. Using Lemma 1.10, the power–mean inequality, and the property of harmonic (s,P)–function of $|\Omega'|^q$, we have

$$\left|\frac{\Omega(r)+\Omega(k)}{2}-\frac{rk}{k-r}\int_r^k \frac{\Omega(\varkappa)}{\varkappa^2}d\varkappa\right|$$

$$\leq \frac{rk(k-r)}{2}\int_0^1 \frac{|1-2\lambda|}{A_\lambda^2}\left|\Omega'\left(\frac{rk}{A_\lambda}\right)\right|d\lambda$$

$$\leq \frac{rk(k-r)}{2}\left(\int_0^1 \frac{|1-2\lambda|}{A_\lambda^2}d\lambda\right)^{1-1/q}\left(\int_0^1 \frac{|1-2\lambda|}{A_\lambda^2}\left|\Omega'\left(\frac{rk}{A_\lambda}\right)\right|^q d\lambda\right)^{1/q}$$

$$\leq \frac{rk(k-r)}{2}\mu_1^{1-1/q}\left(\int_0^1 \frac{|1-2\lambda|}{A_\lambda^2}[(\lambda^s+(1-\lambda)^s)(|\Omega'(r)|^q + |\Omega'(k)|^q)]d\lambda\right)^{1/q}$$

$$\leq \frac{rk(k-r)}{2}\mu_1^{1-1/q}\left((\mu_2+\mu_3)(|\Omega'(r)|^q+|\Omega'(k)|^q)\right)^{1/q}$$

where

$$\mu_1=\int_0^1 \frac{|1-2\lambda|}{A_\lambda^2}d\lambda,$$
$$\mu_2=\int_0^1 \frac{|1-2\lambda|}{A_\lambda^2}\lambda^s d\lambda,$$
$$\mu_3=\int_0^1 \frac{|1-2\lambda|}{A_\lambda^2}(1-\lambda)^s d\lambda.$$

Calculating μ_1, μ_2 and μ_3, we have

$$\mu_1=\int_0^1 \frac{|1-2\lambda|}{A_\lambda^2}d\lambda$$

$$=\int_0^{1/2}\frac{1-2\lambda}{A_\lambda^2}d\lambda+\int_{1/2}^1\frac{2\lambda-1}{A_\lambda^2}d\lambda$$

$$=\int_0^1\frac{2\lambda-1}{A_\lambda^2}d\lambda+2\int_0^{1/2}\frac{1-2\lambda}{A_\lambda^2}d\lambda$$

$$= \int_0^1 \lambda A_\lambda^{-2} d\lambda - \int_0^1 A_\lambda^{-2} d\lambda + \int_0^1 (1-u)k^{-2}\left(1 - u\frac{1}{2}\left(1-\frac{r}{k}\right)\right)^{-2} du$$

$$= k^{-2}\Bigg({}_2F_1\left(2,2;3;1-\frac{r}{k}\right) - {}_2F_1\left(2,1;2;1-\frac{r}{k}\right) + \frac{1}{2}\,{}_2F_1\left(2,1;3;\frac{1}{2}\left(1-\frac{r}{k}\right)\right)\Bigg)$$

$$= \kappa_1(r,k).$$

Similarly, we get

$$\mu_2 = \int_0^1 \frac{|1-2\lambda|\lambda^s}{A_\lambda^2} d\lambda$$

$$= \int_0^1 \frac{2\lambda-1}{A_\lambda^2}\lambda^s d\lambda + 2\int_0^{1/2} \frac{1-2\lambda}{A_\lambda^2}\lambda^s d\lambda$$

$$= 2\int_0^1 \lambda^{s+1} A_\lambda^{-2} d\lambda - \int_0^1 \lambda^s A_\lambda^{-2} d\lambda + \frac{1}{2^s}\int_0^1 (1 - u)u^s k^{-2}\left(1 - u\frac{1}{2}\left(1-\frac{r}{k}\right)\right)^{-2} du$$

$$= \frac{2k^{-2}}{2+s}\,{}_2F_1\left(2,2+s;3+s;1-\frac{r}{k}\right) - \frac{k^{-2}}{1+s}\,{}_2F_1\left(2,1+s;2+s;1-\frac{r}{k}\right) + \frac{k^{-2}}{2^s(1+s)(2+s)}\,{}_2F_1\left(2,1+s;3+s;\frac{1}{2}\left(1-\frac{r}{k}\right)\right)$$

$$= \kappa_2(s;r,k),$$

and

$$\mu_3 = \int_0^1 \frac{|1-2\lambda|(1-\lambda)^s}{A_\lambda^2} d\lambda$$

$$= \int_0^1 \frac{2\lambda-1}{A_\lambda^2}(1-\lambda)^s d\lambda + 2\int_0^{1/2} \frac{1-2\lambda}{A_\lambda^2}(1-\lambda)^s d\lambda$$

$$\leq 2\int_0^1 \lambda(1-\lambda)^s A_\lambda^{-2}d\lambda - \int_0^1 (1-\lambda)^s A_\lambda^{-2}d\lambda + 2\int_0^{1/2} \frac{1-2\lambda}{A_\lambda^2}d\lambda$$

$$= k^{-2}\left(\frac{2}{(1+s)(2+s)}\ {}_2F_1\left(2,2;3+s;1-\frac{r}{k}\right)\right.$$
$$-\frac{1}{s+1}\ {}_2F_1\left(2,1;2+s;1-\frac{r}{k}\right)$$
$$\left.+\frac{1}{2}\ {}_2F_1\left(2,1;3;\frac{1}{2}\left(1-\frac{r}{k}\right)\right)\right)$$

$$= \kappa_3(s;r,k).$$

Theorem 2.3. Let $s \in (0,1]$. Suppose $\Omega: J \subset (0,\infty) \to \mathbb{R}$ is a differentiable mapping on J^0 such that $\Omega' \in L[r,k]$, where $r,k \in J^0$ with $r<k$. If $|\Omega'|^q$ is a harmonic (s,P)–function on $[r,k]$ for $q>1$, then

$$\left|\frac{\Omega(r)+\Omega(k)}{2} - \frac{rk}{k-r}\int_r^k \frac{\Omega(\varkappa)}{\varkappa^2}d\varkappa\right|$$

$$\leq \frac{r(k-r)}{2k}\left(\frac{1}{p+1}\right)^{1/p}\left(\left({}_2F_1\left(2q,1+s;2+s;1-\frac{r}{k}\right)\right.\right.$$
$$\left.+\ {}_2F_1\left(2q,1;2+s;1-\frac{r}{k}\right)\right)$$
$$\left.\times(1+s)^{-1}\left(|\Omega'(r)|^q+|\Omega'(k)|^q\right)\right)^{1/q}$$

where $(1/p)+(1/q)=1$.

Proof. Let $A_\lambda = \lambda r + (1-\lambda)k$. Utilizing Lemma 1.10, the Hölder inequality, and the property of harmonic (s,P)–function of $|\Omega'|^q$, we have

$$\left|\frac{\Omega(r)+\Omega(k)}{2} - \frac{rk}{k-r}\int_r^k \frac{\Omega(\varkappa)}{\varkappa^2}d\varkappa\right|$$

$$\leq \frac{rk(k-r)}{2}\int_0^1 \frac{|1-2\lambda|}{A_\lambda^2}\left|\Omega'\left(\frac{rk}{A_\lambda}\right)\right|d\lambda$$

$$\leq \frac{rk(k-r)}{2}\left(\int_0^1 |1-2\lambda|^p d\lambda\right)^{1/p}\left(\int_0^1 \frac{1}{A_\lambda^{2q}}\left|\Omega'\left(\frac{rk}{A_\lambda}\right)\right|^q d\lambda\right)^{1/q}$$

$$\leq \frac{rk(k-r)}{2}\mu_4^{1/p}\left(\int_0^1 \frac{1}{A_\lambda^{2q}}[(\lambda^s+(1-\lambda)^s)(|\Omega'(r)|^q + |\Omega'(k)|^q)]d\lambda\right)^{1/q}$$

$$= \frac{rk(k-r)}{2}\mu_4^{1/p}[(\mu_5+\mu_6)(|\Omega'(r)|^q+|\Omega'(k)|^q)]^{1/q}$$

where

$$\mu_4 = \int_0^1 |1-2\lambda|^p d\lambda = \frac{1}{p+1},$$

$$\mu_5 = \int_0^1 A_\lambda^{-2q}\lambda^s d\lambda$$

$$= k^{-2q}\int_0^1 \lambda^s\left(1-\lambda\left(1-\frac{r}{k}\right)\right)^{-2q} d\lambda$$

$$= \frac{1}{(1+s)k^{2q}}\,{}_2F_1\left(2q, 1+s; 2+s; 1-\frac{r}{k}\right),$$

$$\mu_6 = \int_0^1 A_\lambda^{-2q}(1-\lambda)^s d\lambda$$

$$= k^{-2q}\int_0^1 (1-\lambda)^s\left(1-\lambda\left(1-\frac{r}{k}\right)\right)^{-2q} d\lambda$$

$$= \frac{1}{(1+s)k^{2q}}\,{}_2F_1\left(2q, 1; 2+s; 1-\frac{r}{k}\right).$$

3. Inequalities for Products of Harmonic (s, P)–Functions

Theorem 3.1. Let $\Omega, \zeta: [r,k] \to [0,\infty), r,k \in (0,\infty), r < k,$ be functions such that $\Omega, \zeta, \Omega\zeta \in L[r,k]$. If Ω is a harmonic (s_1, P)–function and ζ is a harmonic (s_2, P)–function on $[r,k]$ for some fixed $s_1, s_2 \in (0,1]$, then

$$\frac{rk}{k-r}\int_r^k \frac{\Omega(\varkappa)\zeta(\varkappa)}{\varkappa^2}d\varkappa \le M(r,k)\left(\frac{2}{1+s_1+s_2}+\frac{2\Gamma(1+s_1)\Gamma(1+s_2)}{\Gamma(2+s_1+s_2)}\right).$$

where $M(r,k) = \Omega(r)\zeta(r) + \Omega(k)\zeta(k) + \Omega(r)\zeta(k) + \Omega(k)\zeta(r)$.

Proof. Since Ω is a harmonic (s_1, P)–function and ζ is a harmonic (s_2, P)–function on $[r,k]$, then for $\lambda \in [0,1]$ we get

$$\Omega\left(\frac{rk}{\lambda r+(1-\lambda)k}\right) \le (\lambda^{s_1}+(1-\lambda)^{s_1})\big(\Omega(r)+\Omega(k)\big),$$

$$\zeta\left(\frac{rk}{\lambda r+(1-\lambda)k}\right) \le (\lambda^{s_2}+(1-\lambda)^{s_2})(\zeta(r)+\zeta(k)).$$

Multiplying the above inequalities, we get

$$\begin{aligned}\Omega\left(\frac{rk}{\lambda r+(1-\lambda)k}\right)\zeta\left(\frac{rk}{\lambda r+(1-\lambda)k}\right) &\le (\lambda^{s_1+s_2}+(1-\lambda)^{s_1+s_2}+\lambda^{s_1}(1-\lambda)^{s_2}+(1-\lambda)^{s_1}\lambda^{s_2})\\ &\quad\times(\Omega(r)\zeta(r)+\Omega(k)\zeta(k)\\ &\quad+\Omega(r)\zeta(k)\\ &\quad+\Omega(k)\zeta(r)).\end{aligned}$$

Integrating both sides of the above inequality with respect to λ over $[0,1]$, we obtain

$$\int_0^1 \Omega\left(\frac{rk}{\lambda r+(1-\lambda)k}\right)\zeta\left(\frac{rk}{\lambda r+(1-\lambda)k}\right)d\lambda$$

$$= \frac{rk}{k-r}\int_r^k \frac{\Omega(\varkappa)\zeta(\varkappa)}{\varkappa^2}d\varkappa$$

$$\leq M(r,k)\left(\int_0^1 [\lambda^{s_1+s_2}+(1-\lambda)^{s_1+s_2}]d\lambda \right.$$
$$\left. +\int_0^1 [\lambda^{s_1}(1-\lambda)^{s_2}+(1-\lambda)^{s_1}\lambda^{s_2}]d\lambda\right).$$

From

$$\int_0^1 [\lambda^{s_1+s_2}+(1-\lambda)^{s_1+s_2}]d\lambda = \frac{2}{1+s_1+s_2},$$

$$\int_0^1 [\lambda^{s_1}(1-\lambda)^{s_2}+(1-\lambda)^{s_1}\lambda^{s_2}]d\lambda = 2\beta(1+s_1,1+s_2),$$

we get

$$\frac{rk}{k-r}\int_r^k \frac{\Omega(\varkappa)\zeta(\varkappa)}{\varkappa^2}d\varkappa \leq M(r,k)\left(\frac{2}{1+s_1+s_2}+2\beta(1+s_1,1+s_2)\right).$$

Remark 3.2. If we choose $s_1 = s_2 = 1$ in Theorem 3.1, then we obtain

$$\frac{rk}{k-r}\int_r^k \frac{\Omega(\varkappa)\zeta(\varkappa)}{\varkappa^2}d\varkappa \leq M(r,k).$$

Remark 3.3. Putting $s_1 = s_2 = 1$ and $\zeta \equiv 1$ in Theorem 3.1 gives

$$\frac{rk}{k-r}\int_r^k \frac{\Omega(\varkappa)}{\varkappa^2}d\varkappa \leq 2\big(\Omega(r)+\Omega(k)\big).$$

Theorem 3.4. Let $\Omega, \zeta: [r,k] \to [0,\infty), r,k \in (0,\infty), r<k,$ be functions such that $\Omega, \zeta, \Omega\zeta \in L[r,k]$. If Ω is a harmonic (s_1,P)–function and ζ is a harmonic (s_2,P)–function on $[r,k]$ for some fixed $s_1, s_2 \in (0,1]$, then

$$2^{s_1+s_2-3}\Omega\left(\frac{2rk}{r+k}\right)\zeta\left(\frac{2rk}{r+k}\right)$$
$$\leq \frac{rk}{k-r}\int_r^k \frac{\Omega(\varkappa)\zeta(\varkappa)}{\varkappa^2}d\varkappa$$
$$+ M(r,k)\left(\frac{1}{1+s_1+s_2}+\frac{\Gamma(1+s_1)\Gamma(1+s_2)}{\Gamma(2+s_1+s_2)}\right),$$

where $M(r,k) = \Omega(r)\zeta(r) + \Omega(k)\zeta(k) + \Omega(r)\zeta(k) + \Omega(k)\zeta(r)$.

Proof. Using the properties of harmonically (s,P)–functions Ω and ζ, we have for all $x, z \in [r,k]$

$$\Omega\left(\frac{2xz}{x+z}\right) \leq \frac{\Omega(x)+\Omega(z)}{2^{s_1-1}},$$

$$\zeta\left(\frac{2xz}{x+z}\right) \leq \frac{\zeta(x)+\zeta(z)}{2^{s_2-1}}.$$

Choosing $x = rk/(\lambda r + (1-\lambda)k)$ and $z = rk/(\lambda k + (1-\lambda)r)$, we have

$$\Omega\left(\frac{2rk}{r+k}\right)\zeta\left(\frac{2rk}{r+k}\right)$$

$$\leq \frac{\Omega(rk/(\lambda r + (1-\lambda)k)) + \Omega(rk/(\lambda k + (1-\lambda)r))}{2^{s_1-1}}$$

$$\times \frac{\zeta(rk/(\lambda r + (1-\lambda)k)) + \zeta(rk/(\lambda k + (1-\lambda)r))}{2^{s_2-1}}$$

$$= \frac{1}{2^{s_1+s_2-2}}\left[\Omega\left(\frac{rk}{\lambda r + (1-\lambda)k}\right)\zeta\left(\frac{rk}{\lambda r + (1-\lambda)k}\right) + \Omega\left(\frac{rk}{\lambda r + (1-\lambda)k}\right)\zeta\left(\frac{rk}{\lambda k + (1-\lambda)r}\right)\right.$$

$$\left. + \Omega\left(\frac{rk}{\lambda k + (1-\lambda)r}\right)\zeta\left(\frac{rk}{\lambda r + (1-\lambda)k}\right) + \Omega\left(\frac{rk}{\lambda k + (1-\lambda)r}\right)\zeta\left(\frac{rk}{\lambda k + (1-\lambda)r}\right)\right]$$

$$\leq \frac{1}{2^{s_1+s_2-2}}\left[\Omega\left(\frac{rk}{\lambda r + (1-\lambda)k}\right)\zeta\left(\frac{rk}{\lambda r + (1-\lambda)k}\right) + \Omega\left(\frac{rk}{\lambda k + (1-\lambda)r}\right)\zeta\left(\frac{rk}{\lambda k + (1-\lambda)r}\right)\right.$$

$$+ \frac{1}{2^{s_1+s_2-2}}\{[(\lambda^{s_1} + (1-\lambda)^{s_1})(\Omega(r) + \Omega(k))(\zeta(r) + \zeta(k))]$$

$$+ [(\lambda^{s_2} + (1-\lambda)^{s_2})(\Omega(r) + \Omega(k))(\zeta(r) + \zeta(k))]\}$$

$$= \frac{1}{2^{s_1+s_2-2}}\left[\Omega\left(\frac{rk}{\lambda r + (1-\lambda)k}\right)\zeta\left(\frac{rk}{\lambda r + (1-\lambda)k}\right) + \Omega\left(\frac{rk}{\lambda k + (1-\lambda)r}\right)\zeta\left(\frac{rk}{\lambda k + (1-\lambda)r}\right)\right]$$

$$+\frac{1}{2^{s_1+s_2-2}}M(r,k)[\lambda^{s_1}(1-\lambda)^{s_2}+(1-\lambda)^{s_1}\lambda^{s_2} + (1-\lambda)^{s_1+s_2}+\lambda^{s_1+s_2}].$$

Integrating the resulting inequality with respect to λ over $[0,1]$, we get

$$\Omega\left(\frac{2rk}{r+k}\right)\zeta\left(\frac{2rk}{r+k}\right)$$

$$\leq \frac{1}{2^{s_1+s_2-2}}\left[\int_0^1 \Omega\left(\frac{rk}{\lambda r+(1-\lambda)k}\right)\zeta\left(\frac{rk}{\lambda r+(1-\lambda)k}\right)d\lambda\right.$$

$$\left.+\int_0^1 \Omega\left(\frac{rk}{\lambda k+(1-\lambda)r}\right)\zeta\left(\frac{rk}{\lambda k+(1-\lambda)r}\right)d\lambda\right]$$

$$+\frac{1}{2^{s_1+s_2-2}}M(r,k)\left(\int_0^1 [\lambda^{s_1}(1-\lambda)^{s_2}+(1-\lambda)^{s_1}\lambda^{s_2}]d\lambda + \int_0^1 [(1-\lambda)^{s_1+s_2}+\lambda^{s_1+s_2}]d\lambda\right)$$

That is,

$$\Omega\left(\frac{2rk}{r+k}\right)\zeta\left(\frac{2rk}{r+k}\right)$$

$$\leq \frac{1}{2^{s_1+s_2-3}}\frac{rk}{k-r}\int_a^b \frac{\Omega(\varkappa)\zeta(\varkappa)}{\varkappa^2}d\varkappa$$

$$+\frac{1}{2^{s_1+s_2-2}}M(r,k)\left\{\int_0^1 [\lambda^{s_1}(1-\lambda)^{s_2}+(1-\lambda)^{s_1}\lambda^{s_2}]d\lambda + \int_0^1 [(1-\lambda)^{s_1+s_2}+\lambda^{s_1+s_2}]d\lambda\right\}.$$

From

$$\int_0^1 [\lambda^{s_1}(1-\lambda)^{s_2}+(1-\lambda)^{s_1}\lambda^{s_2}]d\lambda = 2\beta(1+s_1,1+s_2),$$

$$\int_0^1 [(1-\lambda)^{s_1+s_2} + \lambda^{s_1+s_2}]d\lambda = \frac{2}{1+s_1+s_2},$$

we get

$$2^{s_1+s_2-3}\Omega\left(\frac{2rk}{r+k}\right)\zeta\left(\frac{2rk}{r+k}\right)$$

$$\leq \frac{rk}{k-r}\int_r^k \frac{\Omega(\varkappa)\zeta(\varkappa)}{\varkappa^2}d\varkappa + M(r,k)\left(\frac{1}{1+s_1+s_2} + \beta(1+s_1,1+s_2)\right).$$

Remark 3.5. Putting $s_1 = s_2 = 1$ in Theorem 3.4 gives

$$\frac{1}{2}\Omega\left(\frac{2rk}{r+k}\right)\zeta\left(\frac{2rk}{r+k}\right) \leq \frac{rk}{k-r}\int_r^k \frac{\Omega(\varkappa)\zeta(\varkappa)}{\varkappa^2}d\varkappa + \frac{M(r,k)}{2}$$

Remark 3.6. If we choose $s_1 = s_2 = 1$ and $\zeta \equiv 1$ in Theorem 3.4, then we have

$$\frac{1}{2}\Omega\left(\frac{2rk}{r+k}\right) \leq \frac{rk}{k-r}\int_r^k \frac{\Omega(\varkappa)}{\varkappa^2}d\varkappa + \Omega(r) + \Omega(k).$$

REFERENCES

1. Dragomir S.S., Pearce C.E.M., Selected Topics on Hermite–Hadamard Inequalities and Applications. RGMIA Monographs, Victoria University, 2000.

2. Hadamard J., Etude sur les proprietes des fonctions entieres en particulier d'une fonction consideree par Riemann. Journal de Mathematiques Pures et Appliquees Serie 4, 1893; 9, 171–215.

3. Pecaric J.E., Proschan F., Tong Y.L., Convex Functions, Partial Orderings and Statistical Applications. Academic Press, Boston, 1992.

4. Budak H., Ali M.A., Tarhanacı M., Some new quantum Hermite–Hadamard–like inequalities for coordinated convex functions, Journal of Optimization Theory and Applications, 2020; 186 (3), 899–910.

5. Butt S.I., Pecaric J., Generalized Hermite–Hadamard's inequality. Proceedings of A.Razmadze Mathematical Institute, 2013; 163, 9–27.

6. Dragomir S.S., Pearce C.E.M., Quasi–convex functions and Hermite-Hadamard's inequality. Bulletin of the Australian Mathematical Society, 1998; 57 (3), 377–385.

7. Kadakal M., İşcan, İ., Exponential type convexity and some related inequalities. Journal of Inequalities and Applications, 2020; 2020:82.

8. Kadakal H., On generalization of some integral inequalities for multiplicatively P–functions. TWMS Journal of Applied and Engineering Mathematics, 2020; 10 (4): 1023–1035.

9. Kunt M., İşcan İ., Hermite–Hadamard–Fejer type inequalities for p–convex functions. Arab Journal of Mathematical Sciences, 2017; 23 (2), 215–230.

10. Latif M.A., Inequalities of Hermite-Hadamard type for functions whose derivatives in absolute value are convex with applications. Arab Journal of Mathematical Sciences, 2015; 21 (1), 84–97.

11. Maden S., Kadakal H., Kadakal M., İşcan İ., Some new integral inequalities for n-time differentiable convex and concave functions, Journal of Nonlinear Sciences and Applications, 2017; 10, 6141–6148.

12. Noor M.A., Qi F., Awan M.U., Some Hermite–Hadamard type inequalities for log−h-convex functions. Analysis, 2013; 33: 1–9.

13. Özcan S., İşcan İ., Some new Hermite–Hadamard type inequalities for s–convex functions and their applications, Journal of Inequalities and Applications, 2019; 2019:201.

14. Özcan, S., Hermite–Hadamard type inequalities for exponential type multiplicatively convex functions. Filomat, 2023; 37 (28), 9777–9789.

15. Özcan S., Hermite–Hadamard type inequalities for multiplicatively h–convex functions. Konuralp Journal of Mathematics, 2020; 8 (1), 158–164.

16. Özcan, S., Hermite–Hadamard type inequalities for multiplicatively s–convex functions. Cumhuriyet Science Journal, 2020; 41 (1), 245–259.

17. Özcan, S., Hermite–Hadamard type inequalities for multiplicatively P–functions. Gümüşhane University Journal of Science and Technology, 2020; 10 (2), 486–491.

18. Sarıkaya M.Z., Budak H., On generalized Hermite-Hadamard inequality for generalized convex function. International Journal of Nonlinear Analysis and Applications, 2017; 8 (2), 209–222.

19. Set E., İşcan, İ., Sarıkaya M.Z., Özdemir M.E., On new inequalities of Hermite–Hadamard–Fejer type for convex functions via fractional integrals. Applied Mathematics and Computation, 2015; 259, 875–881.

20. Set E., Gözpınar A., Butt S.I., A study on Hermite–Hadamard–type inequalities via new fractional conformable integrals. Asian-European Journal of Mathematics, 2021; 14 (02), 2150016.

21. Shuang Y., Qi F., Integral inequalities of Hermite–Hadamard type for extended s–convex functions and applications. Mathematics, 2018; 6 (11), 223.

22. Turhan S., Demirel A.K., Maden S., İşcan, İ., Hermite–Hadamard type integral inequalities for strongly p–convex functions. Turkish Journal of Mathematics and Computer Science, 2018; 10, 184–189.

23. Xi B.-Y., Qi F., Some integral inequalities of Hermite–Hadamard type for s–logarithmically convex functions, Acta Mathematica Scientis, English Series, 2015; 35A (3), 515–526.

24. İ. İşcan, Hermite–Hadamard type inequalities for harmonically convex functions, Hacettepe J. Math. Stat., 2014; 43 (6), 935–942.

25. M. A. Noor, K. I. Noor, M. U. Awan and S. Costache, Some Integral Inequalities for Harmonically h–Convex Functions, U.P.B. Sci. Bull., Series A, 2015; 77 (1), 5–16.

26. Butt S.I., Akdemir A.O., Nadeem M., Mlaiki N., İşcan İ., Abdeljawad T., (m,n)–harmonically polynomial convex functions and some Hadamard type inequalities on the co–ordinates. AIMS Mathematics, 2021; 6 (5), 4677–4690.

27. Butt S.I., Tariq M., Aslam A., Ahmad H., Nofal T.A., Hermite-Hadamard type inequalities via generalized harmonic exponential convexity and applications, Journal of Function Spaces, 2021; 2021, 5533491.

28. Kadakal H., Hermite-Hadamard type inequalities for two times differentiable arithmetic-harmonically convex functions, Cumhuriyet Science Journal, 2019; 40 (3), 670–678.

29. Latif M.A., Du T., Hermite–Hadamard type inequalities for harmonically–convex functions using fuzzy integrals. Filomat, 2022; 36 (12), 4099–4110.

30. Noor M.A., Noor K.I., Iftikhar S., Some characterizations of harmonic convex functions, International Journal of Analysis and Applications, 2017; 15 (2), 179–187.

31. Özcan S., Some integral inequalities for harmonically (α,s)–convex functions, Journal of Function Spaces, 2019; 2019, 2394021.

32. Numan S., İşcan İ., On (s,P)–functions and related inequalities. Sigma Journal of Engineering and Natural Sciences, 2022; 40 (3), 585–592.

33. Varosanec S., On h–convexity. Journal of Mathematical Analysis and Applications, 2007; 326, 303–311.

34. Mitrinovic, D.S., Pecaric, J.E., Fink, A.M., Classical and New Inequalities in Analysis. Kluwer Academic Publishers, Dordrecth, Boston, London, 1993.

Chapter 6

CONFORMAL $f(R,\Phi,X)$ DOMAIN WALL

Erkan ERASLAN[1]
Melis ULU DOĞRU[2]

1 Çanakkale Onsekiz Mart University, School of Graduate Studies, Department of Physics. Çanakkale, TURKEY, erkan.eraslan@comu.edu.tr, ORCID: https://orcid.org/0000-0002-1741-9399
2 Assoc. Prof. Dr., Çanakkale Onsekiz Mart University, Science Faculty, Department of Physics. Çanakkale, TURKEY, melisulu@comu.edu.tr, ORCID: https://orcid.org/0000-0003-1788-3885

1. INTRODUCTION

General Relativity Theory (GRT) has given us a very different understanding of universe (Einstein, 1915). However, as a result of recent observations, GRT is incomplete in explaining some events of cosmology (Özemre, 1982). Despite all its successes, GRT cannot explain some situations such as early-time inflation and late-time expansion of the universe (Özemre, 1982; Asmodelle, 2017). As a result, research and development of alternative gravitation theories has improved. With the improvement of alternative gravitation theories, observational tests have also developed. The vast majority of alternative gravitation theories are associated with dark matter (DM) and dark energy (DE). Despite all their progress, the theories have still not provided a satisfactory solution. However, it provides a visible progress due to its explanations of the universe in different phases. For this reason, alternative gravitation theories are among the current research topics. Although number of the theories is very large, the teories, we focus on in this study are $f(R)$ theory, $f(R,T)$ theory, k-essence theory and $f(R,\Phi,X)$ theory.

$f(R)$ theory was created by Buchdahl (1970) by including a function f depending on gravitational motion of R in field equations instead of Ricci Scalar. Bamba, Nojiri & Odintsov, (2012) investigated static domain wall solution within scope of $f(R)$ theory. For this purpose, they showed that an effective domain wall could exist by recreating $f(R)$ gravity model. Moreover, they discussed the relationship between breaking of conformal invariance of electromagnetic field and change of structure constant. $f(R,T)$ theory was introduced by Harko, Lobo, Nojiri & Odintsov (2011). Here f represents a function based on Ricci Scalar and trace of Stress-Energy Tensor. Agrawal & Pawar (2017) examined Bianchi type V space-time with magnetic field in $f(R,T)$ theory and reached exact solution of the field equations. They examined behavior of several physical parameters, with and without magnetic fields. They found that obtained solution without magnetic fields appears in the situtation of stiff fluid.

k-essence theory was first proposed by Chiba, Okabe & Yamaguchi (2000). With this theory, inflation dynamics of the universe were tried to be explained by negative pressure. Adam, Grandi, Sanchez-Guillen & Wereszczyński (2008) showed propagation of linear perturbations within domain wall at standard type.

In $f(R,\Phi,X)$ theory, domain wall researches are not yet sufficent. So, the main purpose of this study is to investigate domain wall distributions in $f(R,\Phi,X)$ theory. We consider spherically symmetric and static space-time. We use some symmetry properties of the space-time such as conformal

symmetry. It is desired to determine whether the $f(R,\Phi,X)$ theory supports the existence of conformal domain walls.

This chapter is planned as follows: In Section 2, general definition of conformal symmetries is emphasized again. In Section 3, $f(R,\Phi,X)$ theory is defined with the principle of least action and field equations are mentioned. In Section 4, obtained solutions of conformal symmetric domain wall field equations within the scope of $f(R,\Phi,X)$ theory are calculated. So, their solutions are offered. Obtained results are discussed in Section 5.

2. CONFORMAL SYMMETRY

The space time of a single-parameter conformal motion group produced by a vector field ξ^a satisfies the equation $L_\zeta g_{ab} = \psi g_{ab}$ (Herrera, Jimenez, Leal, Ponce de Leon, Esculpi & Galina, 1984). Here, L_ζ is Lie Derivative with respect to the vector field ζ. ψ is an arbitrary function of coordinates (Eardley, 1974). Symmetries compatible with an arbitrary choice of the ψ function in $L_\zeta g_{ab} = \psi g_{ab}$ are considered. Herrera, Jimenez, Leal, Ponce de Leon, Esculpi & Galina (1984) state that use of general conformal symmetries instead of homothetic symmetries ($\psi: Constant$) may allow us to find static and spherically symmetric distributions of matter.

In this study, domain wall in conformal symmetric space-time is taken into consideration within the framework of $f(R,\Phi,X)$ theory. The conformal symmetric space-time, as is commonly known, is defined as follows (Herrera, Jimenez, Leal, Ponce de Leon, Esculpi & Galina, 1984):

$$ds^2 = \frac{C_1^2}{\psi^2(r)}dr^2 + r^2d\theta^2 + r^2sin^2\theta d\phi^2 - C_2^2r^2dt^2. \qquad (1)$$

Considering metric potentials in Equation (1), with the vector field $\zeta^1 = Constant, \zeta^0 = \zeta^2 = \zeta^3 = 0$, we have a symmetry such as already obtained definition of conformal symmetry given by the equation $L_\zeta g_{ab} = \psi g_{ab}$ (Herrera, Jimenez, Leal, Ponce de Leon, Esculpi & Galina, 1984). Here $\psi(r)$ is any function depending on the radial coordinate, C_1 and C_2 are arbitrary constants (Herrera, Jimenez, Leal, Ponce de Leon, Esculpi & Galina, 1984).

3. $f(R,\Phi,X)$ THEORY

$f(R,\Phi,X)$ theory was introduced by Hwang & Noh (2002). It is a scalar-tensor theory. Respectively, R denotes Ricci Scalar, Φ denotes scalar

potential and X denotes kinetic term (Bahamonde, Böhmer, Lobo & Sáez-Gómez, 2015). This theory includes dark energy together with modified gravity theories such as $f(R)$ theory and k-essence theory. Therefore, it is a theory with high potential for success, especially in examining late time dilation and $\Lambda - CDM$ evolution.

Action function of $f(R, \Phi, X)$ theory is generalized as follows (Tsujikawa, 2007):

$$S = \frac{1}{16\pi G}\int \sqrt{-g}\, f(R, \Phi, X) d^4x + S_m \tag{2}$$

where first part of action integration is defined curvature of space-time, scalar potential and kinetic term. Also, second part is directly interested with cosmic matter in considered space-time. X is given as follows:

$$X(\Phi) \propto \frac{1}{2}\left[\Phi^{,\alpha}\Phi_{,\alpha}\right]\xi \tag{3}$$

here, ξ is parameter. It can be commonly chosen as $\xi = 1$ in field equation solutions (Tsujikawa, 2007). Field equation of $f(R, \Phi, X)$ theory are found from the variation of equation (2) as follows (Bahamonde, Böhmer, Lobo & Sáez-Gómez, 2015):

$$FG_{ik} - \frac{1}{2}(f(R, \Phi, X) - RF)g_{ik} - \nabla_i\nabla_k F + g_{ik}\nabla_\alpha\nabla^\alpha F - \frac{\xi}{2}H(\nabla_i\Phi)(\nabla_k\Phi) = T_{ik} \tag{4}$$

here $F \equiv \frac{df}{dR}$ and $H \equiv \frac{df}{dX}$. Within the scope of $f(R, \Phi, X)$ theory, another important equation, Klein-Gordon equation, is given as follows:

$$\nabla_i\left(H\nabla^i\Phi\right) + \xi N = 0, \tag{5}$$

where $N \equiv \frac{df}{d\Phi}$ (Tsujikawa, 2007).

As it is known, energy-momentum tensor for perfect fluid is defined as follows:

$$T_{ik} = (p + \rho)u_i u_k + p g_{ik} \quad (6)$$

Domain wall can be formed as perfect fluid. In this case, $\rho = \rho_m + \sigma$ and ρ_m refers to energy density of domain wall and $p = p_m - \sigma$ and p_m refers to pressure of domain wall. Also, σ is tension density of domain wall. u_i is the four-velocity vector. In this study, observer co-moving motion was taken into consideration.

4. CONFORMAL SYMMETRIC DOMAIN WALL in $f(R, \Phi, X)$ THEORY

From Equation (1), Ricci Scalar is found as follows:

$$R = \frac{-6\psi\psi' r - 6\psi^2 + 2C_1^2}{C_1^2 r^2}. \quad (7)$$

Field equations and Klein-Gordon equation for conformal simmetric domain wall are found in $f(R, \Phi, X)$ theory as follows:

$$-6F''\psi^2 r^2 - 6F'\psi'\psi r^2 - 12F\psi'\psi r + 6F'\psi^2 r - 3\xi H\Phi'^2\psi^2 r^2 + 12F\psi^2 - 4FC_1^2 - 2C_1^2 r^2(p_m + \rho_m) = 0, \quad (8)$$

$$2F''\psi^2 r^2 + 2F'\psi'\psi r^2 + 4F\psi'\psi r - 2F'\psi^2 r + \xi H\Phi'^2\psi^2 r^2 - 4F\psi^2 + 4FC_1^2 - 2C_1^2 r^2(p_m + \rho_m) = 0, \quad (9)$$

$$-2F''\psi^2 r^2 - 2F'\psi'\psi r^2 - 4F\psi'\psi r + 2F'\psi^2 r - \xi H\Phi'^2\psi^2 r^2 + 4F\psi^2 + 4FC_1^2 - 6C_1^2 r^2(p_m + \rho_m) = 0, \quad (10)$$

$$H'\Phi'\psi^2 r + H(\Phi'\psi'\psi r + \Phi''\psi^2 r + 3\Phi'\psi^2) + \xi N C_1^2 r = 0. \quad (11)$$

In this study, we consider separable model of $f(R, \Phi, X)$ function as follows:

$$f(R,\Phi,X) = f_1(R) + f_2(\Phi) + f_3(X). \tag{12}$$

If one considers Equations (8)-(11) together with Equation (12), a solution set which satisfies the equations and is presented below, is available.

$$F(r) = 1, \tag{13}$$

$$H(r) = 0, \tag{14}$$

$$N(r) = 0, \tag{15}$$

$$\Phi(r) = \Phi_0 r^{C_3}. \tag{16}$$

$$\psi(r) = \frac{\sqrt{4C_4 r^2 + 2C_1^2}}{2}, \tag{17}$$

$$\rho_m(r) = \frac{1}{r^2(w+1)}, \tag{18}$$

$$p_m(r) = \frac{w}{r^2(w+1)} \tag{19}$$

where C_3, C_4 and ϕ_0 are arbitrary constants. The solution set is a model indicates $f(R)$ theory or GRT with cosmological constant. The important functions of the model are obtained as:

$$f_1(R) = R + C_6, \tag{20}$$

$$f_2(\Phi) = \int N(\Phi)\, d\Phi = C_7, \tag{21}$$

$$f_3(X) = \int H(X)\, dX = C_5 \tag{22}$$

Where C_5, C_6 and C_7 are arbitrary constants.

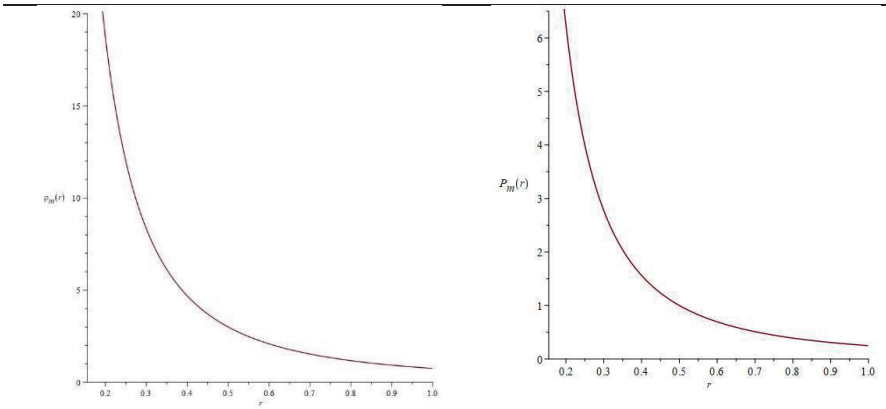

a) $\rho_m(r)$ b) $p_m(r)$

Fig.1. Density (ρ_m) and pressure (p_m) of domain wall ($w = \frac{1}{3}$, $0 < r < 1$).

Obtained domain wall energy density given by Equation (18) is graphized in Figure (1a). Obtained domain wall pressure given by Equation (19) is graphized in Figure (1b). In Equations (18) and (19), $w = \frac{1}{3}$. In Figure (1a), energy density is positive and energy density decreases with increasing radius. In Figure (1b), pressure also has positive values and it can be seen that pressure decreases as radius increases. These two cases are within expected values and are quite consistent. It supports the theory that domain walls can be a source of matter in universe.

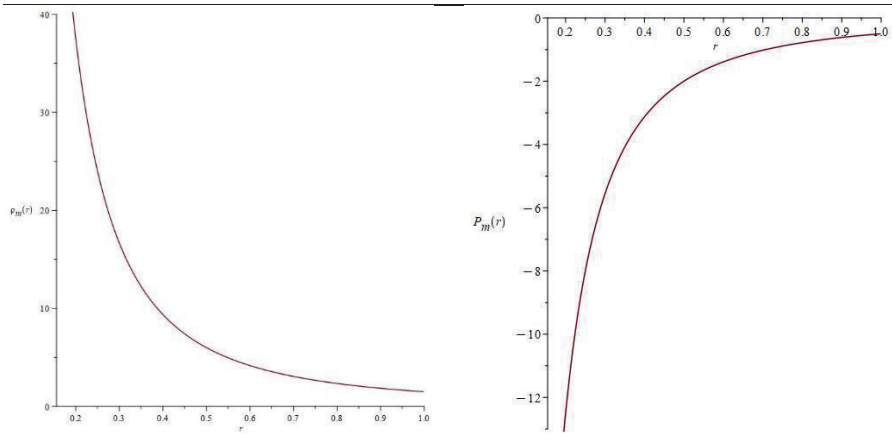

a) $\rho_m(r)$ b) $p_m(r)$

Fig.2. Density (ρ_m) and pressure (p_m) of domain wall ($w = -\frac{1}{3}, 0 < r < 1$).

Figure (2a) represents changes of the domain wall energy density given by Equation (18). Also Figure (2b) shows changes of the domain wall pressure given by Equation (19). Here, $w = -\frac{1}{3}$ is taken in Equations (18)-(19). In Figure (2a), energy density is positive. When radius increases, energy density decreases. In Figure (2b), pressure has negative values depending on value of w. These two situations show us that the domain wall can act as a source of exotic matter in these boundaries.

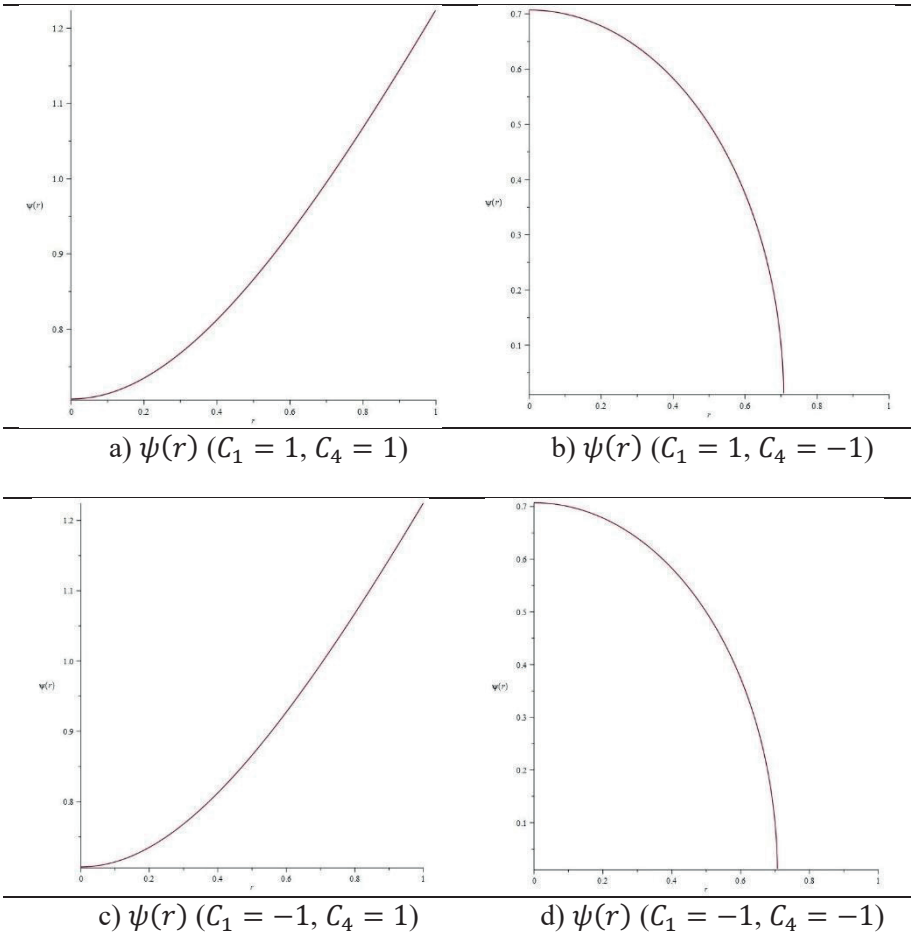

a) $\psi(r)$ $(C_1 = 1, C_4 = 1)$ b) $\psi(r)$ $(C_1 = 1, C_4 = -1)$

c) $\psi(r)$ $(C_1 = -1, C_4 = 1)$ d) $\psi(r)$ $(C_1 = -1, C_4 = -1)$

Fig.3. Change of $\psi(r)$ depending on r $(0 < r < 1)$.

Figure (3) shows the change of $\psi(r)$, which is Equation (17), depending on r. As can be seen from Equation (17), whether C_1 is positive or negative has no effect on obtained solution. However, positive or negative choices of C_4 directly affect on $\psi(r)$. Assuming C_4 to be zero, makes that $\psi(r)$ is a constant.

In Figure (3a), $C_1 = 1$ and $C_4 = 1$ are chosen. Due to C_4 being positive, $\psi(r)$ is increasing function with radius.

In Figure (3b), $C_1 = 1$ and $C_4 = -1$ are chosen. Here, C_4 is negative. Therefore, when radius increases, $\psi(r)$ is degreasing function with radius.

In Figure (3c), $C_1 = -1$ and $C_4 = 1$ are chosen. Again, due to C_4 is positive, $\psi(r)$ increases. In Figure (3d), $C_1 = -1$ and $C_4 = -1$ are chosen. Again, due to the negative effect of C_4, $\psi(r)$ is degreasing function.

As can be seen from Figure (3b) and Figure (3d), $\psi(r)$ could aproximate zero for finite value of radius. This situation indicates geometrical singularity of space-time. Therefore, it is clear that C_4 should be positive.

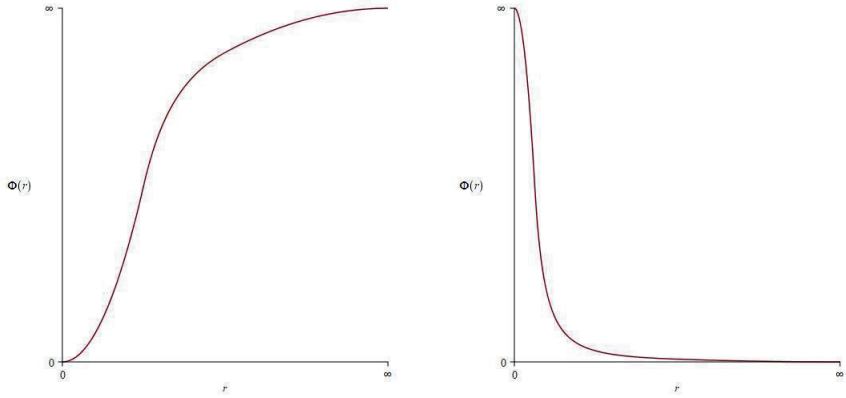

a) $\Phi(r)$ $(C_3 = 2)$ b) $\Phi(r)$ $(C_3 = -2)$

Fig.4. Scalar potential ($\Phi_0 = 1$).

Figure (4) shows the change of $\Phi(r)$ given by Equation (16). In Figure (4a), $C_3 = 2$ and $\Phi_0 = 1$ are chosen. Due to C_3 being positive, $\Phi(r)$ is increasing function with radius. In Figure (4b), $C_3 = -2$ and $\Phi_0 = 1$ are chosen. Due to C_3 being negative, $\Phi(r)$ is degreasing function with radius.

5. CONCLUSION

In this study, behavior of $f(R,\Phi,X)$ theory, one of the alternative gravitation theories, with domain wall under conformal symmetry was examined. It is considered static spherically symmetric and conformal space-time and domain wall in form as perfect fluid. We use Equation of State for the domain wall. Also, we take advantage of Klein-Gordon Equation.

Obtained solution given by Equation (12) and Equation (20) show that considered $f(R,\Phi,X)$ function could be $f(R)$ gravity. If $C_6 \to -2\Lambda$, the model indicates $\Lambda - CDM$ and/or GRT with cosmological constant. The result is important. Because, in $f(R)$ gravity, researches of conformal symmetric domain wall are not sufficent in literature. Therefore, $f_2(\Phi)$ in Equation (21) is obtained as constant. When $C_3 \to 0$, scalar potential is obtained as constant, too. So, it is showed that the subsubstitude indicates $f(R,\Phi)$ domain wall with constant scalar potential. The subsubstitude is important, too. In literature, conformal symmetric domain wall has not studied in $f(R,\Phi)$ gravity. All these results support consistency of $f(R,\Phi,X)$ theory.

In case of $r \to 0$, Equation (16) equals Φ_0. It is an initial value. $\Phi(r)$ is constant in this case. In the case of $r \to \infty$ and $C_3 > 0$, $\Phi(r) \to \infty$. But it is not expected result. For physically meaningful scalar potential, $C_3 < 0$ in obtained solution.

Equation (17) is constant in case of $r \to 0$. Since $\psi(r)$ is a function that determines the metric potential, geometrical structure of the solution decays in centre. In the case of $r \to \infty$, it becomes infinite. $\psi(r)$ gives results as expected in these cases.

Equation (18) becomes infinite in the case of $r \to 0$ singularity. In case of $r \to \infty$, it becomes zero. These two results are as expected. Again, Equation (19) becomes infinite in the case of $r \to 0$ singularity and zero in the case of $r \to \infty$. With this situation, it is seen that the results obtained are in accordance with the expected values in the central singularity and infinite singularities.

As seen in Equations (18)-(19), $w = -1$. This situation leads $\rho_m(r)$ and $p_m(r)$ to infinite singularity. This means that all matter in the universe is a domain wall. Additionally, if as seen from Equation (19), $w = 0$, this situation leads $p_m(r)$ to the central singularity. This means that there is no domain wall matter. In neither case is it possible or consistent. Again, from Equations (18)-(19), it is seen that $w < -1$ makes $\rho_m(r)$ and $p_m(r)$ negative. This is not an expected value. Equation (19) means negative pressure if $-1 < w < 0$. This situation supports the distribution of exotic matter.

The value of the scalar field $\Phi(r)$ is expected to be positive. Therefore equation (16) should be positive. As can be seen, $\Phi_0 \leq 0$ makes equation (16) negative. To avoid this unexpected situation, $\Phi_0 > 0$ should be. These results can be seen from Figure (4). In addition, the constants C_1 and C_4 in equation (17) being zero at the same time make the $\psi(r)$ value zero. This makes the metric potential meaningless. Therefore, these two values should not be zero at the same time.

All obtained results allow existence of conformal domain wall in $f(R, \Phi, X)$ theory.

REFERENCES

Adam, C., Grandi, N., Sanchez-Guillen, J., & Wereszczyński, A. (2008). K fields, compactons and thick branes. Journal of Physics A: Mathematical and Theoretical, 41(21), 212004.

Agrawal, P. K., & Pawar, D. D. (2017). Magnetized domain wall in f (R, T) theory of gravity. New Astronomy, 54, 56-60.

Asmodelle, E. (2017). Tests of General Relativity: A Review. arXiv preprint arXiv:1705.04397.

Bahamonde, S., Böhmer, C. G., Lobo, F. S., & Sáez-Gómez, D. (2015). Generalized f (R, ϕ, X) gravity and the late-time cosmic acceleration. Universe, 1(2), 186-198.

Bamba, K., Nojiri, S. I., & Odintsov, S. D. (2012). Domain wall solution in F (R) gravity and variation of the fine structure constant. Physical Review D, 85(4), 044012.

Buchdahl, H. A. (1970). Non-linear Lagrangians and cosmological theory. Monthly Notices of the Royal Astronomical Society, 150(1), 1-8.

Chiba, T., Okabe, T., & Yamaguchi, M. (2000). Kinetically driven quintessence. Physical Review D, 62(2), 023511.

Eardley, D. M. (1974). Self-similar spacetimes: geometry and dynamics. Communications in Mathematical Physics, 37(4), 287-309.

Harko, T., Lobo, F. S., Nojiri, S. I., & Odintsov, S. D. (2011). f (R, T) gravity. Physical Review D, 84(2), 024020.

Herrera, L., Jimenez, J., Leal, L., Ponce de Leon, J., Esculpi, M., & Galina, V. (1984). Anisotropic fluids and conformal motions in general relativity. Journal of mathematical physics, 25(11), 3274-3278.

Hwang, J. C., & Noh, H. (2002). Cosmological perturbations in a generalized gravity including tachyonic condensation. Physical Review D, 66(8), 084009.

Özemre, A. Y. (1982). Teorik Fizik Dersleri Cild: VII-Gravitasyonun Rölativist Teorileri.

Tsujikawa, S. (2007). Matter density perturbations and effective gravitational constant in modified gravity models of dark energy. Physical Review D, 76(2), 023514.

Chapter 7

FOUR-MOMENT F APPROXIMATION TO THE NULL DISTRIBUTION OF WELCH TEST

Gamze GÜVEN[1]

1 Asst. Prof. Dr., Eskisehir Osmangazi University, Faculty of Science, Department of Statistics, Eskisehir, Turkey, gamzeguven@ogu.edu.tr, ORCID: 0000-0002-8821-3179

1 INTRODUCTION

Consider the one-way analysis of variance (ANOVA) model

$$y_{ij} = \mu + \tau_i + \varepsilon_{ij}, i = 1, \dots, a;\ j = 1, \dots, n_i \quad (1)$$

where μ is the overall mean, τ_i is effect of the ith group and ε_{ij}'s are the random error terms. The null and alternative hypotheses for the one-way ANOVA are defined as

$$H_0: \mu_1 = \mu_2 = \cdots = \mu_a = \mu \quad \text{and} \quad H_1: \mu_i \neq \mu_j,\ \exists i \neq j \quad (2)$$

respectively. For testing the hypothesis in (2), the classical *F* test is used. However, it is not robust to departures from the classical ANOVA assumptions. Therefore, many test statistics have been developed to test the mentioned hypothesis. For example, Welch (1951) and James (1951) proposed Welch (*W*) and James second-order test as an alternative to *F* test. Brown and Forsythe (1974) developed Brown-Forsythe (*BF*) test by modifying the *F* test. Weerahandi (1995) and Krishnamoorthy et al. (2007) proposed new tests called as parametric bootstrap (*PB*) and generalized *F* (*GF*) tests, respectively, etc. It should be noted that the studies mentioned here are proposed for comparing several normal means when the variances are unequal since in real life problems the assumption of homoscedasticity is unrealistic.

Existing tests were also examined in terms of theoretical and comparative perspectives in various fields of science in the literature. De Beuckelaer (1996) presented a simulation experiment to compare the Type I error and power properties of the *F, BF* and *W* tests under normality assumption. They recommended the use of *W* test when one is not sure whether the homoscedasticity assumption does or does not hold. Lix et al. (1996) evaluated the performances of the *BF*, James second order, Kruskal-Wallis (Kruskal and Wallis, 1952) and *W* tests using meta-analytic techniques under heterogeneous variances and non-normality in educational and psychological data. According to their results, James second-order and *W* tests are found to be robust to violations of the variance homogeneity assumptions although they may be sensitive to non-normal distributions. Gamage and Weerahandi (1998) compared the size performances of the *GF*, classical *F*, weighted *F*, *BF* and *W* tests when the samples are coming from normal distribution. Additionally, they employed three sets of samples from Gamma distribution with means 10 and unequal variances to evaluate the robustness of the mentioned tests. They concluded that the performance of the *W* test is better than that of *BF* test when the distributions of the samples deviate from normal. However, *GF* test shows the best performance in all cases. Lee and Ahn (2003) modified the *F* test and derived its approximate distribution. Without the assumption of equal

variances, they compared proposed test with the F test, GF test and Rice and Gaine's (1989) modification of *F* test. The results showed that proposed test is sensitive to the variation of a weight, but it is more reliable than *F* test. In addition, *GF* test has superior performance than the others even for unequal variances. They concluded that proposed test should not be used for small sample sizes like $n_i = 20$. Krishnamoorthy et al. (2007) compared *PB* test with the *W*, James second-order and *GF* tests via Monte Carlo simulation. They pointed out that *W* and *GF* tests exhibit poor Type I error properties for small samples and/or when the number of groups is moderate to large under normality and homogeneity/heterogeneity assumptions. Also, *PB* test performs quite well even when the sample size is small. Cribbie et al. (2012) compared *PB* procedures with the original *W* test, *W* test with trimmed means and winsorized variances and James second-order test under heterogeneity and at least some of the distribution shapes are non-normal. According to the results recorded in their study, the empirical Type I error rates of the *W*, James second-order and *PB* procedures are acceptable when all distributions are normal or moderately skewed. However, these tests do not control the empirical Type I error rates when the shapes of the distributions are extremely non-normal or dissimilar. Therefore, they offered tests based on the trimmed means according to the results recorded for all cases.

As seen from the literature, the *W* test is the well-known and the most widely used test among the proposed procedures. Furthermore, its ease of implementation and inclusion in software packages make it attractive to researchers and practitioners in various fields. Hence, we focused on the *W* test statistics in this study. However, as noted in most studies, when sample sizes are small and/or number of groups are moderate to large, *W* test does not perform satisfactorily in terms of Type I error rates even for normal distribution, see Dajani (2002). Therefore, four-moment *F* approximation to the null distribution of the *W* test is used for small samples and small to moderate values of a when the underlying distribution is normal, see Tiku and Yip (1978) for the details of four-moment *F* approximation. In this study, samples coming from the generalized beta (*GB*) and long-tailed symmetric (LTS) distributions which are plausible alternatives of normal distribution are also considered to make this study complete.

In the next sections, *W* test and four-moment *F* approximation are given and also the accuracies of the four-moment *F* approximation to the null distribution of *W* test are investigated for various different scenarios including different sample sizes, variances and number of groups.

2 FOUR-MOMENT F APPROXIMATION

In this section, the W test and the four-moment F approximation to the null distribution of the W test are briefly described.

2.1 Welch Test

Welch (1951) developed an alternative test to the classical F test under violation of the homogeneity of variances assumption in one-way ANOVA.

Let $Y_{i1}, Y_{i2}, \dots, Y_{in_i}$ be a random sample from $N(\mu_i, \sigma_i^2), i = 1, \dots, a$. $\bar{Y}_i$ and S_i^2 denote the sample mean and sample variance, respectively. They are given as

$$\bar{Y}_i = \frac{1}{n_i}\sum_{j=1}^{n_i} Y_{ij}$$

and

$$S_i^2 = \frac{1}{n_i - 1}\sum_{j=1}^{n_i}\left(Y_{ij} - \bar{Y}_i\right)^2.$$

Based on $\bar{Y}_i$ and S_i^2, W test statistics is defined as follows

$$W = \frac{T_N/(a-1)}{1+2(a-2)/3\nu}. \tag{3}$$

Here,

$$T_N = \sum_{i=1}^{a}\frac{n_i}{S_i^2}\bar{Y}_i^2 - \frac{\left(\sum_{i=1}^{a} n_i \bar{Y}_i / S_i^2\right)^2}{\sum_{i=1}^{a} n_i / S_i^2}$$

and

$$\nu = \left\{\frac{3}{a^2-1}\sum_{i=1}^{a}\frac{1}{(n_i-1)}\left(1 - \left[\left(n_i/S_i^2\right)/\sum_{i=1}^{a} n_i/S_j^2\right]\right)^2\right\}^{-1}$$

where a denotes the number of groups. W test in (3) is asymptotically distributed as F with $(a-1)$ and ν degrees of freedom under the null hypothesis H_0 given in (2). $H_0: \mu_1 = \mu_2 = \cdots = \mu_a = \mu$ is rejected when $p < \alpha$ where

$$p = 1 - F_{\alpha, a-1, \nu}(w).$$

Here, $F_{a-1,\nu}$ denotes the cumulative distribution function of F and $F_{\alpha,a-1,\nu}(w)$ is the probability value corresponding to the calculated value of the W test for the significance level α.

2.2 F Approximation

Four-moment *F* approximation is firstly developed by Tiku and Yip (1978). Then, Tiku and Wong (1998) proposed a new test statistic for testing unit root hypothesis in AR (1) model when the error terms have LTS distribution. They also derived three-moment chi-square and four-moment *F* approximations to the null distribution of the proposed test statistic. Purutçuoğlu (2004) extended the work of Tiku and Wong (1998) when the underlying distributions are gamma and generalized logistic. Sürücü (2008) proposed a new goodness of fit test statistic for testing the normality and obtained the null distribution of it using Tiku's four-moment *F* approximation.

As previously mentioned, in this study, four-moment *F* approximation is used to derive the null distribution of W test. Four-moment *F* approximation is obtained by equating the first four moments on both sides of the following equation

$$W_F = \frac{W+g}{h}. \tag{4}$$

Here, W_F based upon the statistic W is distributed as central *F* with ν_1 and ν_2 degrees of freedom. ν_1, ν_2, g and h are defined as follows

$$\nu_2 = 2\left[3 + \frac{\beta_2^*+3}{\beta_2^*-(3+1.5\beta_1^*)}\right],$$

$$\nu_1 = \frac{1}{2}(\nu_2 - 2)\left(-1 + \sqrt{1 + \frac{32(\nu_2-4)/(\nu_2-6)^2}{\beta_1^*-32(\nu_2-4)/(\nu_2-6)^2}}\right),$$

$$h = \sqrt{\left\{\frac{\nu_1(\nu_2-2)^2(\nu_2-4)}{2\nu_2^2(\nu_1+\nu_2-2)}\mu_2\right\}},$$

and

$$g = \frac{\nu_2}{\nu_2-2}h - \mu_1'$$

where

$$\beta_1^* = \mu_3^2/\mu_2^3 \text{ and } \beta_2^* = \mu_4/\mu_2^2.$$

Here, μ_1', μ_2, μ_3 and μ_4 denote the first four moments of W test statistics, i.e., mean, variance, third central moment and fourth central moment, respectively. Note that in order for equation (4) to be valid, (β_1^*, β_2^*) values of W should satisfy the conditions

$$\beta_1^* > C_1 \text{ and } \beta_2^* > C_2 \tag{5}$$

where $C_1 = \frac{32(\nu_2-4)}{(\nu_2-6)^2}$ and $C_2 = 3 + 1.5\beta_1^*$. For more theoretical details about the four-moment *F* approximation, interested readers can refer to Tiku and Yip (1978).

3 MONTE CARLO SIMULATION

In this section, both empirical Type I error rates of the *W* test statistics and the accuracy of the four-moment *F* approximation are investigated via Monte Carlo simulation study. The simulation program was written in MATLAB R2013 and the following setup is used:

Number of groups

- $a = 3$ and 6

Sample sizes for each group

- $(n_1, n_2, n_3) = (4,4,4)$
- $(n_1, n_2, n_3) = (4,8,12)$
- $(n_1, n_2, n_3, n_4, n_5, n_6) = (4,4,4,4,4,4)$
- $(n_1, n_2, n_3, n_4, n_5, n_6) = (4,6,8,10,11,12)$

Variances for each group

- $(c\sigma_1^2, c\sigma_2^2, c\sigma_3^2) = (1,1,1)$
- $(c\sigma_1^2, c\sigma_2^2, c\sigma_3^2) = (1,1.5,2)$
- $(\sigma c_1^2, c\sigma_2^2, c\sigma_3^2, c\sigma_4^2, c\sigma_5^2, c\sigma_6^2) = (1,1,1,1,1,1)$
- $(c\sigma_1^2, c\sigma_2^2, c\sigma_3^2, c\sigma_4^2, c\sigma_5^2, c\sigma_6^2) = (1,1.2,1.4,1.5,1.7,2)$

Distributions used in the study

- Generalized Beta distribution $(GB(\alpha, \beta, \mu_i^*, \sigma_i), i = 1, \dots, a$ or shortly $GB(\alpha, \beta))$
  - $GB(\alpha = \beta = 1)$
  - $GB(\alpha = \beta = 1.5)$
  - $GB(\alpha = \beta = 3)$
  - $GB(\alpha = \beta = 5)$
- Normal $(N(\mu_i, \sigma_i), i = 1, \dots, a)$
- Long-tailed symmetric $(LTS(p, \mu_i, \sigma_i), i = 1, \dots, a$ or shortly $LTS(p))$
  - $LTS(p = 3)$
  - $LTS(p = 3.5)$
  - $LTS(p = 4)$

- $LTS(p = 4.5)$
- $LTS(p = 5.5)$
- $LTS(p = 10)$

Remark: In simulation setup,

- The constant c is taken to be 1 for the variances of each group in $Normal$ and LTS distributions.
- The constant c is taken to be $\frac{1}{4(2\alpha+1)}$ for the variances of each group in GB distributions. It should be realized that α is taken to be equal to β in this simulation study.
- μ_i^* denotes the location parameter for the ith group in GB distribution.
- The values of μ_i are taken to be zero without loss of generality.
- *Kurtosis* values of the distributions considered in this study are between 1.8 and 2.5 and 3.4 and 9.0 for the GB and *LTS* distributions, respectively.
- Probability density functions (*pdf*s) for the *GB* distribution (see Dudewicz and Karian, 1996) and *LTS* distribution (see Tiku and Kumra, 1985) are given in the Appendix. Their statistical properties are also given.

Note that first four moments of the *W* test statistic are obtained by using 10,000 Monte Carlo runs, because of difficulties encountered in deriving the distribution of *W* or its moments for small samples even under normality assumption.

The simulated Type I error rates of the *W* test statistic and probabilities

$$p_F = 1 - F_{\alpha,\nu_1,\nu_2}(w_F) \tag{6}$$

are given in Table 1. Here, w_F is the calculated value of the W_F in (4) for the significance level α. It is well known that simulated value of p_F is the Type I error rate of the W_F. The closer the probability given in (6) is to α, the more the accuracy and robustness of the four-moment *F* approximation are verified. Additionally, the simulated values of β_1^* and β_2^* for the *W* test statistic and the corresponding C_1 and C_2 values in (5) are also given in Table 1 to assess the applicability of the four-moment *F* approximation.

Table 1. Simulated Type I error rates for W and W_F and simulated values of β_1^* and β_2^* for W test; $\alpha = 0.050$.

Case 1: $a = 3, (n_1, n_2, n_3) = (4,4,4), (c\sigma_1^2, c\sigma_2^2, c\sigma_3^2) = (1,1,1)$							
	Kurtosis	W	W_F	β_1^*	C_1	β_2^*	C_2
$GB(\alpha = \beta = 1)$	1.8	0.060	0.050	59.8919	1.7666	103.5274	92.8379
$GB(\alpha = \beta = 1.5)$	2.0	0.054	0.047	41.3375	1.5438	71.6197	65.0062
$GB(\alpha = \beta = 3)$	2.3	0.052	0.049	47.2080	2.8872	88.0187	73.8120
$GB(\alpha = \beta = 5)$	2.5	0.049	0.047	27.9902	3.2840	55.1443	44.9853
$N(\mu, \sigma^2)$	3.0	0.040	0.050	69.7062	5.7369	150.5760	107.5592
$LTS(p = 10)$	3.4	0.040	0.049	42.2592	6.8484	99.5585	66.3888
$LTS(p = 5.5)$	4.0	0.039	0.047	58.7488	2.9590	108.9847	91.1233
$LTS(p = 4.5)$	4.5	0.038	0.046	22.8533	2.8915	44.7415	37.2799
$LTS(p = 4)$	5.0	0.039	0.047	38.1825	3.6391	75.2094	60.2737
$LTS(p = 3.5)$	6.0	0.034	0.046	24.0450	2.8742	46.8116	39.0675
$LTS(p = 3.0)$	9.0	0.038	0.050	50.8257	4.9123	106.1186	79.2386
Case 2: $a = 3, (n_1, n_2, n_3) = (4,4,4), (c\sigma_1^2, c\sigma_2^2, c\sigma_3^2) = (1,1.5,2)$							
	Kurtosis	W	W_F	β_1^*	C_1	β_2^*	C_2
$GB(\alpha = \beta = 1)$	1.8	0.065	0.046	39.3820	1.2404	67.1444	62.0730
$GB(\alpha = \beta = 1.5)$	2.0	0.054	0.046	43.8198	2.7355	81.2710	68.7297
$GB(\alpha = \beta = 3)$	2.3	0.049	0.047	58.5918	3.8714	114.5654	90.8877
$GB(\alpha = \beta = 5)$	2.5	0.047	0.048	37.6969	3.7364	74.7308	59.5453
$N(\mu, \sigma^2)$	3.0	0.040	0.048	55.4494	7.7026	135.3026	86.1741
$LTS(p = 10)$	3.4	0.037	0.051	61.0990	7.6314	147.8363	94.6485
$LTS(p = 5.5)$	4.0	0.039	0.046	34.5897	3.9078	69.6298	54.8845
$LTS(p = 4.5)$	4.5	0.037	0.046	39.2532	3.9850	78.7580	61.8797
$LTS(p = 4)$	5.0	0.034	0.044	28.9863	2.2151	53.4350	46.4794
$LTS(p = 3.5)$	6.0	0.034	0.044	26.8721	3.0742	52.4546	43.3081
$LTS(p = 3.0)$	9.0	0.035	0.048	27.7656	3.4369	55.2333	44.6484
Case 3: $a = 3, (n_1, n_2, n_3) = (4,8,12), (c\sigma_1^2, c\sigma_2^2, c\sigma_3^2) = (1,1,1)$							
	Kurtosis	W	W_F	β_1^*	C_1	β_2^*	C_2
$GB(\alpha = \beta = 1)$	1.8	0.072	0.048	47.0440	3.4349	90.5641	73.5660
$GB(\alpha = \beta = 1.5)$	2.0	0.070	0.049	34.6104	6.0787	78.9955	54.9156
$GB(\alpha = \beta = 3)$	2.3	0.062	0.046	19.6523	1.6123	36.0843	32.4785
$GB(\alpha = \beta = 5)$	2.5	0.060	0.046	14.6920	0.7468	26.3493	25.0381
$N(\mu, \sigma^2)$	3.0	0.052	0.045	14.0825	1.5859	26.8345	24.1237
$LTS(p = 10)$	3.4	0.053	0.048	37.9904	6.6355	88.9906	59.9856
$LTS(p = 5.5)$	4.0	0.049	0.048	29.2324	6.7912	70.4417	46.8487
$LTS(p = 4.5)$	4.5	0.047	0.045	20.9721	3.7348	43.5485	34.4581
$LTS(p = 4)$	5.0	0.047	0.045	16.2880	3.0072	33.3056	27.4321
$LTS(p = 3.5)$	6.0	0.050	0.046	12.5291	1.0551	23.4350	21.7937
$LTS(p = 3.0)$	9.0	0.043	0.049	17.0953	7.0774	44.3746	28.6430
Case 4: $a = 3, (n_1, n_2, n_3) = (4,8,12), (c\sigma_1^2, c\sigma_2^2, c\sigma_3^2) = (1,1.5,2)$							

	Kurtosis	W	W_F	β_1^*	C_1	β_2^*	C_2
$GB(\alpha=\beta=1)$	1.8	0.067	0.046	24.3158	2.6260	46.5912	39.4737
$GB(\alpha=\beta=1.5)$	2.0	0.064	0.047	30.6153	6.2957	71.4066	48.9230
$GB(\alpha=\beta=3)$	2.3	0.060	0.046	21.2780	3.1241	42.5337	34.9170
$GB(\alpha=\beta=5)$	2.5	0.058	0.046	15.0809	1.9598	29.1702	25.6213
$N(\mu,\sigma^2)$	3.0	0.050	0.051	14.0830	5.7285	34.6605	24.1245
$LTS(p=10)$	3.4	0.047	0.047	12.4702	3.1752	26.7534	21.7054
$LTS(p=5.5)$	4.0	0.046	0.045	10.8426	1.1313	20.8450	19.2639
$LTS(p=4.5)$	4.5	0.047	0.048	16.0617	5.6932	38.6994	27.0926
$LTS(p=4)$	5.0	0.046	0.047	12.0374	2.6137	25.0677	21.0561
$LTS(p=3.5)$	6.0	0.046	0.046	15.2363	4.5236	34.4675	25.8545
$LTS(p=3.0)$	9.0	0.043	0.044	13.0000	2.4135	26.4159	22.5000

Table 1. Continued

Case 5: $a=6,(n_1,n_2,n_3,n_4,n_5,n_6)=(4,4,4,4,4,4),(c\sigma_1^2,c\sigma_2^2,c\sigma_3^2,c\sigma_4^2,c\sigma_5^2,c\sigma_6^2)=(1,1,1,1,1,1)$							
	Kurtosis	W	W_F	β_1^*	C_1	β_2^*	C_2
$GB(\alpha=\beta=1)$	1.8	0.115	0.048	47.7753	6.7127	110.9186	74.6630
$GB(\alpha=\beta=1.5)$	2.0	0.097	0.046	24.5916	3.1440	48.5601	39.8874
$GB(\alpha=\beta=3)$	2.3	0.082	0.047	17.4976	4.5663	38.9716	29.2465
$GB(\alpha=\beta=5)$	2.5	0.073	0.049	14.9251	3.4679	31.7541	25.3876
$N(\mu,\sigma^2)$	3.0	0.068	0.045	22.6396	5.0724	50.4939	36.9594
$LTS(p=10)$	3.4	0.060	0.049	49.5049	9.0695	131.6135	77.2574
$LTS(p=5.5)$	4.0	0.058	0.047	29.6866	8.0484	76.9231	47.5299
$LTS(p=4.5)$	4.5	0.053	0.047	22.3238	5.6435	51.5645	36.4857
$LTS(p=4)$	5.0	0.054	0.051	64.3169	10.2815	181.5642	99.4753
$LTS(p=3.5)$	6.0	0.053	0.046	22.7611	6.6859	55.7925	37.1416
$LTS(p=3.0)$	9.0	0.053	0.047	34.6859	5.7773	77.7885	55.0289
Case 6: $a=6,(n_1,n_2,n_3,n_4,n_5,n_6)=(4,4,4,4,4,4),(c\sigma_1^2,c\sigma_2^2,c\sigma_3^2,c\sigma_4^2,c\sigma_5^2,c\sigma_6^2)=$ (1,1.2,1.4,1.5,1.7,2)							
	Kurtosis	W	W_F	β_1^*	C_1	β_2^*	C_2
$GB(\alpha=\beta=1)$	1.8	0.118	0.052	59.4919	2.8121	109.3753	92.2379
$GB(\alpha=\beta=1.5)$	2.0	0.096	0.046	22.5550	1.7744	41.2951	36.8324
$GB(\alpha=\beta=3)$	2.3	0.081	0.050	51.4951	7.7328	126.3249	80.2427
$GB(\alpha=\beta=5)$	2.5	0.074	0.051	52.2391	6.8429	121.6463	81.3587
$N(\mu,\sigma^2)$	3.0	0.066	0.045	30.4973	4.9685	65.8740	48.7459
$LTS(p=10)$	3.4	0.062	0.047	29.7037	6.4122	69.9198	47.5555
$LTS(p=5.5)$	4.0	0.061	0.047	21.7036	2.7051	42.2187	35.5554
$LTS(p=4.5)$	4.5	0.052	0.044	16.9095	5.0290	38.8865	28.3643
$LTS(p=4)$	5.0	0.052	0.050	38.7836	10.9552	117.3589	61.1753
$LTS(p=3.5)$	6.0	0.053	0.049	48.9571	8.3940	125.1481	76.4356
$LTS(p=3.0)$	9.0	0.046	0.050	68.8003	9.8917	189.1836	106.2005
Case 7: $a=6,(n_1,n_2,n_3,n_4,n_5,n_6)=(4,6,8,10,11,12),(c\sigma_1^2,c\sigma_2^2,c\sigma_3^2,c\sigma_4^2,c\sigma_5^2,c\sigma_6^2)=$ (1,1,1,1,1,1)							
	Kurtosis	W	W_F	β_1^*	C_1	β_2^*	C_2
$GB(\alpha=\beta=1)$	1.8	0.094	0.051	71.1581	8.3597	178.5148	109.7372
$GB(\alpha=\beta=1.5)$	2.0	0.088	0.048	33.3764	8.5652	88.3380	53.0646
$GB(\alpha=\beta=3)$	2.3	0.073	0.042	23.6709	3.9890	49.3159	38.5064
$GB(\alpha=\beta=5)$	2.5	0.071	0.045	26.3443	8.4965	70.8616	42.5164
$N(\mu,\sigma^2)$	3.0	0.059	0.045	12.8722	4.6148	30.0299	22.3083
$LTS(p=10)$	3.4	0.058	0.048	11.9316	5.8097	30.3301	20.8974
$LTS(p=5.5)$	4.0	0.059	0.047	15.1477	7.6356	41.3764	25.7215
$LTS(p=4.5)$	4.5	0.053	0.048	38.4362	12.5914	129.1491	60.6542

$LTS(p=4)$	5.0	0.054	0.045	21.1986	9.1250	60.6018	34.7979
$LTS(p=3.5)$	6.0	0.053	0.047	11.2934	6.5104	30.2704	19.9401
$LTS(p=3.0)$	9.0	0.048	0.045	12.6221	5.8087	31.7729	21.9332
Case 8: $a=6,(n_1,n_2,n_3,n_4,n_5,n_6)=(4,6,8,10,11,12),(c\sigma_1^2,c\sigma_2^2,c\sigma_3^2,c\sigma_4^2,c\sigma_5^2,c\sigma_6^2)=(1,1.2,1.4,1.5,1.7,2)$							
	Kurtosis	W	W_F	β_1^*	C_1	β_2^*	C_2
$GB(\alpha=\beta=1)$	1.8	0.088	0.047	37.2737	4.5062	77.3132	58.9106
$GB(\alpha=\beta=1.5)$	2.0	0.087	0.046	10.7822	2.4271	22.5981	19.1732
$GB(\alpha=\beta=3)$	2.3	0.069	0.049	8.4781	2.5989	18.8202	15.7171
$GB(\alpha=\beta=5)$	2.5	0.066	0.045	10.5824	2.9718	23.0432	18.8736
$N(\mu,\sigma^2)$	3.0	0.062	0.048	12.8793	7.7061	36.2757	22.3189
$LTS(p=10)$	3.4	0.057	0.045	13.1329	5.2728	31.7891	22.6993
$LTS(p=5.5)$	4.0	0.053	0.046	8.3427	3.6355	19.8799	15.5141
$LTS(p=4.5)$	4.5	0.054	0.050	11.5470	8.5028	34.8568	20.3204
$LTS(p=4)$	5.0	0.053	0.048	6.0569	2.1856	14.1770	12.0853
$LTS(p=3.5)$	6.0	0.048	0.046	7.4832	3.6703	18.3279	14.2248
$LTS(p=3.0)$	9.0	0.048	0.048	8.0900	6.1066	22.7152	15.1350

The following conclusions are drawn from simulation study.

Type I error rates of the W_F are close to the nominal level $\alpha=0.050$ and also the conditions $\beta_1^*>C_1$ and $\beta_2^*>C_2$ in (5) are satisfied for all cases considered in this study. Hence, four-moment F approximation is applicable and this approximation performs well for small sample sizes and small to moderate number of groups.

Case 1: $a=3,(n_1,n_2,n_3)=(4,4,4),(c\sigma_1^2,c\sigma_2^2,c\sigma_3^2)=(1,1,1)$
GB: W test is liberal for $GB(\alpha=\beta=1)$ distribution which has the smallest kurtosis value among the distributions of interest.
Normal and LTS: W test is conservative for all distributions of interest.

Case 2: $a=3,(n_1,n_2,n_3)=(4,4,4),(c\sigma_1^2,c\sigma_2^2,c\sigma_3^2)=(1,1.5,2)$
GB: W test is liberal for $GB(\alpha=\beta=1)$ distribution which has the smallest kurtosis value among the distributions of interest.
Normal and LTS: W test is conservative for all distributions of interest.

Case 3: $a=3,(n_1,n_2,n_3)=(4,8,12),(c\sigma_1^2,c\sigma_2^2,c\sigma_3^2)=(1,1,1)$
GB: W test is liberal for all distributions of interest.
Normal and LTS: The I error rates of the W test are close to the nominal level $\alpha=0.050$ except for $LTS(p=3)$ with kurtosis value 9.0. W test is slightly conservative for $LTS(p=3)$.

Case 4: $a=3,(n_1,n_2,n_3)=(4,8,12),(c\sigma_1^2,c\sigma_2^2,c\sigma_3^2)=(1,1.5,2)$
GB: W test is liberal for all distributions of interest.
Normal and LTS: The I error rates of the W test are close to the nominal level $\alpha=0.050$ except for $LTS(p=3)$ with kurtosis value 9.0. W test is slightly conservative for $LTS(p=3)$.

Case 5: $a = 6, (n_1, n_2, n_3, n_4, n_5, n_6) = (4,4,4,4,4,4)$, $(c\sigma_1^2, c\sigma_2^2, c\sigma_3^2, c\sigma_4^2, c\sigma_5^2, c\sigma_6^2) = (1,1,1,1,1,1)$
GB and Normal: W test is liberal for all distributions of interest.
LTS: The I error rates of the W test are close to the nominal level $\alpha = 0.050$ except for $LTS(p = 10)$ and $LTS(p = 5.5)$ with kurtosis values 3.4 and 4.0, respectively. W test is liberal for $LTS(p = 10)$ and $LTS(p = 5.5)$.

Case 6: $a = 6, (n_1, n_2, n_3, n_4, n_5, n_6) = (4,4,4,4,4,4)$, $(c\sigma_1^2, c\sigma_2^2, c\sigma_3^2, c\sigma_4^2, c\sigma_5^2, c\sigma_6^2) = (1,1.2,1.4,1.5,1.7,2)$
GB and Normal: W test is liberal for all distributions of interest.
LTS: The I error rates of the W test are close to the nominal level $\alpha = 0.050$ except for $LTS(p = 10)$ and $LTS(p = 5.5)$ with kurtosis values 3.4 and 4.0, respectively. W test is liberal for $LTS(p = 10)$ and $LTS(p = 5.5)$.

Case 7: $a = 6, (n_1, n_2, n_3, n_4, n_5, n_6) = (4,6,8,10,11,12)$, $(c\sigma_1^2, c\sigma_2^2, c\sigma_3^2, c\sigma_4^2, c\sigma_5^2, c\sigma_6^2) = (1,1,1,1,1,1)$
GB and Normal: W test is liberal for all distributions of interest.
LTS: The I error rates of the W test are close to the nominal level $\alpha = 0.050$ except for $LTS(p = 10)$ and $LTS(p = 5.5)$ with kurtosis values 3.4 and 4.0, respectively. W test is liberal for $LTS(p = 10)$ and $LTS(p = 5.5)$.

Case 8:
$a = 6, (n_1, n_2, n_3, n_4, n_5, n_6) = (4,6,8,10,11,12)$, $(c\sigma_1^2, c\sigma_2^2, c\sigma_3^2, c\sigma_4^2, c\sigma_5^2, c\sigma_6^2) = (1,1.2,1.4,1.5,1.7,2)$
GB and Normal: W test is liberal for all distributions of interest.
LTS: The I error rates of the W test are close to the nominal level $\alpha = 0.050$ except for $LTS(p = 10)$ with kurtosis value 3.4. W test is slightly liberal for $LTS(p = 10)$.

4 CONCLUDING REMARKS

In this study, four-moment *F* approximation to the null distribution of the well-known *W* test statistic is used and the resulting test statistic is called as W_F. Then, the performances of the *W* and W_F test statistics are compared in terms of simulated Type I error rates for small samples and small to moderate number of groups when the underlying distributions are *GB*, *Normal* and *LTS*. Unlike *W* test, simulation results show that W_F is quite robust in terms of Type I error rates since the Type I error rates of the W_F keep the nominal level. It is concluded that the four-moment *F* approximation can comfortably be used for all cases considered in this study.

APPENDIX

LTS Distribution: pdf of *LTS* distribution is as follows

$$f(y) = \frac{1}{\sqrt{k}\beta\left(\frac{1}{2},p-\frac{1}{2}\right)\sigma}\left(1+\frac{(y-\mu)^2}{k\sigma^2}\right)^{-p},\ -\infty < y < \infty;\ p \geq 2,\ k = 2p-3.$$

Here, μ and σ are the location and scale parameters, respectively, and p is the shape parameter, see Tiku and Kumra (1985). If the random variable Y has the *LTS* distribution with the location parameter μ, scale parameter σ and the shape parameter p, then it is denoted as $Y \sim LTS(p,\mu,\sigma)$ or shortly $LTS(p)$. Note that $E(y) = \mu, V(y) = \sigma^2$ and

$$T = \sqrt{(\nu/k)}(Y/\sigma)$$

is distributed as Student t with $\nu = 2p-1$ degrees of freedom. The kurtosis value for the LTS distribution is calculated as follows

$$\beta_2 = 3\left(p-\frac{3}{2}\right)/\left(p-\frac{5}{2}\right).$$

Realize that as the shape parameter p goes to infinity, the $LTS(p)$ distribution converges to *Normal* distribution.

GB Distribution: pdf of *GB* distribution is as follows

$$f(y) = \frac{\Gamma(a+b)}{\Gamma(a)\Gamma(b)}\frac{1}{\sigma}\left(\frac{y-\mu}{\sigma}\right)^{\alpha-1}\left(1-\frac{y-\mu}{\sigma}\right)^{\beta-1}\ \mu \leq y \leq \mu+\sigma$$

Here, μ and σ are the location and scale parameters, respectively, and α and β are the shape parameters, see Dudewicz and Karian (1996). If the random variable Y has the GB distribution with the location parameter μ, scale parameter σ and the shape parameters α and β, then it is denoted as $Y \sim GB(\alpha,\beta,\mu,\sigma)$ or shortly $GB(\alpha,\beta)$. Note that mean $\left(E(y)\right)$ and variance $(V(y))$ are as follows

$$E(y) = \mu + \frac{\sigma\alpha}{\alpha+\beta} \quad \text{and} \quad V(y) = \frac{\sigma^2\alpha\beta}{(\alpha+\beta)^2(\alpha+\beta+1)}.$$

The skewness (β_1) and kurtosis (β_2) values for the *GB* distribution are calculated as follows

$$\beta_1 = \frac{2(\beta-\alpha)\sqrt{\alpha+\beta+1}}{(\alpha+\beta+2)\sqrt{\alpha\beta}} \text{ and } \beta_2 = \frac{3(\alpha+\beta+1)[2(\alpha+\beta)^2+\alpha\beta(\alpha+\beta-6)]}{\alpha\beta(\alpha+\beta+2)(\alpha+\beta+3)}.$$

Realize that if $\mu = 0$ and $\sigma = 1$, then *GB* distribution reduces to standard beta distribution with support [0,1].

REFERENCES

Brown, M. B., & Forsythe, A. B. (1974). The small sample behavior of some statistics which test the equality of several means. *Technometrics*, *16*(1), 129-132.

Cribbie, R. A., Fiksenbaum, L., Keselman, H. J., & Wilcox, R. R. (2012). Effect of non-normality on test statistics for one-way independent groups designs. *British Journal of Mathematical and Statistical Psychology*, *65*(1), 56-73.

Dajani, A.N., (2002). *Contributions to statistical inference for some fixed and random models*. Ph.D. Dissertation, Department of Mathematics and Statistics, University of Maryland, Baltimore County

De Beuckelaer, A. (1996). A closer examination on some parametric alternatives to the ANOVA F-test. *Statistical Papers*, *37*, 291-305.

Dudewicz, E. J., & Karian, Z. A. (1996). The extended generalized lambda distribution (EGLD) system for fitting distributions to data with moments, II: Tables. *American Journal of Mathematical and Management Sciences*, *16*(3-4), 271-332.

Gamage, J., & Weerahandi, S. (1998). Size performance of some tests in one-way ANOVA. *Communications in Statistics-Simulation and Computation*, *27*(3), 625-640.

James, G. S. (1951). The comparison of several groups of observations when the ratios of the population variances are unknown. *Biometrika*, *38*(3/4), 324-329.

Krishnamoorthy, K., Lu, F., & Mathew, T. (2007). A parametric bootstrap approach for ANOVA with unequal variances: Fixed and random models. *Computational Statistics & Data Analysis*, *51*(12), 5731-5742.

Kruskal, W. H., & Wallis, W. A. (1952). Use of ranks in one-criterion variance analysis. *Journal of the American statistical Association*, *47*(260), 583-621.

Lee, S., & Ahn, C. H. (2003). Modified ANOVA for unequal variances. *Communications in Statistics-Simulation and Computation*, *32*(4), 987-1004.

Lix, L. M., Keselman, J. C., & Keselman, H. J. (1996). Consequences of assumption violations revisited: A quantitative review of alternatives to the one-way analysis of variance F test. *Review of educational research*, *66*(4), 579-619.

Purutçuoğlu, V. (2004). Unit root problems in time series analysis, Master Thesis, Middle East Technical University.

Rice, W. R., Gaines, S. D. (1989). One-way analysis of variance with unequal variances. In: Proceedings of National Academy of Science. pp. 8183–8184.

Sürücü, B. (2008). A power comparison and simulation study of goodness-of-fit tests. *Computers & Mathematics with Applications*, *56*(6), 1617-1625.

Tiku, M. L., & Kumra, S. (1985). Expected values and variances and covariances of order statistics for a family of symmetrical distributions (student's t). In: Kennedy WJ, Odeh RE, Davenport JM, editors. Selected tables in mathematical statistics Volume 8. American Mathematical Society. Rhode Island. p. 141–270.

Tiku, M. L., & Yip, D. Y. N. (1978). A four-moment approximation based on the F distribution. *Australian Journal of Statistics*, *20*(3), 257-261.

Tiku, M. L., & Wong, W. K. (1998). Testing for a unit root in an AR (1) model using three and four moment approximations: symmetric distributions. *Communications in Statistics-Simulation and Computation*, *27*(1), 185-198.

Weerahandi, S. (1995). ANOVA under unequal error variances. *Biometrics*, *51*(2), 589-599.

Welch, B. L. (1951). On the comparison of several mean values: an alternative approach. *Biometrika*, *38*(3/4), 330-336.

Chapter 8

A ROBUST STATISTICAL APPROACH FOR ARCHITECTURE SELECTION IN NEURAL NETWORKS

Adil KILIÇ[1]

Birdal ŞENOĞLU[2]

Çağdaş Hakan ALADAĞ[3]

1 Arş. Gör., Kırıkkale University, ORCID: 0000-0003-3114-9118, adilkilic@kku.edu.tr
2 Prof. Dr., Ankara University, ORCID: 0000-0003-3707-2393, senoglu@science.ankara.edu.tr
3 Prof. Dr., Hacettepe University, ORCID: 0000-0002-3953-7601, aladag@hacettepe.edu.tr

1 INTRODUCTION

Artificial neural networks (ANN) have been widely used in various areas of science because of their success to model linear and non-linear datasets. In addition to its modeling success, its flexible structure that does not require assumptions or prior knowledge provides an advantage to practitioners in its usage. However, there are some problems to be careful about the use of ANN. One of the most important of these problems is the inappropriate selection of ANN components, i.e., architecture selection, learning algorithm, and activation function since it negatively affects the performance of the ANN, see Aladag (2011). Here, we focus on architecture selection, defined as the determination of the number of neurons in layers, among the ANN components when modeling univariate time series problems with ANN.

There are many studies in the literature focusing on the architecture selection problem of ANN. For instance, Sietsma and Dow (1988) proposed an approach based on learning with a network which is larger than the minimum size network required for the architecture selection problem and then pruned the solution network. Roy et al. (1993) presented a polynomial time algorithm for building and training a class of multi layer perceptrons for classification. Murata et al. (1994) proposed an architectural selection method based on the AIC information criterion. Rathbun et al. (1997) introduced a new method for architecture selection in multi-layer perceptron models for classification problems. Jun et al. (2007) proposed an ANN model to determine the gross emission emitters of taxis based on remote sensing data and used an architecture selection method based on principal components analysis. Durbin et al. (2008) proposed a data adaptive method to select the most suitable network architecture using a deletion/substitution/addition algorithm for certain types of classification problems. Egrioglu et al. (2008) introduced a new architecture selection strategy based on AIC, BIC, RMSE, MAPE, DA and MDA criteria. Balestrassi et al. (2009) used the methodology of Experimental design to better determine the components of the ANN for the nonlinear time series problem. Hosseinzadeh Talaee (2014) applied multi layer perceptron networks optimized with three training algorithms, i.e., flexible backpropagation, variable learning rate and Levenberg Marquardt, to forecast the streamflow of the Aspas Watershed in Fars province, southwest Iran. Aladag (2019) proposed a new architecture selection method based on regression analysis which is a supervised learning technique.

In this study, the architecture selection method based on linear regression proposed by Aladag (2019) is extended to robust linear regression which is insensitive to the outliers existing in the data set. A real life data is analyzed to show the effectiveness of the proposed robust architecture selection method at the end of the study.

The remaining sections of this work are organized as follows. ANN is briefly described in section 2. Section 3 includes a description of Huber M regression in subsection 3.1 and an alternative methodology for architecture problem in subsection 3.2. Section 4 presents an application to demonstrate the implementation of the proposed methodology and comparing with Aladag (2019). Finally, concluding remarks are given in Section 5.

2 ARTIFICIAL NEURAL NETWORKS

ANN is a computational and data driven method which imitates the features and organization of the human brain. It consists of three basic components known as learning algorithm, activation function, and architecture structure. Since appropriate selection of these components positively affects the performance of the ANN the selection of components is highly important step in ANN, see Hagan et al. (1997).

In the literature, there exist many different ANN forms, i.e., feed forward neural networks, multiplicative neural networks, and recurrent neural networks. Feed forward neural networks have been the most popular form among them since it is simple to use and have a wide range of successful applications. They consist of three layers called as input, hidden and output, each layer has at least one neuron. It should also be noted that the number of hidden layers can be more than one, see for example Figure 1 for the architecture of the feed forward neural network model with one hidden layer. Neurons in the layers are connected to each other with corresponding weight values. It can be realized that Figure 1 is a model representing matematical relationship between input(s) and output neurons. Basically, the neurons in the input layer are lagged variables represented by $X_{t-1}, X_{t-2}, \dots, X_{t-n}$, and the neuron in the output layer corresponds to the output represented by X_t. The activation function is an important component of ANN as it allows to model the relationship between the input and output neurons. There are many different activation functions used for this purpose such as linear, logistic, hyperbolic tangent, and rectified linear unit, etc.

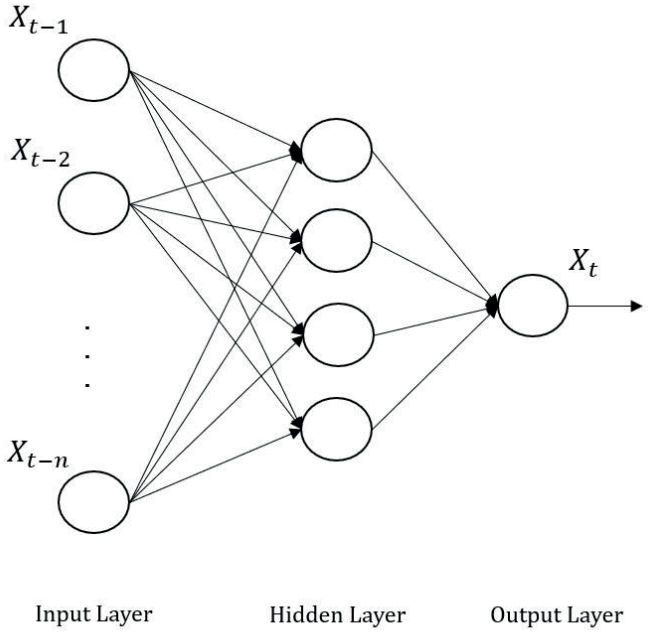

Figure 1: The architecture of the feed forward neural network model.

After selecting activation functions and determining the number of neurons for the ANN model, the model is trained with an optimization algorithm called as learning algorithm. This process is used to obtain the best output value (forecasts) by optimizing the weight values between neurons. In fact, these weight values can be thought as parameters in the mathematical expression of the corresponding ANN model.

The process of dividing the dataset into train and test is another important point of interest in ANN. The train and test set are used for training the model and testing the performance of the model, respectively. The size of the train set is an important factor affecting the training process of the ANN. After training the ANN, the performance of the ANN is measured via a selected performance measure by using the forecasts obtained as the output of the network and the corresponding observations in the test set. For the detailed information about the structure and working principles of feed forward ANN, see for example Zhang et al. (1998).

3 ARCHITECTURE SELECTION VIA ROBUST LINEAR REGRESSION

In this section, first robust linear regression is presented in subsection 3.1 and then the proposed methodology based on robust linear regression for the architecture selection is given in subsection 3.2.

3.1 Robust Linear Regression

Linear regression is a statistical technique used to model the relationship between the response variable and the explanatory variables. Mathematical model is given by

$$y_i = \beta_0 + \beta_1 x_{i1} + \cdots + \beta_p x_{ip} + \varepsilon_i, i = 1,2, \dots, n \quad (1)$$

where y_i is i-th observation of the response variable, x_{ip} is i-th observation of the p-th explanatory variable, $\beta_0, \beta_1, \dots, \beta_p$ are the regression parameters, and ε_i are the random error terms.

Ordinary least squares (OLS) estimators have the best performance in estimating the regression parameters when the usual regression assumptions are satisfied. They are obtained by minimizing the sum of squares of errors, i.e.,

$$\hat{\beta}_{j(OLS)} = arg \min_{\beta_j} \sum_{i=1}^{n} \varepsilon_i^2 , j = 0,1, \dots, p. \quad (2)$$

OLS estimators are shown in matrix notation as below

$$\hat{\beta}_{OLS} = (X'X)^{-1}X'Y \quad (3)$$

where Y is $(n \times 1)$ vector of response variables, X is $n \times (p+1)$ matrix of explanatory variables, and $\hat{\beta}_{OLS}$ is $(p+1) \times 1$ vector of parameter estimators. Then, the corresponding prediction equation is obtained as

$$\hat{Y} = X\hat{\beta}_{OLS} \quad (4)$$

where $\hat{Y}$ is $(n \times 1)$ vector of prediction values.

It should be noted that OLS estimators lose their efficiencies when the usual normality assumption is not satisfied or there exist outliers in the data set. In this case, robust estimators are used as an alternative to OLS estimators

because they are insensitive to the deviations from the normal distribution and also to the outliers. Here, we use M estimation method among the robust estimation methods as parallel to its wide usage in the literature, see Huber (1992). Details of the Huber M estimation method are described below.

Huber M Estimation Method

M estimation method removes the outlier's detrimental effects on parameter estimates. It aims to minimize the function of the residuals (e_i) denoted by $\rho(e_i)$ with respect to the regression parameters. Here, $e_i = y_i - \sum_{j=0}^{n} x_{ij}\,\beta_j$ where $x_{i0} = 1$. Therefore, the objective function to be minimized is defined as follows

$$\min_{\beta_j} \sum_{i=1}^{n} \rho(e_i) = \min_{\beta_j} \sum_{i=1}^{n} \rho\left(y_i - \sum_{j=0}^{p} x_{ij}\,\beta_j\right), j = 0,1,\dots,p. \quad (5)$$

Since the objective function given in equation (5) does not have scale invariance with respect to the response variable, the residuals are divided by a robust estimator of the scale parameter and standardized as follows

$$\min_{\beta_j} \sum_{i=1}^{n} \rho(u_i) = \min_{\beta_j} \sum_{i=1}^{n} \rho\left(\frac{e_i}{\hat{\sigma}_{MAD}}\right) = \min_{\beta_j} \sum_{i=1}^{n} \rho\left(\frac{y_i - \sum_{j=0}^{p} x_{ij}\beta_j}{\hat{\sigma}_{MAD}}\right) \quad (6)$$

where $\hat{\sigma}_{MAD} = \frac{median|e_i - median(e_i)|}{0.6745}$ is a robust estimator of σ. The constant 0.6745 makes $\hat{\sigma}_{MAD}$ nearly unbiased estimate of σ in case of a large n and a Normal distribution.

In this study, we use Huber's ρ function defined by

$$\rho(u_i) = \begin{cases} \frac{1}{2}u_i^2, & |u_i| \le 0 \\ c|u_i| - \frac{c^2}{2}, & |u_i| > 0 \end{cases} \quad (7)$$

where $c = 1.345$ is the correction parameter. See for example Beaton and Tukey (1974) and Hampel (2002) for the other widely used ρ functions in the literature.

The objective function is differentiated with respect to β_j's as given below

$$\frac{\partial}{\partial \beta_j} \sum_{i=1}^{n} \rho(u_i) = \sum_{i=1}^{n} x_{ij}\,\rho'(u_i) = \sum_{i=1}^{n} x_{ij}\,\psi(u_i) = 0 \quad (8)$$

where $\psi(u_i) = \begin{cases} u_i, & |u_i| \leq 0 \\ csgn(u_i), & |u_i| > 0 \end{cases}$ is the influence function and $sgn(.)$ is the sign function.

Equation (8) can be written in terms of weight function as follows

$$\sum_{i=1}^{n} x_{ij} \frac{\psi\left(\frac{y_i - \sum_{j=0}^{p} x_{ij}\beta_j}{\hat{\sigma}_{MAD}}\right)}{\left(\frac{y_i - \sum_{j=0}^{p} x_{ij}\beta_j}{\hat{\sigma}_{MAD}}\right)} \left(\frac{y_i - \sum_{j=0}^{p} x_{ij}\beta_j}{\hat{\sigma}_{MAD}}\right) = \sum_{i=1}^{n} x_{ij} w(u_i) \left(y_i - \sum_{j=0}^{p} x_{ij}\,\beta_j\right) = 0 \quad (9)$$

where $w(u_i) = \begin{cases} 1, & |u_i| \leq 0 \\ \frac{c}{|u_i|}, & |u_i| > 0 \end{cases}$ is the weight function.

Then, the solution of the system of weighted equations obtained in equation (9) gives the Huber M estimators $\left(\hat{\beta}_j\right)$. Equation (9) can be solved by using iteratively reweighted least squares (IRLS) algorithm. Also, the matrix notation of Huber M estimator of β is represented by

$$\hat{\beta}_j = (X'WX)^{-1}(X'WY) \quad (10)$$

where W is $n \times n$ matrix whose diagonal elements are the weights corresponding to residuals.

3.2 Robust Methodology for Architecture Selection

In this section, a robust statistical method is proposed as an alternative to Aladag (2019) for the architecture selection problem of ANN. In Aladag (2019), prediction equation is obtained to determine the ANN architecture via linear regression. The number of neurons (in the input and hidden layers) and the performance measure (RMSE, MAPE, etc.) corresponding to each architecture are taken to be the explanatory variables and the response variable, respectively. By obtaining linear regression model based on OLS, it is aimed to show the relationship between the number of neurons (in the input and hidden layers) and the ANN performance statistically. In this study, robust linear regression is used instead of OLS regression in the methodology proposed by Aladag (2019). We preferred to use the Huber M as a robust linear regression method as mentioned before because of its superior performance and widespread usage for the long tailed symmetric distributions. The steps of the proposed robust methodology for architecture selection are given as follows.

Step 1. Determine ANN architectures to be examined, e.g., the number of neurons in the input and hidden layers are determined. The number of neurons in the output layer is taken to one, as in many studies.

Step 2. Determine initial weights for the specified architectures. The commonly preferred method for this process is the random selection of the weights by the computer. Note that the initial weights directly affect the output values of the ANN.

Step 3. Calculate the selected performance measure (RMSE, MAPE, etc.) for each specified architecture.

Step 4. Obtain OLS prediction equation

$$\hat{y}_{prfm} = \hat{\beta}_0 + \hat{\beta}_1 x_{input} + \hat{\beta}_2 x_{hidden}. \quad (11)$$

Here, x_{input}, x_{hidden}, and $\hat{y}_{prfm}$ denote the number of neurons in the input layer, the number of neurons in the hidden layers, and the predicted value of the performance measure, respectively.

Step 5. Check whether there exist outliers in the data set or not via Normal QQ plot. If there is no outliers, use the method proposed by Aladag (2019) and terminate the algorithm. Otherwise, use the Huber M method to obtain the estimators of the regression parameters, i.e., $\hat{\beta}_0$, $\hat{\beta}_1$, and $\hat{\beta}_2$ and the corresponding prediction equation.

Step 6. Test the statistical significance of the estimators of the regression parameters for the prediction equation obtained by using Huber M methodology via t-test. If the regression model is significant, then obtain the $\hat{y}_{prfm}$ values for each ANN architectures determined in Step 1. Select the x_{input} and x_{hidden} values correspondig to the minimum $\hat{y}_{prfm}$ value as an appropriate architecture. Otherwise, repeat the algorithm k (predefined value) times till the significant regression model is obtained.

4 APPLICATION

In this section, the proposed methodology is applied to a real-life data for architecture selection. The considered data set consists of monthly consumer price index (CPI) values of Turkey between January 2005 and December 2014. This dataset contains 120 monthly time series observations.

Here, a feedforward neural network structure with one neuron in the output layer and one hidden layer is used. In modeling CPI data with ANN,

144 different architectures were examined for architecture selection problem. That is, the number of neurons in the input and hidden layers are taken to be $x_{input} = 1,2, \dots ,12$ and $x_{hidden} = 1,2, \dots ,12$ specific to this data set. Also, the data set is divided into 90% and 10% for the training and testing, respectively. The sigmoid and linear activation functions are used for the neurons in the hidden layer and the neuron in the output layer, respectively. RMSE is chosen as the performance measure whose mathematical formula is given below

$$RMSE = \sqrt{\frac{\sum_{i=1}^{n}(\hat{y}_i - y_i)^2}{s}}. \quad (12)$$

Here, y_i and $\hat{y}_i$ are the observed value and the output value of the ANN at time i, respectively, s is the test set size, and is taken to be 12 in our case. R software is used for all calculations in the application.

CPI data is modeled with 144 different ANN architectures and RMSE values corresponding to each architecture are computed. Structure of the data used in the regression analysis is shown in Table 1. It can be seen that $RMSE_1$ shows the y_{prfm} value corresponding to $x_{input} = 1$ and $x_{hidden} = 1$, see first row of Table 1.

Table 1: Structure of the data used for the regression analysis in the architecture selection problem.

y_{prfm}	x_{input}	x_{hidden}
$RMSE_1$	1	1
$RMSE_1$	1	2
.	.	.
.	.	.
.	.	.
$RMSE_{12}$	1	12
.	.	.
.	.	.
.	.	.
$RMSE_{133}$	12	1
$RMSE_{134}$	12	2
.	.	.
.	.	.
.	.	.
$RMSE_{144}$	12	12

Based on the values of y_{prfm}, x_{input} and x_{hidden}, OLS parameter estimates and the corresponding t-values are obtained as shown in Table 2.

Table 2: OLS estimates of the model parameters and the corresponding t-values.

Coefficients	Estimate	Std. Error	t-value	p-value
β_0	0.7500	0.00910	84.926	0.0000*
β_1	-0.0112	0.00093	−12.072	0.0000*
β_2	-0.0020	0.00093	−2.248	0.0261*

$*$ significant at $\alpha = 0.05$

It is seen from Table 2 that regression coefficients are statistically significant. Based on these estimate values, the prediction equation for the CPI data is given below

$$\hat{y}_{prfm,OLS} = 0.7500 - 0.0112x_{input} - 0.0020x_{hidden}. \quad (13)$$

To see whether there exist or not outliers in the CPI data set, Normal QQ plot of the residuals is obtained as shown in Figure 2.

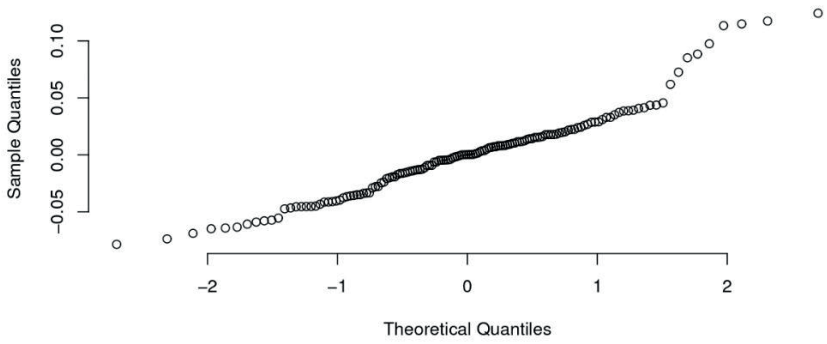

Figure 2: Normal QQ plot of the residuals for the CPI data.

In Figure 2, it is seen that some values deviate from the straight line at the right tail of the data. This is the indication of outliers in the CPI data set. Obviously, presence of outliers makes the OLS prediction equation unreliable. That's why we resort to Huber M method which is not sensitive to the outlying observations. Huber M estimates of the regression parameters and the corresponding t-values are given in Table 3.

Table 3: Huber M estimates of the regression parameters and the corresponding t-values.

Coefficients	Estimate	Std. Error	t-value	p-value
β_0	0.7620	0.0080	95.4385	0.0000*
β_1	-0.0128	0.0008	−15.6993	0.0000*
β_2	-0.0029	0.0008	−3.5333	0.00055*

$*$ significant at $\alpha = 0.05$

According to the estimate values in Table 3, the prediction equation for the CPI data is given as follows

$$\hat{y}_{prfm,Huber} = 0.7620 - 0.0128x_{input} - 0.0029x_{hidden}. \quad (14)$$

It is clear from Table 3 that increases in the explanatory variables x_{input} and x_{hidden} result in decrease in the dependent variable y_{prfm}. However, x_{input} is much more significant variable than the x_{hidden} in explaining the variability in the dependent variable y_{prfm} according to the t-values. Therefore, it can easily be seen from equation (14) that the architecture 12-12-1 gives the most accurate forecasts with the smallest RMSE value among the examined 144 architecture in this example. Realize that RMSE value corresponding to architecture 12-12-1 is equal to 0.5736.

The success of the 12-12-1 architecture in modeling CPI data can be seen from Figure 3 that the CPI observations and the corresponding forecasts are very close to each other. Note that the solid line shows the CPI observations and the dashed line shows the corresponding forecasts for the test set in Figure 3.

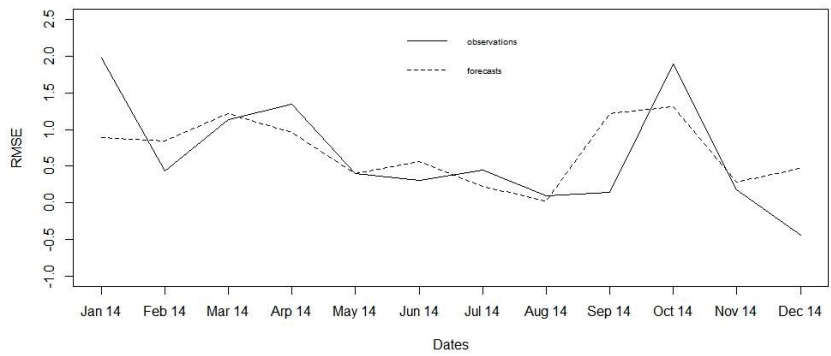

Figure 3: The CPI observations in test set and the corresponding forecasts of the 12-12-1 architecture.

To compare the modelling performances of the proposed methodology based on Huber M regression with the methodology given in Aladag (2019), actual and predicted y_{prfm} values are given for some selected architectures, see Table 4.

Table 4: The modelling performances of the proposed methodology and the methodology given in Aladag (2019) for some selected architectures.

x_{input}	x_{hidden}	y_{prfm}	$\hat{y}_{prfm,OLS}$	$\hat{y}_{prfm,Huber}$
2	6	0.7366	0.7192	0.7149
5	10	0.6331	0.6694	0.6727
8	8	0.6081	0.6369	0.6431
10	7	0.6368	0.6227	0.6142
12	3	0.5903	0.5973	0.6065

It can also be seen from Table 4 that the proposed methodology is more successful than the corresponding methodology based on OLS regression in modelling the ANN performance for CPI data.

It should also be noted that predicted values for the architectures which are not examined in this study can be calculated by using the prediction equation obtained for Huber M regression. For example, prediction value for the architecture 14-9-1 is calculated as

$$\hat{y}_{prfm,Huber} = 0.7620 - 0.127 \times 14 - 0.0028 \times 9 = 0.5574. \qquad (14)$$

Indeed, RMSE value is obtained as 0.5792 when the CPI data is modeled with the 14-9-1 architecture. It is seen that this value is quite close to $\hat{y}_{prfm,Huber} = 0.5574$. Then, it is concluded that the performance of ANN can be calculated by using the prediction equation in (14).

5 CONCLUSION

In this study, an alternative methodology to Aladag (2019) is proposed for selecting the architecture of ANN in modeling univariate time series problems. The proposed method is compared with Aladag (2019) in terms of modeling success on a real-life data set containing outliers. It is seen that the proposed methodology shows better performance than the methodology in Aladag (2019) in the case of existing outliers in the data set. Also, the RMSE values of the architectures that are not examined in this study can be predicted using the proposed methodology.

REFERENCES

Aladag, C. H. (2011). A new architecture selection method based on tabu search for artificial neural networks. *Expert Systems with Applications*, *38*(4), 3287-3293.

Aladag, C. H. (2019). Architecture selection in neural networks by statistical and machine learning. *Oriental Journal of Computer Science and Technology*, *12*(3), 76-89.

Balestrassi, P. P., Popova, E., Paiva, A. D., & Lima, J. M. (2009). Design of experiments on neural network's training for nonlinear time series forecasting. *Neurocomputing*, *72*(4-6), 1160-1178.

Beaton, A. E., & Tukey, J. W. (1974). The Fitting of Power Series, Meaning Polynomials, Illustrated on Band-Spectroscopic Data. *Technometrics*, *16*(2), 147–185. https://doi.org/10.2307/1267936

Durbin, B., Dudoit, S., & van der Laan, M. J. (2008). A deletion/substitution/addition algorithm for classification neural networks, with applications to biomedical data. *Journal of Statistical Planning and Inference*, *138*(2), 464-488.

Eğrioğlu, E., Aladağ, Ç. H., & Günay, S. (2008). A new model selection strategy in artificial neural networks. *Applied Mathematics and Computation*, *195*(2), 591-597.

Huber, P. J. (1992). Robust estimation of a location parameter. In *Breakthroughs in statistics: Methodology and distribution* (pp. 492-518). New York, NY: Springer New York.

Hagan, M. T., Demuth, H. B., & Beale, M. (1997). *Neural network design*. PWS Publishing Co..

Hampel, F. (2002). Robust Inference. *Encyclopedia of environmetrics*. John Wiley & Sons.

Hosseinzadeh Talaee, P. (2014). Multilayer perceptron with different training algorithms for streamflow forecasting. *Neural Computing and Applications*, *24*, 695-703.

Jun, Z. E. N. G., Guo, H. F., & Hu, Y. M. (2007). Artificial neural network model for identifying taxi gross emitter from remote sensing data of vehicle emission. *Journal of Environmental Sciences*, *19*(4), 427-431.

Murata, N., Yoshizawa, S., & Amari, S. I. (1994). Network information criterion-determining the number of hidden units for an artificial neural network model. *IEEE transactions on neural networks*, *5*(6), 865-872.

Roy, A., Kim, L. S., & Mukhopadhyay, S. (1993). A polynomial time algorithm for the construction and training of a class of multilayer perceptrons. *Neural networks*, *6*(4), 535-545.

Rathbun, T. F., Rogers, S. K., DeSimio, M. P., & Oxley, M. E. (1997). MLP iterative construction algorithm. *Neurocomputing*, *17*(3-4), 195-216.

Sietsma, & Dow. (1988, July). Neural net pruning-why and how. In *IEEE 1988 international conference on neural networks* (pp. 325-333). IEEE.

Zhang, G., Patuwo, B. E., & Hu, M. Y. (1998). Forecasting with artificial neural networks: The state of the art. *International journal of forecasting*, *14*(1), 35-62.

Chapter 9

SOME RESULTS ON FERMATEAN FUZZY SOFT TOPOLOGICAL SPACES

Adem YOLCU[1]

Taha Yasin OZTURK[2]

1 Assoc. Prof. Dr., Kafkas University, yolcu.adem@gmail.com, 0000-0002-4317-652X
2 Prof. Dr., Kafkas University, taha36100@hotmail.com, 0000-0003-2402-6507.

1 Introduction

In engineering, economics, medical sciences, and other fields, there are several theories and intricate models that are used to explore uncertainties in the literature. The most well-known theories among these are the fuzzy set theory [36], intuitionistic fuzzy set theory [2], soft set theory [17], and rough set theory [20]. One of these theories, soft set theory, was developed by Molodtsov [17], and it differs from other theories in existence because of its parameterization tools. Fuzzy set theory, rough set theory, inherent complexities, and ambiguous information are all exempt from soft set theory. Soft set research has been quite active, and significant advancements have been made in the field's theoretical understanding. Different algebraic operations were developed in soft set theory by Maji et al. [16]. Ali et al. [1] enhanced the current literature even further and included several fresh soft set theory operations. Soft topological spaces were given by Shabir and Naz [28]. Additionally, they established a few soft set concepts on soft topological spaces. Soft set theory and fuzzy set theory's mixed structure fuzzy soft sets was introduced by Maji et al. [14]. The concept of fuzzy soft topology was first introduced by Tanay and Kandemir [32] utilising fuzzy soft sets and Chang [5] provided some fundamental ideas about it. Atanassov [2]developed intuitionistic fuzzy set (IFS) consists of two functions: like a fuzzy set and the generalisation of fuzzy sets. The unit closed interval is also mapped by these two functions. The concept of intuitionistic fuzzy topology was first discussed by Coker [6], who also examined several analogous forms of classical topology including continuity and compactness. Soft sets were expanded by Maji et al. to intuitionistic fuzzy soft sets, which were covered in Maji et al. [15] In addition, several authors researched the idea of intuitionistic fuzzy soft topological spaces [4, 12, 35].

Yager [33], introduced Pythagorean fuzzy set characterized by a membership degree and a non-membership degree that satisfies the case in which the square sum of its membership degree and a non-membership degree is less than or equal to one. Yager and Abbasov [34], gave an example to illustrate this situation: An expert giving his support for membership of an alternative is $\frac{\sqrt{3}}{2}$ and his non-membership is $\frac{1}{2}$. Since the sum of two values is bigger than 1, they are not avaliable for intuitionistic fuzzy set but it feasible for pythagorean fuzzy set. Obviously, pythagorean fuzzy set is more effective than intuitionistic fuzzy set [23]. Some different author studied on pythagorean fuzzy set theory [3, 10, 29, 37]. In 2019, Olgun et al. [18] introduced pythagorean fuzzy topological space and studied continuity, some importan properties on pythagorean fuzzy topological spaces.Peng et al. [22], defined the pythagorean fuzzy soft set theory and studied its important properties. Guleria and Bajaj [9], investigated pythagorean fuzzy soft matrix and its diverse feasible types. M. Kirisci [13] defined new type of pythagorean

fuzzy soft set and proposed to the solution of decision-making problem. By viewing existing literature, it is clear that, there does not axist any concepts of Pythagorean fuzzy soft topological spaces.

Senepati and Yager constructed the Fermatean fuzzy set (ffs) [25]. The membership and non-membership degrees in the (ffs) satisfy condition $0 \le (\pi_P(\epsilon))^3 + (\eta_P(\epsilon))^3 \le 1$. When defining uncertainty, (ffs), a notion that is new to the literature, performs better than the intuitionistic fuzzy set (ifs) and Pythagorean fuzzy set (Pfs). For instance, $0.9^2 + 0.6^2 > 1$ and $0.9^3 + 0.6^3 < 1.$ [25] provides several characteristics, score, and accuracy functions of (ffs)s. Additionally, (ffs) has been applied the TOPSIS approach, which is often used in Multi Criteria Decision Making (MCDM) situations. The TOPSIS approach, which is often employed in MCDM issues, has also been used to (ffs), according to Senepathy and Yager [25]. Senapati ve Yager [26] examined numerous new operations as a follow-up to this work, including subtraction, division, and Fermatean arithmetic mean operations over (ffs)s, and used the Fermatean fuzzy weighted product model to tackle MCDM issues. New aggregation operators that fall within the (ffs) category have been defined and their associated features have been studied in [27]. The notion of Fermatean fuzzy linguistic term sets (fflt) is presented in the work of Donghai and et al. [7]. These sets' operations, scoring, and accuracy functions were provided. A new (fflt)s-related similarity measure is created in [8]. The new measurement combines the cosine similarity measure and the Euclidean distance measure. Also, Fermatean fuzzy soft sets have been studied by different researchers [24, 30, 31, 13].

In this paper, we introduce the some imprtant properties of fermatean fuzzy soft topological spaces. We also define fermatean fuzzy soft closure, fermatean fuzzy soft interior and some important properties on fermatean fuzzy soft topological spaces. Finally, fermatean fuzzy soft continuous mapping is investigated and some interesting results are derived which may be of value for further research.

2 Preliminaries

Definition 1 *[36] Let* Υ *be an universe. A fuzzy set* F *in* Υ, $F = \{(\epsilon, \pi_F(\epsilon)) : \epsilon \in \Upsilon\}$, *where* $\pi_F : \Upsilon \to 0,1]$ *is the membership function of the fuzzy set* F; $\pi_F(\epsilon) \in 0,1]$ *is the membership of* $\epsilon \in \Upsilon$ *in* f. *The set of all fuzzy sets over* Υ *will be denoted by* $FS(\Upsilon)$.

Definition 2 *[2] An intuitionistic fuzzy set* F *in* Υ *is* $F = \{(\epsilon, \pi_F(\epsilon), \eta_F(\epsilon)) : \epsilon \in \Upsilon\}$, *where* $\pi_F : \Upsilon \to 0,1]$, $\eta_F : \Upsilon \to 0,1]$

with the condition $0 \le \pi_F(\epsilon) + \eta_F(\epsilon) \le 1, \forall \epsilon \in \Upsilon$. *The numbers* $\pi_F, \eta_F \in 0,1]$ *denote the degree of membership and non-membership of* ϵ *to* F, *respectively. The set of all intuitionistic fuzzy sets over* Υ *will be denoted by* $IFS(\Upsilon)$.

Definition 3 *[17] Let* Δ *be a set of parameters and* Υ *be the universal set. A pair* (F, Δ) *is called a soft set over* Υ, *where* F *is a mapping* $F : \Delta \to \mathcal{P}(\Upsilon)$. *In other words, the soft set is a parameterized family of subsets of the set* Υ.

Definition 4 *[14] Let* Δ *be a set of parameters and* Υ *be the universal set. A pair* (F, Δ) *is called a fuzzy soft set over* Υ, *If* $F : \Delta \to FS(\Upsilon)$ *is a mapping from* Δ *into set of all fuzzy sets in* Υ, *where* $FS(\Upsilon)$ *is set of all fuzzy subset of* Υ.

Definition 5 *[15] Let* Υ *be an initial universe* Δ *be a set of parameters*. *A pair* (F, Δ) *is called an intuitionistic fuzzy soft set over* Υ, *where* F *is a mapping given by,* $F : \Delta \to IFS(\Upsilon)$.

In general, for every $\delta \in \Delta$, $F(\delta)$ is an intuitionistic fuzzy set of Υ and it is called intuitionistic fuzzy value set of parameter δ. Clearly, $F(\delta)$ can be written as a intuitionistic fuzzy set such that $F(\delta) = \{(\epsilon, \pi_F(\epsilon), \eta_F(\epsilon)) : \epsilon \in \Upsilon\}$

Definition 6 *[25] Let* Υ *be a universe of discourse. A fermatean fuzzy set (PFS) in* Υ *is given by,* $P = \{(\epsilon, \pi_P(\epsilon), \eta_P(\epsilon)) : \epsilon \in \Upsilon\}$ *where,* $\pi_P : \Upsilon \to 0,1]$ *denotes the degree of membership and* $\eta_p : \Upsilon \to 0,1]$ *denotes the degree of nonmembership of the element* $\epsilon \in \Upsilon$ *to the set* P *with the condition that* $0 \le (\pi_P(\epsilon))^3 + (\eta_P(\epsilon))^3 \le 1$.

Definition 7 *[13] Let* $P_1 = \{(\epsilon, \pi_{P_1}(\epsilon), \eta_{P_1}(\epsilon)) : \epsilon \in \Upsilon\}$ *and* $P_2 = \{(\epsilon, \pi_{P_2}(\epsilon), \eta_{P_2}(\epsilon)) : \epsilon \in \Upsilon\}$ *be two fermatean fuzzy sets. Then their operations are defined as follows;*

1. $P_1 \cup P_2 = \left\{(\epsilon, \max\{\pi_{P_1}(\epsilon), \pi_{P_2}(\epsilon)\}, \min\{\eta_{P_1}(\epsilon), \eta_{P_2}(\epsilon)\})\right\}$
2. $P_1 \cap P_2 = \left\{(\epsilon, \min\{\pi_{P_1}(\epsilon), \pi_{P_2}(\epsilon)\}, \max\{\eta_{P_1}(\epsilon), \eta_{P_2}(\epsilon)\})\right\}$
3. $P^c = \{(\epsilon, \eta_P(\epsilon), \pi_P(\epsilon)) : \epsilon \in \Upsilon\}$

4. $P_1^c \cup P_2^c = (P_1 \cap P_2)^c$
5. $P_1^c \cap P_2^c = (P_1 \cup P_2)^c$

Definition 8 *[11] Let* $\Upsilon \neq \varnothing$ *be a set and let* τ *be a family of fermatean fuzzy subsets of* Υ. *If*

1. $1_\Upsilon, 0_\Upsilon \in \tau,$
2. for any $P_1, P_2 \in \tau,$ we have $P_1 \cap P_2 \in \tau,$
3. for any $\{P_i\}_{i\in I} \subset \tau,$ we have $\underset{i\in I}{\cup} P_i \in \tau$

where I is an arbitrary index set then τ is called a fermatean fuzzy topology on Υ.

Definition 9 *[30] Let* Υ *be the universal set and* Δ *be a set of parameters. The fermatean fuzzy soft set is defined as the pair* (F,Δ) *where,* $F:\Delta \to PFS(\Upsilon)$ *and* $PFS(\Upsilon)$ *is the set of all fermatean fuzzy subsets of* Υ. *If* $\mu_F^3(\epsilon)+\eta_F^3(\epsilon)\leq 1$ *, then fermatean fuzzy soft sets degenerate into intuitionistic fuzzy soft sets.*

Definition 10 *[30]Let* $A,B \subseteq \Delta$ *and* $(F,A),(G,B)$ *be two fermatean fuzzy soft sets over* Υ. (F,A) *is said to be fermatean fuzzy soft subset of* (G,B) *denoted by* $(F,A)\tilde{\subseteq}(G,B)$ *if,*

1. $A \subseteq B$
2. $\forall \delta \in A,$ $F(\delta)$ is a fermatean fuzzy subset of $G(\delta)$ that is, $\forall \epsilon \in U$ and $\forall \delta \in A,$ $\pi_{F(\delta)}(\epsilon) \leq \pi_{G(\delta)}(\epsilon)$ and $\eta_{F(\delta)}(\epsilon) \geq \eta_{G(\delta)}(\epsilon).$ If $(F,A)\tilde{\subseteq}(G,B)$ and $(G,B)\tilde{\subseteq}(F,A)$ then $(F,A),(G,B)$ are said to be equal.

Definition 11 *[30] Let* (F,Δ) *two fermatean fuzzy soft sets over* Υ. *The complement of* (F,Δ) *is denoted by* $(F,\Delta)^c$ *and is defined by*

$$(F,\Delta)^c = \{(\delta,(\epsilon,\eta_{F(\delta)}(\epsilon),\pi_{F(\delta)}(\epsilon)):\epsilon \in \Upsilon):\delta \in \Delta\}$$

Definition 12 *[31] a) A fermatean fuzzy soft set* (F,Δ) *over the universe* Υ *is said to be null fermatean fuzzy soft set if* $\pi_{F(\delta)}(\epsilon)=0$ *and* $\eta_{F(\delta)}(\epsilon)=1$*;* $\forall \delta \in \Delta, \forall \epsilon \in \Upsilon.$ *It is denoted by* $\tilde{0}_{(\Upsilon,\Delta)}$.

b) A fermatean fuzzy soft set (F,Δ) over the universe Υ is said to be absolute fermatean fuzzy soft set if $\pi_{F(\delta)}(\epsilon)=1$ and $\eta_{F(\delta)}(\epsilon)=0$;

$\forall \delta \in \Delta, \forall \epsilon \in \Upsilon$. It is denoted by $\tilde{1}_{(\Upsilon,\Delta)}$.

3 Fermatean Fuzzy Soft Topological Spaces

In this section, we introduce some important properties of fermatean fuzzy soft topological spaces and we define the fermatean fuzzy soft closure and fermatean fuzzy soft interior set.

Let Υ be an initial universe and $PFS(\Upsilon)$ denote the family of fermatean fuzzy sets over Υ and $FFSS(\Upsilon,\Delta)$ be the family of all fermatean fuzzy soft sets over Υ with parameters in Δ.

Definition 13 *[31] Let $\Upsilon \neq \emptyset$ be a universe set and $\tilde{\tau} \subset FFSS(\Upsilon,\Delta)$ be a collection of fermatean fuzzy soft sets over Υ, then τ is said to be on fermatean fuzzy soft topology on Υ if*
(i) $\tilde{0}_{(\Upsilon,\Delta)}$, $\tilde{1}_{(\Upsilon,\Delta)}$ belong to $\tilde{\tau}$,
(ii) The union of any number of fermatean fuzzy soft sets in $\tilde{\tau}$ belongs to $\tilde{\tau}$,
(iii) The intersection of any two fermatean fuzzy soft sets in $\tilde{\tau}$ belongs to $\tilde{\tau}$.
The triple $\left(\Upsilon,\tilde{\tau},\Delta\right)_f$ is called an fermatean fuzzy soft tpological space over Υ. Every member of τ is called a fermatean fuzzy soft open set in Υ.

Definition 14 *a) Let Υ be an initial universe set, Δ be the set of parameters and $\tilde{\tau} = \left\{\tilde{0}_{(\Upsilon,\Delta)}, \tilde{1}_{(\Upsilon,\Delta)}\right\}$. Then $\tilde{\tau}$ is called a fermatean fuzzy soft indiscrete topology on Υ and $\left(\Upsilon,\tilde{\tau},\Delta\right)_f$ is said to be a fermatean fuzzy soft indiscrete space over Υ.*

b) Let Υ be an initial universe set, Δ be the set of parameters and $\tilde{\tau}$ be the collection of all fermatean fuzzy soft sets which can be defined over Υ. Then $\tilde{\tau}$ is called a fermatean fuzzy soft discrete topology on Υ and $\left(\Upsilon,\tilde{\tau},\Delta\right)_f$ is said to be a fermatean fuzzy soft discrete space over Υ.

Example 1 *Let* $\Upsilon = \{\epsilon_1, \epsilon_2\}$, $\Delta = \{\delta_1, \delta_2\}$ *and*

$$\tilde{\tau} = \left\{\tilde{0}_{(\Upsilon,\Delta)}, \tilde{1}_{(\Upsilon,\Delta)}, (G_1,\Delta), (G_2,\Delta), (G_3,\Delta), (G_4,\Delta)\right\}$$

where $(G_1,\Delta), (G_2,\Delta), (G_3,\Delta), (G_4,\Delta)$ fermatean fuzzy soft sets over Υ, defined as;

$$(G_1,\Delta)=\left\{\begin{matrix}(\delta_1,\{(\epsilon_1,0.6,0.8),(\epsilon_2,0.5,0.6)\})\\(\delta_2,\{(\epsilon_1,0.3,0.4),(\epsilon_2,0.6,0.6)\})\end{matrix}\right\}$$

$$(G_2,\Delta)=\left\{\begin{matrix}(\delta_{1,},\{(\epsilon_1,0.6,0.6),(\epsilon_2,0.8,0.2)\})\\(\delta_2,\{(\epsilon_1,0.7,0.1),(\epsilon_2,0.2,0.4)\})\end{matrix}\right\}$$

$$(G_3,\Delta)=\left\{\begin{matrix}(\delta_1,\{(\epsilon_1,0.6,0.6),(\epsilon_2,0.8,0.2)\})\\(\delta_2,\{(\epsilon_1,0.7,0.1),(\epsilon_2,0.6,0.4)\})\end{matrix}\right\}$$

$$(G_4,\Delta)=\left\{\begin{matrix}(\delta_1,\{(\epsilon_1,0.6,0.8),(\epsilon_2,0.5,0.6)\})\\(\delta_2,\{(\epsilon_1,0.3,0.4),(\epsilon_2,0.2,0.6)\})\end{matrix}\right\}$$

$$(\tilde{0}_{(\Upsilon,\Delta)})^c=\tilde{1}_{(\Upsilon,\Delta)},(\tilde{1}_{(\Upsilon,\Delta)})^c=\tilde{0}_{(\Upsilon,\Delta)}$$

Then $\tilde{\tau}$ defines a fermatean fuzzy soft topology on Υ and hence $\left(\Upsilon,\tilde{\tau},\Delta\right)_P$ is a fermatean fuzzy soft topolojical space over Υ.

Proposition 1 *Let* $\left(\Upsilon,\tilde{\tau}_1,\Delta\right)_f$ *and* $\left(\Upsilon,\tilde{\tau}_2,\Delta\right)_f$ *be two fermatean fuzzy soft topological space over* Υ *. If* $\tilde{\tau}_1\cap_\Delta\tilde{\tau}_2=\left\{(H,\Delta):(H,\Delta)\in\tilde{\tau}_1\text{and}(H,\Delta)\in\tilde{\tau}_2\right\}$ *. Then* $\tilde{\tau}_1\cap_\Delta\tilde{\tau}_2$ *is a fermatean fuzzy soft topology on* Υ.

Proof. Obviously $\tilde{0}_{(\Upsilon,\Delta)},\tilde{1}_{(\Upsilon,\Delta)}\in\tilde{\tau}_1\cap_\Delta\tilde{\tau}_2$. Let $(H,\Delta),(G,\Delta)\in\tilde{\tau}_1\cap_\Delta\tilde{\tau}_2$. Then $(H,\Delta),(G,\Delta)\in\tilde{\tau}_1$ and $(H,\Delta),(G,\Delta)\in\tilde{\tau}_2$. Since $\tilde{\tau}_1$ and $\tilde{\tau}_2$ are two fermatean fuzzy soft topolojies on Υ, then $(H,\Delta)\cap_\Delta(G,\Delta)\in\tilde{\tau}_1$ and $(H,\Delta)\cap_\Delta(G,\Delta)\in\tilde{\tau}_2$. Hence $(H,\Delta)\cap_\Delta(G,\Delta)\in\tilde{\tau}_1\cap_\Delta\tilde{\tau}_2$. Let $\{(F_s,\Delta):s\in S\}\subseteq\tilde{\tau}_1\cap_\Delta\tilde{\tau}_2$. Then $(F_s,\Delta)\in\tilde{\tau}_1$ and $(F_s,\Delta)\in\tilde{\tau}_2$ for any $s\in S$. Since $\tilde{\tau}_1$ and $\tilde{\tau}_2$ are two fermatean fuzzy soft topologies on Υ, $\cup\{(F_s,\Delta):s\in S\}\in\tilde{\tau}_1$ and $\cup\{(F_s,\Delta):s\in S\}\in\tilde{\tau}_2$. Therefore, $\cup\{(F_s,\Delta):s\in S\}\in\tilde{\tau}_1\cap_\Delta\tilde{\tau}_2$.

Proposition 2 *Let* $\left(\Upsilon,\tilde{\tau},\Delta\right)_f$ *be two fermatean fuzzy soft topological space over* Υ. *For any* $\delta\in\Delta$,

$$\tau_\delta=\left\{f(\delta):(F,\Delta)\in\tilde{\tau}\right\}$$

in a fermatean fuzzy topology on Υ.

Proof. (i) $\tilde{0}_{(\Upsilon,\Delta)},\tilde{1}_{(\Upsilon,\Delta)}\in\tau_\delta$

(ii) Let $A,B\in\tau_\delta$. Then there exist $\left(F,\Delta\right),\left(G,\Delta\right)\in\tilde{\tau}$ such that $A=f(\delta)$ and $B=g(\delta)$. By $\tilde{\tau}$ be a fermatean fuzzy soft topology on Υ, $\left(F,\Delta\right)\cap_\Delta\left(G,\Delta\right)\in\tilde{\tau}$. Put $\left(H,\Delta\right)=\left(F,\Delta\right)\cap_\Delta\left(G,\Delta\right)$. Then $\left(H,\Delta\right)\in\tilde{\tau}$. Note that $A\cap_\Delta B=f(\delta)\cap_\Delta g(\delta)=h(\delta)$ and $\tau_\delta=\left\{F\left(\delta\right):\left(F,\Delta\right)\in\tilde{\tau}\right\}$. Then $A\cap_\Delta B\in\tau_\delta$.

(iii) Let $\left\{A_s:s\in S\right\}\subseteq\tau_\delta$. Then for every $s\in\tilde{\tau}$, there exist $\left(F_s,\Delta\right)\in\tilde{\tau}$ such that $A_s=(F_s,\Delta)$. By $\tilde{\tau}$ be on fermatean fuzzy soft topology on Υ, $\bigcup\left\{\left(F_s,\Delta\right):s\in S\right\}\in\tilde{\tau}$. Put $\left(F,\Delta\right)=\bigcup\left\{\left(F_s,\Delta\right):s\in S\right\}$. Then $\left(F,\Delta\right)\in\tilde{\tau}$. Note that $\bigcup_{s\in S}A_s=\bigcup\left\{\left(F_s,\Delta\right):s\in S\right\}=(F,\Delta)$ and $\tau_\delta=\left\{F(\delta):\left(F,\Delta\right)\in\tilde{\tau}\right\}=f(\delta)$. Therefore $\tau_\delta=\left\{F(\delta):\left(F,\Delta\right)\in\tilde{\tau}\right\}$ is a fermatean fuzzy soft topology on Υ.

Definition 15 *Let* $\left(\Upsilon,\tilde{\tau},\Delta\right)_f$ *be a fermatean fuzzy soft topological space over* Υ. *A fermatean fuzzy soft set* (F,Δ) *over* Υ *is said to be a fermatean fuzzy soft closed set in* Υ, *if its complement* $(F,\Delta)^c$ *belongs to* $\tilde{\tau}$.

Example 2 *Consider the Example-1. It is clear that* $\left(\tilde{0}_{(\Upsilon,\Delta)}\right)^c,\left(\tilde{1}_{(\Upsilon,\Delta)}\right)^c,\left(G_1,\Delta\right)^c,\left(G_2,\Delta\right)^c,\left(G_3,\Delta\right)^c$ *and* $\left(G_4,\Delta\right)^c$ *are fermatean fuzzy soft closed set in* Υ.

$$(G_1,\Delta)^c=\left\{\begin{matrix}(\delta_1,\left\{\left(\epsilon_1,0.8,0.6\right),\left(\epsilon_2,0.6,0.5\right)\right\})\\(\delta_2,\left\{\left(\epsilon_1,0.4,0.3\right),\left(\epsilon_2,0.6,0.6\right)\right\})\end{matrix}\right\}$$

$$(G_2,\Delta)^c=\begin{Bmatrix}(\delta_{1,}\{(\epsilon_1,0.6,0.6),(\epsilon_2,0.2,0.8)\})\\(\delta_2,\{(\epsilon_1,0.1,0.7),(\epsilon_2,0.4,0.2)\})\end{Bmatrix}$$

$$(G_3,\Delta)^c=\begin{Bmatrix}(\delta_1,\{(\epsilon_1,0.6,0.6),(\epsilon_2,0.2,0.8)\})\\(\delta_2,\{(\epsilon_1,0.1,0.7),(\epsilon_2,0.4,0.6)\})\end{Bmatrix}$$

$$(G_4,\Delta)^c=\begin{Bmatrix}(\delta_1,\{(\epsilon_1,0.8,0.6),(\epsilon_2,0.6,0.5)\})\\(\delta_2,\{(\epsilon_1,0.4,0.3),(\epsilon_2,0.6,0.2)\})\end{Bmatrix}$$

Proposition 3 *Let* $\left(\Upsilon,\tilde{\tau},\Delta\right)_f$ *be a fermatean fuzzy soft topological space over* Υ. *Then, the following properties hold.*
(i) $\tilde{0}_{(\Upsilon,\Delta)},\tilde{1}_{(\Upsilon,\Delta)}$ are fermatean fuzzy soft closed set over Υ.
(ii) The intersection of any number of fermatean fuzzy soft closed set is a fermatean fuzzy soft closed set over Υ.
(iii) The union of any two fermatean fuzzy soft closed set is a fermatean fuzzy soft closed set over Υ.

Proof. Straightforward.

Definition 16 *Let* $\left(\Upsilon,\tilde{\tau},\Delta\right)_f$ *be a fermatean fuzzy soft topological space over* Υ *and* $\left(F,\Delta\right)$ *be a fermatean fuzzy soft sets over* Υ. *The fermatean fuzzy soft closure of* $\left(F,\Delta\right)$ *denoted by* $fcl(F,\Delta)$ *is the intersection of all fermatean fuzzy soft closed super sets of* (F,Δ).
Clearly $fcl(F,\Delta)$ is the smallest fermatean fuzzy soft closed set over Υ which contain (F,Δ).

Theorem 1 *Let* $\left(\Upsilon,\tilde{\tau},\Delta\right)_f$ *be a fermatean fuzzy soft topological space over* Υ *and* $\left(F,\Delta\right)\in FFSS(\Upsilon,\Delta)$. *Then the following propeties hold.*
(i) $fcl(\tilde{0}_{(\Upsilon,\Delta)})=\tilde{0}_{(\Upsilon,\Delta)}$ and $fcl(\tilde{1}_{(\Upsilon,\Delta)})=\tilde{1}_{(\Upsilon,\Delta)}$,
(ii) $\left(F,\Delta\right)\subseteq fcl\left(F,\Delta\right)$,
(iii) $\left(F,\Delta\right)$ is a fermatean fuzzy soft closed set $\Leftrightarrow$ $fcl(F,\Delta)=(F,\Delta)$,
(iv) $fcl\left(fcl\left(F,\Delta\right)\right)=fcl(F,\Delta)$,

(v) $(F,\Delta)\subseteq (G,\Delta)\Rightarrow fcl(F,\Delta)\subseteq fcl(G,\Delta)$,

(vi) $fcl\left((F,\Delta)\cup_{\Delta}(G,\Delta)\right)=fcl(F,\Delta)\cup_{\Delta}fcl(G,\Delta)$.

Proof. (i) and *(ii)* are clear.

(iii) If (F,Δ) is a fermatean fuzzy soft closed set over Υ then $fcl(F,\Delta)$ is itselt a fermatean fuzzy soft closed set over Υ which contain (F,Δ). So $fcl(F,\Delta)$ is the smallest fermatean fuzzy soft closed set containing (F,Δ) and $(F,\Delta)=fcl(F,\Delta)$

(iv) Since $fcl(F,\Delta)$ is a fermatean fuzzy soft closed set therefore by part *(iii)*. We have $fcl(F,\Delta)=fcl\left(fcl(F,\Delta)\right)$.

(v) If $(F,\Delta)\subseteq(G,\Delta)$, then $(G,\Delta)=(F,\Delta)\cup_{\Delta}(G,\Delta)\Rightarrow$
$fcl(G,\Delta)=fcl\left((F,\Delta)\cup_{\Delta}(G,\Delta)\right)=fcl(F,\Delta)\cup_{\Delta}fcl(G,\Delta)\Rightarrow fcl(F,\Delta)\subseteq fcl(G,\Delta)$

(vi) Since $(F,\Delta)\subseteq(F,\Delta)\cup_{\Delta}(G,\Delta)$ and $(G,\Delta)\subseteq(F,\Delta)\cup_{\Delta}(G,\Delta)$, from the *(v)*,

$fcl(F,\Delta)\subseteq fcl\left((F,\Delta)\cup_{\Delta}(G,\Delta)\right)$,

$fcl(G,\Delta)\subseteq fcl\left((F,\Delta)\cup_{\Delta}(G,\Delta)\right)$

Therefore $fcl(F,\Delta)\cup_{\Delta}fcl(G,\Delta)\subseteq fcl\left((F,\Delta)\cup_{\Delta}(G,\Delta)\right)$

Conversely, suppose that $(F,\Delta)\subseteq fcl(F,\Delta)$ and $(G,\Delta)\subseteq fcl(G,\Delta)$. From the proposition 3, $fcl(F,\Delta)\cup_{\Delta}fcl(G,\Delta)$ is a fermatean fuzzy soft closed set over Υ being the union of two fermatean fuzzy soft closed set. Then, $fcl\left((F,\Delta)\cup_{\Delta}(G,\Delta)\right)\subseteq fcl(F,\Delta)\cup_{\Delta}fcl(G,\Delta)$. Hence $fcl\left((F,\Delta)\cup_{\Delta}(G,\Delta)\right)=fcl(F,\Delta)\cup_{\Delta}fcl(G,\Delta)$ is obtained.

Definition 17 *Let* $\left(\Upsilon,\tilde{\tau},\Delta\right)_f$ *be a fermatean fuzzy soft topological space over* Υ *and* $(H,\Delta)\in FFSS(\Upsilon,\Delta)$. *The fermatean fuzzy soft interior of* (H,Δ), *denoted by* $fint(H,\Delta)$, *is the union of all the fermatean fuzzy soft open sets contained in* (H,Δ).

Theorem 2 *Let* $\left(\Upsilon,\tilde{\tau},\Delta\right)_f$ *be a fermatean fuzzy soft topological space over*

Υ *and* $(H,\Delta)\in FFSS(\Upsilon,\Delta)$. *Then the following properties hold.*

(*i*) $fint(\tilde{0}_{(\Upsilon,\Delta)})=\tilde{0}_{(\Upsilon,\Delta)}$ and $fint(\tilde{1}_{(\Upsilon,\Delta)})=\tilde{1}_{(\Upsilon,\Delta)}$,

(*ii*) $fint(H,\Delta)\subseteq (H,\Delta)$,

(*iii*) (H,Δ) is a fermatean fuzzy soft open set $\Leftrightarrow$ $fint(H,\Delta)=(H,\Delta)$,

(*iv*) $fint(fint(H,\Delta))=fint(H,\Delta)$,

(*v*) $(H,\Delta)\subseteq (G,\Delta)\Rightarrow fint(H,\Delta)\subseteq fint(G,\Delta)$,

(*vi*) $fint\left((H,\Delta)\cap_{\Delta}(G,\Delta)\right)=fint(H,\Delta)\cap_{\Delta}fint(G,\Delta)$.

Proof. (i) and *(ii)* are clear.

(iii) If (H,Δ) is fermatean fuzzy soft open set over Υ, then $fint(H,\Delta)$ is a larger fermatean fuzzy soft open set which contained in (H,Δ). So $(H,\Delta)=fint(H,\Delta)$ is obtained.

(iv) Since $fint(H,\Delta)$ is a fermatean fuzzy soft open set, then by part *(iii)*, we have $fint(fint(H,\Delta))=fint(H,\Delta)$.

(v) By the part *(ii)*, $fint(H,\Delta)\subseteq(H,\Delta)$ and $fint(H,\Delta)\subseteq(H,\Delta)\subseteq(G,\Delta)$ is obtained. Since $fint(h,\Delta)$ is fermatean fuzzy soft open set and $fint(G,\Delta)$ is largest fermatean fuzzy soft open set which contained in (G,Δ), then $fint(H,\Delta)\subseteq fint(G,\Delta)\subseteq(G,\Delta)$ and $fint(H,\Delta)\subseteq fint(G,\Delta)$ is obtained.

(vi) By the part *(v)*,

$$(H,\Delta)\cap_{\Delta}(G,\Delta)\subseteq(H,\Delta)\Rightarrow fint\left((H,\Delta)\cap_{\Delta}(G,\Delta)\right)\subseteq fint(H,\Delta)$$

$$(H,\Delta)\cap_{\Delta}(G,\Delta)\subseteq(G,\Delta)\Rightarrow fint\left((H,\Delta)\cap_{\Delta}(G,\Delta)\right)\subseteq fint(G,\Delta)$$

Therefore $fint\left((H,\Delta)\cap_{\Delta}(G,\Delta)\right)\subseteq fint(H,\Delta)\cap_{\Delta}fint(G,\Delta)$.

Conversely, $fint\left((H,\Delta)\cap_{\Delta}(G,\Delta)\right)$ is largest fermatean fuzzy soft open set which contained in $(H,\Delta)\cap_{\Delta}(G,\Delta)$. Then $fint(H,\Delta)\cap_{\Delta}fint(G,\Delta)\subseteq fint\left((H,\Delta)\cap_{\Delta}(G,\Delta)\right)$. Hence $fint\left((H,\Delta)\cap_{\Delta}(G,\Delta)\right)=fint(H,\Delta)\cap_{\Delta}fint(G,\Delta)$ is obtained.

Example 3 *Let* $\Upsilon=\{\epsilon_1,\epsilon_2\}$, $\Delta=\{\delta_1,\delta_2\}$

$$(H_1,\Delta)=\left\{\begin{matrix}(\delta_1,\{(\epsilon_1,0.6,0.3),(\epsilon_2,0.8,0.4)\})\\(\delta_2,\{(\epsilon_1,0.5,0.1),(\epsilon_2,0.6,0.2)\})\end{matrix}\right\}$$

$$(H_2,\Delta)=\left\{\begin{matrix}(\delta_1,\{(\epsilon_1,0.5,0.4),(\epsilon_2,0.3,0.5)\})\\(\delta_2,\{(\epsilon_1,0.4,0.3),(\epsilon_2,0.5,0.6)\})\end{matrix}\right\}$$

Obviously $\tilde{\tau}=\{\tilde{0}_{(\Upsilon,\Delta)},\tilde{1}_{(\Upsilon,\Delta)},(H_1,\Delta),(H_2,\Delta)\}$ is a frematean fuzzy soft topology on Υ.

(i) Suppose that any $(G,\Delta)\in FFSS(\Upsilon,\Delta)$ is defined as following:

$$(G,\Delta)=\left\{\begin{matrix}(\delta_1,\{(\epsilon_1,0.7,0.2),(\epsilon_2,0.8,0.3)\})\\(\delta_2,\{(\epsilon_1,0.6,0.1),(\epsilon_2,0.7,0.1)\})\end{matrix}\right\}$$

Then $\tilde{0}_{(\Upsilon,\Delta)},(H_1,\Delta),(H_2,\Delta)\subseteq(G,\Delta)$. Therefore $fint(G,\Delta)=\tilde{0}_{(\Upsilon,\Delta)}\cup_\Delta(H_1,\Delta)\cup_\Delta(H_2,\Delta)=(H_1,\Delta)$.

(ii) Suppose that any $(F,\Delta)\in FFSS(\Upsilon,\Delta)$ is defined as following:

$$(F,\Delta)=\left\{\begin{matrix}(\delta_1,\{(\epsilon_1,0.2,0.7),(\epsilon_2,0.3,0.8)\})\\(\delta_2,\{(\epsilon_1,0.1,0.6),(\epsilon_2,0.1,0.7)\})\end{matrix}\right\}$$

Now, we find the complement of $(H_1,\Delta),(H_2,\Delta)$.

$$(H_1,\Delta)^c=\left\{\begin{matrix}(\delta_{1,}\{(\epsilon_1,0.3,0.6),(\epsilon_2,0.4,0.8)\})\\(\delta_2,\{(\epsilon_1,0.1,0.5),(\epsilon_2,0.2,0.6)\})\end{matrix}\right\}$$

$$(H_2,\Delta)^c=\left\{\begin{matrix}(\delta_1,\{(\epsilon_1,0.4,0.5),(\epsilon_2,0.5,0.3)\})\\(\delta_2,\{(\epsilon_1,0.3,0.4),(\epsilon_2,0.6,0.5)\})\end{matrix}\right\}$$

$$(\tilde{0}_{(\Upsilon,\Delta)})^c=\tilde{1}_{(\Upsilon,\Delta)},(\tilde{1}_{(\Upsilon,\Delta)})^c=\tilde{0}_{(\Upsilon,\Delta)}$$

Obviously, $(\tilde{0}_{(\Upsilon,\Delta)})^c$, $(\tilde{1}_{(\Upsilon,\Delta)})^c,(H_1,\Delta)^c,(H_2,\Delta)^c$ are all frematean fuzzy soft closed sets over $\left(\Upsilon,\tilde{\tau},\Delta\right)_f$.Then $(\tilde{1}_{(\Upsilon,\Delta)})^c,(H_1,\Delta)^c,(H_2,\Delta)^c\supset(F,\Delta)$.

Therefore $fcl(F,\Delta)=(\tilde{1}_{(\Upsilon,\Delta)})^c\cap_\Delta(H_1,\Delta)^c\cap_\Delta(H_2,\Delta)^c=(H_1,\Delta)^c$

Theorem 3 *Let* $\left(\Upsilon,\tilde{\tau},\Delta\right)_f$ *be a frematean fuzzy soft topological space over*

Υ *and* $(H,\Delta)\subset FFSS(\Upsilon,\Delta)$. *Then*

(i) $\left(fcl(H,\Delta)\right)^c = fint((H,\Delta)^c)$

(ii) $fint((H,\Delta))^c = fcl((H,\Delta)^c)$

Proof. (i)

$$fcl(H,\Delta) = \cap_\Delta\left\{(F,\Delta)\in\tau^c : (F,\Delta)\supset(H,\Delta)\right\}$$

$$\Rightarrow\left(fcl(H,\Delta)\right)^c = \left(\left\{\cap_\Delta(F,\Delta)\in\tau^c : (F,\Delta)\supset(H,\Delta)\right\}\right)^c$$

$$= \cup_\Delta\left\{(F,\Delta)\in\tau : (F,\Delta)^c\subset(H,\Delta)^c\right\} = fint((H,\Delta)^c)$$

(ii)

$$fint(H,\Delta) = \cup_\Delta\left\{(F,\Delta)\in\tau : (F,\Delta)\subset(H,\Delta)\right\}$$

$$\Rightarrow\left(fint(F,\Delta)\right)^c = \left(\left\{\cup_\Delta(F,\Delta)\in\tau : (F,\Delta)\subset(H,\Delta)\right\}\right)^c$$

$$= \cap_\Delta\left\{(F,\Delta)^c\in\tau^c : (F,\Delta)^c\supset(H,\Delta)^c\right\} = fcl((H,\Delta)^c)$$

4. Fermatean Fuzzy Soft Continuity

Let Υ and Y be non-empty initial universe and Δ,Δ' be parameter set and $A\subseteq\Delta$, $B\subseteq\Delta'$.

Definition 18 *Let* $(\Upsilon,\tilde{\tau}_1,\Delta)_f$, $(Y,\tilde{\tau}_2,\Delta')_f$ *be two fermatean fuzzy soft topological spaces and* $\psi:\Upsilon\to Y$, $\sigma:\Delta\to\Delta'$ *be mappings. Then a mapping* $f=(\psi,\sigma):FFSS(\Upsilon,\Delta)\to FFSS(Y,\Delta')$ *is defined as: for* $(H,A)\in FFSS(\Upsilon,\Delta)$ *the image of* (H,A) *under* f, *denoted by* $f((H,A))$, *is a fermatean fuzzy soft set in* $FFSS(Y,\Delta')$ *given by*

$$\pi_{\psi(H)}(\delta')(y) = \begin{cases} \sup\limits_{\delta\in\sigma^{-1}(\delta')\cap A,\epsilon\in\psi^{-1}(y)} \pi_{H(\delta)}(\epsilon), & \text{if}\ \psi^{-1}(y)\neq\varnothing \\ 0 \quad , & \text{otherwise} \end{cases}$$

$$\eta_{\psi(H)}(\delta')(y) = \begin{cases} \inf\limits_{\delta\in\sigma^{-1}(\delta')\cap A,\epsilon\in\psi^{-1}(y)} \eta_{H(\delta)}(\epsilon), & \text{if}\ \psi^{-1}(y)\neq\varnothing \\ 1 \quad , & \text{otherwise} \end{cases}$$

For $(F,B)\in FFSS(Y,\Delta')$, the inverse image of (F,B) under f, denoted by $f^{-1}((F,B))$, is a fermatean fuzzy soft set in $FFSS(\Upsilon,\Delta)$ given by:

$$\pi_{\psi^{-1}(F)}(\delta)(\epsilon)=\pi_{F(\sigma(\delta))}(\psi(\epsilon)),$$
$$\eta_{\psi^{-1}(F)}(\delta)(\epsilon)=\eta_{F(\sigma(\delta))}(\psi(\epsilon))$$

for all $\delta\in\Delta$ and $\epsilon\in\Upsilon$.

Remark 2 *$f((H,A))$ and $f^{-1}((F,B))$ are fermatean fuzzy soft subsets. We can obtain*

$$\pi^2_{\psi(H)}(\delta')(y)+\eta^2_{\psi(H)}(\delta')(y)=\left(\sup_{\delta\in\sigma^{-1}(\delta')\cap A,\epsilon\in\psi^{-1}(y)}\pi_{H(\delta)}(\epsilon)\right)^2+\left(\inf_{\delta\in\sigma^{-1}(\delta')\cap A,\epsilon\in\psi^{-1}(y)}\eta_{H(\delta)}(\epsilon)\right)^2$$
$$=\sup_{\delta\in\sigma^{-1}(\delta')\cap A,\epsilon\in\psi^{-1}(y)}\pi^2_{H(\delta)}(\epsilon)+\inf_{\delta\in\sigma^{-1}(\delta')\cap A,\epsilon\in\psi^{-1}(y)}\eta^2_{H(\delta)}(\epsilon)$$

$$\leq\sup_{\delta\in\sigma^{-1}(\delta')\cap A,\epsilon\in\psi^{-1}(y)}(1-\eta^2_{H(\delta)}(\epsilon))+\inf_{\delta\in\sigma^{-1}(\delta')\cap A,\epsilon\in\psi^{-1}(y)}\eta^2_{H(\delta)}(\epsilon)=1,$$

whenever $\psi^{-1}(y)\neq\varnothing$ is non-empty. On the other hand if $\psi^{-1}(y)=\varnothing$, then we have $\pi^2_{\psi(H)}(\delta')(y)+\eta^2_{\psi(H)}(\delta')(y)=1$. Thus, we showed fermatean fuzzy membership grade condition is provide for fermatean fuzzy soft image and pre-image.

The proof for $f^{-1}((F,B))$ is similar. The following proposition gives some basic properties of image f.

Proposition 4 *Let $f:FFSS(\Upsilon,\Delta)\to FFSS(Y,\Delta')$ be a fermatean fuzzy soft mapping. Then for fermatean fuzzy soft sets (H,A) and (G,B) in $FFSS(\Upsilon,\Delta)$, we have,*

1. $f(\tilde{0}_{(\Upsilon,\Delta)})=\tilde{0}_{(Y,\Delta)}$
2. $f(\tilde{1}_{(\Upsilon,\Delta)})\tilde{\subseteq}\tilde{1}_{(Y,\Delta)}$
3. $f\left((H,A)\cup_\Delta(G,B)\right)=f((H,A))\cup_\Delta f((G,B))$
4. $f\left((H,A)\cap_\Delta(G,B)\right)\subseteq f((H,A))\cap_\Delta f((G,B))$
5. $f\left((H,A)\cup_R(G,B)\right)=f((H,A))\cup_R f((G,B))$
6. $f\left((H,A)\cap_R(G,B)\right)\subseteq f((H,A))\cap_R f((G,B))$

7. If $(H,A)\subseteq(G,B)$, then $f((H,A))\subseteq f((G,B))$

Proof. We only proof (3), (4) and (7). The others can be similarly proved.

(3) We consider $(H,A)\cup_{\Delta}(G,B)=(O,A\cup B)$ and

$$f\Big((H,A)\cup_{\Delta}(G,B)\Big)=(\psi(H),\sigma(A))\cup_{\Delta}(\psi(G),\sigma(B))=(I,\sigma(A)\cup\sigma(B)).$$

Then

$$f\Big((H,A)\cup_{\Delta}(G,B)\Big)=(\psi(O),\sigma(A\cup B))=(\psi(O),\sigma(A)\cup\sigma(B)).$$

For any $y\in Y$ and $\delta^{'}\in\sigma(A)\cup\sigma(B)$, if $\psi^{-1}(y)\neq\varnothing$, then $\pi_{I}(\delta^{'})(y)=\pi_{\psi(O)}(\delta^{'})(y)=0$ and $\eta_{I}(\delta^{'})(y)=\eta_{\psi(O)}(\delta^{'})(y)=1$.

Otherwise,

(i) If $\delta^{'}\in\sigma(A)-\sigma(B)$, then $I(\delta^{'})=\psi(H)(\delta^{'})$. On the other hand, $\delta^{'}\in\sigma(A)-\sigma(B)$ implies that there does not exist $\delta\in B$ such that $\sigma(\delta)=\delta^{'}$. That is, for any $\delta\in\sigma^{-1}(\delta^{'})\cap(A\cup B)$, we have $\delta\in\sigma^{-1}(\delta^{'})\cap(A-B)$. Hence by Definition 18, we have

$$\pi_{\psi(O)}(\delta^{'})(y)=\sup_{\delta\in\sigma^{-1}(\delta^{'})\cap(A\cup B),\epsilon\in\psi^{-1}(y)}\pi_{O(\delta)}(\epsilon)=\sup_{\delta\in\sigma^{-1}(\delta^{'})\cap(A-B),\epsilon\in\psi^{-1}(y)}\pi_{O(\delta)}(\epsilon)$$
$$=\sup_{\delta\in\sigma^{-1}(\delta^{'})\cap(A\cup B),\epsilon\in\psi^{-1}(y)}\pi_{H(\delta)}(\epsilon)=\pi_{I(\delta^{'})}(y)$$

Similarly, we obtain $\eta_{\psi(O)}(\delta^{'})(y)=\eta_{I(\delta^{'})}(y)$.

(ii) If $\delta^{'}\in\sigma(B)-\sigma(A)$, analogous to *(i)*, we have $\pi_{\psi(O)}(\delta^{'})(y)=\pi_{I(\delta^{'})}(y),\eta_{\psi(O)}(\delta^{'})(y)=\eta_{I(\delta^{'})}(y)$.

(iii) If $\delta^{'}\in\sigma(A)\cap\sigma(B)$, then

$$\pi_{\psi(O)}(\delta^{'})(y)=\sup_{\delta\in\sigma^{-1}(\delta^{'})\cap(A\cup B),\epsilon\in\psi^{-1}(y)}\pi_{O(\delta)}(\epsilon)=\sup_{\delta\in(\sigma^{-1}(\delta^{'})\cap A)\cup(\sigma^{-1}(\delta^{'})\cap B),\epsilon\in\psi^{-1}(y)}\pi_{O(\delta)}(\epsilon)$$
$$=\left(\sup_{\delta\in(\sigma^{-1}(\delta^{'})\cap A)-(\sigma^{-1}(\delta^{'})\cap B),\epsilon\in\psi^{-1}(y)}\pi_{H(\delta)}(\epsilon)\right)$$

$$\vee\left(\sup_{\delta\in(\sigma^{-1}(\delta^{'})\cap A)\cap(\sigma^{-1}(\delta^{'})\cap B),\epsilon\in\psi^{-1}(y)}\max\{\pi_{H(\delta)}(\epsilon),\pi_{G(\delta)}(\epsilon)\}\right)$$

$$\vee\left(\sup_{\delta\in(\sigma^{-1}(\delta')\cap B)-(\sigma^{-1}(\delta')\cap A),\,\epsilon\in\psi^{-1}(y)}\pi_{G(\delta)}(\epsilon)\right)$$

$$=\max\left\{\sup_{\delta\in(\sigma^{-1}(\delta')\cap A),\,\epsilon\in\psi^{-1}(y)}\pi_{H(\delta)}(\epsilon),\ \sup_{\delta\in(\sigma^{-1}(\delta')\cap B),\,\epsilon\in\psi^{-1}(y)}\pi_{G(\delta)}(\epsilon)\right\}$$

$$=\max\left\{\pi_{\psi(H)}(\delta')(y),\pi_{\psi(G)}(\delta')(y)\right\}=\pi_{I(\delta')}(y)$$

Similarly, we obtain $\eta_{\psi(O)}(\delta')(y)=\eta_{I(\delta')}(y)$. Therefore $\left((H,A)\cup_{\Delta}(G,B)\right)=f((H,A))\cup_{\Delta}f((G,B))$.

(4) Suppose that $(H,A)\cap_{\Delta}(G,B)=(H,A\cup B)$ and ($f\left((H,A)\cap_{\Delta}(G,B)\right)=(\psi(H),\sigma(A))\cap_{\Delta}(\psi(G),\sigma(B))=(I,\sigma(A)\cup\sigma(B))$. Then

$$f\left((H,A)\cap_{\Delta}(G,B)\right)=(\psi(O),\sigma(A\cup B))=(\psi(O),\sigma(A)\cup\sigma(B)).$$

For any $y\in Y$ and $\delta'\in\sigma(A)\cup\sigma(B)$, if $\psi^{-1}(y)\neq\varnothing$, then $\pi_I(\delta')(y)=\pi_{\psi(O)}(\delta')(y)=0$ and $\eta_I(\delta')(y)=\eta_{\psi(O)}(\delta')(y)=1$. Otherwise,

(i) If $\delta'\in\sigma(A)-\sigma(B)$, then $I(\delta')=\psi(H)(\delta')$. On the other hand, $\delta'\in\sigma(A)-\sigma(B)$ implies that there does not exist $\delta\in B$ such that $\sigma(\delta)=\delta'$. That is, for any $\delta\in\sigma^{-1}(\delta')\cap(A\cup B)$, we have $\delta\in\sigma^{-1}(\delta')\cap(A-B)$. Hence by Definition 18, we have

$$\pi_{\psi(O)}(\delta')(y)=\sup_{\delta\in\sigma^{-1}(\delta')\cap(A\cap B),\,\epsilon\in\psi^{-1}(y)}\pi_{O(\delta)}(\epsilon)=\sup_{\delta\in\sigma^{-1}(\delta')\cap(A-B),\,\epsilon\in\psi^{-1}(y)}\pi_{O(\delta)}(\epsilon)$$

$$=\sup_{\delta\in\sigma^{-1}(\delta')\cap(A-B),\,\epsilon\in\psi^{-1}(y)}\pi_{H(\delta)}(\epsilon)$$

$$\leq\min\left\{\sup_{\delta\in(\sigma^{-1}(\delta')\cap A),\,\epsilon\in\psi^{-1}(y)}\pi_{H(\delta)}(\epsilon),\ \sup_{\delta\in(\sigma^{-1}(\delta')\cap B),\,\epsilon\in\psi^{-1}(y)}\pi_{G(\delta)}(\epsilon)\right\}$$

$$=\min\left\{\pi_{\psi(H)}(\delta')(y),\pi_{\psi(G)}(\delta')(y)\right\}=\pi_{I(\delta')}(y)$$

Similarly, we obtain $\eta_{\psi(O)}(\delta')(y)\geq\eta_{I(\delta')}(y)$.

(ii) If $\delta'\in\sigma(B)-\sigma(A)$, analogous to *(i)*, we have

$\pi_{\psi(O)}(\delta')(y) = \pi_{I(\delta')}(y), \eta_{\psi(O)}(\delta')(y) = \eta_{I(\delta')}(y).$

(iii) If $\delta' \in \sigma(A) \cap \sigma(B),$ then

$$\pi_{\psi(O)}(\delta')(y) = \sup_{\delta \in \sigma^{-1}(\delta') \cap (A \cap B), \epsilon \in \psi^{-1}(y)} \pi_{O(\delta)}(\epsilon) = \pi_{\psi(O)}(\delta')(y)$$

$$= \sup_{\delta \in \sigma^{-1}(\delta') \cap (A \cap B), \epsilon \in \psi^{-1}(y)} \max\left\{\pi_{H(\delta)}(\epsilon), \pi_{G(\delta)}(\epsilon)\right\}$$

$$\leq \max\left\{\sup_{\delta \in (\sigma^{-1}(\delta') \cap A), \epsilon \in \psi^{-1}(y)} \pi_{H(\delta)}(\epsilon), \sup_{\delta \in (\sigma^{-1}(\delta') \cap B), \epsilon \in \psi^{-1}(y)} \pi_{G(\delta)}(\epsilon)\right\}$$

$$= \max\left\{\pi_{\psi(H)}(\delta')(y), \pi_{\psi(G)}(\delta')(y)\right\} = \pi_{I(\delta')}(y)$$

Similarly, we obtain $\eta_{\psi(O)}(\delta')(y) = \eta_{I(\delta')}(y).$ Therefore $f\left((H,A) \cap_{\Delta} (G,B)\right) \subseteq f((H,A)) \cap_{\Delta} f((G,B)).$

(7) Suppose that $(H,A) \subseteq (G,B).$ Then $A \subseteq B$ and for any $\delta \in A$ and $\epsilon \in \Upsilon,$ we have $\psi(A) \subseteq \psi(B).$ We have,

$$\pi_{\psi(H)}(\delta')(y) = \begin{cases} \sup_{\delta \in (\sigma^{-1}(\delta') \cap A), \epsilon \in \psi^{-1}(y)} \pi_{H(\delta)}(\epsilon), \text{if} \psi^{-1}(y) \neq \varnothing \\ 0 \qquad\qquad , \quad \text{otherwise} \end{cases}$$

$$\leq \begin{cases} \sup_{\delta \in (\sigma^{-1}(\delta') \cap B), \epsilon \in \psi^{-1}(y)} \pi_{H(\delta)}(\epsilon), \text{if} \psi^{-1}(y) \neq \varnothing \\ 0 \qquad\qquad , \quad \text{otherwise} \end{cases}$$

$$= \pi_{\psi(G)}(\delta')(y)$$

Similarly, $\eta_{\psi(H)}(\delta')(y) \geq \eta_{\psi(G)}(\delta')(y).$ Therefore $f((H,A)) \subseteq f((G,B)).$

Proposition 5 *Let* $f : FFSS(\Upsilon, \Delta) \to FFSS(Y, \Delta')$ *be a fermatean fuzzy soft mapping. Then for fermatean fuzzy soft sets* $(H,A),(G,B) \in FFSS(\Upsilon, \Delta),$ *we have,*

1. $f^{-1}(\tilde{0}_{(Y,\Delta')}) = \tilde{0}_{(\Upsilon,\Delta)}$

2. $f^{-1}(\tilde{1}_{(Y,\Delta')}) \subseteq \tilde{1}_{(\Upsilon,\Delta)}$
3. $f^{-1}\left((H,A) \cup_{\Delta} (G,B)\right) = f^{-1}((H,A)) \cup_{\Delta} f^{-1}((G,B))$
4. $f^{-1}\left((H,A) \cap_{\Delta} (G,B)\right) \subseteq f^{-1}((H,A)) \cap_{\Delta} f^{-1}((G,B))$
5. If $(H,A) \subseteq (G,B)$, then $f^{-1}((H,A)) \subseteq f^{-1}((G,B))$
6. $(H,A) \subseteq f^{-1}\left(f\left((H,A)\right)\right)$, then $f(f^{-1}\left((G,B)\right)) = (G,B) \cap_{\Delta} f(\tilde{1}_{\Upsilon})$

Proof. Straightforward

Definition 19 *Let* $(\Upsilon, \tilde{\tau}_1, \Delta)$ *and* $(Y, \tilde{\tau}_2, \Delta')$ *be two fermatean fuzzy soft topological spaces, a fermatean fuzzy soft mapping* $f = (\psi, \sigma) : FFSS(\Upsilon, \Delta) \to FFSS(Y, \Delta')$ *is called a fermatean fuzzy soft continuous if* $f^{-1}((G,B)) \in \tilde{\tau}_1$ *for all* $(G,B) \in \tilde{\tau}_2$

Example 4 *Let* $\Upsilon = \{\epsilon_1, \epsilon_2\}$, $Y = \{y_1, y_2\}$, $\Delta = \{\delta_1, \delta_2\}$ *and* $\Delta' = \{\delta_1', \delta_2'\}$.

$\tilde{\tau}_1 = \{\tilde{0}_{\Upsilon}, \tilde{1}_{\Upsilon}, (H_1,\Delta), (H_2,\Delta)\}$ where $(H_1,\Delta), (H_2,\Delta)$, fermatean fuzzy soft sets over Υ, defined as follows.

$$(H_1,\Delta) = \begin{Bmatrix} (\delta_1, \{(\epsilon_1, 0.8, 0.5), (\epsilon_2, 0.7, 0.4)\}) \\ (\delta_2, \{(\epsilon_1, 0.4, 0.3), (\epsilon_2, 0.5, 0.6)\}) \end{Bmatrix}$$

$$(H_2,\Delta) = \begin{Bmatrix} (\delta_1, \{(\epsilon_1, 0.6, 0.7), (\epsilon_2, 0.3, 0.5)\}) \\ (\delta_1, \{(\epsilon_1, 0.1, 0.5), (\epsilon_2, 0.2, 0.8)\}) \end{Bmatrix}$$

Then $\tilde{\tau}_1$ is a fermatean fuzzy soft topology over Υ and hence $(\Upsilon, \tilde{\tau}_1, \Delta)$ is a fermatean fuzzy soft topological space.

$\tilde{\tau}_2 = \{\tilde{0}_{(Y,\Delta')}, \tilde{1}_{(Y,\Delta')}, (G_1,\Delta'), (G_2,\Delta')\}$ where $(G_1,\Delta'), (G_2,\Delta')$, fermatean fuzzy soft sets over Y, defined as follows.

$$(G_1,\Delta') = \begin{Bmatrix} (\delta_1', \{(y_1, 0.7, 0.4), (y_2, 0.8, 0.5)\}) \\ (\delta_2', \{(y_1, 0.5, 0.6), (y_2, 0.4, 0.3)\}) \end{Bmatrix}$$

$$(G_2,\Delta) = \begin{Bmatrix} (\delta_1', \{(y_1, 0.3, 0.5), (y_2, 0.6, 0.7)\}) \\ (\delta_2', \{(y_1, 0.2, 0.8), (y_2, 0.1, 0.5)\}) \end{Bmatrix}$$

Then $\tilde{\tau}_2$ is a fermatean fuzzy soft topology over Y and hence $(Y, \tilde{\tau}_1, \Delta')$

is a fermatean fuzzy soft topological space.

If $f=(\psi,\sigma):FFSS(\Upsilon,\Delta)\to FFSS(Y,\Delta')$ defined as follows:

$$\psi(\epsilon_1)=y_2 \qquad \sigma(\delta_1)=\delta_1'$$
$$\psi(\epsilon_2)=y_1 \qquad \sigma(\delta_2)=\delta_2'$$

Then it is easy to verify that $f^{-1}((G,\Delta'))\in\tilde{\tau}_1$ for all $(G,\Delta')\in\tilde{\tau}_2$. Thus $f=(\psi,\sigma)$ is a fermatean fuzzy soft continuous mapping.

Theorem 4 *Let $(\Upsilon,\tilde{\tau}_1,\Delta)_f$ and $(Y,\tilde{\tau}_2,\Delta')_f$ be two fermatean fuzzy soft topological spaces, $f=(\psi,\sigma):FFSS(\Upsilon,\Delta)\to FFSS(Y,\Delta')$ be a fermatean fuzzy soft continuous mapping. If $(G,\Delta')\in FFSS(Y,\Delta')$ is a fermatean fuzzy soft closed set, then $f^{-1}((G,\Delta'))\in FFSS(\Upsilon,\Delta)$ is a fermatean fuzzy soft closed set.*

Proof. Let $f:FFSS(\Upsilon,\Delta)\to FFSS(Y,\Delta')$ be a fermatean fuzzy soft continuous mapping on fermatean fuzzy soft topological space $(\Upsilon,\tilde{\tau}_1,\Delta)_f$ and (G,Δ') be any fermatean fuzzy soft closed set in Y. Then, since $f^{-1}((G,\Delta')^c)=(\ f^{-1}((G,\Delta')))^c$ and $(G,\Delta')^c$ is fermatean fuzzy soft open set are obtained. Therefore $f^{-1}((G,\Delta')))^c$ is fermatean fuzzy soft openset in Υ. This means that $f^{-1}((G,\Delta'))$ is a fermatean fuzzy soft closed set in Υ.

Conversely, suppose that $f^{-1}((G,\Delta'))$ is a fermatean fuzzy soft closed set in Υ whenever (G,Δ') is a fermatean fuzzy soft closed set in Y. For any fermatean fuzzy soft open set (H,Δ') in Y. $f^{-1}((H,\Delta')^c)=f^{-1}((H,\Delta')))^c$. From the hypothesis, $f^{-1}((H,\Delta')^c)$ is a fermatean fuzzy soft closed set in Υ. Therefore $f^{-1}((H,\Delta'))$ is a fermatean fuzzy soft continuous mapping on fermatean fuzzy soft topological space $(\Upsilon,\tilde{\tau}_1,\Delta)_f$.

Theorem 5 *Let $(\Upsilon,\tilde{\tau}_1,\Delta)_f$ and $(Y,\tilde{\tau}_2,\Delta')_f$ be two fermatean fuzzy soft topological spaces and $f=(\psi,\sigma):FFSS(\Upsilon,\Delta)\to FFSS(Y,\Delta')$ be a fermatean fuzzy soft continuous mapping. Then f is a fermatean fuzzy soft continuous mapping on fermatean fuzzy soft topological space $(\Upsilon,\tilde{\tau}_1,\Delta)_f$ if*

and only if $f^{-1}(fint(G,\Delta')) \subseteq fint\left(f^{-1}((H,\Delta'))\right)$ *for each* $(G,\Delta') \in FFSS(Y,\Delta')$.

Proof. $(\Rightarrow)$ Suppose that f be a fermatean fuzzy soft continuous mapping and $(G,\Delta') \in FFSS(Y,\Delta')$. Then $f^{-1}(fint(G,\Delta')^o) \in \tilde{\tau}_1$ and from $fint(G,\Delta') \subseteq (G,\Delta')$ we have $f^{-1}(fint(G,\Delta')) \subseteq f^{-1}((G,\Delta'))$. Because of $fint(f^{-1}((G,\Delta')))$ is a largest fermatean fuzzy soft open set contained by $f^{-1}((G,\Delta'))$,

$$f^{-1}(fint(G,\Delta')) \subseteq fint(f^{-1}((G,\Delta'))).$$

$(\Leftarrow)$ Conversely, suppose that $f^{-1}(fint(G,\Delta')) \subseteq fint(f^{-1}((G,\Delta')))$, for all $(G,\Delta') \in FFSS(Y,\Delta')$. If $(G,\Delta') \in \tilde{\tau}_2$, then we have, $f^{-1}((G,\Delta')) = f^{-1}(fint(G,\Delta')) \subseteq fint(f^{-1}((G,\Delta'))) \subseteq f^{-1}((G,\Delta'))$. So, $f^{-1}((G,\Delta')) \in \tilde{\tau}_1$. It means that, f is fermatean fuzzy soft continuous mapping.

Theorem 6 *Let* $(\Upsilon,\tilde{\tau}_1,\Delta)_f$ *and* $(Y,\tilde{\tau}_2,\Delta')_f$ *be two fermatean fuzzy soft topological spaces and* $f : FFSS(\Upsilon,\Delta) \to FFSS(Y,\Delta')$ *be a fermatean fuzzy soft continuous mapping. Then* $f = (\psi,\sigma)$ *is a fermatean fuzzy soft continuous mapping on fermatean fuzzy soft topological space* $(\Upsilon,\tilde{\tau}_1,\Delta)_f$ *if and only if* $f(fcl(H,\Delta)) \subseteq fcl(f((H,\Delta)))$ *for* $(H,\Delta) \in FFSS(\Upsilon,\Delta)$.

Proof. $(\Rightarrow)$ Suppose that f be a fermatean fuzzy soft continuous mapping on fermatean fuzzy soft topological space $(\Upsilon,\tilde{\tau}_1,\Delta)_f$ and $(H,\Delta) \in FFSS(\Upsilon,\Delta)$. Since $fcl(f((H,\Delta)))$ is a fermatean fuzzy soft closed set in, $f^{-1}(fcl(f((H,\Delta))))$ is a fermatean fuzzy soft closed set in Υ. Then $fcl(f^{-1}(fcl(f((H,\Delta))))) = f^{-1}(fcl(f((H,\Delta))))$ and $f((H,\Delta)) \subseteq fcl(f((H,\Delta)))$. Thus $(H,\Delta) \subseteq f^{-1}(f((F,\Delta))) \subseteq f^{-1}\left(fcl(f((H,\Delta)))\right)$ then, we obtain $(H,\Delta) \subseteq fcl(f^{-1}(fcl(f((H,\Delta))))) \subseteq f^{-1}(fcl(f((H,\Delta))))$. Hence $f(fcl(H,\Delta)) \subseteq fcl(f((H,\Delta)))$.

($\Leftarrow$) Suppose that $f(fcl(H,\Delta))\subseteq fcl(f((H,\Delta)))$ for every $(H,\Delta)\in FFSS(\Upsilon,\Delta)$ and (G,Δ') be any fermatean fuzzy soft closed set in Y. So $fcl(G,\Delta')=(G,\Delta')$. From the hypothesis, $f(fcl(f^{-1}((G,\Delta'))))\subseteq fcl(f(f^{-1}((G,\Delta'))))\subseteq fcl(G,\Delta')=(G,\Delta')$ is obtained. Hence $fcl(f^{-1}((G,\Delta')))=f^{-1}((G,\Delta'))$ and $f^{-1}((G,\Delta'))\subseteq fcl(f^{-1}((G,\Delta')))$. That is, $fcl(f^{-1}((G,\Delta')))=f^{-1}((G,\Delta'))$ and, so $f^{-1}((G,\Delta'))$ is a fermatean fuzzy soft closed set in Υ. Thus f is a fermatean fuzzy soft continuous mapping on fermatean fuzzy soft topological space $(\Upsilon,\tilde{\tau}_1,\Delta)_f$.

REFERENCES

1. Ali, M. I., Feng, F., Liu, X., Min, W. K., & Shabir, M. (2009). On some new operations in soft set theory. *Computers & Mathematics with Applications*, *57*(9), 1547-1553.

2. Atanassov, K. T., & Stoeva, S. (1986). Intuitionistic fuzzy sets. *Fuzzy sets and Systems*, *20*(1), 87-96.

3. Athira, T. M., John, S. J., & Garg, H. (2019). Entropy and distance measures of Pythagorean fuzzy soft sets and their applications. *Journal of Intelligent & Fuzzy Systems*, *37*(3), 4071-4084.

4. Bayramov, S., & Gunduz, C. (2014). On intuitionistic fuzzy soft topological spaces. *TWMS J Pure Appl Math*, *5*(1), 66-79.

5. Chang, C. L. (1968). Fuzzy topological spaces. *Journal of mathematical Analysis and Applications*, *24*(1), 182-190.

6. Çoker, D. (1997). An introduction to intuitionistic fuzzy topological spaces. *Fuzzy sets and systems*, *88*(1), 81-89.

7. Liu, D., Liu, Y., & Chen, X. (2019). Fermatean fuzzy linguistic set and its application in multicriteria decision making. *International Journal of Intelligent Systems*, *34*(5), 878-894.

8. Liu, D., Liu, Y., & Wang, L. (2019). Distance measure for Fermatean fuzzy linguistic term sets based on linguistic scale function: An illustration of the TODIM and TOPSIS methods. *International Journal of Intelligent Systems*, *34*(11), 2807-2834.

9. Guleria, A., & Bajaj, R. K. (2019). On Pythagorean fuzzy soft matrices, operations and their applications in decision making and medical diagnosis. *Soft Computing*, *23*, 7889-7900.

10. Hussain, A., Ali, M. I., & Mahmood, T. (2020). Pythagorean fuzzy soft rough sets and their applications in decision-making. *Journal of Taibah University for Science*, *14*(1), 101-113.

11. Ibrahim, H. Z. (2022). Fermatean fuzzy topological spaces. *Journal of applied mathematics & informatics*, *40*(1_2), 85-98.

12. Karata, S., & Akdag, M. (2014). On intuitionistic fuzzy soft continuous mappings. *Journal of New Results in Science*, *3*(4), 55-70.

13. Kirisci, M. (2021). Fermatean fuzzy soft set with enttropy measure. *Journal of Ambient Intelligence & Humanized Computing*.

14. Maji, P. K., Biswas, R., & Roy, A. R. (2001). Fuzzy soft sets, *Journal of Fuzzy Mathematics* 9(3), 589–602.

15. Maji, P. K., Biswas, R., & Roy, A. R. (2001). Intuitionistic fuzzy soft sets. *Journal of fuzzy mathematics*, *9*(3), 677-692.
16. Maji, P. K., Biswas, R., & Roy, A. R. (2003). Soft set theory. *Computers & mathematics with applications*, *45*(4-5), 555-562.

17. Molodtsov, D. (1999). Soft set theory—first results. *Computers & mathematics with applications*, *37*(4-5), 19-31.

18. Olgun, M., Ünver, M., & Yardımcı, Ş. (2019). Pythagorean fuzzy topological spaces. *Complex & Intelligent Systems*, *5*(2), 177-183.

19. Osmanoglu, I., & Tokat, D. (2013). On intuitionistic Fuzzy soft topology. *General mathematics notes*, *19*(2), 59-70.

20. Pawlak, Z. (1982). Rough sets. *International journal of computer & information sciences*, *11*, 341-356.

21. Peng, X., & Yang, Y. (2015). Some results for Pythagorean fuzzy sets. *International Journal of Intelligent Systems*, *30*(11), 1133-1160.

22. Peng, X. D., Yang, Y., Song, J., & Jiang, Y. (2015). Pythagorean fuzzy soft set and its application. *Computer engineering*, *41*(7), 224-229.

23. Peng, X. (2019). New operations for interval-valued Pythagorean fuzzy set. *Scientia iranica*, *26*(2), 1049-1076.

24. Salsabeela, V., & John, S. J. (2021, March). TOPSIS techniques on Fermatean fuzzy soft sets. In AIP conference proceedings (Vol. 2336, No. 1, p. 040022). AIP Publishing LLC.

25. Senapati, T., & Yager, R. R. (2020). Fermatean fuzzy sets. J*ournal of Ambient Intelligence and Humanized Computing*, 11, 663-674.

26. Senapati, T., & Yager, R. R. (2019). Some new operations over Fermatean fuzzy numbers and application of Fermatean fuzzy WPM in multiple criteria decision making. *Informatica*, *30*(2), 391-412.

27. Senapati, T., & Yager, R. R. (2019). Fermatean fuzzy weighted averaging/geometric operators and its application in multi-criteria decision-making methods. *Engineering Applications of Artificial Intelligence*, *85*, 112-121.

28. Shabir, M., & Naz, M. (2011). On soft topological spaces. *Computers & Mathematics with Applications*, *61*(7), 1786-1799.

29. Shahzadi, G., & Akram, M. (2019). Hypergraphs based on Pythagorean fuzzy

soft model. *Mathematical and Computational Applications*, *24*(4), 100.

30. Sivadas, A., & John, S. J. (2021). Fermatean fuzzy soft sets and its applications. In Computational Sciences-Modelling, Computing and Soft Computing: First International Conference, CSMCS 2020, Kozhikode, Kerala, India, September 10-12, 2020, Revised Selected Papers 1 (pp. 203-216). Springer Singapore.

31. Sivadas, A., & John, S. J. (2023, June). Fermatean fuzzy soft topological spaces. In AIP Conference Proceedings (Vol. 2875, No. 1). AIP Publishing.

32. Tanay, B., & Kandemir, M. B. (2011). Topological structure of fuzzy soft sets. *Computers & Mathematics with Applications*, *61*(10), 2952-2957.

33. Yager, R. R. (2013, June). Pythagorean fuzzy subsets. In *2013 joint IFSA world congress and NAFIPS annual meeting (IFSA/NAFIPS)* (pp. 57-61). IEEE.

34. Yager, R. R., & Abbasov, A. M. (2013). Pythagorean membership grades, complex numbers, and decision making. *International Journal of Intelligent Systems*, *28*(5), 436-452.

35. Yin, Y., Li, H., & Jun, Y. B. (2012). On algebraic structure of intuitionistic fuzzy soft sets. *Computers & Mathematics with Applications*, *64*(9), 2896-2911.

36. Zadeh, L. A. (1965). Fuzzy sets. *Information and control*, *8*(3), 338-353.

37. Zeng, S., Chen, J., & Li, X. (2016). A hybrid method for Pythagorean fuzzy multiple-criteria decision making. *International Journal of Information Technology & Decision Making*, *15*(02), 403-422.

Chapter 10

A NOTE ON TZITZEICA CURVES IN EUCLIDEAN 4-SPACE $\mathbb{E}^4$*

Emrah TUNÇ[1]

Bengü BAYRAM[2]

1 Ph.D. , Balikesir University, Faculty of Arts and Sciences Department of Mathematics, ORCID: 0000-0002-7630-0996

2 Prof. Dr., Balıkesir University, Faculty of Arts and Sciences Department of Mathematics, ORCID: 0000-0002-1237-5892

* Produced from the doctoral thesis titled "A Characterization of Tzitzeica Curves and Surfaces (2021)"

1. Introduction

Gheorgha Tzitzeica, Romanian mathematician (1872-1939), in 1912, at the Conference in Cambridge, lectured about so-called general method as follows: “Let be given a class of figures in plane or space (curves, surfaces, congruences). In order to study their infinitesimal properties which are invariant with respect to the transformations of a group, we have to find certain system of coordinates and determine an arbitrary element of the figure. Then we have to get an equation or a system of differential equations satisfied by the coordinates of an arbitrary element of a figure and thus of all transformed figures”. By this method Tzitzeica already studied curves, surfaces, webs of curves and congruences and obtained important centro-affine, affine, projective and conformal properties of them. For this reason Tzitzeica should be considered as a founder of centro-affine, affine, projective and conformal geometries [4].

Tzitzeica introduced a class of surfaces [13], nowadays called Tzitzeica surfaces in 1907 and a class of curves [14], called Tzitzeica curves in 1911. A Tzitzeica curve in $\mathbb{E}^3$ is a spatial curve $x = x(s)$ with the Frenet frame $\{T, N_1, N_2\}$ and Frenet curvatures $\{k_1, k_2\}$, for which the ratio of its torsion k_2 and the square of the distance d_{osc} from the origin to the osculating plane at an arbitrary point *x(s)* of the curve is constant, i.e., $\frac{k_2}{{d_{osc}}^2} = a$, where $d_{osc} = \langle N_2, x\rangle$ and $a \neq 0$ is a real constant, N_2 is the binormal vector field of *x*.

A Tzitzeica surface in $\mathbb{E}^3$ is a spatial surface *M* given with the parametrization *X(u,v)*, for which the ratio of its Gaussian curvature *K* and the distance d_{tan} from the origin to the tangent plane at any arbitrary point of the surface is constant, i.e., $\frac{K}{{d_{tan}}^4} = a_1$, for a constant $a_1 \neq 0$. The ortogonal distance from the origin to the tangent plane is defined by $d_{tan} = \langle X, N\rangle$ where *X* is the position vector of surface and *N* is unit normal vector

field of the surface. In [1, 2], authors studied Tz-curve and Tz-surfaces in Euclidean 3-Space $\mathbb{E}^3$.

Tzitzeica curves in Euclidean 4-space $\mathbb{E}^4$ have been determined as three types.

Definition 1.1 Let $x: I \subset \mathbb{R} \to \mathbb{E}^4$ be a unit speed curve in Euclidean 4-space $\mathbb{E}^4$. If the ratio of its second Frenet curvature k_2 and the square of the distance $d_{\{T,N_1,N_3\}}$ from the origin to the hyperplane spanned by $\{T, N_1, N_3\}$ at an arbitrary point $x(s)$ of the curve is constant, i.e.,

$$\frac{k_2}{d^2_{\{T,N_1,N_3\}}} = a_1, \quad (a_1 \neq 0 \text{ is a real constant}) \tag{1}$$

where

$$d_{\{T,N_1,N_3\}} = \langle x, N_2 \rangle \tag{2}$$

then the curve $x = x(s)$ called *first type Tzitzeica curve.* If the ratio of its first Frenet curvature k_1 and the square of the distance $d_{\{T,N_2,N_3\}}$ from the origin to the hyperplane spanned by $\{T, N_2, N_3\}$ at an arbitrary point $x(s)$ of the curve is constant, i.e.,

$$\frac{k_1}{d^2_{\{T,N_2,N_3\}}} = a_2, \qquad (a_2 \neq 0 \text{ is a real constant}) \tag{3}$$

where

$$d_{\{T,N_2,N_3\}} = \langle x, N_1 \rangle \tag{4}$$

then the curve $x = x(s)$ called *second type Tzitzeica curve.* If the ratio of its third Frenet curvature k_3 and the square of the distance $d_{\{T,N_1,N_2\}}$ from the origin to the hyperplane spanned by $\{T, N_1, N_2\}$ at an arbitrary point $x(s)$ of the curve is constant, i.e.,

$$\frac{k_3}{d^2_{\{T,N_1,N_2\}}} = a_3 \ , \ (a_3 \neq 0 \text{ is a real constant}) \tag{5}$$

where

$$d_{\{T,N_1,N_2\}} = \langle x, N_3 \rangle \tag{6}$$

then the curve $x = x(s)$ called *third type Tzitzeica curve* [12].

In the present study, we investigate the conditions for some specially defined curves to be Tzitzeica curves under these three types in Euclidean 4-space $\mathbb{E}^4$ whose position vector $x = x(s)$ satisfies the parametric equation

$$x(s) = m_0(s)T(s) + m_1(s)N_1(s) + m_2(s)N_2(s) + m_3(s)N_3(s) \quad (7)$$

for some differentiable functions $m_i(s), 0 \leq i \leq 3$, where $\{T, N_1, N_2, N_3\}$ is the Frenet frame of *x*. And we express these curves in terms of their Frenet curvatures k_1, k_2 and k_3.

2. Preliminaries

Let $x: I \subset \mathbb{R} \to \mathbb{E}^4$ be a unit speed curve in Euclidean 4-space $\mathbb{E}^4$. Let us denote $T(s) = x'(s)$ and call $T(s)$ a unit tangent vector of *x* at *s*. We denote the first Serret-Frenet curvature of *x* by $k_1(s) = \|x''(s)\|$. If $k_1(s) \neq 0$, then the unit principal normal vector $N_1(s)$ of the curve *x* at *s* is given by $T'(s) = k_1(s)N_1(s)$. If $k_2(s) \neq 0$, then the unit second principal normal vector $N_2(s)$ of the curve *x* at *s* is given by ${N_1}'(s) + k_1(s)T(s) = k_2(s)N_2(s)$, where k_2 is the second Serret-Frenet curvature of *x*. ${N_2}'(s) + k_2(s)N_1(s) = k_3(s)N_3(s)$, where k_3 is the third Serret-Frenet curvature of *x*. Then we have the Serret-Frenet formulae [7]:

$$T'(s) = k_1(s)N_1(s)$$

$${N_1}'(s) = -k_1(s)T(s) + k_2(s)N_2(s)$$

$${N_2}'(s) = -k_2(s)N_1(s) + k_3(s)N_3(s)$$

$${N_3}'(s) = -k_3(s)N_2(s). \quad (8)$$

If the Serret-Frenet curvatures $k_1(s), k_2(s)$ and $k_3(s)$ of *x* are constant functions then *x* is called a *screw line* or a *helix* [8]. Since these curves are the traces of 1-parameter family of the groups of Euclidean transformations, F. Klein and S. Lie called them *W-curves* [9]. If the tangent vector *T* of the

curve x makes a constant angle with a unit vector U of $\mathbb{E}^4$ then this curve is called a *general helix* (or inclined curve) in $\mathbb{E}^4$ [11].

Let $x: I \subset \mathbb{R} \to \mathbb{E}^4$ be a unit speed curve in Euclidean 4-space $\mathbb{E}^4$. Position vector of $x = x(s)$ satisfies (7) vectorial equation for some differentiable functions $m_i(s), 0 \leq i \leq 3$.

Differentiating (7) with respect to arclength parameter s and using Serret-Frenet equations (8), we obtain

$$x'(s) = \big(m_0'(s) - m_1(s)k_1(s)\big)T(s)$$

$$+\big(m_0(s)k_1(s) + m_1'(s) - m_2(s)k_2(s)\big)N_1(s)$$

$$+\big(m_1(s)k_2(s) + m_2'(s) - m_3(s)k_3(s)\big)N_2(s)$$

$$+(m_2(s)k_3(s) + m_3'(s))N_3(s)$$

$$= T(s).$$

It follows that

$$m_0' - k_1 m_1 = 1,$$

$$m_1' + k_1 m_0 - k_2 m_2 = 0,$$

$$m_2' + k_2 m_1 - k_3 m_3 = 0,$$

$$m_3' + k_3 m_2 = 0. \tag{9}$$

Furthermore, for a *first type Tzitzeica curve* in $\mathbb{E}^4$

$$m_0' - k_1 m_1 = 1$$

$$m_1' + k_1 m_0 - k_2 m_2 = 0$$

$$m_2' + k_2 m_1 - k_3 m_3 = 0$$

$$m_3' + k_3 m_2 = 0$$

$$k_2' m_2 + 2k_2^2 m_1 - 2k_2 k_3 m_3 = 0, \tag{10}$$

for a *second type Tzitzeica curve* in $\mathbb{E}^4$

$$\begin{aligned} &m_0' - k_1 m_1 = 1 \\ &m_1' + k_1 m_0 - k_2 m_2 = 0 \\ &m_2' + k_2 m_1 - k_3 m_3 = 0 \\ &m_3' + k_3 m_2 = 0 \\ &k_1' m_1 + 2k_1^2 m_0 - 2k_1 k_2 m_2 = 0 \end{aligned} \tag{11}$$

and for a *third type Tzitzeica curve* in $\mathbb{E}^4$

$$\begin{aligned} &m_0' - k_1 m_1 = 1 \\ &m_1' + k_1 m_0 - k_2 m_2 = 0 \\ &m_2' + k_2 m_1 - k_3 m_3 = 0 \\ &m_3' + k_3 m_2 = 0 \\ &k_3' m_3 + 2k_3^2 m_2 = 0 \end{aligned} \tag{12}$$

holds [12].

For a unit speed curve $x: I \subset \mathbb{R} \to \mathbb{E}^4$, the hyperplanes at each point of $x(s)$ which are spanned by $\{T, N_1, N_3\}, \{T, N_2, N_3\}$ are known as the *first osculating hyperplane* and the *second osculating hyperplane*, respectively. If the position vector x lies on its first (resp. second) osculating hyperplane then $x(s)$ is called *osculating curve of first (resp. second) kind* [10]. If the position vector x lies on its hyperplane spanned by $\{T, N_1, N_2\}$ then $x(s)$ is called *osculating curve of third kind*.

For a regular curve $x(s)$, the position vector x can be decomposed into its tangential and normal components at each point, i.e., $x = x^T + x^N$.

A curve in Euclidean 4-space $\mathbb{E}^4$ is called *T-constant* (resp. *N-constant*) if the tangential component x^T (resp. the normal component x^N) of its position vector x is of constant lenght [3].

For a unit speed *T-constant* curve in Euclidean 4-space $\mathbb{E}^4$, it is called *second type* (resp. *first type*) if $\|x^T\| = \lambda$ (resp. $\|x^T\| = 0$) which is non-zero differentiable function. Similarly, for a unit speed *N-constant* curve in Euclidean 4-space $\mathbb{E}^4$, it is called *second type* (resp. *first type*) if $\|x^N\| = \mu$ (resp. $\|x^N\| = 0$) which is non-zero differentiable function [4,5].

3. The First Type Tzitzeica Curves in Euclidean 4-Space $\mathbb{E}^4$

Proposition 3.1 Let $x: I \subset \mathbb{R} \to \mathbb{E}^4$ be a unit speed first type Tzitzeica curve in Euclidean 4-space $\mathbb{E}^4$ whose position vector satisfies parametric equation (7). If x is first type T-constant curve ($m_0 = 0$) then we get

$$m_1 = \frac{-1}{k_1}$$

$$m_2 = \frac{c_1 k_3'}{(k_2^2 + k_3^2)^{\frac{3}{2}}}$$

$$m_3 = \frac{c_1}{(k_2^2 + k_3^2)^{\frac{1}{2}}} \tag{13}$$

where $k_2 > 0$ is constant and $c_1 \neq 0$ integral constant.

Proof Let x be first type T-constant curve ($m_0 = 0$) then $m_1 = \frac{-1}{k_1}$ is obtained from the first equation of (10). Taking m_1', m_2', m_3' from the second, the third and the fourth equation of (10) respectively, and substituting these equalities in the derivative of the fifth equation of (10) with $m_1 = \frac{-1}{k_1}$, then we obtain

$$m_2\left(k_2'' + 2k_2^3 + 2k_2{k_3}^2\right) + m_3(-{k_2}'k_3 - 2k_2{k_3}') = \frac{3k_2{k_2}'}{k_1}.$$

If the expression $m_2 = \frac{-{m_3}'}{k_3}$ obtained from the fourth equation of (10) is written into the above equation and rearranged that $k_2 > 0$ (constant), we get ${m_3}'\left(k_2^2 + {k_3}^2\right) = -m_3(k_3{k_3}')$. After solving this differential equation, $m_3 = \frac{c_1}{\left(k_2^2+k_3^2\right)^{\frac{1}{2}}}$ is found, where c_1 non-zero integral constant, and then taking the derivative of m_3, ${m_3}' = \frac{-c_1k_3{k_3}'}{\left(k_2^2+k_3^2\right)^{\frac{3}{2}}}$ is obtained. Substituting ${m_3}'$ into the fourth equation of (10) then, $m_2 = \frac{c_1{k_3}'}{\left(k_2^2+k_3^2\right)^{\frac{3}{2}}}$ is obtained and the proof is complete.

Proposition 3.2 Let $x: I \subset \mathbb{R} \to \mathbb{E}^4$ be a unit speed first type Tzitzeica curve with the constant Frenet curvatures k_1 and k_3 whose position vector satisfies parametric equation (7) in Euclidean 4-space $\mathbb{E}^4$. If x is second type T-constant curve ($m_0 \neq 0$ constant) then the equations

$$m_1 = \frac{-1}{k_1}$$

$$m_2 = -\frac{m_3'}{k_3}$$

$$m_3 = e^{-\left\{\frac{\left(\frac{2m_0k_1^2}{3}k_3^2\right)s}{\frac{4{m_0}^2k_1^4}{9}+2k_3^2} - \frac{\frac{2m_0k_1^2}{3}k_3^2}{\left(\frac{4{m_0}^2k_1^4}{9}+2k_3^2\right)\left(-\frac{4m_0k_1^2}{3}\right)}.log\left[\frac{2}{c_2^2}e^{\left(-\frac{4m_0k_1^2}{3}\right)s} + \frac{4{m_0}^2k_1^4}{9}+2k_3^2\right]+C\right\}} \quad (14)$$

are hold where $k_2 = \frac{e^{\frac{-2m_0k_1^2}{3}s}}{c_2}$.

Proof Let x be second type T-constant curve ($m_0 = c \neq 0$ constant). Then ${m_0}' = 0$. Also $m_1 = \frac{-1}{k_1}$ is obtained from the first equation of (10). Taking m_1', m_2', m_3' from the second, the third and the fourth equation of (10) respectively, and substituting these equalities in the derivative of the fifth equation of (10) with $m_1 = \frac{-1}{k_1}$, then we obtain

$$m_2\left(k_2'' + 2k_2^3 + 2k_2{k_3}^2\right) + m_3(-{k_2}'k_3 - 2k_2{k_3}') = \frac{3k_2k_2'}{k_1} + 2ck_1k_2^2.$$

If the expression $m_2 = -\frac{m_3'}{k_3}$ obtaining from the fourth equation of (10) is written into the above equation and rearranged. If the right-hand side of the equation is zero and the arrangement is made, $-k_2k_3(3k_2' + 2ck_2k_1^2) = 0$ is obtained. Let k_2 and k_3 be non-zero and $3k_2' + 2ck_1^2k_2 = 0$. If $k_1 > 0\ (= c_1)$ is assumed constant and this differential equation is solved, $k_2 = \frac{e^{\frac{-2cc_1^2}{3}s}}{c_2}$ is obtained. We get

$$\frac{m_3'}{m_3} = -\frac{{k_2}'{k_3}^2 + 2k_2k_3{k_3}'}{k_2'' + 2k_2^3 + 2k_2{k_3}^2}.$$

If $k_3 > 0\ (= c_3)$ is assumed constant and this differential equation is solved,

$$m_3 = e^{-\left\{\frac{\left(\frac{2m_0k_1^2}{3}k_3^2\right)s}{\frac{4{m_0}^2k_1^4}{9}+2k_3^2} - \frac{\frac{2m_0k_1^2}{3}k_3^2}{\left(\frac{4{m_0}^2k_1^4}{9}+2k_3^2\right)\left(-\frac{4m_0k_1^2}{3}\right)}.log\left[\frac{2}{c_2^2}e^{\left(-\frac{4m_0k_1^2}{3}\right)s} + \frac{4{m_0}^2k_1^4}{9}+2k_3^2\right]+C\right\}}$$

is obtained.

Proposition 3.3 Let $x: I \subset \mathbb{R} \to \mathbb{E}^4$ be a unit speed first type Tzitzeica curve whose position vector satisfies parametric equation (7) in Euclidean 4-space

$\mathbb{E}^4$. If x is first type N-constant curve or second type N-constant curve ($m_1^2 + m_2^2 + m_3^2 = 0$ *or* $m_1^2 + m_2^2 + m_3^2 = c$ constant) then the equations

$$m_0 = c_3 \frac{1}{k_1}\,, \qquad c_3 = \frac{c(k_2^2+k_3^2)}{k_2} \text{ (constant)}$$

$$m_1 = \frac{k_3}{k_2}(c_1 s + c_2)\,, \qquad c_1 = -ck_3 \text{ (constant)}, \qquad c_2 = \text{integral constant}$$

$$m_2 = c \text{ (constant)}$$

$$m_3 = c_1 s + c_2\,, \qquad c_1 = -ck_3 \text{ (constant)}, \quad c_2 = \text{ integral constant} \quad (15)$$

are satisfied, where $k_2 \neq 0$ and $k_3 \neq 0$ are constants.

Proof From derivative of $m_1^2 + m_2^2 + m_3^2 = 0$, we get $m_1 m_1{}' + m_2 m_2{}' + m_3 m_3{}' = 0$. Using fifth equation of (10) and substituting m_2^2 then we get

$$m_1^2\left(-{k_2}'^2 + 4k_2^4\right) + m_3^2\left(-{k_2}'^2 + 4k_2^2 k_3^2\right) + 4k_2^2 k_2{}' m_1 m_2 - 4k_2 k_2{}' k_3 m_2 m_3 - 8k_2^3 k_3 m_1 m_3 = 0.$$

Taking the derivative of this equation and substituting $m_1 m_1{}' = -m_2 m_2{}' - m_3 m_3{}'$ and taking $k_2 \neq 0$ and $k_3 \neq 0$ as constants,

$$8k_2^2(k_2 m_1{}' - k_3 m_3{}')(k_2 m_1 - k_3 m_3) = 0$$

is obtained,which completes the proof.

Proposition 3.4 Let $x: I \subset \mathbb{R} \to \mathbb{E}^4$ be a unit speed first type Tzitzeica curve whose position vector satisfies parametric equation (7) in Euclidean 4-space $\mathbb{E}^4$. If x is second type osculating curve ($m_1 = 0$) then we get $k_1 = c_2(s + c_1)$ and $e^{\int (s+c_1)k_3^2 ds} = \frac{k_3^2}{(s+c_1)^2}$ where $k_2 \neq 0$ is constant, c_1, c_2 are integral constants.

Proof Let x be second type osculating curve. Then from the first equation of (10) we obtain $m_0 = s + c_1$ (c_1 constant). Substituting m_0 in the second

equation of (10) we get $m_2 = \frac{k_1}{k_2}(s + c_1)$. Taking the derivative of m_2 and substituting in the third equation of (10), we get

$$m_3 = \frac{\left(\frac{k_1}{k_2}\right)'(s + c_1)}{k_3} + \frac{k_1}{k_2 k_3}.$$

If values of m_2, m_3 are written in the fifth of (10) with the constant $k_2 \neq 0$, $-2k_1'(s + c_1) - 2k_1 = 0$ is obtained. If these differential equations are solved, we find $k_1 = c_2(s + c_1)$ (c_2 constant). If these expressions are written in the fourth of (10) and the obtained differential equation is solved, the relation

$$e^{\int (s+c_1)k_3^2 ds} = \frac{k_3^2}{(s + c_1)^2}$$

is obtained.

Proposition 3.5 Let $x: I \subset \mathbb{R} \to \mathbb{E}^4$ be a unit speed first type Tzitzeica curve whose position vector satisfies parametric equation (7) in Euclidean 4-space $\mathbb{E}^4$. If x is third type osculating curve ($m_3 = 0$) then, the equations $k_3 = 0$ and

$$m_0 = \frac{c k_2^{\frac{3}{2}}}{k_1} + \frac{c k_2''}{2k_2^{\frac{3}{2}} k_1} - \frac{3c k_2'^2}{4k_2^{\frac{5}{2}} k_1}$$

$$m_1 = \frac{-c k_2'}{2k_2^{\frac{3}{2}}}$$

$$m_2 = c k_2^{\frac{1}{2}} \tag{16}$$

hold.

Proof Let x be a third type osculating curve. Since $m_2 \neq 0$, from the fourth equation of (10) we get $k_3 = 0$. From the fifth equation of (10), $m_1 = \frac{-k_2'}{2k_2^2} m_2$. In the third equation of (10), substituting the value of m_1, we get $\frac{m_2'}{m_2} = \frac{k_2'}{2k_2}$. If these differential equations are solved, $m_2 = ck_2^{\frac{1}{2}}$ (c is integral constant) is obtained. In the second equation of (10), if we substitute the values of m_1' and m_2, we find

$$m_0 = \frac{ck_2^{\frac{3}{2}}}{k_1} + \frac{ck_2''}{2k_2^{\frac{3}{2}}k_1} - \frac{3ck_2'^{\,2}}{4k_2^{\frac{5}{2}}k_1}.$$

Corollary 3.6 Let $x: I \subset \mathbb{R} \to \mathbb{E}^4$ be a unit speed first type Tzitzeica and third type osculating curve whose position vector satisfies parametric equation (7) in Euclidean 4-space $\mathbb{E}^4$. If $k_2 \neq 0$ is constant, then the equations $m_0 = \frac{ck_2^{\frac{3}{2}}}{k_1}$, $m_1 = 0$, $m_2 = ck_2^{\frac{1}{2}}$, $k_1 = \frac{ck_2^{\frac{3}{2}}}{s + c.c_1.k_2^{\frac{3}{2}}}$ are hold where c, c_1 are integral constants.

Proposition 3.7 Let $x: I \subset \mathbb{R} \to \mathbb{E}^4$ be a unit speed first type Tzitzeica curve whose position vector satisfies parametric equation (7) in Euclidean 4-space $\mathbb{E}^4$. If x is *W* curve the equations

$$m_0 = c_3 \sin(k_1 s) - c_2 \cos(k_1 s) + (cs + c_1)\frac{k_2}{k_1}$$

$$m_1 = c_2 \sin(k_1 s) + c_3 \cos(k_1 s) + \frac{ck_2 - k_1}{k_1^2}$$

$$m_2 = cs + c_1$$

$$m_3 = \frac{c}{k_3} + \frac{c_2 \sin(k_1 s)}{k_3} + \frac{c_3 \cos(k_1 s)}{k_3} + \frac{ck_2 - k_1}{k_3 k_1^2} \tag{17}$$

are hold, where c, c_1, c_2, c_3 are integral constants.

Proof Let x be W curve with the constant curvatures of k_1, k_2, k_3. From the derivatives of the second, third and fifth the equations of (10), from the first and fourth the equations of (10) we get ${m_1}' = \frac{-{k_3}^2}{k_2} m_2$. If the necessary calculations are made, the proof is completed.

4. The Second Type Tzitzeica Curves in Euclidean 4-Space $\mathbb{E}^4$

Proposition 4.1 Let $x: I \subset \mathbb{R} \to \mathbb{E}^4$ be a unit speed second type Tzitzeica curve whose position vector satisfies parametric equation (7) in Euclidean 4-space $\mathbb{E}^4$. If x is first type T-constant curve ($m_0 = 0$) then we get

$$m_1 = \frac{-1}{k_1}, \quad m_2 = -2k_3 e^{2k_3^2 s + c}, \quad m_3 = e^{2k_3^2 s + c} \tag{18}$$

where $k_2 > 0$, $k_3 > 0$ are constants, $k_1 = c_1 \sin(\sqrt{2}k_2 s) + c_2 \cos(\sqrt{2}k_2 s)$, c, c_1, c_2 are integral constants.

Proof Let x be first type T-constant curve ($m_0 = 0$) then we get $m_1 = \frac{-1}{k_1}$. Taking the derivatives m_1', m_2' from the second and the third equation of (11) respectively, and substituting these equalitites in the derivatives of the fifth equation of (11) with $m_1 = \frac{-1}{k_1}$, then we obtain

$$(k_1'' + 2k_1 k_2^2)\frac{-1}{k_1} - (k_1' k_2 + 2k_1 k_2')m_2 - 2k_1 k_2 k_3 m_3 = 0. \tag{19}$$

If the expression $m_2 = \frac{-{m_3}'}{k_3}$ is written into (19) and rearranged that $k_2 > 0$, $k_3 > 0$ are constants, we get

$${m_3}' - 2{k_3}^2 m_3 = \frac{2k_2 k_3}{k_1} + \frac{k_1'' k_3}{k_1^2 k_2} \tag{20}$$

Suppose that right side of the equality (20) is equal to zero, then we get $k_1'' + 2{k_2}^2 k_1 = 0$. Solving this differential equation, we get

$$k_1 = c_1 \sin\left(\sqrt{2}k_2 s\right) + c_2 \cos\left(\sqrt{2}k_2 s\right) \tag{21}$$

where c_1, c_2 are integral constants. Thus, for k_1 from (21) and $k_2 > 0, k_3 > 0$ are constant , left side of the equality (20) is equal to zero. Hence, we obtain ${m_3}' - 2{k_3}^2 m_3 = 0$ and solving this differential equation we get $m_3 = e^{2{k_3}^2 s + c}$ (c integral constant). Taking the derivative of m_3 and substituting ${m_3}'$ into fourth equation of (11) then, we get $m_2 = -2k_3 e^{2{k_3}^2 s + c}$.

Proposition 4.2 Let $x: I \subset \mathbb{R} \to \mathbb{E}^4$ be a unit speed second type Tzitzeica curve whose position vector satisfies parametric equation (7) in Euclidean 4-space $\mathbb{E}^4$. If x is second type T-constant curve ($m_0 \neq 0$ constant) then we get

$$m_1 = \frac{-1}{k_1}, \quad m_2 = \frac{-k_2 k_3'}{k_1 k_3^3}, \quad m_3 = \frac{-k_2}{k_1 k_3} \tag{22}$$

where $k_1 \neq 0,\ k_2 \neq 0$ are constants.

Proof Let x be second type T-constant curve ($m_0 \neq 0$ constant). Then ${m_0}' = 0$. From the first equation of (11) we obtain $m_1 = \frac{-1}{k_1}$. Taking the values m_1', m_2', m_2 from the second, the third and the fourth equation of (11) respectively, and substituting these equalities in the derivative of the fifth equation of (11) with $m_1 = \frac{-1}{k_1}$, then we obtain

$$(k_1 k_1' k_2 + 2k_1^2 k_2')m_3' - 2{k_1}^2 k_2 {k_3}^2 m_3 = k_1'' k_3 - 3c{k_1}^2 k_1' k_3 + 2k_1 {k_2}^2 k_3.$$

If $k_1 > 0$ and $k_2 > 0$ are assumed as constants, we get

$$m_3 = -\frac{k_2}{k_1 k_3} \Rightarrow m_3' = \frac{k_2 {k_3}'}{k_1 {k_3}^2}$$

and substituting m_3' into the fourth equation of (11) we obtain $m_2 = -\frac{k_2 k_3'}{k_1 k_3^3}$.

Proposition 4.3 Let $x: I \subset \mathbb{R} \to \mathbb{E}^4$ be a unit speed second type Tzitzeica curve whose position vector satisfies parametric equation (7) in Euclidean 4-space $\mathbb{E}^4$. If x is first type N-constant curve or second type N-constant curve ($m_1^2 + m_2^2 + m_3^2 = 0$ *or* $m_1^2 + m_2^2 + m_3^2 = c$ constant) then the equations

$$m_0 = (1 + c_1 k_1)s + c_2, \qquad m_1 = c_1$$

$$m_2 = \frac{k_1[(1 + c_1 k_1)s + c_2]}{k_2}, \quad m_3 = \frac{k_1 + c_1 k_1^2 + c_1 k_2^2}{k_2 k_3} \tag{23}$$

are satisfied, where $k_1 \neq 0,\ k_2 \neq 0$ are constants, $k_3 = \frac{\mp\sqrt{k_1 + c_1 k_1^2 + c_1 k_2^2}}{\sqrt{c_3 - s[k_1(1 + c_1 k_1)s + 2c_2 k_1]}}$ and c_1, c_2 are integral constants.

Proof If the fifth equations of (11) is squared, arranged and $-m_2^2 - m_3^2$ is written instead of m_1^2, we get

$$m_2^2\left(-{k_1'}^2 + 4k_1^2 {k_2}^2\right) - {k_1'}^2 m_3^2 + 4{k_1}^2 m_0(k_1' m_1 + k_1^2 m_0 - 2k_1 k_2 m_2) - 4k_1 k_1' k_2 m_1 m_2 = 0.$$

Taking the derivative of this equation and assuming that $k_1 \neq 0$, $k_2 \neq 0$ are constants, we obtain

$$({k_2 m_2}' - k_1 {m_0}')(k_2 m_2 - k_1 m_0) = 0.$$

Thus, the equations ${m_2}' = \frac{k_1}{k_2}{m_0}'$ *or* $m_2 = \frac{k_1}{k_2} m_0$ are hold. Because of k_1 and k_2 being constants, these two cases are equal to each other and we get $k_2 m_2 = k_1 m_0$. If the necessary calculations are made, the proof is completed.

Proposition 4.4 Let $x: I \subset \mathbb{R} \to \mathbb{E}^4$ be a unit speed second type Tzitzeica curve whose position vector satisfies parametric equation (7) in Euclidean 4-space $\mathbb{E}^4$. If x is first type osculating curve ($m_2 = 0$) then the equations

$$m_0 = \frac{-ck_1'k_3}{2k_1^2k_2}, \qquad m_1 = \frac{ck_3}{k_2}, \qquad m_3 = c \text{ (constant)},$$

$$k_1m_1'' - k_1'm_1' + k_1^3m_1 + k_1^2 = 0 \tag{24}$$

are hold. If $k_1 \neq 0$ is assume as constant , x curve lies on $\{N_1, N_3\}$ plane. In this case, we get

$$m_1 = c_1\, sin(k_1s) + c_2\, cos(k_1s) - \frac{1}{k_1}, \quad m_3 = c \text{ (constant)}. \tag{25}$$

Proof Let x is first type osculating curve. Then, from the fourth equation of (11) we get $m_3 = c$ (c constant). Substituting m_2 and m_3 values in the third equation of (11), we obtain $m_1 = \frac{ck_3}{k_2}$. Values of m_2 and m_1 are substituted in the fifth equation of (11) and we obtain $m_0 = -\frac{ck_1'k_3}{2k_1^2k_2}$. In addition, by the use of $m_2 = 0$ in the second equations of (11) and taking the derivative of m_0, we get $m_0' = \frac{-m_1''k_1 + m_1'k_1'}{k_1^2}$. Substituting m_0' in the first equation of (11), we obtain $k_1m_1'' - k_1'm_1' + k_1^3m_1 + k_1^2 = 0$. If k_1 is taken as constant different from zero, we get $m_0 = 0$. Thus, x curve lies on $\{N_1, N_3\}$ plane. In this case, we get

$$m_1 = c_1\, sin(k_1s) + c_2\, cos(k_1s) - \frac{1}{k_1}, \quad m_3 = c \text{ (constant)}.$$

Proposition 4.5 Let $x: I \subset \mathbb{R} \to \mathbb{E}^4$ be a unit speed second type Tzitzeica curve whose position vector satisfies parametric equation (7) in Euclidean 4-space $\mathbb{E}^4$. If x is third type osculating curve ($m_3 = 0$) then we get

$$m_0 = \frac{k_2^2}{k_1^2 + k_2^2} s + c, \quad m_1 = \frac{-k_1}{k_1^2 + k_2^2}, \quad m_2 = \frac{k_1 k_2}{k_1^2 + k_2^2} s + c_1 \tag{26}$$

where $k_1 \neq 0,\ k_2 \neq 0$ are constants and c, c_1 are integral constants.

Proof Let x is third type osculating curve. Then, from the fourth equation of (11) we get $k_3 = 0$. Moreover, taking m_0', m_1', m_2' from the first, second, third equations of (11) respectively, these values are substituted in the derivative of the fifth equation of (11) and arranged we obtain

$$m_1(k_1'' + 2k_1^3 + 2k_1 k_2^2) + m_2(k_1' k_2 - 2(k_1 k_2)') + 3k_1 k_1' m_0 + 2k_1^2 = 0.$$

If k_1 and k_2 are taken as nonzero constants, then from above expression we get

$$m_1 = \frac{-k_1}{k_1^2 + k_2^2}.$$

If the necessary calculations are made, the proof is completed.

Proposition 4.6 Let $x: I \subset \mathbb{R} \to \mathbb{E}^4$ be a unit speed second type Tzitzeica curve whose position vector satisfies parametric equation (7) in Euclidean 4-space $\mathbb{E}^4$. If x is W curve ($k_1 \neq 0, k_2 \neq 0, k_3 \neq 0$ are constants) then we get

$$m_0 = \frac{k_2}{k_1} c_3 \sin(k_3 s) + \frac{k_2}{k_1} c_4 \cos(k_3 s) - \frac{k_2^2 c_1}{k_1 k_3^2} - \frac{c_1}{k_1}$$

$$m_1 = c_1 s + c_2$$

$$m_2 = c_3 \sin(k_3 s) + c_4 \cos(k_3 s) - \frac{c_1 k_2}{k_3^2}$$

$$m_3 = c_3 \cos(k_3 s) - c_4 \sin(k_3 s) + (c_1 s + c_2)\frac{k_2}{k_3} \tag{27}$$

where c_1, c_2, c_3, c_4 are integral constants.

Proof Let x be W curve with the constant curvatures of k_1, k_2, k_3. Taking m_0' from the first equation of (11) and subtituted in the derivative of second and fifth equations of (11) and in addition, taking m_3' from the fourth equation of (11) and subtituted in the derivative of third equation of (11) and after some calculations we obtain $m_1 = c_1 s + c_2$ (c_1, c_2 constants). If taking the derivative of m_1 and the necessary calculations are made, the proof is completed.

5. The Third Type Tzitzeica Curves in Euclidean 4-Space $\mathbb{E}^4$

Proposition 5.1 Let $x: I \subset \mathbb{R} \to \mathbb{E}^4$ be a unit speed third type Tzitzeica curve whose position vector satisfies parametric equation (7) in Euclidean 4-space $\mathbb{E}^4$. If x is first type T-constant curve ($m_0 = 0$) then we get

$$m_1 = \frac{-1}{k_1}, \quad m_2 = c, \quad m_3 = \frac{-k_2}{k_1 k_3} \tag{28}$$

where $k_1 = \frac{\mp c k_3}{\sqrt{c^4 k_3^4(-2c_2 s - c_2^2 - s^2) + c_1}}$, $k_2 = \frac{k_1'}{c k_1^2}$ and $k_3 \neq 0$ is constant and c, c_1, c_2 are non-zero integral constants.

Proof Let x be first type T-constant curve ($m_0 = 0$) then from the first equation of (12) we obtain $m_1 = \frac{-1}{k_1}$. Taking m_3', m_2' from the fourth and the third equations of (12) respectively, and substituting these equalities in the derivative of the fifth equation of (12) with $m_1 = \frac{-1}{k_1}$, then we obtain

$$m_3(k_3'' + 2k_3^3) + 3k_3 k_3' m_2 = \frac{-2k_2 k_3^2}{k_1}.$$

In the above expression, if k_3 is taken as positive constant then, we obtain $m_3 = \frac{-k_2}{k_1 k_3}$. Then, substituting the values of m_1 and m_3 in the third equation of (12), we get $m_2 = c$. Substituting m_2 and derivative of m_1 in the second

equation of (12), then we get $k_2 = \frac{k_1'}{ck_1^2}$. And then, after some necessary calculations we find $k_1 = \frac{\bar{+}ck_3}{\sqrt{c^4k_3^4(-2c_2s-c_2^2-s^2)+c_1}}$.

Proposition 5.2 Let $x: I \subset \mathbb{R} \to \mathbb{E}^4$ be a unit speed third type Tzitzeica curve whose position vector satisfies parametric equation (7) in Euclidean 4-space $\mathbb{E}^4$. If x is second type T-constant curve ($m_0 \neq 0$ constant) then we get

$$m_1 = \frac{-1}{k_1}, \quad m_2 = c_1, \quad m_3 = \frac{-k_2}{k_1k_3} \tag{29}$$

where $k_1 = \frac{\bar{+}c_1k_3}{\sqrt{{c_1}^4k_3^4(-2c_2s-c_2^2-s^2)+c_3}}$, $k_2 = \frac{k_1'}{c_1k_1^2} + \frac{c}{c_1}k_1$, $k_3 \neq 0$ (constant) and $c \neq 0$ (constant) and c_1, c_2, c_3 are integral constants.

Proof Let x be second type T-constant curve ($m_0 \neq 0$ constant). Then ${m_0}' = 0$. Also from the first equation of (12) we obtain $m_1 = \frac{-1}{k_1}$. From this part, obtaining m_2, m_3 is the same as Proposition 5.1 on condition that $k_3 = c$ (constant). By taking the derivatives of m_1, m_2, m_3 and by the use of these values in the (12) with m_1, m_2, m_3 together where it is required then, we obtain k_1, k_2 .

Proposition 5.3 Let $x: I \subset \mathbb{R} \to \mathbb{E}^4$ be a unit speed third type Tzitzeica curve whose position vector satisfies parametric equation (7) in Euclidean 4-space $\mathbb{E}^4$. If x is first type N-constant curve or second type N-constant curve ($m_1^2 + m_2^2 + m_3^2 = 0$ or $m_1^2 + m_2^2 + m_3^2 = c$) then x is W curve ($k_1 \neq 0$, $k_2 \neq 0$, $k_3 \neq 0$ are constants) with

$$m_0 = 0, \quad m_1 = \frac{c_1k_3}{k_2}, \quad m_2 = 0, \quad m_3 = c_1 \text{ (constant)} \tag{30}$$

where $k_2, k_3 \neq 0$ are constants and $k_1 = \frac{-k_2}{c_1 k_3}$ is constant and lies on $\{N_1, N_3\}$ plane.

Proof . Let x is first type N-constant curve, we get $m_1 m_1{}' + m_2 m_2{}' + m_3 m_3{}' = 0$. If the fifth equations of (12) is squared, arranged and $-m_1^2 - m_3^2$ is written instead of m_2^2 we obtain

$$m_3^2\left(k_3'^{\,2} - 4k_3^4\right) + 4k_3^2 k_3' m_2 m_3 - 4k_3^4 m_1^2 = 0.$$

Taking the derivative of above equation and assuming that $k_3 \neq 0$ is constant and arranged $-m_3 m_3{}' - m_1 m_1{}' = 0$ is found. This expression is considered with $m_1 m_1{}' + m_2 m_2{}' + m_3 m_3{}' = 0$ from the beginning of the proof, then we get $m_2 m_2{}' = 0$. Thus, we have two cases

$$m_2 = 0 \quad or \quad m_2{}' = 0 \Rightarrow m_2 = c \text{ (constant)}.$$

If $m_2 = 0$ then, from the fourth equation of (12), we get $m_3 = c_1$ (constant) substituting the values of m_3 in the third equation of (12) with $m_2 = 0$ and arranged, then we obtain $m_1 = \frac{c_1 k_3}{k_2}$. Derivative of m_1 is substituted in the second equation of (12) with $m_2 = 0$, then m_0 is obtained, $m_0{}'$ and m_1 are substituted in the first equation of (12) and arranged we get

$$c_1 k_3 \left(k_1 {k_2}^2 {k_2}'' - {k_1}' {k_2}^2 {k_2}' - 2k_1 k_2 {k_2}'^2\right) = {k_1}^2 {k_2}^4 + c_1 {k_1}^3 {k_2}^3 k_3.$$

Assuming that $k_2 \neq 0$ is constant then, we obtain $k_1 = \frac{-k_2}{c_1 k_3}$ (constant). On the other hand, if m_2 is taken as non-zero constant then, from the fifth equation of (12) we get $2k_3^2 c = 0$. Because of $k_3 \neq 0$ is constant, we obtain $c = 0 = m_2$.

Proposition 5.4 Let $x: I \subset \mathbb{R} \to \mathbb{E}^4$ be a unit speed third type Tzitzeica curve whose position vector satisfies parametric equation (7) in Euclidean 4-space $\mathbb{E}^4$. If x is second type osculating curve ($m_1 = 0$) then we get

$$m_0 = s + c, \quad m_2 = \frac{(s+c)k_1}{k_2}, \quad m_3 = \frac{-2(s+c)k_1k_3^2}{k_2k_3'} \tag{31}$$

where $k_1 = \frac{c_3(c_2+s)}{[c_1^2(c_2+s)^2+16]^{\frac{1}{2}}(s+c)}$, $k_2 \neq 0$ (constant), $k_3 = \frac{4c_1}{c_1^2s^2+2c_2c_1^2s+c_2^2c_1^2+16}$

and c, c_1, c_2, c_3 are integral constants.

Proof Let x is second type osculating curve. Then, from the first equation of (12) we obtain $m_0 = s + c_1$ (c_1 constant) . If the value of m_0 is substituted in the second equation of (12),we get $m_2 = \frac{k_1}{k_2}(s + c_1)$. If the value of m_2 is substituted in the fifth equation of (12) and arranged, we obtain $m_3 = -\frac{2(s+c)k_1k_3^2}{k_2k_3'}$. Taking the derivative of m_2 and substituting in the third equation of (12) with the value of m_3 and assuming that $k_2 \neq 0$ is constant then, we obtain $\frac{k_1'}{k_1} = \frac{-2k_3^3}{k_3'} - \frac{1}{(s+c)}$. The value $\frac{k_1'}{k_1}$ is substituted in the fourth equation of (12) with the values of m_3' and m_2 and arranged then, we obtain

$$k_3 = \frac{4c_1}{{c_1}^2s^2 + 2c_2{c_1}^2s + {c_2}^2{c_1}^2 + 16}, (c_1, c_2 \text{ integral constants}).$$

By continuing required calculations, we get

$$k_1 = \frac{c_3(c_2 + s)}{({c_1}^2(c_2 + s)^2 + 16)^{\frac{1}{2}}(s + c)},$$

which complete the proof.

Proposition 5.5 Let $x: I \subset \mathbb{R} \to \mathbb{E}^4$ be a unit speed third type Tzitzeica curve whose position vector satisfies parametric equation (7) in Euclidean 4-space $\mathbb{E}^4$. If x is first type osculating curve $(m_2 = 0)$, then we get

$$m_0 = c_2 \sin(k_1 s) + c_3 \cos(k_1 s)$$

$$m_1 = c_2 \cos(k_1 s) - c_3 \sin(k_1 s)$$

$$m_3 = c \tag{32}$$

where $k_1 \neq 0$ (constant) $k_2 = \frac{cc_1}{c_2 \cos(k_1 s) - c_3 \sin(k_1 s)}$, $k_3 = c_1$ and c, c_1, c_2, c_3 are non-zero integral constants.

Proof Let x is first type osculating curve . Then, from the fourth equation of (12) we get $m_3 = c$ (c constant). $m_3 = c$ is substituted in the fifth equation of (12) with $m_2 = 0$ then, we obtain $k_3 = c_1$ (non-zero constant). Taking m_1' from the second equation of (12) and substituting in the derivative of first equation of (12) and assuming that $k_1 \neq 0$ is constant then, we obtain $m_0'' + m_0 k_1^2 = 0$. If this differential equation is solved, we get

$$m_0 = c_2 \sin(k_1 s) + c_3 \cos(k_1 s) \ \ (c_2, c_3 \text{ integral constants}).$$

The value of m_0 is substituted in the second equation of (12) and arranged then, we obtain

$$m_1 = c_2 \cos(k_1 s) - c_3 \sin(k_1 s).$$

Besides, the value of m_1 is substituted in the third equation of (12) with $m_3 = c$ and $k_3 = c_1$ and after some necessary calculations, we obtain $k_2 = \frac{cc_1}{c_2 \cos(k_1 s) - c_3 \sin(k_1 s)}$.

Proposition 5.6 Let $x: I \subset \mathbb{R} \to \mathbb{E}^4$ be a unit speed third type Tzitzeica curve whose position vector satisfies parametric equation (7) in Euclidean 4-

space $\mathbb{E}^4$. If x is W curve ($k_1 \neq 0, k_2 \neq 0, k_3 \neq 0$ are constants), then we get

$$m_0 = 0, m_1 = \frac{-1}{k_1}\ (\text{constant}),\ m_2 = 0, \qquad m_3 = \frac{-k_2}{k_1 k_3}(\text{constant}) \qquad (33)$$

and W curve lies on $\{N_1, N_3\}$ plane.

Proof Let x is W curve, so ${k_3}' = 0$. From the fifth equation of (12), we obtain $m_2 = 0$. This value is substituted in the fourth equation of (12) then, we obtain $m_3 = c$ (constant) . Again, the value of m_2 is substituted in the third of the equations (12) and arranged then, we get $m_1 = \frac{m_3 k_3}{k_2}$ (constant). The values of m_1' and m_2 are substituted in the second equation of (12) with $k_1 \neq 0$ is constant then, we obtain $m_0 = 0$. The value of m_0 is substituted in the first equation of (12) then, we obtain $m_1 = \frac{-1}{k_1}$. And $m_1 = \frac{-1}{k_1}$ is equal to $\frac{m_3 k_3}{k_2}$ which is found before. From here, $m_3 = \frac{-k_2}{k_1 k_3}$ is found. The proof is complete.

Corollary 5.7 A regular W curve in $\mathbb{E}^4$ is third type Tz-curve if and only if $m_2 = 0$ [12].

REFERENCES

[1] B. Bayram, E. Tunç, K. Arslan, G. Öztürk, ‘‘On Tzitzeica Curves in Euclidean 3-Space IE^3’’, *Facta Universitatis Ser.Math.İnform,* vol.33, no 3, p. 409 – 416, 2018.

[2] B. Bayram, E. Tunç, ‘‘On Tzitzeica Surfaces in Euclidean 3-Space IE^3’’, *BAUN Fen Bil.Enst.Dergisi,* 23(1), 277 – 290, 2021.

[3] B. Y. Chen, “Constant ratio Hypersurfaces”, Soochow J. Math., vol. 28, p. 353-362, 2001.

[4] B. Y. Chen, “Geometry of warped products as Riemannian submanifolds and related problems”, *Soochow Journal of Mathematics,* vol. 28, no 2, p. 125-156, 2002.

[5] B. Y. Chen, “Geometry of position function of totally real submanifolds in complex Euclidean spaces”, *Kragujevac Journal of Mathematics*, vol. 37, no 2, p. 201-215, 2013.

[6] V. Cruceanu, “Research Works of Romanian mathematicians on Centro-Affine Geometry”, *Balkan Journal of Geometry and Its Applications*, vol. 10, no 1, p. 1-5, 2005.

[7] H. Gluck, “Higher Curvatures of Curves in Euclidean Space”, *The American Mathematical Monthly*, vol. 73, no 7, p. 243-245, 1966.

[8] A. Gray, “Modern differential geometry of curves and surfaces”, *CRC Press*, 1993.

[9] F. Klein, S. Lie, “Uber diejenigen ebenenen kurven welche durch ein geschlossenes system von einfach unendlich vielen vartauschbaren linearen Transformationen in sich übergehen”, *The American Mathematical Monthly*, vol. 4, p. 50-84, 1871.

[10] G. Öztürk, S. Gürpınar, K. Arslan, “A new characterization of curves in Euclidean 4-space $\mathbb{E}^4$”, *Buletinul Academiei de Stiinte a Republicii Moldova. Matematica,* vol. 83, no 1, p. 39-50, 2017.

[11] G. Öztürk, K. Arslan, H. Hacısalihoğlu, "A characterization of ccr-curves in $\mathbb{R}^n$", *Proceedings of the Estonian Academy of Sciences*, vol. 57, p. 217-224, 2008.

[12] E. Tunç, B. Bayram, "A New Characterization of Tzitzeica Curves in Euclidean 4-Space $\mathbb{E}^4$", *Fundamentals of Contemporary Mathematical Sciences,* vol. 4, no 2, p. 77 – 86, 2023.

[13] G. Tzitzeica, "Sur une nouvelle classe de surfaces", *Comptes Rendus des S´eances de l'Acad´emie des Sciences Paris,* vol. 144, no 1, p. 1257-1259, 1907.

[14] G. Tzitzeica, "Sur certaines courbes gauches", *Annales scientifiques de l'École Normale Supérieure,* vol. 28, no 3, p. 9-32, 1911.

Chapter 11

APPLICATIONS OF MICROBIAL EXOPOLYSACCHARIDES

Elif YÜRÜMEZ CANPOLAT[1]

1 Assist. Prof. Dr. Elif YÜRÜMEZ CANPOLAT, Niğde Ömer Halisdemir University, Faculty of Arts and Sciences, Department of Biotechnology, Niğde, Turkey
ORCID: 0000-0003-1470-1169

Introduction

Natural polymers have gained popularity in recent years for their use in industrial settings. Extracellular exopolysaccharides (EPS) are the most significant and renewable type of polymeric materials. They are produced by microorganisms. EPS have a wide range of applications in a variety of industries, such as dairy products, cosmetics, biofilms, and agriculture, indicating their significance in biotechnology. Many researches have mostly concentrated on EPS production because of their biocompatibility, biodegradability, and environmental and human compatibility. Since, EPS have significant production costs, only a few number have achieved commercial viability. The most significant and prevalent class of substances are polysaccharides, which are macromolecules that are produced by bacteria, fungi, and algae. Because of their industrial applications, polysaccharides have garnered a lot of attention lately (Moradi *et al.,* 2021). Polysaccharides are a subclass of carbohydrates. Microbial polysaccharides are categorized depending on where they are located within the microbial cell. EPS are carbohydrate polymers that are created by many bacteria and released into the extracellular environment or adhered to the surface of the cell to form capsules. They are crucial for the metabolism of cells. Molds and yeasts produce lower amounts of EPS than bacteria and microalgae, which can be used on an industrial basis. These molecules have long, branching chains and are soluble in water. Homopolysaccharides and heteropolysaccharides are the two categories of EPS. Heteropolysaccharides are made up of many monosaccharides, whereas homopolysaccharides are made up of just one type of monosaccharide. Heteropolysaccharides are the class that most bacterial EPS belong to. According to Nwodo *et al.* (2012), EPS play crucial roles in the microbial cell's defense against biotic and abiotic stress. Additionally, their synthesis increases resilience, affects how the microorganism interacts with its surroundings and makes them suitable for use as a growth substrate for microorganisms.

Typically, a set of genes within the biosynthetic gene cluster in the producing microorganism's genome encode a series of enzymes that carry out the manufacture of EPS (Mahmoud *et al.,* 2021). In addition, the growth stage, the environment, and the availability of nutrients all influence the formation of EPS (Ibrahim *et al.,* 2022). The advancement of synthetic biology has made it feasible to modify microbes to generate particular EPS with desired characteristics. Using synthetic promoters to control the expression of these genes, or inserting or deleting genes, the metabolic pathways of microbes are modified (Wagner and Alper, 2016). Synthetic biology offers numerous benefits over traditional techniques for producing EPS. For instance, it makes it possible to produce EPS with better solubility, more stability, and more usefulness. Additionally, synthetic biology allows to production of EPS on a large scale, which is crucial for commercial applications (Sathiyanarayanan *et*

al., 2017).

Because of their water solubility, polysaccharides produced by biotechnological processes -particularly EPS- represent an established market with stable physical and chemical qualities that may be manufactured by a variety of microorganisms, including molds, yeasts, and bacteria. The potential to use renewable resources, provide a variety of desired properties, enhance the rheological qualities of various products in the food and pharmaceutical industries, and be used as polymer substitutes for their antitumor and immunostimulatory properties have all contributed to the gradual expansion of the market for microbial polysaccharides. Xanthan gum, which is generated by *Xanthomonas campestris*, is one of the most important exopolysaccharides manufactured today. Its yearly production capacity is 50,000 tons, and its market worth ranges from 600 to 800 million USD (Subhash *et al.,* 2015). Xanthan is mostly utilized by the food industry in sauces, frozen foods, drinks, and sweets, making up 6% of the polysaccharide market. Further EPS include gellan, dextran, and pullulan, which are specifically used to improve the rheological properties of certain food and pharmaceutical products (Freitas *et al.,* 2011). A novel non-toxic EPS called microbactan offers an option for the removal of heavy metals, particularly in industrial waters, and has the potential for bioabsorption in cadmium-treated waters (Camacho-chab *et al*., 2018). EPS produced by co-cultivation of *Escherichia coli* and *Rhodotorula mucilaginosa* UANL-001L inhibits bacterial colonization and has several uses in the industrial and medical sectors (Vazquezrodriguez *et al.,* 2018). Moreover, *Lactobacillus plantarum* BR2 produces EPS with antioxidant, cholesterol-lowering, and antidiabetic properties, that has great promise for use in functional foods (Sasikumar *et al.* 2017).

Some Exopolysaccharides of Industrial Importance

Kefiran

One of the bioactive hetero EPS candidates for use in the pharmaceutical and food industry is known as kefiran. Exopolysaccharides in kefir grains were first discovered by La Riviére et al. (1967) and named kefiran. Kefiran, which makes up 50% of the dry basic mass of kefir, is a transparent or light yellow, slimy EPS that is soluble in water, edible, and biodegradable. *Lactobacillus kefiranofaciens*, *L. parakefir, L. kefirgranum*, *L. kefir*, and *L. delbrueckii* subsp. create kefiran (Wang *et al.,* 2010). Kefiran has been designated as a GRAS (generally recognized as safe) drug by the US Food and Drug Administration, indicating that it has a variety of potential applications in the food and pharmaceutical industries (Badel *et al.,* 2011).

Despite being found in 1967, only recent studies have been able to identify and characterize the significant biological activities of kefir, including its ability to modulate blood pressure, blood glucose, lipids, and inflammation. It

also has antioxidant, anticancer, and antimicrobial properties. Furthermore, the potential applications of kefir as a functional diet to prevent oncological diseases with important prevalence are suggested by its pro-apoptotic and anti-proliferative actions on human colon cancer cell lines (Caco-2 and HT-29). Microorganisms present in kefir produce kefiran, a branching, water-soluble molecule with roughly equal amounts of D-glucose and D-galactose. Research studies indicate that this EPS can be used in the food industry in three ways: 1) to increase the viscosity of aqueous solutions and acid milk gels; 2) to produce a transparent and edible EPS that is comparable to most polysaccharide-based films and can be used to control the transfer of flavors, oils, aromas, and gases in a food system; and 3) to extend the shelf life and improve the quality of food products. The potential applications of this EPS are growing as research on kefiran advances (Tan *et al.,* 2020). Additional uses for kefiran that are frequently brought up include the creation of films and nanocomposites that may find use in food packaging, as well as the creation of capsules and other drug-delivery structures that may one-day yield standardized kefiran for use as a medication (Shahabi-Ghahfarrokhi and Babaei-Ghazvini, 2019; Gagliarini *et al.,* 2019).

Xanthan

Xanthan gum is one of the most common exopolysaccharides made today; 50,000 tons are produced annually. According to Barcelos *et al.* (2020), its market value is projected to reach 1.2 billion dollars by 2030. Applications in the food, agrochemical, cosmetic, drilling fluid, and foam stabilizer segments are driving the increase in demand (Ul-Islam *et al.,* 2020). Due to the fact that glucose and sucrose are used as only carbon sources in production and the high cost of downstream processing (which accounts for roughly 50% of the total cost), xanthan is among the most expensive EPS. Bacteria in the class Gammaproteobacteria of the phylum Proteobacteria, specifically those in the genus *Xanthomonas*, are the producers of xanthan. It is one of the most important microbial polysaccharides produced by *Xanthomonas campestris*. Most of the studies on xanthan gum production have been reported with strains obtained from the culture collection, mainly *X. campestris* NRRL-B 1459 or ATCC 13951 and their derivatives (Netrusov *et al.,* 2023).

Xanthan is an extracellular polysaccharide made up of trisaccharide side chains that have been modified with varying degrees of O-acetyl and pyruvic acid acetal, and a homopolysaccharide D glucose backbone. Its molecular weight is variable and this variability is due to the bacterial genus and species (Donot *et al.,* 2012). Due to its rheological properties, it can be used in many different industrial fields. Most of its rheological properties are due to its double helical structure, which allows it to adapt to solution. Even at low concentrations, it demonstrates excellent particle suspension, emulsion stabilization, and recoverable shear thinning activity with high viscosities.

Xanthan solution is highly pseudoplastic and rapidly regains viscosity upon stress relief. The rheology, stability, and function of xanthan are intimately correlated with its molecular structure and conformational state (Bhat *et al.,* 2022; Al-Muhanna *et al.,* 2023).

It is the first industrially produced microbial biopolymer. It is also the most widespread and widely accepted microbial biopolymer, with an annual production of over 20,000 tons from various sources (Freitas *et al.,* 2011). Xanthan was approved for use in foods by the FDA in 1969 in the USA. In Europe, it started to be used in 1980 with the code E-415. Xanthan changes the rheological properties in the presence of water and provides many physical advantages. Xanthan is added to a large number of foodstuffs and provides many additives. For example, it accelerates the perception of the taste of foodstuffs or enhances the taste of other food components such as proteins, lipids and carbohydrates. Due to its properties, xanthan has also found a place in the petroleum, pharmaceutical, cosmetics, paper, paint and textile industries. It is used as a stabilizer, emulsifier, gelling agent, thickening agent in the food industry. It is also used as an inhibitor of gum and ice crystal form. Xanthan is a dry, tasteless, white-cream-colored biodegradable powder and is cheaper compared to synthetic polymers. Because of its high viscosity, pseudoplastic nature, and resilience in the face of salt, temperature, and alkaline conditions, it is extensively utilized in enhanced oil recovery (EOR) technology (Sampaio *et al.,* 2020).

Additionally, toothpaste and paintings with a water base can be made with it. Paints containing xanthan do not drip off the brush because they are extremely viscous at low shear rates. Xanthan finds application in numerous industries such as paint, cosmetics, printing inks, pharmaceuticals, cleaning crude oil and insecticide, detergent, and dye synthesis. Moreover, it lubricates drilling equipment when used in oil well drilling muds (Delbarre-Ladrat *et al.,* 2014).

Dextran

Lactic acid bacteria (LAB) produce dextran, an exopolysaccharide, when they are exposed to sucrose. The generating strain affects the molecular weight and branching characteristics of dextran. Due to its solubility, viscosity, temperature, and rheological qualities, dextran is a commercially significant exopolysaccharide used in culinary, pharmaceutical, and research areas (Díaz-Montes, 2021). The industrial process of obtaining dextran involves cultivating *Leuconostoc mesenteroides* NRRL B512. This bacteria is thought to be extremely stable and safe (GRAS). Strain NRRL B512 is fermented in a sucrose medium supplemented with modest concentrations of calcium and phosphate, casein, yeast extracts, malt extracts, and peptone. Non-ionic detergents are frequently added to fermentation to preserve the stability of

the bacteria and their enzymes since lactic acid production causes the pH to decrease from 7 to 5 during the process. In the therapeutic setting, native dextran from *L. mesenteroides* NRRL B512 is often hydrolyzed with acids (such as sulfuric and hydrochloric acids) to produce dextran. This process allows for the regulation of the dextran's molecular weights. *Leuconostoc* sp. produces primarily α-1,6 bonds in its dextran, with trace amounts of branched α-1,2, α-1,3, or α1,4 bonds. In both acidic and alkaline environments, dextran shields the bacteria (Papagianni *et al.,* 2001). Dextran, the first polysaccharide produced industrially by lactic acid bacteria, was discovered in 1880 in sugar cane and beet syrup. Dextran has been used in food and pharmaceuticals since 1940. Due to their different structures, some dextrans are soluble in water while others are not. Due to its rheological properties and high industrial demand, it is produced in large quantities with high purity (Patel and Prajapati, 2013). In the food industry, it is used in candy production to retain moisture and regulate viscosity and sugar crystallization. It is also used as a gelling and crystallization inhibitor in jelly candies and ice cream.

Some studies indicate that dextran synthesis is affected by the amount of substrate. The highest dextran production was found using 10% to 20% sucrose. The overabundance of sucrose (20%) inhibits the formation of EPS. Each glucan is complicated and unique due to variations in the molecular weight as well as the kinds and amounts of branches in each dextran, which are dependent on the producing strain and the conditions of fermentation (or synthesis) (Caipang *et al.,* 2015).

Gellan

Ten years after its discovery in 1978, gellan was utilized for the first time in culinary products in Japan. Its usage as a thickener and stabilizer in the US and Europe was authorized by the FDA in 1990. According to Moscovici (2015), it is an anionic linear heteropolysaccharide with two b-D-glucose and b-D-glucuronate residues, as well as repeated a-rhamnose units. It also has high viscosity and heat stability. *Sphingomonas elodea* naturally produces this anionic water-soluble EPS, which is utilized extensively in the food industry as a stabilizer, thickening agent, and gelling agent. Microbial growth and gellan formation are strongly correlated, and things that hinder microbial development can also inhibit gellan production. Gellan production is known to be maximized by using yeast extract as a source of nitrogen and sucrose as a source of carbon (Zhang *et al.,* 2015).

Bakery fillings, dairy goods, low-fat spreads, sweet gels, jams, jellies, and sauces are among the food items that include gellan. Additionally, it's employed in the creation of edible coatings that increase fruits' shelf life (Freitas *et al.,* 2013; Prajapati *et al.,* 2013). Gellan can also be used to make films with mechanical and water vapor barrier qualities. Additional applications include

gelling agent in dental and personal care products, ophthalmic drugs and vehicle for drug release, gellan hydrogel in paper cleaning, inhibition of acid corrosion of iron casting, and use in hot drink paper cups and in combination with purple sweet potato for pH monitoring (Douglas *et al.,* 2016; Zhang *et al.,* 2017; Wei *et al.,* 2017).

Gellan has been investigated for use as a drug delivery carrier material in tablet, capsule, bead, and hydrogel form in pharmaceutical technology and medicine. Oral, ophthalmic, and nasal gellan-based formulations have been produced. Gellan has been studied for its potential use in tissue engineering (e.g., directed bone regeneration and cartilage rebuilding) and wound healing (e.g., wound dressings to prevent wound development and post-surgical adhesion). Because of their ability to selectively bind fibronectin molecules and their anticoagulant activity, gellan sulfate derivatives have been targeted for the development of cell hybrid materials for artificial vessel design, making them promising materials for the treatment of rheumatoid arthritis (Miyamoto *et al.,* 2002).

Levan

Levan is a naturally occurring homo-EPS made up of monomers of fructose. *Zymomonas, Bacillus, Rahnella, Halomonas, Pseudomonas, Erwinia, Aerobacter, Streptococcus*, *Microbacterium*, and a few yeasts and fungi are the primary producers of this molecule (Andhare *et al.,* 2014; Moscovici, 2015). It is remarkable how the molecular weights and degrees of branching of levan produced by various organisms vary, affecting the range of applications for this substance. According to some research, a variety of bacteria, including *Bacillus subtilis*, *Pseudomonas syringae*, and *Brenneria goodwinii* (Liu *et al.,* 2017), efficiently synthesize levan using sucrose. According to Abdul-Fattah *et al.* (2012), levan has several key characteristics, including neutral charge, high water solubility, low viscosity, antioxidant, anti-tumor, anti-inflammatory, and cholesterol-lowering effects. It possesses a wide range of qualities, including the ability to form films, adhesiveness, high biocompatibility, and fat solubility. As a novel functional biopolymer, it offers enormous potential in the food, chemical, pharmaceutical, and animal feed industries. Its application as a cryoprotectant, bioflocculation agent, prebiotic, peptide-based drug nanocarrier system, and multilayer adhesive film-forming has also been documented in other studies (Sarilmisar *et al.,* 2015).

Levan has never found its rightful place in the polymer market due to its high production costs. Microorganisms producing high-quality levan are gaining increasing industrial importance. Since immobilized cells make it easier to separate the product and reuse the biocatalyst, they can be advantageous for industrial production. Molasses and sugarcane substrates have been used by *Zymomonas mobilis* for the low-cost production of levan.

Although it is lower than that obtained from commercially used sucrose, there is great potential for its use (de Oliveira *et al.,* 2007). Levan plays a biological role in the production of biofilms in certain bacteria. Furthermore, levan encourages the development of cell aggregates on abiotic surfaces and salt tolerance in bacteria that live in soil (Dogsa *et al.,* 2013).

One biopolymer that shows promise for creating nanomaterials is levan. Levan's primary use to date has been in the manufacture of nanoparticles because of its amphiphilic characteristics. Vancomycin, for instance, is included in 200–600 nm levan nanoparticles. Future research may suggest levan-containing nanoparticle complexes as effective drug delivery agents for medications, including those for cancer. Resveratrol-containing levan-based nanoparticles have been created; these can be applied to wound healing, tissue engineering, and drug delivery systems. Peptides and proteins can also be administered by levan nanoparticles as drug carriers (Tabernero and Cardea, 2020; Cinan *et al.,* 2021; Aktürk, 2022).

Pullulan

Produced through the fermentation of *Aureobasidium pullulans*, a bacterium of high biotechnological interest that may produce many bioproducts, pullulan is an exopolysaccharide with numerous industrial applications. It is a significant polymer utilized in the food, cosmetics, and pharmaceutical industries. Its intriguing qualities, in contrast to those of other EPSs, include non-toxicity, water solubility, biodegradability, and biocompatibility (Agrawal *et al.,* 2022). Microorganisms produce this polysaccharide to help with natural processes such as cell adhesion, flocculation, and aggregation in various conditions (Barcelos *et al.,* 2020). The specific structure and GRAS status of pullulan allow for extensive applications in the food industry as a stabilizer, adhesive, coating or packaging material. In addition to its probiotic properties, pullulan has been shown to have a higher Prebiotic Activity Score (PAS) than both xanthan and gellan (Nithya BalaSundari *et al.,* 2020). In addition, pullulan can be enhanced and changed by using additional ingredients such as herbal extracts, bacteriocins, and essential oils. In order to satisfy the unique needs of food items, this extension seeks to maximize its functioning (Ghosh *et al.,* 2022).

According to Singh *et al.* (2017), pullulan has additional potential uses in oral thin films, blood plasma substitutes, and cosmetics. Tissue engineering, pharmaceutical coatings, drug administration, plasma expanders, vaccines, gene targeting, oral hygiene products, general health, and other parenteral forms are among the pharmaceutical industry uses for pullulan (Tiwari *et al.,* 2019; Singh *et al.,* 2023). Food coating and packaging is another industrial application. In addition to being utilized in toothpaste, hairspray, lipstick, shampoo, fixing lotion, and other personal care products, it is also extensively

employed in the cosmetics sector, primarily as an immediate firming agent. It quickly creates a coating that smooths out wrinkles and enhances skin texture. The biopolymer's capacity to solidify and stick to the skin is what allows it to have this impact, which makes it an important active component in anti-aging treatments (Roy *et al,* 2020). Applications in photography, optics, and electronics are less common uses of pullulan (Goswami *et al.,* 2021).

The demand for pullulan has increased significantly in recent years, and the three countries that manufacture the most of this biopolymer worldwide right now are the US, China, and Japan. The manufacture of pullulan requires innovative approaches due to the high cost and low yields of bioprocessing; one such approach might be to employ lignocellulosic biomass, a material that is widely available, as feedstock (Li *et al.,* 2023). There could be new commercial prospects if pullulan applications are expanded. While research and development can guarantee pullulan's strong performance as a profitable solution in three areas of sustainable development, process improvements can make it easier to apply and produce industrially.

Alternan

Alternan is a natural hetero-EPS produced by *Leuconostoc mesenteroides*, which has exceptional resistance to enzymatic hydrolysis due to its unique structure. It has high solubility in water and low viscosity, which allows the biopolymer to be considered as a low-viscosity texture former in foods. The average molecular weight of natural alternan is estimated to be 106-107 Da (Leathers *et al.,* 2003). Since then, *L. mesenteroides* NRRL B-1355, the first strain known to produce alternans, has been used in baked goods (Harutoshi, 2013). High concentrations of alternan-dextran are generated during fermentation by the growth of the bacteria on an appropriate nutritional medium that contains sucrose as a carbon source. Inorganic salts and sources of nitrogen are also present in the growth media. Complex growth factors, vitamins, and various amino acids, such as biotin, glutamate, nicotinic acid, pantothenic acid, thiamine, and valine, are necessary for its production. The large-scale manufacturing of this polysaccharide is restricted by the need for sophisticated and costly components, such as sources of nitrogen. Alteransucrase can be used to create alternan *in vitro* in a cell-free environment in addition to *in vivo* microbial production. As in the purification of alternan from the microbial cell system, cell-free synthesis involves incubating the alternansucrase preparation in a sucrose solution and isolating the resultant alternan through precipitation using an organic solvent. Alternan is used commercially as a low-viscosity and volume-expanding agent in food and cosmetics. It is also used as a low glycemic index sweetener and prebiotic in candy production (Patel *et al.,* 2012). Almost all natural strains that produce alternans also produce dextran simultaneously due to the presence of dextransucrases.

Welan

Welan is an anionic polysaccharide produced by *Sphingomonas* sp ATCC 31555 (Gram-negative bacteria). It has a main chain consisting of repeated (1→4)-linked glucose, glucuronic acid, glucose and L-rhamnose units. One side chain per repeating unit is linked to the second component (1→3) of the glucose repeating unit. The side chain consists of only one monosaccharide, either L-rhamnose or L-mannose. Along with gellan or diutan, L-mannose is a member of the Sphingans family, which shares a linear tetrasaccharide backbone structure with L-rhamnose, D-glucose, and D-glucuronic acid. Even at high temperatures, welan works well as a thickening and suspending agent, binding and emulsifying agent, and stabilizer (Huang *et al.,* 2009; Wei *et al.,* 2012). It is intriguing for numerous industrial applications because of these qualities. Welan as a matrix for bionanocomposites has very little data accessible in the literature (Gao, 2016).

The manufacture of cement is one of the primary fields in which welan is being explored. Low viscosity welan is useful in cement compositions because it enhances cement suspension characteristics, lowers fluid loss in these compositions, and works well at low concentrations (Kaur *et al.,* 2014). Welan solutions provided higher apparent viscosity and higher viscoelastic moduli (loss and storage moduli) for the same biopolymer concentration in comparison to xanthan, according to the rheological properties of welan in aqueous environments. Furthermore, according to Xu et al. (2013), xanthan molecular aggregation is more sensitive to temperature fluctuations than welan solution, which can retain high viscosity at high temperatures. Welan is a polysaccharide-containing rhamnose, therefore research into its biological activity and its uses in medicine, cosmetics, and pharmaceuticals is important.

Clavan

One of the richest polymers in the uncommon sugar fucose is klavan, which is made up of repeating units of glucose, galactose, fucose, and pyruvic acid in molar ratios of 1:1:2:1. *Clavibacter* strains, particularly *Clavibacter michiganensis*, are the ones that produce it. The polysaccharide klavan, which contains L-fucose, has several applications in medicine, including the treatment of rheumatoid arthritis, inhibition of lung tumor cell colonization, control over white blood cell formation, regulation of antigen synthesis for the generation of antibodies, and skin moisturizing in cosmetic products. On the other hand, Fucogel, which is marketed by Solabia (France), is a linear anionic polymer that is produced by *Klebsiella pneumoniae* and is utilized in the cosmetics sector. It is composed of trisaccharide repeating units of galacturonic acid, L-fucose, and D-galactose (Roca, 2015). It has also been reported that the marine bacterium *Enterobacter cloacae* produces a polymer with a molar ratio of 2:1:1:1 that consists of fucose, galactose, glucose, and glucuronic acid (Iyer

et al., 2005). The high fucose concentration of *Enterobacter* sp. strain A47's EPS is another characteristic (Antunes *et al.,* 2017).

Conclusion

Microbial EPS are biocompatible, biodegradable, and renewable materials having a variety of uses, including enhancing or changing the rheological characteristics of various products. Researches on bacterial hetero- and homo-EPSs continue in parallel with the demand for technical advances in the group, especially for the discovery of new molecules with bioactive properties and more efficient production processes. However, despite their potential, there are some challenges in the production and purification processes due to the high cost and low yields obtained, which may hinder the scaling up of production and, consequently, the expansion of commercial applications. In this context, further exploratory studies on new natural resources and the development of these biopolymers are needed to improve the efficiency of the production processes of EPS applied to these industrial segments or to discover new molecules of these biopolymers with particular bioactive properties. Many studies are being carried out to determine the optimal techniques for the extraction and purification of EPS, as well as to optimize its production and gain a better understanding of how process variables can affect its biosynthesis. It is feasible to modify the yield as well as the structural and functional characteristics of bacterial EPS by employing methods that use genetic and metabolic engineering to optimize growth conditions. The metabolic regulation of EPS biosynthesis and the generation of genetically resistant strains which are not yet available for industrial production are both predicated on these factors. Even the yields of the most known bacterial EPS are still insufficient for industrial production. Therefore, it is crucial to isolate new producers and generate high-yielding strains through genetic and metabolic engineering. In the future, a considerably greater variety of distinct structural and functional materials of a new generation with a broad range of uses will be able to be created thanks to the already developed methodological techniques and the acquired data on their modification.

REFERENCES

Abdel-Fattah, A. M., Gamal-Eldeen, A. M., Helmy, W. A., & Esawy, M. A. (2012). Antitumor and antioxidant activities of levan and its derivative from the isolate Bacillus subtilis NRC1aza. Carbohydrate polymers, 89(2), 314-322.

Agrawal, S., Budhwani, D., Gurjar, P., Telange, D., & Lambole, V. (2022). Pullulan based derivatives: Synthesis, enhanced physicochemical properties, and applications. Drug Delivery, 29(1), 3328-3339.

Akturk, O. (2022). The anticancer activity of doxorubicin-loaded levan-functionalized gold nanoparticles synthesized by laser ablation. International Journal of Biological Macromolecules, 196, 72-85.

Al-Muhanna, M. K., Anwar, N., Hasnain, M. S., & Nayak, A. K. (2023). Synthesis of tailor-made polysaccharides: An overview. Tailor-Made Polysaccharides in Drug Delivery, 1-27.

Andhare, P., Chauhan, K., Dave, M., & Pathak, H. (2014). Microbial exopolysaccharides: advances in applications and future prospects. Biotechnology, 3(July 2015), 25.

Antunes, S., Freitas, F., Sevrin, C., Grandfils, C., & Reis, M. A. (2017). Production of FucoPol by Enterobacter A47 using waste tomato paste by-product as sole carbon source. Bioresource technology, 227, 66-73.

Badel, S., Bernardi, T., & Michaud, P. (2011). New perspectives for Lactobacilli exopolysaccharides. Biotechnology advances, 29(1), 54-66.

Barcelos, M. C., Vespermann, K. A., Pelissari, F. M., & Molina, G. (2020). Current status of biotechnological production and applications of microbial exopolysaccharides. Critical Reviews in Food Science and Nutrition, 60(9), 1475-1495.

Bhat, I. M., Wani, S. M., Mir, S. A., & Masoodi, F. A. (2022). Advances in xanthan gum production, modifications and its applications. Biocatalysis and Agricultural Biotechnology, 42, 102328.

Bondarenko, O. M., Ivask, A., Kahru, A., Vija, H., Titma, T., Visnapuu, M., ... & Alamaee, T. (2016).

Bacterial polysaccharide levan as stabilizing, non-toxic and functional coating material for microelement-nanoparticles. Carbohydrate polymers, 136, 710-720.

Caipang, C. M. A., & Lazado, C. C. (2015). Nutritional impacts on fish mucosa: immunostimulants, pre-and probiotics. In Mucosal health in aquaculture (pp. 211-272). Academic Press.

Camacho-Chab, J. C., Castañeda-Chávez, M. D. R., Chan-Bacab, M. J., Aguila-Ramírez, R. N.,

Galaviz-Villa, I., Bartolo-Pérez, P., ... & Ortega-Morales, B. O. (2018). Biosorption of cadmium by non-toxic extracellular polymeric substances (EPS) synthesized by bacteria from marine intertidal biofilms. International journal of environ-

mental research and public health, 15(2), 314.

Cinan, Z. M., Erol, B., Baskan, T., Mutlu, S., Savaskan Yilmaz, S., & Yilmaz, A. H. (2021). Gamma irradiation and the radiation shielding characteristics: For the lead oxide doped the crosslinked polystyrene-b-polyethyleneglycol block copolymers and the polystyrene-b-polyethyleneglycol-boron nitride nanocomposites. Polymers, 13(19), 3246.

de Oliveira, M. R., da Silva, R. S. S. F., Buzato, J. B., & Celligoi, M. A. P. C. (2007). Study of levan production by Zymomonas mobilis using regional low-cost carbohydrate sources. Biochemical Engineering Journal, 37(2), 177-183.

Díaz-Montes, E. (2021). Dextran: sources, structures, and properties. Polysaccharides, 2(3), 554-565.

Dogsa, I., Brloznik, M., Stopar, D., & Mandic-Mulec, I. (2013). Exopolymer diversity and the role of levan in Bacillus subtilis biofilms. PloS one, 8(4), e62044.

Donot, F., Fontana, A., Baccou, J. C., & Schorr-Galindo, S. (2012). Microbial exopolysaccharides: main examples of synthesis, excretion, genetics and extraction. Carbohydrate Polymers, 87(2), 951-962.

Douglas, T. E., Krawczyk, G., Pamula, E., Declercq, H. A., Schaubroeck, D., Bucko, M. M., ... &

Dubruel, P. (2016). Generation of composites for bone tissue-engineering applications consisting of gellan gum hydrogels mineralized with calcium and magnesium phosphate phases by enzymatic means. Journal of tissue engineering and regenerative medicine, 10(11), 938-954.

Freitas, F., Alves, V. D., & Reis, M. A. (2011). Advances in bacterial exopolysaccharides: from production to biotechnological applications. Trends in biotechnology, 29(8), 388-398.

Freitas, F., Alves, V. D., Coelhoso, I., & Reis, M. A. (2013). Production and food applications of microbial biopolymers. Engineering Aspects of Food Biotechnology. Part I: Use of Biotechnology in the Development of Food Processes and Products, 61-88.

Gagliarini, N., Diosma, G., Garrote, G. L., Abraham, A. G., & Piermaria, J. (2019). Whey protein-kefiran films as driver of probiotics to the gut. Lwt, 105, 321-328.

Gao, C. (2016). Potential applications of Welan gum in upstream petroleum industry. Int. J. Oil Gas Coal Eng, 4(2), 16.

Ghosh, T., Priyadarshi, R., de Souza, C. K., Angioletti, B. L., & Rhim, J. W. (2022). Advances in pullulan utilization for sustainable applications in food packaging and preservation: A mini-review. Trends in Food Science & Technology, 125, 43-53.

Goswami, S., Sharma, A., & Bhattacharya, M. (2021). Pullulan films and natural compounds: applications and perspectives. In Biopolymer-Based Nano Films (pp. 19-41). Elsevier.

Gupta, J., Rathour, R., Medhi, K., Tyagi, B., & Thakur, I. S. (2020). Microbial-derived

natural bioproducts for a sustainable environment: a bioprospective for waste to wealth. In Refining biomass residues for sustainable energy and bioproducts (pp. 51-85). Academic Press.

Harutoshi, T. (2013). Exopolysaccharides of lactic acid bacteria for food and colon health applications. In Lactic acid bacteria-R & D for food, health and livestock purposes. IntechOpen.

Ibrahim, H. A., Abou Elhassayeb, H. E., & El-Sayed, W. M. (2022). Potential functions and applications of diverse microbial exopolysaccharides in marine environments. Journal of Genetic Engineering and Biotechnology, 20(1), 151

Iyer, A., Mody, K., & Jha, B. (2005). Characterization of an exopolysaccharide produced by a marine Enterobacter cloacae.

Kaur, V., Bera, M. B., Panesar, P. S., Kumar, H., & Kennedy, J. F. (2014). Welan gum: microbial production, characterization, and applications. International journal of biological macromolecules, 65, 454-461.

Leathers, T. D., Nunnally, M. S., Ahlgren, J. A., & Côté, G. L. (2003). Characterization of a novel modified alternan. Carbohydrate polymers, 54(1), 107-113.

Li, B., Li, B., Wang, P., Feng, Y., Xu, X., Zhang, Y., & Zou, X. (2023). Bio-refinery of xylose processing wastes for green polymalic acid production and l-malic acid recovery by engineered Aureobasidium pullulans in a non-waste-disposal system. Chemical Engineering Journal, 454, 140533.

Liu, Q., Yu, S., Zhang, T., Jiang, B., & Mu, W. (2017). Efficient biosynthesis of levan from sucrose by a novel levansucrase from Brenneria goodwinii. Carbohydrate Polymers, 157, 1732-1740.

Mahmoud, Y. A. G., El-Naggar, M. E., Abdel-Megeed, A., & El-Newehy, M. (2021). Recent advancements in microbial polysaccharides: Synthesis and applications. Polymers, 13(23), 4136.

Miyamoto, K., Sugihara, K., Abe, Y., Nobori, T., Tokita, M., & Komai, T. (2002). Novel plasma-separation dilayer gellan–gellan-sulfate adsorber for direct removal of extra domain A containing fibronectin from the blood of rheumatoid arthritis patients. International journal of biological macromolecules, 30(3-4), 197-204.

Moradi, M., Guimarães, J. T., & Sahin, S. (2021). Current applications of exopolysaccharides from lactic acid bacteria in the development of food active edible packaging. Current Opinion in Food Science, 40, 33-39.

Moscovici, M. (2015). Present and future medical applications of microbial exopolysaccharides. Frontiers in microbiology, 6, 1012.

Netrusov, A. I., Liyaskina, E. V., Kurgaeva, I. V., Liyaskina, A. U., Yang, G., & Revin, V. V. (2023). Exopolysaccharides Producing Bacteria: A Review. Microorganisms, 11(6), 1541.

NithyaBalaSundari, S., Nivedita, V., Chakravarthy, M., Srisowmeya, G., Antony, U., & Dev, G. N. (2020). Characterization of microbial polysaccharides and prebiotic enrichment of wheat bread with pullulan. Lwt, 122, 109002.

Nwodo, U. U., Green, E., & Okoh, A. I. (2012). Bacterial exopolysaccharides: functionality and prospects. International journal of molecular sciences, 13(11), 14002-14015.

Papagianni, M., Psomas, S. K., Batsilas, L., Paras, S. V., Kyriakidis, D. A., & Liakopoulou-Kyriakides, M. (2001). Xanthan production by Xanthomonas campestris in batch cultures. Process Biochemistry, 37(1), 73-80.

Patel S, Majumder A, Goyal A. Potentials of exopolysaccharides from lactic acid bacteria. Indian J Microbiol. 2012;52(1):3–12.

Patel, A., & Prajapati, J. B. (2013). Food and health applications of exopolysaccharides produced by lactic acid bacteria. Adv Dairy Res, 1(2), 1-7.

Roca, C., Alves, V. D., Freitas, F., & Reis, M. A. (2015). Exopolysaccharides enriched in rare sugars: bacterial sources, production, and applications. Frontiers in microbiology, 6, 288.

Roy, S., Das, S. K., Chakraborty, S., Pandey, K., Mukherjee, A., & Rajabalaya, R. (2020). Role of 7 Pullulans in Cosmetics. In Pullulan (pp. 239-255). Jenny Stanford Publishing.

Sampaio, I. C., Crugeira, P. J., Soares, L. G., Dos Santos, J. N., de Almeida, P. F., Pinheiro, A. L., &

Silveira Jr, L. (2020). Composition of Xanthan gum produced by Xanthomonas campestris using produced water from a carbonated oil field through Raman spectroscopy. Journal of Photochemistry and Photobiology B: Biology, 213, 112052.

Sarilmiser, H. K., Ates, O., Ozdemir, G., Arga, K. Y., & Oner, E. T. (2015). Effective stimulating factors for microbial levan production by Halomonas smyrnensis AAD6T. Journal of bioscience and bioengineering, 119(4), 455-463.

Sasikumar, K., Vaikkath, D. K., Devendra, L., & Nampoothiri, K. M. (2017). An exopolysaccharide (EPS) from a Lactobacillus plantarum BR2 with potential benefits for making functional foods. Bioresource technology, 241, 1152-1156.

Sathiyanarayanan, G., Dineshkumar, K., & Yang, Y. H. (2017). Microbial exopolysaccharide-mediated synthesis and stabilization of metal nanoparticles. Critical reviews in microbiology, 43(6), 731-752.

Shahabi-Ghahfarrokhi, I., & Babaei-Ghazvini, A. (2019). Using photo-modification to compatibilize nano-ZnO in development of starch-kefiran-ZnO green nanocomposite as food packaging material. International journal of biological macromolecules, 124, 922-930.

Singh, R. S., Kaur, N., Rana, V., & Kennedy, J. F. (2017). Pullulan: A novel molecule for biomedical applications. Carbohydrate polymers, 171, 102-121.

Singh, R. S., Kaur, N., Singh, D., Purewal, S. S., & Kennedy, J. F. (2023). Pullulan in pharmaceutical and cosmeceutical formulations: A review. International Journal of Biological Macromolecules, 123353.

Subhash, M., Jadhav, A., & Jana, S. (2015). Sustainable production of microbial polysaccharide xanthan gum from supplemental substrate. Int J Sci Res, 4(8), 9-11.

Tabernero, A., & Cardea, S. (2020). Microbial exopolysaccharides as drug carriers. Polymers, 12(9), 2142.

Tan, K. X., Chamundeswari, V. N., & Loo, S. C. J. (2020). Prospects of kefiran as a food-derived biopolymer for agri-food and biomedical applications. RSC advances, 10(42), 25339-25351.

Tiwari, S., Patil, R., Dubey, S. K., & Bahadur, P. (2019). Derivatization approaches and applications of pullulan. Advances in Colloid and Interface Science, 269, 296-308.

Ul-Islam, M., Ullah, M. W., Khan, S., & Park, J. K. (2020). Production of bacterial cellulose from alternative cheap and waste resources: A step for cost reduction with positive environmental aspects. Korean Journal of Chemical Engineering, 37, 925-937.

Vazquez-Rodriguez, A., Vasto-Anzaldo, X. G., Barboza Perez, D., Vázquez-Garza, E., Chapoy-

Villanueva, H., García-Rivas, G., ... & Morones-Ramirez, J. R. (2018). Microbial competition of Rhodotorula mucilaginosa UANL-001L and E. coli increase biosynthesis of non-toxic exopolysaccharide with applications as a wide-spectrum antimicrobial. Scientific reports, 8(1), 798.

Wagner, J. M., & Alper, H. S. (2016). Synthetic biology and molecular genetics in non-conventional yeasts: current tools and future advances. Fungal Genetics and Biology, 89, 126-136.

Wang, Y., Li, C., Liu, P., Ahmed, Z., Xiao, P., & Bai, X. (2010). Physical characterization of exopolysaccharide produced by Lactobacillus plantarum KF5 isolated from Tibet Kefir. Carbohydrate Polymers, 82(3), 895-903.

Wei, Y. C., Cheng, C. H., Ho, Y. C., Tsai, M. L., & Mi, F. L. (2017). Active gellan gum/purple sweet potato composite films capable of monitoring pH variations. Food Hydrocolloids, 69, 491-502.

Xu, L., Xu, G., Liu, T., Chen, Y., & Gong, H. (2013). The comparison of rheological properties of aqueous welan gum and xanthan gum solutions. Carbohydrate polymers, 92(1), 516-522.

Zhang, W., Luan, D., Tang, J., Sablani, S. S., Rasco, B., Lin, H., & Liu, F. (2015). Dielectric properties and other physical properties of low-acyl gellan gel as relevant to microwave assisted pasteurization process. Journal of Food Engineering, 149, 195-203.

Zhang, N., Xu, J., Gao, X., Fu, X., & Zheng, D. (2017). Factors affecting water resistance of alginate/gellan blend films on paper cups for hot drinks. *Carbohydrate Polymers*, *156*, 435-442.

Chapter 12

AGE AND BODY SIZE OF THE ENDANGERED LIZARD SPECIES, *ACANTHODACTYLUS SCHREIBERI* (BOULENGER, 1878) IN TÜRKİYE

Ufuk BÜLBÜL[1]

Halime KOÇ-GÜR[2]

Hatice ÖZKAN[3]

1 Prof. Dr., Karadeniz Technical University, Faculty of Science, Department of Biology, 61080 Trabzon, Türkiye, ORCID ID: 0000-0001-6691-6968

2 Dr., Karadeniz Technical University, Faculty of Science, Department of Biology, 61080 Trabzon, Türkiye, ORCID ID: 0000-0003-2998-4384

3 PhD.(c), Karadeniz Technical University, Faculty of Science, Department of Biology, 61080 Trabzon, Türkiye, ORCID ID: 0000-0002-7810-864X

Introduction

The Schreiber's fringe-fingered lizard, *Acanthodactylus schreiberi* (Boulenger, 1878) is located in Cyprus, Israel, Lebanon and Türkiye (Hraoui-Bloquet et al., 2009) and shows a discrete distribution in the form of seven areas (329.82 ha) close to each other only in the coastal regions of Erzin and Dörtyol districts of Hatay province of Türkiye where 326.26 hectares (3.26 km2) of areas of the distribution is located in the former, while 3.56 hectares is located in the latter (Akman, 2019).

Acanthodactylus schreiberi has been classified as EN (Endangered) category in the IUCN Red List. The populations of *A. schreiberi* are decreasing worldwide because of coastal urbanization, including the development of touristic facilities and the extraction of sand from beaches for construction, and human disturbance through the high numbers of tourists visiting sites. There is a major petrol pipeline project, industrial activities of petrol pipeline project in its habitat and pollution from petrol and other industries that threaten its limited range in Türkiye (Hraoui-Bloquet et al., 2009).

In case of the preservation of an endangered species, knowledge of life features (age, snout vent length, and body mass) in natural populations is at critical importance (Andreone et al., 2005). In age determination, counting of the lines of arrested growth (LAGs) observed in the cross-sections obtained from the phalanges of animals is used. Occurrence of LAGs every year mirrors etesian alterations in the growth rate of amphibians and reptiles (Smirina, 1994; Arakelyan, 2002). Knowing life expectancy of reptiles reflects mean period of life for individuals living in their habitats. Skeletochronology is an available method to estimate age structure of these animals (Caetano et al., 1986; Leclair & Castanet, 1987; Zug & Rand, 1987; Castanet & Smirina, 1990; Castanet, 1994; Miaud et al., 1999; Esteban et al., 2002; Leclair & Leclair, 2011; Yakın et al., 2012; Yakın & Tok, 2015). This method has also an advantage that researchers only need bone tissues from individuals and give minimal damage to animals (Kurita & Toda, 2013).

Although life features of *Acanthodactylus boskianus* (Daudin, 1802) and *Acanthodactylus harranensis* (Baran, Kumlutaş, Lanza, Sindaco, Ilgaz, Avcı & Crucitti, 2005) were reported by Üzüm et al. (2014) and Beşer et al. (2019) respectively, current literature lacks information on the age structure of *A. schreiberi*. Being an oviparous lizard species, the knowledge related to biology of *A. schreiberi* is limited. The females of *A. schreiberi* from Lebanon emerge from hibernation in mid-April while this activation starts one month before in males. Reproductively active period of the females lasts from May to August. The males simultaneously undergo vernal spermiogenesis after a short period of regression in September and subsequent testicular recrudescence in October and November (Akiki et al., 2015). There is no published information about the activity periods (months) in Türkiye. The breeding period of the species

in Türkiye begins in May and continues until the end of October, according to the findings of Yalçınkaya & Göçmen (2012).

The present study aimed to gain information on some life features (e.g. mean age, SVL, longevity) in a population of the endangered lizard species, *A. schreiberi* using skeletochronology.

Materials and Methods

The lizards are located in the district of Erzin, province of Hatay which consists of a coastal habitat of *A. schreiberi*, which includes beaches and sand dunes with low vegetation. The population of the species is located (36°55'341'' N, 36°01'378'' E) in a lower altitude area (1 m a.s.l.) in Erzin, Türkiye. Our sampling was done in an area of approximately 1 km^2.

A total of 30 *Acanthodactylus schreiberi* individuals (15 ♂ and 15 ♀) were caught. The lizards were found during the daytime (10:00 a.m. and 6:30 p.m.) on 10-12 July 2018 while they were collected between 4:00 and 7:00 p.m. on 13-15 July 2018.

The individuals were captured on the sand or under the bushes where they were hidden. All lizards were collected by hand. Air temperature was recorded as 29-36°C in the sampling period.

The lizards were sexed by the presence or absence of hemipenis pockets and by examination of the secondary sex characteristics (red ventral color in the males and greenish yellow ventral color in females during the breeding season). We measured body size (SVL) to the nearest 0.01 mm using by a digital caliper. We quantified sexual size dimorphism (SSD) in accordance with sexual dimorphism index (SDI) as defined in the formula: SDI = (average SVL of the larger sex / average body size of the smaller sex) ± 1. If males were larger than females, the value +1 was used and if the opposite was true, –1 was used. The result was optionally defined as positive if the females were larger and if the males were larger, it was negative (Lovich & Gibbons, 1992).

Each second phalange of the longest finger of the hind limb obtained from the lizards was clipped and identified by individually. Then, we retained them in 10% formalin solution separately for following skeletochronology analyses. When we completed toe-clipping, we released the lizards back to their natural habitat. We treated captured lizards according to the instructions of the local ethics committee of Karadeniz Technical University.

We used the standard skeletochronology process [using a portion of the second phalanx from the longest toe, counting of the lines of arrested growth (LAGs) in the cross-sections of the middle part of phalangeal diaphyses (Bülbül et al., 2018)].

After initial toe-clip and preservation, skin and flesh were removed from each sample. Then, they were transferred to 5% nitric acid solution in order

to obtain most suitable condition for decalcification of bone tissue. Then, the tissue samples were uploaded into a tissue processing system (Leica TP1020 tissue processor). Subsequently, we embedded the tissue samples in paraffin with a tissue embedding device (Thermo Scientific, UK). We obtained the cross-sections (12 μm) from embedded phalanges by a rotary microtome. Later, the cross-sections were stained using hematoxylin (non-acidified type, Thermo Scientific™ Shandon™ Harris Hematoxylin) waiting for 2 minutes. In order to mount stained cross-sections on the microscope slides, Entellan (Merck brand) was employed. Finally, we observed the cross-sections by 40x objective under a light microscope (Merck, Germany).

Two observers (H. Koç-Gür & U. Bülbül) calculated independently the numbers of LAGs through direct observation using the microscope and the results were compared.

We processed the statistic tests with IBM SPSS 22.0 for Windows. Because body measurements (SVL) and age classes were normally distributed (one-sample Kolmogorov-Smirnov test, $P > 0.05$), the parametric independent-samples *t*-test ($P < 0.05$) in comparison of averages and Pearson's rank correlation test ($P < 0.01$) to analyze correlations were used. In order to estimate SVL and the age structure of the population (for both sexes), Frequency Analysis was used with the histograms.

Results

In body size (SVL), the intersexual differences were male-biased (SDI = -0.13). Between sexes, the average SVL was significantly (*t*-test = -5.431, df = 28, $P < 0.001$) different (Table 1). We found a strong correlation (Figures 1-2) between age and body size in females (Pearson's correlation coefficient (r = 0.842, $P < 0.001$), while we did not find such a correlation between SVL and age in males (r = -0.076, P = 0.990).

Table 1. *Statistics of Body Size (SVL, mm) and Age (year) of the Erzin Population of Acanthodactylus schreiberi (Boulenger, 1878). Abbreviations: N, Number of Samples; SE, Standard Error*

Characters	Sex	*n*	Mean	Range	SE
SVL	♀♀	15	64.55	59.26-71.02	0.86
Age		15	5.93	4-11	0.51
SVL	♂♂	15	72.71	60.01-78.77	1.22
Age		15	6.0	4-7	0.29
SVL	♀♀+♂♂	30	68.63	59.26-78.77	1.05
Age		30	5.97	4-11	0.29

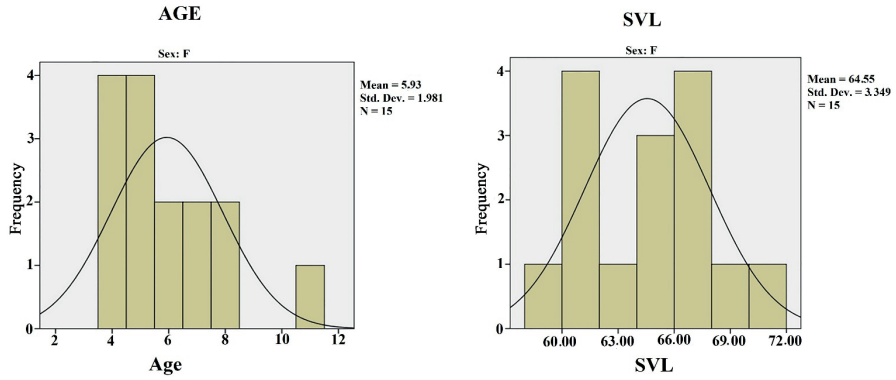

Figure 1. *Age and SVL distributions for females of A. schreiberi from the Erzin population*

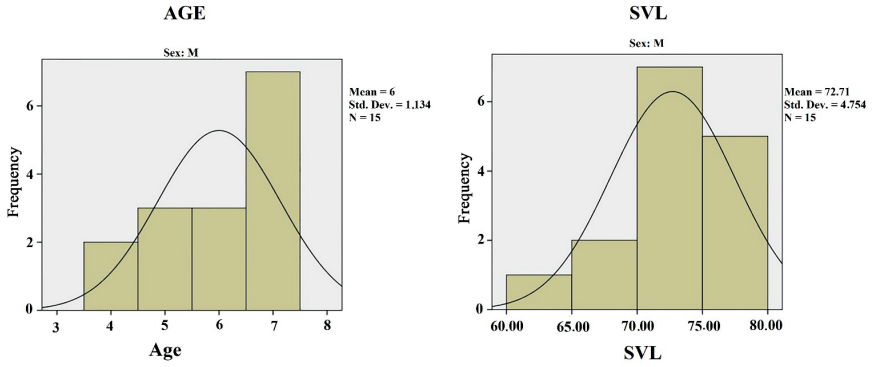

Figure 2. *Age and SVL distributions for males of A. schreiberi from the Erzin population*

In preparations, an outer line stained with hematoxylin (which corresponds to a winter line of arrested growth) and a clear growth zone were present in 100% (n = 30) of adult lizards (Figure 3). In all specimens, we did not observe any resorption zone reaching the first LAG.

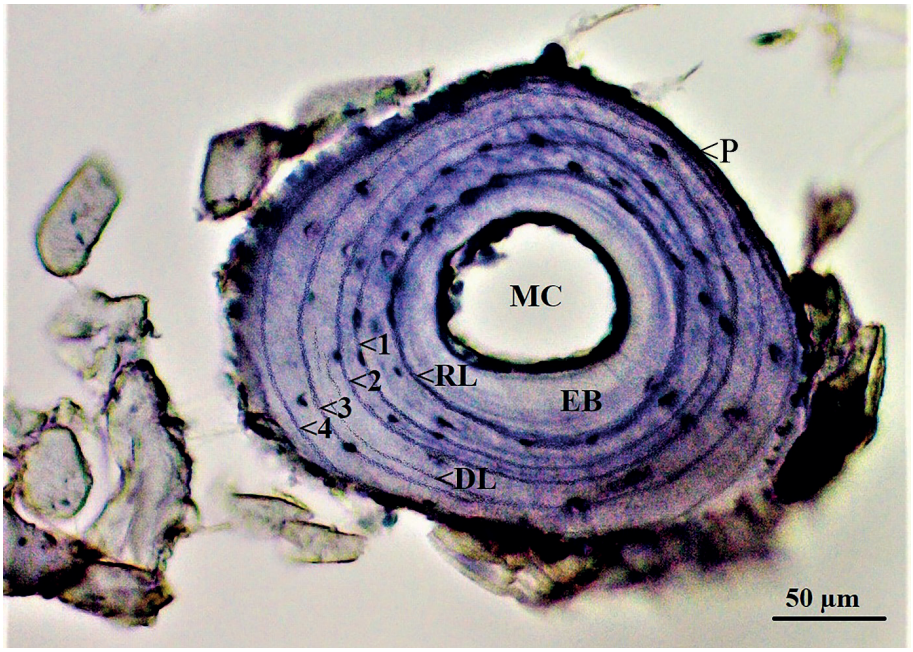

Figure 3. *A cross-section (12µm thick) through phalange of a four-year-old female (SVL= 61.10 mm) of A. schreiberi from the Erzin population. For abbreviations, see text (MC: Marrow Cavity; EB: Endosteal Bone; RL: Resorption Line; DL: Double Line; and P: Periphery)*

We found that, the youngest males and females of *A. schreiberi* in the Erzin population were 4 years old while the oldest ones were 7 and 11 years old, respectively. Within males, two individuals (13.3%) were 4 years old, three of them (20%) were 5 years old, and three individuals (20%) were 6 years old. Seven males (46.6%) were 7 years old. Within females, four individuals (26.6%) were 4 years old and four of them (26.6%) were 5 years old. Two individuals (13.3%) were 6 years old, two of them (13.3%) were 7 years old, and 2 individuals (13.3%) were 8 years old. A female (6.6%) was 11 years old. Between the sexes, we did not found a significant difference in the average age of the adult lizards (independent-samples *t*-test; t = -0.113, df = 28, P = 0.655). We found the average age as 5.93 years (4-11 years in range) in females belonged to the Erzin population of *A. schreiberi* and it was 6 years (4-7 years in range) in males.

Discussion

Some of the characteristics related to life processes of reptiles are linked by body size and other morphometric features which constitute life history of these animals (Pal et al., 2010). Relationships of body size and age may have important roles on breeding tactics of animals (Leary et al., 2005). In

ectothermic animals along latitudinal and altitudinal gradients, intraspecific variation in body size is a common occurrence (Yamahira & Conover, 2002). The mean body size of males was significantly higher than females in the Erzin population of *A. schreiberi*. Üzüm et al. (2014) reported a similar result for *A. boskianus*. Contrary to these findings, the average body size was not different significantly between the males and females of *A. harranensis* according to results of Beşer et al. (2019).

In the present study, we observed a male-biased sexual size dimorphism (SSD) in the Erzin population of *A. schreiberi*. Parallel results were found by Üzüm et al. (2014) and Beşer et al. (2019) for *A. boskianus* and *A. harranensis*, respectively. The types of SSD variation might be occurred due to biotic and abiotic environmental factors (Bülbül et al., 2016). According to Roitberg (2007), differences in body size, age, climate (e.g., precipitation and temperature), and phylogeny between females and males may be reason of SSD in lizards. SVL difference was observed between males and females of *A. boskianus*, *A. harranensis* and *A. schreiberi* in the populations of Birecik, Harran and Erzin, respectively. However, there is no data showing that SVL is a more effective factor to determine SSD than age, phylogeny, or climate in these three populations.

Our results show that there was a strong correlation between body size and age in females while we did not find such a correlation between SVL and age in males. SVL increased in parallel with age for females while it was not increased for males. The small sample size in the present study is not enough to support any correlation. Increasing SVL in parallel with age for females may be related to the clutch size that female individuals carry during the active season. It is known that SVL and clutch size of female individuals is in correlation with many reptiles (Ford & Seigel, 1989). In addition, male to male combat may be one of the reasons why SVL and age did not increase in parallel in male specimens. The male to male combat may lead to loss of energy (Zhao & Liu, 2014), so that a part of the energy that need to use in development may be consumed during male to male combat.

The lizards located in higher altitudes and northern latitudes live longer than those from lower altitudes and southern latitudes (Wapstra et al., 2001; Roitberg & Smirina, 2006; Guarino et al., 2010). An increment in the average age along high-elevation sites has been specified in different lizard species living in colder environments (Roitberg & Smirina, 2006). Although the Erzin population located in a coastal area having hot climate, the longevity was not found low (7 years in males and 11 years in females). A similar trend was reported by Beşer et al. (2019) in a population (located in a hot climate zone in the Şanlıurfa province) of an endemic species, *A. harranensis* of Türkiye. They found longevity as 10 years in males and 9 years in females according to the numbers of LAGs. The lizards in the population consisted of older

individuals. The populations of both species are distributed in the relatively narrow areas in Türkiye. In addition, the longevity of *A. boskianus* specimens in a population of the species from the Şanlıurfa province of Türkiye was reported as 9 years in males and 7 years in females by Üzüm et al. (2014).

In the present study, we provided data related to life features of the endangered lizard species, *A. schreiberi*. Because there is a major petrol pipeline project and industrial activities in the restricted distributional area of the Schreiber's fringe-fingered lizard in Türkiye, pollution from petrol and other industries threaten the species (Hraoui-Bloquet et al., 2009). To demonstrate the dynamics of populations of a species living in such a narrow space and under threat can contribute to the preservation measures, which are necessary.

As a conclusion, our presented results life history traits and SVL of the endangered lizard species, *A. schreiberi* having limited distribution in a small coastal area of Türkiye may contribute to knowledge on life features and future preservation action plans of the species.

Acknowledgements

Our study was performed with permission from the Ministry of Agriculture and Forestry (number of the permission to capture: 72784983-488.04-67410) and the Animal Care and Ethics Committee of Karadeniz Technical University (number of the permission: KTÜ.53488718-71/2017/43). We would like to thank Hüsne Kuş and Mustafa Albayrak for their contributions to the fieldwork and laboratory studies. We thankful to Dr. Ali Şükrü Özbay (Western Language and Literature Department of Karadeniz Technical University) and Mehmet Malcı (English Teacher at Doğa College in Aydın province of Türkiye) for the linguistic revision of the manuscript.

REFERENCES

Akiki, Y. S., Saadé, J. H., Hokayem, M. L., Hraoui-Bloquet, S., Nassar, F. (2015): Female reproductive cycle of the lacertid lizard *Acanthodactylus schreiberi syriacus* (Reptilia: Squamata) from Lebanon. Herpetology Notes 8: 439-443.

Akman, B. (2019): Distribution and some ecological features of *Acanthodactylus schreiberi* Boulenger, 1878 in Anatolia. Biodiversity and Preservation 12: 1-8.

Andreone, F., Guarino, F. M., Randrianirina, J.E. (2005): Life features, age profile, and preservation of the panther chameleon, *Furcifer pardalis* (Cuvier, 1829), at Nosy Be, NW Madagascar. Tropical Zoology 18: 209-225.

Arakelyan, M. (2002): The study of age, growth, and longevity in the triploid hybrids of rock lizards of the genus *Darevskia* in Armenia. Russian Journal of Herpetology 9: 63-68.

Beşer, N., Ilgaz, Ç., Kumlutaş, Y., Avcı, A., Candan, K., Üzüm, N. (2019): Age structure and body size of a critically endangered species, *Acanthodactylus harranensis* (Squamata: Lacertidae) and its demography. Animal Biology 69: 421-431.

Bülbül, U., Kurnaz, M., Eroğlu, A. İ., Koç, H., Kutrup, B. (2016): Body size and age structure of the endangered Clark's lizard (*Darevskia clarkorum*) populations from two different altitudes in Turkey. Amphibia-Reptilia 37: 450-456.

Bülbül, U., Kutrup, B., Eroğlu, A. İ., Koç, H., Kurnaz, M., Odabaş, Y. (2018): Life history traits of a Turkish population of the yellow-bellied toad, *Bombina variegata* (Linnaeus, 1758) (Anura: Bombinatoridae). Herpetozoa 31: 11-19.

Caetano, M. H., Castanet, J., Crespo, E. G. (1986): Skeletochronology used for age identification of a Portuguese population of *Podarcis hispanica* (Sauria: Lacertidae) Revue Suisse de Zoologie 93: 117-128.

Castanet, J., Smirina, E. M. (1990): Introduction to the skeletochronological methods in amphibians and reptiles. Annales des Sciences Naturelles: Zoologie archives (Paris) 13: 191-196.

Castanet, J. (1994): Age estimation and longevity in Reptiles. Gerontology 40: 174-192.

Esteban, M., Sánchez-Herráiz, M. J., Barbadillo, L. J., Castanet, J., Márquez, R. (2002): Effects of age, size and temperature on the advertisement calls of two Spanish populations of *Pelodytes punctatus*. Amphibia-Reptilia 23: 249-258.

Ford, N., Seigel, R. A. (1989): Relationships among body size, clutch size, and egg size in three species of oviparous snakes. Herpetology 45: 75-83.

Guarino, F. M., Gia I. D., Sindaco, R. (2010): Age and growth of the sand lizards (*Lacerta agilis*) from a high Alpine population of north-western Italy. Acta Herpetologica 5: 23-29.

Hraoui-Bloquet, S., Sadek, R., Werner, Y., Lymberakis, P., Tok, V., Ugurtas, İ. H., Sevinç, M., Böhme, W., Kaska, Y., Kumlutaş,Y., Kaya, U., Avci, A., Üzüm, N.,

Yeniyurt, C., Akarsu, F. (2009): The IUCN Red List of Threatened Species, *Acanthodactylus schreiberi*.<http://dx.doi.org/10.2305/IUCN.UK.2009.RLTS.T61462A12489118.en., accessed at: 2019.06.02.>

Kurita, T., Toda, M. (2013): Validation and application of skeletochronology for age determination of the Ryukyu ground Gecko, *Goniurosaurus kuroiwae* (Squamata: Eublepharidae). Asian Herpetological Research 4: 233-241.

Leary, C. J., Fox, D. J., Shepard, D. B., Garcia, A. M. (2005): Body size, age growth and alternative mating tactics in toads: satellite males are smaller but not younger than calling males. Animal Behaviour 70: 663-671.

Leclair, R., Castanet, J. (1987): A skeletochronological assessment of age and growth in the frog *Rana pipiens* Schreber (Amphibia, Anura) from Southwestern Quebec. Copeia 1987: 361-369.

Leclair, R. Jr., Leclair, M. H. (2011): Life-history traits in a population of the dwarf Gecko, *Sphaerodactylus vincenti ronaldi*, from a xerophytic habitat in Martinique, West Indies. Copeia 2011: 566-576.

Lovich, J. E., Gibbons, J. W. (1992): A review of techniques for quantifying sexual size dimorphism. Growth Development and Aging 56: 269-281.

Miaud, C., Guyėtant, R., Elmberg, J. (1999): Variations in life history traits in the common frog *Rana temporaria* (Amphibia: Anura): a literature review and new data from the French Alps. Journal of Zoology 249: 61-73.

Pal, A., Swain, M. M., Rath, S. (2010): Growth and demography of the Fan-throated lizard *Sitana ponticeriana* (Sauria: Agamidae) from a tropical environment in India. Herpetological Bulletin 111: 25-35.

Roitberg, E. S., Smirina, E. M. (2006): Age, body size and growth of *Lacerta agilis boemica* and *L. agilis strigata*: A comparative study of two closely related lizard species based on skeletochronology. Journal of Herpetology 16: 133-148.

Roitberg, E. S. (2007): Variation in sexual size dimorphism within a widespread lizard species. pp. 143 – 217. In: Fairbairn, D. J., Blanckenhorn, W. U. and Székely T. (eds.), Sex, Size, and Gender Roles: Evolutionary Studies of Sexual Size Dimorphism. Oxford University Press.

Smirina, E. M. (1994): Age determination and longevity in Amphibians. Gerontology 40: 133-146.

Üzüm, N., Ilgaz, Ç., Kumlutaş, Y., Gümüş, Ç., Avcı, A. (2014): The body size, age structure, and growth of Bosc's fringe-toed lizard, *Acanthodactylus boskianus* (Daudin, 1802). Turkish Journal of Zoology 38: 383-388.

Wapstra, E., Swan, R., O'Reilly, J. M. (2001): Geographic variation in age and size at maturity in a small Australian viviparous skink. Copeia 2001: 646-655.

Yakın, B. Y., Gürkan, M., Hayretdağ, S., Tok, C. V. (2012): Preliminary data on age estimation and body size of dwarf lizard, *Parvilacerta parva* (Boulenger, 1887) (Reptilia: Lacertilia) from Akşehir, Konya (Turkey). Ecologica Balkanica 4: 81-85.

Yakın, B. Y., Tok, C. V. (2015): Age estimation of *Anatololacerta anatolica* (Werner, 1902) in the vicinity of Çanakkale by skeletochronology. Turkish Journal of Zoology 39: 66-73.

Yalçınkaya, D., Göçmen, B. (2012): A new subspecies from Anatolia, *Acanthodactylus schreiberi* Boulenger, 1879 *ataturi* n. ssp. (Squamata: Lacertidae). Biharean Biologist 6: 19-31.

Yamahira, K., Conover, D. O. (2002): Intra- vs. interspecific latitudinal variation in growth: adaptation to temperature or seasonality? Ecology 83: 1252-1262.

Zhao, W., Liu, N. F. (2014): The proximate causes of sexual size dimorphism in *Phrynocephalus przewalskii*. PLoS ONE 9: 1-9.

Zug, G. R., Rand, A. R. (1987): Estimation of age in nesting female *Iguana iguana*: Testing skeletochronology in a tropical lizard. Amphibia-Reptilia 8: 237-250.

Chapter 13

RESONANT OPTICAL SOLITON PERTURBATION WITH FULL NONLINEARTIY IN THREE NONLINEAR MEDIUM

Esma ULUTAŞ[1]

1 Karadeniz Technical University, Faculty of Technology, Department of Electronics and Communication Engineering, https://orcid.org/0000-0001-7302-3674

Introduction

Optical solitons have received a great deal of attention as they can propagate without dispersing over long distance. Since they conserve their features such as amplitude, profile, speed over long distances, they play a considerably important role in optical fiber communication. Optical solitons have become a promising area of research that has led to major advances in their extensive application in nonlinear optics.

Various formulations of nonlinear Schrödinger equations are in the spotlight of numerous research studies in optics. Currently, there is increasing interest in the study of generalized nonlinear Schrödinger equations with resonance phenomena. Specifically, the resonant nonlinear Schrödinger equation (RNLSE) serves as a governing equation for optical pulse propagation within optics, characterized by distict forms of nonlinearity.

In a study by (Meradjia S., 2020), the evolution of optical pulses was elucidated, considering self-similar light wave propagation within optical fibers with varying resonant and dispersion properties using a generalized RNLSE and distributed parameters. Moreover, in a work by (Pathania S., 2021) the existence of nonlinear resonant states in a higher-order Schrödinger model governing femtosecond fiber optics propagation was demonstrated. Soliton solutions were obtained the perturbed RNLSE with t-dependent coefficients via modified simple equation method in (Biswas, 2018). In (Kudryashov, 2021), exact solutions has been found with changing the refractive index. While in (Seadawy, 2021), the conservation laws have been constructed. In addition, further relevant research studies on RNLSE have been carried out in the literature (Eslami M.)- (Abdel-Gawad).

In this current study, the Jacobi elliptic function ansatz method is employed to address the Resonant Nonlinear Schrödinger Equation (RNLSE), encompassing three distinct types of nonlinearity to attain a diverse array of solutions. The considered nonlinearity types comprise quadratic-cubic, anti-cubic, and cubic-quintic-septic nonlinearities. Within this framework, both dark and bright optical soliton solutions are uncovered.Furthermore, the study reveals Jacobi elliptic sine and cosine function solutions for each of these non-Kerr law nonlinearities. These solutions are thoroughly documented, and their corresponding criteria for existence are presented for comprehensive understanding.

Mathematical Analysis

The governing RNLSE with perturbation terms is given in its dimensionless form as:

$$iq_t + \alpha q_{xx} + \beta F(|q|^2)q + \gamma\left(\frac{|q|_{xx}}{|q|}\right)q = i[\delta q_x + \lambda(|q|^{2m} q)_x + \mu(|q|^{2m})_x q] \quad (1)$$

The first term on the left side of Equation (1) corresponds to the temporal evolution. In this equation, we have α and β, which stand for the coefficients of group velocity dispersion and nonlinearity, respectively. Additionally, γ represents the coefficient of the Bohm potential, particularly for chiral solitons with a quantum Hall effect. On the right side of the equation, you'll find δ, which characterizes the inter-modal dispersion, while λ and μ are coefficients that account

for self-steepening of short pulses and higher-order dispersion, respectively. The parameter 'm' is

responsible for incorporating full nonlinearity into the equation. In Equation (1), the function 'F' represents the specific type of nonlinearity under study. 'F(|q|²)q:C→C' indicates that this function operates on complex numbers, mapping from the complex plane 'C' to 'C,' and is k times continuously differentiable, so that

$$F(|q|^2)q \in U_{m,n=1}^{\infty} C^k((-n,n)\times(-m,m);R^2)$$

(2)

The initial assumption is:

$$q(x,t) = u(\xi)e^{i\phi}, \quad (3)$$

In Equation (3), the symbols 'u(ξ)' and 'φ' are used to denote specific components of the soliton: 'u(ξ)' represents the amplitude component of the soliton. It describes the magnitude or intensity of the soliton wave at a given point in space and time.'φ' represents the phase component of the soliton. The phase of a wave determines its position within its oscillatory cycle and plays a crucial role in describing the behavior of the soliton. In (3), u(ξ) and φ represent amplitude and phase component of the soliton respectively

and here

$$\xi = x - vt, \quad (4)$$

$$\phi = -\kappa x + \omega t + \theta \quad (5)$$

where v represents the velocity, κ is the frequency while ω and θ are the wave number and the phase constant of the soliton respectively. To further explain the process, we substitute Equation (3) into Equation (1) and then proceed to separate it into two parts: the real part and the imaginary part. This separation is commonly done to analyze and solve complex equations in terms of their real and imaginary components, making it easier to work with the equations and understand the physical implications of the solutions.

$$(\alpha+\gamma)u''-(\omega+\alpha\kappa^2+\delta\kappa)u-\kappa\lambda u^{2m+1}+\beta\mathrm{F}\left(u^2\right)u=0, \tag{6}$$

$$v+2\alpha\kappa+\delta+[\lambda(2m+1)+2m\mu]u^{2m}=0\,. \tag{7}$$

From the imaginary part (7) it is acquired the velocity of the soliton as

$$\mathrm{v}=-2\alpha\kappa-\delta \tag{8}$$

with the constraint condition on the perturbation parameters

$$\lambda(2\mathrm{m}+1)+2\mathrm{m}\mu=0 \tag{9}$$

Quadratic-cubic law

In this case

$$\mathrm{F(s)}=\beta_1\sqrt{s}+\beta_2 s \tag{10}$$

where β_1 and β_2 are constants. Therefore RNLSE is given by

$$iq_t+\alpha q_{xx}+(\beta_1|q|+\beta_2|q|^2)q+\gamma\left(\frac{|q|_{xx}}{|q|}\right)q=i[\delta q_x+\lambda(|q|^{2m}q)_x+\mu(|q|^{2m})_x q] \tag{11}$$

Eq. (6) simplifies to

$$(\alpha+\gamma)u''-(\omega+\alpha\kappa^2+\delta\kappa)u-\kappa\lambda u^{2m+1}+\beta_1u^2+\beta_2u^3=0 \tag{12}$$

The starting hypothesis is

$$u(\xi)=Asn^p(B\xi,l) \tag{13}$$

where sn represents the Jacobi elliptic sine function, l is the modulus this function and $0<l<1$. A and B are amplitude and inverse width of the soliton respectively.

If it is used hypothesis (13), Eq. (7) reduces to

$$(\alpha+\gamma)(p-1)pAB^2sn^{p-2}(B\xi,l)-(\alpha+\gamma)p[l^2(p-1)+l+p]AB^2sn^{p}(B\xi,l)$$
$$+(\alpha+\gamma)lp(lp+1)AB^2sn^{p+2}(B\xi,l)-(w+\alpha\kappa^2+\delta\kappa)Asn^{p}(B\xi,l)-\kappa\lambda A^{2m+1}sn^{(2m+1)p}(B\xi,l)$$
$$+\beta_1A^2sn^{2p}(B\xi,l)+\beta_2A^3sn^{3p}(B\xi,l)=0. \quad (14)$$

In Eq. (14), matching the terms $sn^{p+2}(B\xi,l)$ and $sn^{2p}(B\xi,l)$ and also $sn^{(2m+1)p}(B\xi,l)$ and $sn^{3p}(B\xi,l)$ yields

$$p+2=2p \quad (15)$$

and

$$(2m+1)p=3p \quad (16)$$

which gives

$$p=2, \quad (17)$$

$$m=1. \quad (18)$$

Equating coefficient of these terms and also setting coefficients of $sn^{p+j}(B\xi,l)$ for j=-2,0, to zero in (4) due to the fact that these functions are linearly independent

$$\beta_2=\kappa\lambda \quad (19)$$

$$A=\frac{l(2l+1)(\omega+\alpha\kappa^2+\delta\kappa)}{\beta_1\left(l^2+l+2\right)}, \quad (20)$$

$$B=\sqrt{-\frac{\omega+\alpha\kappa^2+\delta\kappa)}{2(\alpha+\gamma)\left(l^2+l+2\right)}} \quad (21)$$

which requires the constraint

$$\left(\omega+\alpha\kappa^2+\delta\kappa\right)(\alpha+\gamma)<0\,. \tag{22}$$

So, for quadratic-cubic law nonlinearity, the Jacobi elliptic sine function solution is obtained as follows:

$$q(x,t)=\frac{l(2l+1)(\omega+\alpha\kappa^2+\delta\kappa)}{\beta_1\left(l^2+l+2\right)}.sn^2\sqrt{-\frac{\omega+\alpha\kappa^2+\delta\kappa)}{2(\alpha+\gamma)\left(l^2+l+2\right)}}(x+(2\alpha\kappa+\delta)t),l].e^{i(-\kappa x+\omega t+\theta)}$$

(23)

When the modulus ℓ→1 in Eq. (23), it is obtained following dark optical soliton solution.

$$q(x,t)=\frac{3(\omega+\alpha\kappa^2+\delta\kappa)}{4\beta_1}.\tanh^2\sqrt{-\frac{\omega+\alpha\kappa^2+\delta\kappa}{8(\alpha+\gamma)}}(x+(2\alpha\kappa+\delta)t)].e^{i(-\kappa x+\omega t+\theta)} \tag{24}$$

In order to get exact solutions of RNLSE, we use

$$u(\xi)=Acn^p(B\xi,l) \tag{25}$$

where cn is the Jacobi elliptic cosine function. From (25), Eq. (12) reduces to

$$\begin{aligned}&(\alpha+\gamma)\left(1-l^2\right)(p-1)pAB^2cn^{p-2}(B\xi,l)+(\alpha+\gamma)p[l^2(2p-1)+l-p]AB^2cn^p(B\xi,l)\\&-(\alpha+\gamma)lp(lp+1)AB^2cn^{p+2}(B\xi,l)-(w+\alpha\kappa^2+\delta\kappa)Acn^p(B\xi,l)-\kappa\lambda A^{2m+1}cn^{(2m+1)p}(B\xi,l)\\&+\beta_1A^2cn^{2p}(B\xi,l)+\beta_2A^3cn^{3p}(B\xi,l)=0.\end{aligned} \tag{26}$$

Using the same strategy applied for Eq. (14), we get same values of which are in (17)- (19), and also

$$A=\frac{l(2l+1)(\omega+\alpha\kappa^2+\delta\kappa)}{\beta_1\left(3l^2+l-2\right)} \tag{27}$$

$$B=\sqrt{\frac{\omega+\alpha\kappa^2+\delta\kappa}{2(\alpha+\gamma)\left(3l^2+l-2\right)}} \tag{28}$$

which requires the constraints

$$\left(\omega+\alpha\kappa^2+\delta\kappa\right)(\alpha+\gamma)\left(3l^2+l-2\right)>0 \tag{29}$$

So, for quadratic-cubic law nonlinearity, we get

$$q(x,t)=\frac{l(2l+1)(\omega+\alpha\kappa^2+\delta\kappa)}{\beta_1\left(3l^2+l-2\right)}.cn^2\sqrt{\frac{\omega+\alpha\kappa^2+\delta\kappa)}{2(\alpha+\gamma)\left(3l^2+l-2\right)}}(x+(2\alpha\kappa+\delta)t),l].e^{i(-\kappa x+\omega t+\theta)} \tag{30}$$

When $l\to 1$ in Eq. (30), bright optical soliton solution is given by

$$q(x,t)=\frac{3(\omega+\alpha\kappa^2+\delta\kappa)}{2\beta_1}.\mathrm{sech}^2\sqrt{\frac{\omega+\alpha\kappa^2+\delta\kappa)}{4(\alpha+\gamma)}}(x+(2\alpha\kappa+\delta)t)].e^{i(-\kappa x+\omega t+\theta)} \tag{31}$$

Anti-cubic law

In this case

$$F(s)=\frac{\beta_1}{s^2}+\beta_2 s+\beta_3 s \tag{32}$$

where β_1,β_2 and β_3 are constants. Therefore RNLSE is given by

$$iq_t+\alpha q_{xx}+(\beta_1\frac{1}{|q|^4}+\beta_2|q|^2+\beta_3|q|^4)q+\gamma\left(\frac{|q|_{xx}}{|q|}\right)q=i[\delta q_x+\lambda(|q|^{2m}q)_x+\mu(|q|^{2m})_x q] \tag{33}$$

Eq. (6) reduces to

$$(\alpha+\gamma)u''-(\omega+\alpha\kappa^2+\delta\kappa)u-\kappa\lambda u^{2m+1}+\beta_1u^{-3}+\beta_2u^3+\beta_3u^5=0 \tag{34}$$

Using the hypothesis (13), Eq. (34) simplifies to

$$(\alpha+\gamma)(p-1)pAB^2sn^{p-2}(B\xi,l)-(\alpha+\gamma)p[l^2(p-1)+l+p]AB^2sn^p(B\xi,l)$$
$$+(\alpha+\gamma)lp(lp+1)AB^2sn^{p+2}(B\xi,l)-(w+\alpha\kappa^2+\delta\kappa)Asn^p(B\xi,l)-\kappa\lambda A^{2m+1}sn^{(2m+1)p}(B\xi,l)$$

$$+\beta_1 A^{-3} sn^{-3p}(B\xi,l)+\beta_2 A^{3} sn^{3p}(B\xi,l)+\beta_3 A^{5} sn^{5p}(B\xi,l)=0. \quad (35)$$

From Eq. (35), matching the exponents of functions $sn^{p-2}(B\xi,l)$ and $sn^{-3p}(B\xi,l)$ and also $sn^{p+2}(B\xi,l)$ and $sn^{5p}(B\xi,l)$ and then also $sn^{(2m+1)p}(B\xi,l)$ and $sn^{3p}(B\xi,l)$ yields

$$p-2=-3p \quad (36)$$

$$p+2=5p \quad (37)$$

and

$$(2m+1)p=3p \quad (38)$$

which gives

$$p=\frac{1}{2} \quad (39)$$

$$m=1. \quad (40)$$

Equating coefficients of them and setting coefficients of $sn^{p}(B\xi,l)$ to zero in (35), yields

$$\beta_2=\kappa\lambda \quad (41)$$

$$A=\left(\frac{l(l+2)(\omega+\alpha\kappa^2+\delta\kappa)}{\beta_3\left(l^2-2l-1\right)}\right)^{\frac{1}{4}} \quad (42)$$

$$B=\sqrt{\frac{-4\left(\omega+\alpha\kappa^2+\delta\kappa\right)}{(\alpha+\gamma)\left(l^2-2l-1\right)}} \quad (43)$$

with conditions

$$l(l+2)\left(\omega+\alpha\kappa^2+\delta\kappa\right)^2=\beta_1\beta_3\left(-l^2+2l+1\right)^2 \tag{44}$$

$$(\omega+\alpha\kappa^2+\delta\kappa)\beta_3\left(l^2-2l-1\right)>0 \tag{45}$$

$$(\omega+\alpha\kappa^2+\delta\kappa)(\alpha+\gamma)\left(l^2-2l-1\right)<0 \tag{46}$$

Based on above results, one gets

$$q(x,t)=\left(\frac{l(l+2)(\omega+\alpha\kappa^2+\delta\kappa)}{\beta_3\left(l^2-2l-1\right)}\right)^{\frac{1}{4}} sn^{\frac{1}{2}}\sqrt{\frac{-4\left(\omega+\alpha\kappa^2+\delta\kappa\right)}{(\alpha+\gamma)\left(l^2-2l-1\right)}}(x+(2\alpha\kappa+\delta)t),l].e^{i(-\kappa x+\omega t+\theta)} \tag{47}$$

If the modulus $l\to 1$, we get dark optical soliton solution for anti-cubic nonlinearity as follows:

$$q(x,t)=\left(-\frac{3(\omega+\alpha\kappa^2+\delta\kappa)}{2\beta_3}\right)^{\frac{1}{4}}\tanh^{\frac{1}{2}}\sqrt{\frac{2\left(\omega+\alpha\kappa^2+\delta\kappa\right)}{(\alpha+\gamma)}}(x+(2\alpha\kappa+\delta)t)].e^{i(-\kappa x+\omega t+\theta)} \tag{48}$$

In order to construct exact solutions for Eq. (33); we use hypothesis (25) so Eq. (34) reduces to

$$\begin{aligned}&(\alpha+\gamma)\left(1-l^2\right)(p-1)pAB^2cn^{p-2}(B\xi,l)+(\alpha+\gamma)p[l^2(2p-1)+l-p]AB^2cn^p(B\xi,l)\\&-(\alpha+\gamma)lp(lp+1)AB^2cn^{p+2}(B\xi,l)-(w+\alpha\kappa^2+\delta\kappa)Acn^p(B\xi,l)-\kappa\lambda A^{2m+1}cn^{(2m+1)p}(B\xi,l)\\&+\beta_1A^{-3}cn^{-3p}(B\xi,l)+\beta_2A^3cn^{3p}(B\xi,l)+\beta_3A^5cn^{5p}(B\xi,l)=0.\end{aligned} \tag{49}$$

Using the same strategy applied for Eq. (35), we acquire the same values of which are in (39)- (41) and also

$$A=\left(\frac{l(l+2)(\omega+\alpha\kappa^2+\delta\kappa)}{\beta_3\left(2l-1\right)}\right)^{\frac{1}{4}} \tag{50}$$

$$B=\sqrt{\frac{4\left(\omega+\alpha\kappa^2+\delta\kappa\right)}{(\alpha+\gamma)\left(2l-1\right)}} \tag{51}$$

with conditions

$$2(l+2)(1-l^2)=\beta_1\beta_3 \tag{52}$$

$$(\omega+\alpha\kappa^2+\delta\kappa)\beta_3(2l-1)>0 \tag{53}$$

$$(\omega+\alpha\kappa^2+\delta\kappa)(\alpha+\gamma)(2l-1)>0. \tag{54}$$

So, for anti-cubic law nonlinearity, the Jacobi elliptic function solution is obtained as follows:

$$q(x,t)=\left(\frac{l(l+2)(\omega+\alpha\kappa^2+\delta\kappa)}{\beta_3(2l-1)}\right)^{\frac{1}{4}} cn^{\frac{1}{2}}\sqrt{\frac{4(\omega+\alpha\kappa^2+\delta\kappa)}{(\alpha+\gamma)(2l-1)}}(x+(2\alpha\kappa+\delta)t),l]e^{i(-\kappa x+\omega t+\theta)} \tag{55}$$

When modulus ℓ→1 in Eq. (55), bright optical soliton solution is retrieved as:

$$q(x,t)=\left(\frac{3(\omega+\alpha\kappa^2+\delta\kappa)}{\beta_3}\right)^{\frac{1}{4}} \operatorname{sech}^{\frac{1}{2}}\sqrt{\frac{4(\omega+\alpha\kappa^2+\delta\kappa)}{(\alpha+\gamma)}}(x+(2\alpha\kappa+\delta)t)]e^{i(-\kappa x+\omega t+\theta)}$$

(56)

Cubic-quintic-septic law

Taking into consideration that

$$F(s)=\beta_1 s+\beta_2 s^2+\beta_3 s^3 \tag{57}$$

where β_1,β_2 and β_3 are constants. For this law, RNLSE is reduced to

$$iq_t+\alpha q_{xx}+(\beta_1|q|^2+\beta_2|q|^4+\beta_3|q|^6)q+\gamma\left(\frac{|q|_{xx}}{|q|}\right)q=i[\delta q_x+\lambda(|q|^{2m}q)_x+\mu(|q|^{2m})_x q]$$

(58)

and Eq. (6) changes to

$$(\alpha+\gamma)u''-(\omega+\alpha\kappa^2+\delta\kappa)u-\kappa\lambda u^{2m+1}+\beta_1 u^3+\beta_2 u^5+\beta_3 u^7=0$$

(59)

The initial hypothesis as given below

$$u(\xi) = A\left[G + sn(B\xi, l)\right]^{p} \tag{60}$$

So we get

$$\begin{aligned}
&(\alpha+\gamma)\left(1-G^2\right)\left(1-l^2G^2\right)(p-1)pAB^2\left[G+sn(B\xi,l)\right]^{p-2}\\
&+(\alpha+\gamma)p\left\{2p(1-l^2G^2)+l(1-l^2G^2)+l^2(3G^2-2)-1\right\}AB^2G\left[G+sn(B\xi,l)\right]^{p-1}\\
&+(\alpha+\gamma)p\left\{(lG^2\left(6lp-4lG+l+2\right)+l^2\left(l-2G-p\right)-l-p)\right\}AB^2\left[G+sn(B\xi,l)\right]^{p}\\
&+(\alpha+\gamma)lp\left(3l-4lp-3\right)AB^2G\left[G+sn(B\xi,l)\right]^{p+1}\\
&+(\alpha+\gamma)lp\left(lp+1\right)AB^2\left[G+sn(B\xi,l)\right]^{p+2}\\
&-(w+\alpha\kappa^2+\delta\kappa)A\left[G+sn(B\xi,l)\right]^{p}-\kappa\lambda A^{2m+1}\left[G+sn(B\xi,l)\right]^{(2m+1)p}\\
&-\beta_1A^3\left[G+sn(B\xi,l)\right]^{3p}+\beta_2A^5\left[G+sn(B\xi,l)\right]^{5p}+\beta_3A^7\left[G+sn(B\xi,l)\right]^{7p}=0.
\end{aligned} \tag{61}$$

Setting the exponents and the coefficients $\left[G+sn(B\xi,l)\right]^{p+1}$ and $\left[G+sn(B\xi,l)\right]^{3p}$ and then $\left[G+sn(B\xi,l)\right]^{p+2}$ and $\left[G+sn(B\xi,l)\right]^{5p}$ and also $\left[G+sn(B\xi,l)\right]^{(2m+1)p}$ and $\left[G+sn(B\xi,l)\right]^{7p}$ equal to one another, then equating the coefficients of $\left[G+sn(B\xi,l)\right]^{p+j}$,j=-2,-1,0 to zero, in the Eq. (61), one gets

$$p = \frac{1}{2} \tag{62}$$

$$m = 3 \tag{63}$$

$$G = \pm 1 \tag{64}$$

$$\beta_3 = \kappa\lambda \tag{65}$$

$$A = \sqrt{\frac{\beta_1\left(l+2\right)}{G\beta_2\left(l-3\right)}} \tag{66}$$

$$B=\sqrt{\frac{2\left(\omega+\alpha\kappa^2+\delta\kappa\right)}{(\alpha+\gamma)\left[8l^2G^2\left(1-G\right)+4lG\left(G-l\right)+l^2-2l-1\right]}} \tag{67}$$

It is essential to have

$$\beta_1\beta_2\left(l-3\right)>0 \tag{68}$$

$$\left(\omega+\alpha\kappa^2+\delta\kappa\right)(\alpha+\gamma)\left[8l^2G^2\left(1-G\right)+4lG\left(G-l\right)+l^2-2l-1\right]>0 \tag{69}$$

Based on above results, Jacobi elliptic function solution for cubic-quintic-septic law is given by:

$$q(x,t)=\sqrt{\frac{\beta_1(l+2)}{G\beta_2(l-3)}}\left[D+sn\sqrt{\frac{2\left(\omega+\alpha\kappa^2+\delta\kappa\right)}{(\alpha+\gamma)\left[8l^2G^2\left(1-G\right)+4lG\left(G-l\right)+l^2-2l-1\right]}}(x+(2\alpha\kappa+\delta)t,l)\right]^{\frac{1}{2}} .e^{i(-\kappa x+\omega t+\theta)} \tag{70}$$

When the modulus ℓ→1 , we acquire dark optical soliton solution as

$$q(x,t)=\sqrt{-\frac{3\beta_1}{2G\beta_2}}\left[D+\tanh\sqrt{\frac{2\left(\omega+\alpha\kappa^2+\delta\kappa\right)}{(\alpha+\gamma)\left[4G\left(3G-2G^2-1\right)-2\right]}}(x+(2\alpha\kappa+\delta)t)\right]^{\frac{1}{2}} e^{i(-\kappa x+\omega t+\theta)} \tag{71}$$

Consider the solutions in the following form

$$u(\xi)=A\left[G+cn(B\xi,l)\right]^p \tag{72}$$

Eq. (59) changes to

$$\begin{aligned}
&(\alpha+\gamma)\left(1-G^2\right)\left(1+l^2\right)(p-1)pAB^2\left[G+cn(B\xi,l)\right]^{p-2}\\
&+(\alpha+\gamma)p\left\{\left[l^2(4p-3)+l\right](G^2-1)+2p-1\right\}AB^2G\left[G+cn(B\xi,l)\right]^{p-1}\\
&+(\alpha+\gamma)p\left\{\left(1-3G^2\right)\left(2l^2p-l^2+l\right)-p\right\}AB^2G\left[G+cn(B\xi,l)\right]^{p}\\
&+(\alpha+\gamma)lp\left(4lp-l+3\right)AB^2G\left[G+cn(B\xi,l)\right]^{p+1}-(\alpha+\gamma)lp\left(lp+1\right)AB^2G\left[G+cn(B\xi,l)\right]^{p+2}\\
&-(w+\alpha\kappa^2+\delta\kappa)A\left[G+cn(B\xi,l)\right]^{p}-\kappa\lambda A^{2m+1}\left[G+cn(B\xi,l)\right]^{(2m+1)p}
\end{aligned}$$

$$+\beta_1 A^3\left[G+cn(B\xi,l)\right]^{3p}+\beta_2 A^5\left[G+cn(B\xi,l)\right]^{5p}+\beta_3 A^7\left[G+cn(B\xi,l)\right]^{7p}=0. \quad (72)$$

By doing the similar operations here that we have done for Eq. (61), values are obtained same as Eq.s (62)-(65) and yields

$$A=\sqrt{\frac{-2\beta_1\left(l+2\right)}{G\beta_2\left(l+3\right)}} \quad (73)$$

$$\mathrm{B}=2\sqrt{\frac{\left(\omega+\alpha\kappa^2+\delta\kappa\right)}{(\alpha+\gamma)\left[2l\left(1-3G^2\right)-1\right]}} \quad (74)$$

with conditions

$$\beta_1 G\beta_2<0 \quad (75)$$

$$\left(\omega+\alpha\kappa^2+\delta\kappa\right)(\alpha+\gamma)\left[2l\left(1-3G^2\right)-1\right]>0 \quad (76)$$

So, for cubic-quintic-septic law, one gets

$$q(x,t)=\sqrt{\frac{-2\beta_1\left(l+2\right)}{G\beta_2\left(l+3\right)}}\left[D+cn\sqrt{\frac{\left(\omega+\alpha\kappa^2+\delta\kappa\right)}{(\alpha+\gamma)\left[2l\left(1-3G^2\right)-1\right]}}(x+(2\alpha\kappa+\delta)t,l)\right]^{\frac{1}{2}}e^{i(-\kappa x+\omega t+\theta)} \quad (77)$$

If the modulus ℓ→1, we get bright optical soliton solution as follows:

$$q(x,t)=\sqrt{-\frac{3\beta_1}{2G\beta_2}}\left[D+\operatorname{sech}2\sqrt{\frac{\left(\omega+\alpha\kappa^2+\delta\kappa\right)}{(\alpha+\gamma)\left(1-6G^2\right)}}(x+(2\alpha\kappa+\delta)t)\right]^{\frac{1}{2}}e^{i(-\kappa x+\omega t+\theta)} \quad (78)$$

REFERENCES

1. Meradjia S., Triki H., Zhou Q., Biswas A., Ekici M., Liu W. (2020). Chirped self-similar cnoidal waves and similaritons in an inhomogeneous optical medium with resonant nonlinearity. Chaos Solitons Fractals, 141 Article 110441

2. Pathania S., Goyal A., Raju T.S., Kumar C.N. (2021). Chirped nonlinear resonant states in femtosecond fiber optics. Optik, 227 Article 166094

3. Biswas, A.,Yildirim, Y., Yasar, E., Zhou, Q., Moshokoac, S.P., Belic, M. (2018). Optical soliton perturbation with resonant nonlinear Schrödinger's equation having full nonlinearity by modified simple equation method. Optik 160 33—43

4. Kudryashov, N.A. (2021). Optical solitons of the resonant nonlinear Schrödinger equation with arbitrary index. Optik, 235 Article 166626

5. Seadawy, A.R., Ali, M.N., Husnin, S.M., Noor S. (2021). Conservation laws and optical solutions of the resonant nonlinear Schrödinger's equation with parabolic nonlinearity. Optik, 225Article 165762

6. Eslami M., Mirzazadeh M., Biswas A. (2013). Soliton solutions of the resonant nonlinear Schrödinger's equation in optical fibers with time-dependent coefficients by simplest equation approach. J. Modern Opt., 60 pp. 1627-1636

7. Das A., Saha A., Ghosh N. (2020). Dynamical behavior of the optical traveling pulses for the resonant nonlinear Schrodinger equation with external periodic force Int. J. Modern Phys. B, 34 (27) Article 2050255

8. El-Dessoky M.M., Islam S. (2020). Resonant optical solitons of nonlinear Schrodinger equation with dual power law nonlinearity. Optik, 543 Article 122445

9. Vahidi J., Zabihi A., Rezazadeh H., Ansari R. (2020). New extended direct algebraic method for the resonant nonlinear Schrodinger equation with Kerr law nonlinearity. Optik, Article 165936

10. Seadawy, A.R., Lu, D., Nasreen, N., Nasreen, S., (2019). Structure of optical solitons of resonant Schrödinger equation with quadratic cubic nonlinearity and modulation instability analysis. Physica A 534 122155

11. Bulut, H., Sulaiman, T. A., Baskonus, H. M. (2018). Optical solitons to the resonant nonlinear Schrödinger equation with both spatio-temporal and inter-modal dispersions under Kerr law nonlinearity, Optik 163 49-55

12. Das, A., Jash, S., Paul, S., Mondal, Y. A., Das, A. (2021). Optical chirped soliton structures in generalized derivative resonant nonlinear Schrödinger equation and modulational stability analysis. Optik 226, 1, 165701

13. Inc M., Aliyu A.I., Yusuf A. (2017). Solitons and conservation laws to the resonance nonlinear Shrödinger's equation with both spatio-temporal and inter-modal dispersions. Optik, 142, 509-522.

14. Abdel-Gawad, H. I., Park C. (2021). Interactions of pulses produced by two- mode resonant nonlinear Schrodinger equations, Results in Physics 24 Article 104113

Chapter 14

ELECTRONIC STATES OF DISORDERED AND QUASICRYSTALS: A THEORETICAL APPROXIMATION*

Abdulkadir YILDIZ[1]

1 Abdulkadir YILDIZ, Prof.Dr., Kahramanmaraş Sütçü İmam University, Faculty of Science, Department of Physics, Kahramanmaraş, Türkiye, ORCID:0000-0001-7724-6090.

* This review mostly produced from myPhD thesis, 'Yildiz, A. (1995). A new technique to calculate the electronic structure of disordered and quasicrystal systems in two-dimensions. University of Leicester (U.K). Supervisor: Prof.Dr.J.L.Beeby to whom this review attributed,

I. Introduction

The subject of electronic states of disordered and quasicrystals has been continuous theoretical and experimental interest for a couple decades due to their great applications in technological use. During this period, significant progress has been made in both theoretical and experimental aspects of these systems, in particular, disordered materials such as silica and metallic glasses, amorphous semiconductors, binary and ternary alloys, organic semiconductors, etc,. Although much effort has been put into the field of disordered systems over a long period, the progress in the study of these systems, in particular, structurally disordered systems, has been relatively slow and delayed in comparison with that of ordered (crystalline) materials. Two principal reasons for this delay may be pointed out; the first is the complexity of the mathematical problems that naturally arise in the study of electronic features in these systems, and the other is the absence of any real simplifying feature in the geometry of such systems. Basically, there is no periodicity in the structure to carry out the elegant theorems implicit as in the theory of crystalline solids such as Bloch's theorem [**1**, and the **refs.** in there].

In a crystal an electron outside an atomic core can be represented by a wavelike excitation which extends spatially throughout the whole structure with equal probability just as in free electron case. Therefore, Bloch's theorem can be implemented easily to determine the band structure of the system over the reduced the infinite problem to a single unit cell, and the band structure can then calculated from the so-called dispersion relation. On the other hand, in the case of disordered systems, the conventional concepts such as Bloch's theorem, quasi-momentum (k), unit cell, Brillion zone, symmetry, wave numbers, which describe the electron states and properties in an ordered system (or crystal), are no longer valid due to the lack of translational symmetry. In addition, the lack of periodicity allows the wave functions to be localized or extended depending on the degree of disorder, the energy of state and the dimensionality of system. As result, various theoretical approaches/techniques (such as CPA, ATA, DFT..) have been devised and developed in order to investigate the electronic properties of these systems in one-dimension (1D), two dimensions (2D) and three-dimensions (3D). Many are restricted to simplified forms of approximations such as tight-binding theory, nearly free electron theory and variational method [**2,3**], and are not powerful enough to describe fully the electronic properties in all non-periodic materials.

However, interest in a newly defined non-periodic material, the so-called quasicrystals, has also been grown considerably in the past few decades [**1,4,5**]. Note that by non-periodic materials we mean substances that range from liquids or amorphous solids (structurally disordered) to quasicrystals with perfect long-range order (but with no three-dimensional periodicity

ingredient). Quasicrystals brought a dramatic change to scientists' way of thinking about the structure of solids since their diffraction pattern has no crystallographic symmetries but, nevertheless consists of sharp peaks [1]. They have long-range directional order and sort-range disorder, and can be crystallographically forbidden rotational symmetries (e.g. five-fold, ten-fold, etc.). Investigations into the microstructure of these materials have confirmed that they embody a new kind of order, neither crystalline nor completely amorphous, but somewhere in between the two limits. The fundamental physical properties of quasicrystals are expected to have intriguing features since their structures are situated between regular crystals and disordered systems [**1**].

In this chapter, a theoretical method based on multiple scattering theory, called Beeby&Hayes (BH) method [**6**] will be reviewed in brief, and the new formalism and applications developed by Yildiz&Beeby in the previous studies for calculating the electronic structure of 2D disordered systems, alloys and quasicrystals will be presented to keep the theory on the agenda of theoretical studies based on the multiple scattering theory. We believe that there are many aspects of the method that are unexplored or open to be developed for calculating the electronic structure of disordered systems because there is no yet a powerful theoretical method to overcome fully the electronic structure of disordered systems and quasicrystals. Though the calculations based on the computational quantum methods, such as Density of Function theory (DFT) which is now a dominant method among the others, they have even some limitations such as the weakness of correctly treat the exchange interaction. For sake of all these reasons we strongly believe that BH method or as such theoretical methods should be in agenda of scientific activities and instruments, and so that it may go further from than where we left.

1.1 Disorder Systems

The concept of disorder implies defective order, and in statistical terms means *random stochastic, unpredictable* as described by Ziman [**7**]. Generally speaking, a system having a non-periodic random structure, i.e. consisting of atom or molecule arranged in a pattern that does not repeat periodically, can be called disordered. Though many authors [**8**] have classified disorder as structural, compositional, cellular, topological, quantitative, magnetic, and so-called ice disorder, these systems can, in principle, be divided into two classes depending on *the type* and *degree* of disorder in their structure. The first depending on the type is called substitutional (compositional) disorder in which some of host atoms of a periodic lattice are replaced by different atoms arising in metals, some

semiconductors and ionic crystals. The other type depending on its degree is called topological or structural disorder occurring in liquids, amorphous materials. Simple models of 2D disordered systems are representatively shown in Figure 1. Understanding of electronic structure of such materials in various fields science are of great interest because of their potential application in technology such as steel alloys, amorphous semiconductors, liquid metals, glasses and their application in photovoltaic cells, thin film devices, and so on.

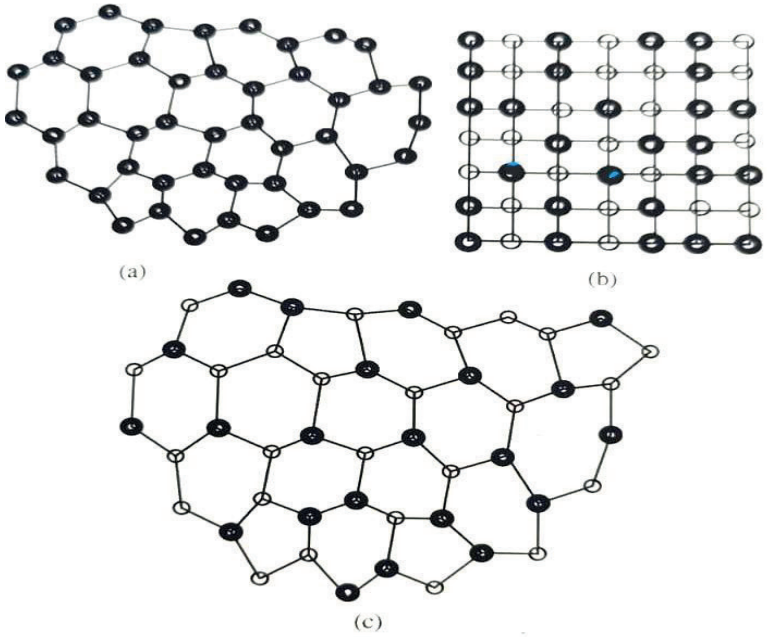

Figure 1.: Disordered systems: (a) structural, (b) compositional and (c) structural and compositional [1].

2. Beeby&Hayes Method

Beeby&Hayes method (from now on to be referred as BH method) is based on multiple scattering theory for non-overlapping muffin-tin potentials and first applied to tetrahedrally bonded disordered systems [6,8] in three dimension for calculating the electronic structure, which gave confidence for application to the other systems possessing short-range order (SRO). Note that the detailed theory of the method for 3D disordered system are discussed in detail in refs [**9,10**]. The application and expansion of the method for the

electronic structure, in particular the density of states (DOS), in 2D disordered and quasi-crystals will be introduced in this section.

The method that we used to evaluate the DOS yields a powerful approximation for determining the electronic structure of disordered and crystalline systems. The calculated function is the total scattering matrix T which represents the sum over all atoms of the set of all possible scattering paths from the given atom [**1,2**]. Once this total scattering matrix is found, the DOS can be evaluated from its imaginary part. If the scattering from successive atoms are treated as being independent and separated by the motion of the electron between those atoms the total scattering matrix can be written as an infinite expansion, in a simplified but reasonably clear notation:

$$\mathbf{T} = \sum_a \mathbf{T}^a = \sum_a (\boldsymbol{t_a} + \sum_{b(\neq a)} \boldsymbol{t}_a \boldsymbol{G}_0^{ab} \boldsymbol{t}_b + \sum_{b(\neq a),c(\neq b)} \boldsymbol{t}_a \boldsymbol{G}_0^{ab} \boldsymbol{t}_b \, G_0^{bc} \boldsymbol{t}_c + \cdots) \quad (1)$$

Here $\boldsymbol{t_a}$ and **G** are matrices, and the t-matrix describing electron scatterin from atom *a* and $\mathbf{G}_0^{ij}$ is the free electron propagator from site *i* to site *j* and contains all the information about the arrangement of the atoms which bears on the density of electronic states. This is an exact result when the potential is of muffin-tin form. Basically, $\mathbf{T}^a$ in eqn. (1) refers to the contribution to the scattering matrix associated with successive neighbours of atom *a*. Eqn (1) for a 2D disordered system as function of electron momentum k has been defined as [**1,2**]

$$\mathbf{T}(\mathbf{k}) = 2\pi \sum_{a,mm'} (-i)^{m-m'} \exp[i(m - m')\theta_k] \, [\, (\boldsymbol{t}(k,k) + \sum_{b(\neq a)} \boldsymbol{t}(k,\kappa)\mathbf{G}^{ab}(\kappa,\mathrm{k})\boldsymbol{t}(\kappa,\mathrm{k}) + \sum_{b(\neq a),c(\neq b)} \boldsymbol{t}\,(k,\kappa)\mathbf{G}^{ab}(\kappa,\mathrm{k})\boldsymbol{t}(\kappa,\kappa)\mathbf{G}^{bc}(\kappa,\mathrm{k})\boldsymbol{t}(\kappa,\mathrm{k}) + \cdots]'_{mm} \quad (2)$$

where **t** and **G** are functions of k and of the energy E through $\kappa \equiv E^{1/2}$. *m* and *m'* are angular momentum indices. The matrix **t** for an atomic potential, which is non-zero only a given circle or so called muffin-tin potential, has been Fourier transformed into a matrix with elements

$$t_{mm'}(p,p') = \frac{1}{2\pi} \int J_m(pr) \exp(-im\theta_r) t(\boldsymbol{r},\boldsymbol{r}') J_{m'}(p'r') \exp\left(im'^{\theta_{r'}}\right) d\boldsymbol{r} d\boldsymbol{r}'. \quad (3)$$

If the potential is circularly symmetric, $t_{mm'} = t_m \delta_{mm'}$, *and so t is* dioganal in angular momentum. The elements of the matrix **G** are related to the particle propagator $\mathbf{G}_0$ through the equation [1]

$$\boldsymbol{G}_{mm'}^{ab} = -\frac{1}{2\pi}\frac{\exp\left[-i\boldsymbol{k}.(\boldsymbol{R_a}-\boldsymbol{R_b})\right]\int \exp\left(-im\theta_r\right)G_0(\boldsymbol{r}-\boldsymbol{r'}+\boldsymbol{R_a}-\boldsymbol{R_b})\exp\left(im'\theta_{r'}\right)d\theta d\theta_{r'}}{J_m(\kappa r)J_{m'}(\kappa r')} \quad (4)$$

Integrating this expression using the free electron form of G_0 and expanding the exponential gives

$$G_{mm'}^{ab} = -\sum_v (-i)^{m'-m+v} J_v(kR) K_{m-m'}(\mu R) \exp[i(m'-m-v)\theta_R] \exp(iv\theta_k), \quad (5)$$

where $\mu = (-E)^{1/2}$ is real for E < 0 and R is the distance between two atoms. The bond direction is denoted by θ_R and is defined precisely below. If a circularly symmetry potential is used and s-wave scattering is considered, then the only non-zero terms are those for which $m, m' = (0,0)$. $\mathbf{G}^{ab}$ then includes as a factor the modified Bessel function of zero order, namely $K_0(\mu R)$, which is equivalent to the factor $exp(-\mu R)$ which apears in the 3D systems and is approximately of the same exponential form in the 2D systems. In the case of E < 0 this factor implies the unimportance of all $\mathbf{G}^{ab}$ expect those atom a and b are near neighbours of each other. We note that the calculations which have been evaluated here are confined to the energy range E < 0 for which $\mu = (-E)^{1/2}$ is real.

In order to understand some physical properties of disordered systems, such as the density of states (N(E)), through eqn. (2) the imaginary part in 2D systems has been written as,

$$Im < \mathbf{T}(\mathrm{k}) >$$
$$= 2\pi \mathrm{Im}\left[\sum_{m,m'} (-i)^{m-m'} \exp[i(m-m')\theta_k] \frac{t_m(k, i\mu)}{t_m(i\mu, i\mu)} \times \right.$$
$$\left. < \sum_a \boldsymbol{F}^a(i\mu, k) >_{mm'} t_{m'}(i\mu, i\mu) \frac{t_m(i\mu, k)}{t_{m'}(i\mu, i\mu)} \right] \quad (6)$$

where the term $\mathbf{F}^a$ is another representation of the total scattering beginning at one atom and reflects motion of the electron through system discussed in detail by Beeby and Hayes in [**6**];

$$\mathbf{F}^a = 1 + \sum \boldsymbol{tG}^{ab} + \sum \boldsymbol{tG}^{ab}\, \boldsymbol{tG}^{bc} + \cdots = 1 + \sum \boldsymbol{tG}^{ab}\, \mathbf{F}^b \quad (7)$$

Note that each $\mathbf{F}^a$ contains all those multiple atom-scattering paths in which the electron starts atom *a*, moves to another potential at atom *b* and scatters from there and so on. Thus the continuity of this scattering sequences actually makes the contribution to the spectral density dependent on the position of neighbouring atom.

In disordered systems one of a useful physical quantity of interest related to the density of states of electronic states is the spectral density $\rho(\boldsymbol{k}, E)$, which is defined as the probability of finding an electron having energy E and real momentum **k**. This function is given in terms of the total scattering matrix by

$$\rho(\boldsymbol{k}, E) = -(\pi\Omega_0)^{-1} (\mathrm{E} - \mathrm{k}^2)^{-2} \mathrm{Im}\langle \mathbf{T}(\mathbf{k}) \rangle, \quad (8)$$

where Ω_0 is the volume of the system. As can be seen that the spectral density is related to imaginary part of the average of **T**(**k**), which is the diagonal part of the double Fourier transform of the scattering matrix.

2.1 Applications to Two-Dimensional Systems

In the earlier Studies [**1-3**], the method was applied to both 2D disordered models, e.g triangle-like, honeycomb-like, square-like, five-fold, etc., and a

2D quasicrystal (Penrose lattice) in which we demonstrated the applicability of the method by calculating the density of states which will be reviewed in brief and the formulation will be given in a compact form. We note that two-dimensional systems can be realized in layer compounds, such as graphite intercalation compound, in which the atomic layers are widely separated and weakly interacting. In experimental studies, the inversion layers used in quantum Hall-effect provide an example of 2D system important in technology as do MOS space charge layers and semiconductor heterostructures [**3**].

We illustrate then procedure initially by using a continuous structural network with threefold coordination of atoms in a planar structure related to the honeycomb lattice, and the bond lengths between two atoms being treated as always the same. This corresponds to neglecting variations in the motion of electrons between pairs of atoms, often referred to as hopping. In the system the disorder manifests itself in the bond angles, giving a structure with rings of various sizes. The disorder of system have been described in a statistical way by defining a distribution function on the bond angles which approximates the discrete distribution of the bond angles arising from the actual ring statistics. Each atom and its environment has been defined in terms of a set of coordinate axes. Thus, the propagator modifier **F** in eqn. (7) are established as a function of all the angles, bond lengths, the number of species of neighbours required to specify the system. For example, a simple model with three-fold coordinated structure has been taken in the *xy* plane Figure (1). In order to characterise an atomic environment in terms of the angular variables, a suitable set of Fourier functions will be introduced leading to a matrix element depending on the rotation angles between circular harmonics in the laboratory coordinate system. In a large system of figure (1), we assume that the first scattering is taking place at atom (or ion) *a,* and after scattering

there the electron may propagate to the nearest neighbour atom, and scattering goes on throughout the system. The contribution to the DOS of these sequences from atom *a* depends on the positions of the other potentials, such as atom *b*, relative to *a*. However, the major contribution to the DOS comes from the nearest neighbouring atoms (or ions). This is one of the powerful property of this method to be applied to disordered systems having sort range order (SRO). Therefore, for a particular atom, the function **F** can be approximately described by treating it as a function only of its local set of angles. Averaging over the spread of distant angles but keeping the local angles fixed, the scattering function corresponding to atom *a* can be written in terms of its neighbour, atom *b*, as

$$<\mathbf{F}^a>_a = \mathbf{1} + \sum \boldsymbol{t} < \boldsymbol{G}^{ab}\,\mathbf{F}^b >_a \qquad (9)$$

where the subscript a on the averages indicates that the angles at *a* are fixed

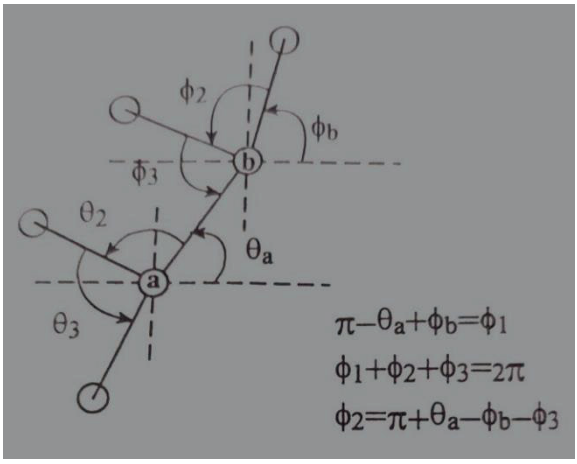

Figure 2: A simple model with threefold coordinated structure [**1**]

It can be approximated each $\mathbf{F}^a$ by a Fourier series involving the local angles only using the notaion of Figure 1 as

$$\boldsymbol{F}^{a}(\theta_a, \theta_2, \theta_3) = \sum_{m_i=-\infty}^{\infty} \boldsymbol{A}_m e^{(im_1\theta_a + im_2\theta_2 + im_3\theta_3)} \tag{10}$$

and

$$\boldsymbol{F}^{b}(\emptyset_a, \emptyset_2, \emptyset_3) = \sum_{m'_i=-\infty}^{\infty} \boldsymbol{A}_m e^{(im'_1\emptyset_a + im'_2\emptyset_2 + im'_3\emptyset_3)} \tag{11}$$

The subscript m on **A** represents the vector (m_1, m_2, m_3), and the m_i are integers, i.e. 0, ±1, ±2, …. The function to be averaged over angles in eqn. (9) is only $\mathbf{F}^b$ because the magnitude of R is taken to be the same for all atoms for now. In order to implement the averaging, a probability function $P(\theta_i)$, for the angles around atom *a*, are defined in a Gaussian form as $P(\theta_i) = Nexp\ [-(\theta_i - 2\pi/n)^2 / w^2)]$. This function describes the probability of finding a particle between θ_i + and $\theta_i + d\theta_i$ and where N is the normalization coefficient, *n* is the coordination number, and *w* stands for the degree of disorder which can be varied from *0.0* to ∞ representing from complete order to complete disorder. However, eqn. (11) is required to be averaged by multiplying the probability function and integrate over the angles which gives;

$$< \boldsymbol{F}^{b} > = \sum A_m e^{im'_1\theta_b}\, \Gamma(\, m'_1, m'_2, \ldots.; w) \tag{12}$$

Where $\Gamma(\, m'_1, m'_2, \ldots.; w)$ is called structural factor consisting the terms related to the rotational angles and disorder parameter. Eqn.(12) gives some information about atom *b* relevant to second nearest neighbour atoms to atom *a*. As result, eqn.(9) takes the form,

$$\begin{aligned} \boldsymbol{A}_{m_1 m_2 m_3} = {} & \delta_{m_{1,0}}\delta_{m_{2,0}}\delta_{m_{3,0}} 1 \\ & - \sum_{\upsilon m'_1 m'_{2_3} m''} tG_{\upsilon m''} A_{m'_1 m'_2\ m'_3}\, \Gamma(\, m'_1, m'_2, \ldots.; w)\delta(m'_1 \\ & + m'' - \vartheta - m_1) \\ & \times \Big(\delta_{m_{2,0}}\delta_{m_{3,0}} + \delta_{m_{1,m_2}}\delta_{m_{3,0}} \\ & + \delta_{m_{1,m_2}}\delta_{m_{1,m_3}} \Big) \end{aligned} \tag{13}$$

where $G_{\upsilon m''} = (-i)^{m''+\upsilon} J_\upsilon(kR) K_{m''}(\mu R)$ and the two types of index are linked because $m'' = m' - m$, and the three terms in the final brackets originate from the three neighbours. Finally the coefficient A satisfies a matrix equation and

gives **F** through eqn. (10). Eqn.(13) can be written in a matrix form to evaluate its eigenvalues and eigenvectors for calculating the spectral density. That is,

$$\mathbf{A} = \mathbf{e} + \mathbf{MA} \tag{14}$$

The solution of matrix **M** can be found in terms of the eigenvalues and eigenvectors ;

$$\boldsymbol{A} = \sum_i \boldsymbol{u_i} (1-\lambda)^{-1} \boldsymbol{u_i^T}.\boldsymbol{e} \tag{15}$$

where **e** is a column vector with element which are equal to one when m = 0 and zero otherwise. ρ (**k**, E) = depends on the imaginary part of $\mathbf{A}_{000}$ and is non-zero only for values of *k* and E such that $\lambda_i = 1$ giving

$$\int \rho(\boldsymbol{k}, E) d\theta_k$$

$$= -\frac{1}{2\pi} \sum_{mm'} \left[\frac{s_m(k)}{s_m(i\mu)}\right]\left[\frac{s_{m'}(k)}{s'_m(i\mu)}\right] \frac{s_m(i\mu)}{\frac{\pi}{2}}\, Im[\boldsymbol{A}_{000}]_{mm'} \tag{16}$$

Where $Im\boldsymbol{A}_{000} = -\pi \sum_i [u_i]_{000} \delta\,(E - E_i(k))(\partial\lambda_i/\partial E)^{-1}(\boldsymbol{u_i^T}.\boldsymbol{e}\,)$. Here the function s is related to the scattering potential and must be derives from the chosen potential. When an explicit potential is used, the functions *s(k)* and *s(iμ)* must be evaluated. In this study a circularly symmetric potential has been used and only s- wave scattering is taken into account for calculation of the DOS of the systems considered here. In general case **t** and the coefficients **G**, and hence **A**, are matrices in the angular momentum representation. But for circularly symmetric potential the matrix t is diagonal in angular momentum, but **G** is not, propagating from one atom site to another giving rise to effects as s-p hybridization. The expression for $\mathbf{G}_{vm''}$ in eqn. (13) becomes

$G_{vm''} = -(-i)vJ_v(kR)K_0(\mu R)\delta_{m'',0}$. Thus the momentum dependence of the matrix is due to $J_{m'1}(kR)$ and the energy dependence takes the form $U(E) = t_0(i\mu, i\mu)K_0(\mu R)$. Finally, one has a matrix equation for the vector **Ω** which is the general expression that we used to evaluate the eigenvalues and eigenvectors for calculating the DOS.

$$\Omega_{m1} = \delta_{m1,0} - t_0 \sum \sqrt{\gamma_{m1}}\sqrt{\gamma_{m'1}} J_{m'_1}(kR) K_0(\mu R)(-)^{m'_1}\Omega_{m'_1}$$

$$= \delta_{m1,0} + U(E)\sum_{m_1} H_{m_{1,m'_{1,}}}(k)\Omega_{m'_1} \tag{17}$$

For example, for a narrow s band and E<<0 the energy dependence is given by $U(E) \approx W/(E - E_b)$, where E_b is the bound state energy of single muffin-tin potential and W is a parameter related to the bond.

2.2 Calculation of The density of states

In order to illustrate the method, the DOS for honeycomb, square lattice and penrose lattice will presented in this section. Appropriate values for atomic parameters of the systems, such as the strength of the potential and the bond length are taken. For example the potential radius r = 0.5 (a.u) and the bond length between two atoms or ions R = 2.0, which results in a ground state energy of E_0 = -30 (a.u). In this case, the atoms are far apart from each other and so these assumptions lead to a very narrow band of allowed states around the atomic ground state energy, E_0. We have first calculated the DOS of a threefold system in 2D in which several values of disordered parameters have been into account as seen in Figure 3. For example, if the value of $w = 0.0$, corresponding to a perfect honeycomb lattice, two singularities appear as expected (two atoms in a unite cell), and as value of w increases or $\neq 0.0$ the order of bond angles varies, and thus via that the order of system is broken and becomes disorder. Hence, as the value of w increased the DOS spread towards the gap and the singularities were reduced. Likewise, similar calculations have been done for triangle structure, square lattice. The results are shown in Figures (4).

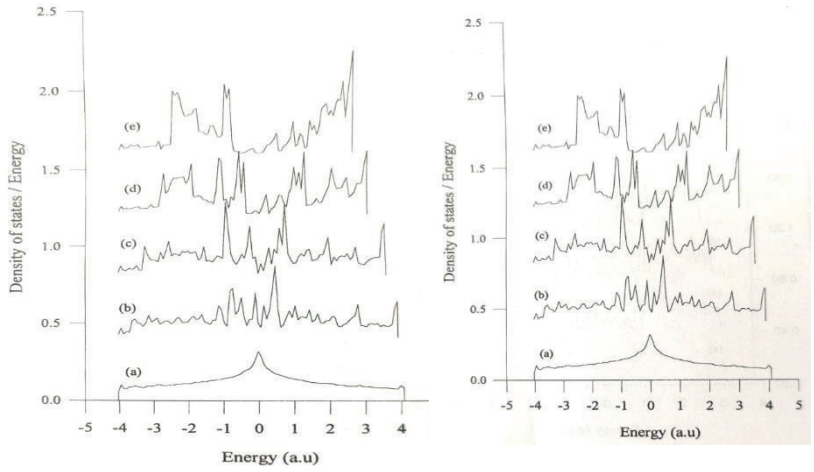

Figure 3: The density of states for honeycom-lattice-like structural disorder (w) (on the LHS) and The density of states for square-lattice-like structural disorder (w) (on the RHS): a) w = 0.0, b) w = 0.1, c) w = 0.4, d) w = 0.7. [**1,3**]

As can be seen in the Figure 4 that the variation of the DOS with respect to the disorder parameter (w) is observed, and the results for these cases showed good agreement with theoretical expectation. The variation of the DOS significantly changed or shift towards edges when the value of disorder (w) exceed 0.25 rad. We suspect that such shift may be related to localisation of electrons which is an important physical quantity of research. On the other hand, for small disorder (w <<0.25) the DOS spread towards the gap and the sharp edges were reduced in amplitude as expected. As a result, this method can be extended to more realistic problems in theoretical studies.

Secondly, the method has applied to two-dimensional quasicrystal, i.e. Penrose lattice / Penrose Tiling given in Figure 4. There are two man types of Penrose lattice; one is R Penrose tiling constructed with thick and thin rhombi which is of interest of this study, and the other is KD Penrose tiling by kites and darts, which is not of interest in this review. However, in real applications, x-rays and electron reflected from the crystals, say tiny metallic crystals of aluminum and manganese, showed Penrose five-fold symmetry. For example, the diffraction patterns that the Penrose tiling produce are intriguingly similar to those of decagonal (ten-sided) quasisystems as seen in Figure 4. Althoug there has been considerable progress on the electronic structure of this structure in recent years [4,12,13], the question to be investigated what the theoretical calculation of elecronic structure of these systems in an infine limit.

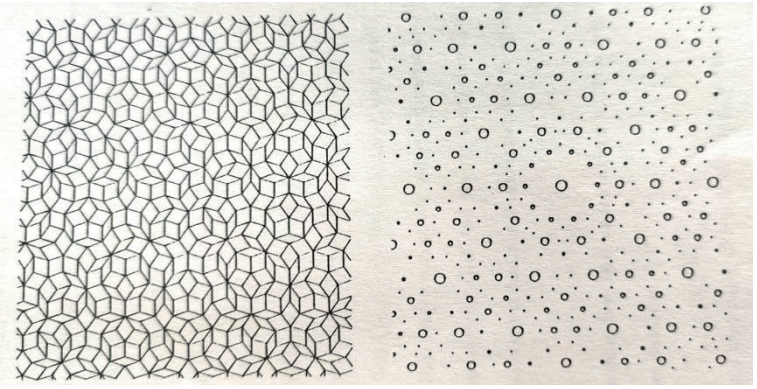

Figure 4: R Penrose tiling (LHS) produced a diffraction pattern of spots (RHS) that has a five-fold symmetry [1].

In the R type of Penrose tiling there are eight types of vertices assigned as D,J,Q, K, S3, S4, S5 and S which are given in almost every one of textbook

related quasicrystals. Each has a different concentration and neighbourhood distribution in the structure. The contribution to the DOS from each atom , or pattern, is directly proportional to the concentration of each pattern in the system. The application of the method is straighforward provided that the essential parameters, such as the bond length and the angles between two atoms, the probability of finding a particular relation of a atom to its near neighbourhood atoms and the frequency of each atom, associated with the local structure of each atom are known. These parameters are well- known and defined by Kumar *et al*.[11]. Hence, for each vertex or pattern eqn. (7) can be easily defined and evaluated. Here the axis is represented by θ_b, defined relative to some absulate direction, and fitted on a symmetric bond as illustrated in detail in ref. [2]. The general form of the equation for the scattering function describing each pattern environment can be written as

$$\boldsymbol{F}^i(\theta) = \mathbf{1} + \sum_{i,j} P_{i,j}\, \boldsymbol{t}\ \ \boldsymbol{G}^{ij}\boldsymbol{F}^j(\theta \pm \gamma) \qquad (18)$$

Hence it is possible to write for a pattern of Penrose tiling the $\mathbf{F}^i$ matrix in terms of the local parameters, including its orientation, neighbours and average probability distributions of those neigbours as

$$\begin{aligned} F^{S4}(\theta_b) &= 1 + \mathbf{t}\,[G_{II}(\theta_b-\pi)P_{S3,J}F^J(\theta_b-\pi) + G_{II}(\theta_b-\tfrac{3\pi}{5})P_{S3,J}F^J(\theta_b-\tfrac{3\pi}{5}) \\ &+ G_{II}(\theta_b+\tfrac{3\pi}{5})P_{S3,J}F^J(\theta_b+\tfrac{3\pi}{5})G_{II}(\theta_b+\tfrac{\pi}{5})P_{S3,D}F^D(\theta_b-\tfrac{2\pi}{5}) \\ &+ G_{II}(\theta_b-\tfrac{\pi}{5})P_{S3,D}F^D(\theta_b+\tfrac{2\pi}{5}) + G_{II}(\theta_b)P_{S3,D}F^Q(\theta_b-\pi)] \end{aligned}$$

where Pij is the probabilities of possible neighbour atoms. Similarly, for the other vertex, **F** matrix function are defined (see in detail ref. [1]), and so that the compact form of the function is reduced to

$$\boldsymbol{F}^a_m = \mathbf{1} + \sum_{neighbours} P_{a,neigh.} \cdot \boldsymbol{t} \sum_{neighbours} G^{a,b}\boldsymbol{F}^b_{m'}(\theta_b) \qquad (19)$$

Or in a compact form,
$\mathbf{F} = \mathbf{e} + t_0\, \mathbf{M}_{m'}\mathbf{F}_{m'}$

where *a* and *b* stand for the atom types, due to 8 different patterns, **F** is a block vector with blocks labelled by pattern type and elements of the blocks labelled by *m*. **e** is a block vector consisting of the identity matrix if *m* = 0, and zero

elsewhere. **e** is a block vector consisting of the identity matrix if $m = 0$, and zero elsewhere. Matrix **M** is *a* complex (through G) and non-symmetric block matrix but physically its eigenvalues must be real. This matrix can be converted to symmetric form which make the solution much easier, Having proceeded this equation and reduced the computational form, the result is reduced to a symmetrik real matrixi that is

$$t_0^{-1}\boldsymbol{\Lambda} = t_0^{-1}\boldsymbol{e}' + \boldsymbol{M}'\boldsymbol{\Lambda} \tag{20}$$

where the matrix **M'** is then a symmetric matrix are written in a open form,

$$\begin{bmatrix} . & . & . & . & . & . & . & . \\ . & \mathbf{M}_3^T & \mathbf{M}_2^T & \mathbf{M}_1 & \mathbf{M}_2 & \mathbf{M}_3 & . & . \\ . & . & \mathbf{M}_3^T & \mathbf{M}_2^T & \mathbf{M}_1 & \mathbf{M}_2 & \mathbf{M}_3 & . \\ . & . & . & \mathbf{M}_3^T & \mathbf{M}_2^T & \mathbf{M}_1 & \mathbf{M}_2 & \mathbf{M}_3 \end{bmatrix} \begin{bmatrix} . \\ \boldsymbol{\Lambda}_{-1} \\ \boldsymbol{\Lambda}_0 \\ \boldsymbol{\Lambda}_1 \\ . \end{bmatrix} = \lambda \begin{bmatrix} . \\ \boldsymbol{\Lambda}_{-1} \\ \boldsymbol{\Lambda}_0 \\ \boldsymbol{\Lambda}_1 \\ . \end{bmatrix} \tag{21}$$

where $\mathbf{M}_1$, $\mathbf{M}_2$, $\mathbf{M}_3$...., are 80×80 matrices of form

$$\boldsymbol{M}_1 = \begin{bmatrix} J_0\boldsymbol{m}_{00} & J_1\boldsymbol{m}_{01} & J_2\boldsymbol{m}_{02} & J_3\boldsymbol{m}_{03} \\ J_1\boldsymbol{m}_{01}^T & J_0\boldsymbol{m}_{11} & J_1\boldsymbol{m}_{01} & J_2\boldsymbol{m}_{02} \\ J_2\boldsymbol{m}_{02}^T & J_1\boldsymbol{m}_{01}^T & J_0\boldsymbol{m}_{22} & J_1\boldsymbol{m}_{01} \\ J_3\boldsymbol{m}_{03}^T & J_2\boldsymbol{m}_{02}^T & J_1\boldsymbol{m}_{01}^T & J_0\boldsymbol{m}_{33} \end{bmatrix}, \boldsymbol{M}_2 = \begin{bmatrix} J_4\boldsymbol{m}_{00} & J_5\boldsymbol{m}_{01} & J_6\boldsymbol{m}_{02} & J_7\boldsymbol{m}_{03} \\ J_5\boldsymbol{m}_{01}^T & J_4\boldsymbol{m}_{11} & J_5\boldsymbol{m}_{01} & J_6\boldsymbol{m}_{02} \\ J_6\boldsymbol{m}_{02}^T & J_5\boldsymbol{m}_{01}^T & J_4\boldsymbol{m}_{22} & J_5\boldsymbol{m}_{01} \\ J_7\boldsymbol{m}_{03}^T & J_6\boldsymbol{m}_{02}^T & J_5\boldsymbol{m}_{01}^T & J_4\boldsymbol{m}_{33} \end{bmatrix},$$

with $\mathbf{m}_{ij}$ the 8x8 matrices for the lattice. Each row of the eigenvector equation can be written

$$\begin{aligned} \boldsymbol{M}_1\Lambda_0 + \left(\boldsymbol{M}_2 e^{i\alpha} + \boldsymbol{M}_2^T e^{-i\alpha}\right)\Lambda_0 + \left(\boldsymbol{M}_3 e^{i2\alpha} + \boldsymbol{M}_3^T e^{-i2\alpha}\right)\Lambda_0 + \ldots \\ + \left(\boldsymbol{M}_N e^{i(N-1)\alpha} + \boldsymbol{M}_N^T e^{-i(N-1)\alpha}\right)\Lambda_0 = \lambda\Lambda_0 \end{aligned} \tag{22}$$

which is a Hermitian 80x80 matrix equation. The normalisation can be done as $\Lambda_0^*(\alpha = 2\pi j/N)\,\Lambda_0\left(\alpha = 2\pi j/N\right) = 1/N$, ($j$=0, 1, N-1). Thus equation (22) has N sets of 80x80 eigenvectors and eigenvalues, and from which the imaginary part related to the spectral function is

$$Im\boldsymbol{\Lambda}_0 = -\frac{\pi}{N} t_0^{-1} \sum_{\alpha,n} \left(\sum_j \eta_j^{\frac{1}{2}} \boldsymbol{\Lambda}_{nj}^{\alpha} \right) \delta(t_0^{-1} - \lambda_n^{\alpha}) \left(\sum_j \eta_j^{\frac{1}{2}} \boldsymbol{\Lambda}_{nj}^{\alpha'} \right) \cdot \boldsymbol{e} \qquad (23)$$

and then the spectral function is

$$\rho(\boldsymbol{k}, E) = \frac{12}{\Omega_0} \frac{1}{[E-k^2]^2} \sum_{mm'} \left[\frac{s_m(k)}{s_m(i\mu)} ç \frac{s_{m'}(k)}{s_{m'}(i\mu)} \right] \quad . Im\, \boldsymbol{\Lambda}_0 \qquad (24)$$

The eigenvalues and eigenvectors are determined from the matrix and the DOS can then evaluated form the eqn. (24). The density of states per atom , N(E), has been calculated from

$$n(E) = \frac{\Omega_0}{4\pi^2} \int_{\boldsymbol{k}} \rho(\boldsymbol{k}, E) d\boldsymbol{k} \qquad (25)$$

We note that h notation is used to represent the magnitude of hopping integral along that bond, which are given $h_i = WK_0(\mu R_i)$. Here W is related to oveplap integral. In order to simplfy the k-dependent factors the potential used in calculation has been taken as V (r) = λδ (r - *a*) .

In the terms of parameters related to Penrose tiling there three hopping term as can be seen in Figure 4. The first is represented h_6 hopping term the shortest interaction, for which h_6 = H/0.618 and where H is a unit of energy representing the overlap integral and fixing the energy scale. In the second model interaction occurs along edges of rhombi ($h_{1\text{-}5}$) plus model I (h_6). The hopping integrals for this case are $h_6 = H/0.618$, $h_{1\text{-}5} = H$ and $h_7 = 0$. In the model III all thre nearest neighbours are included and then the hopping terms for this modl are taken $h_6 = H/0.618$, $h_{1\text{-}5} = H$ and $h_7 = H/1.176$. Hence, the DOS , n (E), has been calculated through eqns. (24 and 25), and the results are presented in Figures (5, and 6) . We note that the detail discussion and illustration of this calculations can be seen in refs. [1,2].

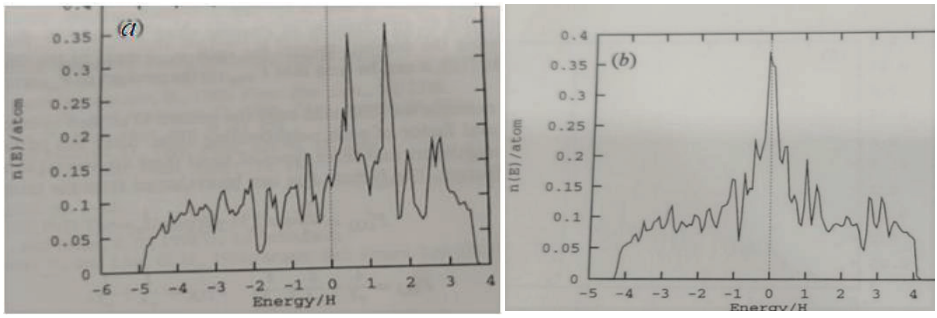

Figure 5.The density of states (states/atom) for different hopping term : (*a*) $h_{1\text{-}6}$ =H, h_7 = 0 (b) $h_{1\text{-}5}$ =H, h_6 =h_7 = 0 [1,**2**].

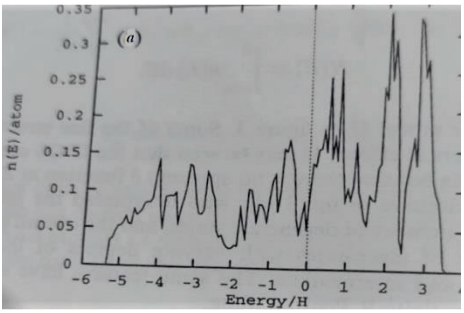

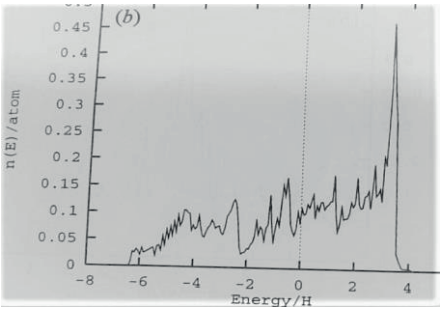

Figure 6.The density of states (states/atom) for different hopping term : (a) h_{1-5} = H, h_6 = H/0.618; (b) h_{1-5} =H, h_6 = H/0.618 and h_7 = 1.176 [1,**2**].

In conclusion, the purpose of this short chapter was to review the Beeby&Hayes method which we implemented to some disordered systems in two dimensions for calculating the electronic structure, in particular, the density of states which is an important physical quantity in material science. The method worked for 2D systems successfully giving good results providing that the potential in muffin tin form and there is non-overlapping among atoms or (ions). The method is based on multiple scattering theory needs strong mathematical background to overcome the solutions of the problem and then gives reasonable results which are very important for experimental studies for comparison. Therefore, This method should be on the agenda again for theoretical studies and are open to For newly curious theoretical physicists.

However, It must, in particular, be emphasized that all the materials used here have been taken my earlier studies which referred in the text.

P.S: This review has been attribute to Prof. John L. Beeby who passed away in Leicester in 2010, with whom I enjoyed theoretical physics.

REFERENCES

[1] Yildiz, A. (1995). *A new technique to calculate the electronic structure of disordered and quasicrystal systems in two-dimensions*. University of Leicester (United Kingdom).

[2] Yildiz, A. K., & Beeby, J. L. (1996). A new technique to calculate the electronic structure of two-dimensional quasicrystals. *Philosophical Magazine B*, *74*(4), 387-405.

[3] Yildiz, A. K., & Beeby, J. L. (1997). A new technique to calculate the electronic structure of two-dimensional disordered systems. *Journal of Physics: Condensed Matter*, *9*(5), 981.

[**4**] Janot, C., and P. Paufler. "Quasicrystals. A Primer. Clarendon Press, Oxford 1992.

[**5**] Steinhardt, P. J., & Ostlund, S. (1987). *The physics of quasicrystals*.

[6] Beeby, J. L., & Hayes, T. M. (1985). New method to calculate the electronic properties of disordered materials. *Physical Review B*, *32*(10), 6464.

[**7**] Ziman, J. M. (1979). *Models of disorder: the theoretical physics of homogeneously disordered systems*. Cambridge university press.

[**8**] Weaire, D., & Thorpe, M. F. (1971). Electronic properties of an amorphous solid. I. A simple tight-binding theory. *Physical Review B*, *4*(8), 2508.

[9] Hayes, T. M., & Beeby, J. L. (1993). Electronic density of states of a disordered tetrahedrally bonded semiconductor. *Physical Review B*, *48*(24), 17732.

[10] Beeby, J. L., & Hayes, T. M. (1994). Calculation of the density of electronic states for a disordered system. *Physical Review B*, *49*(20), 14128.

[11] Kumar, V., Sahoo, D., & Athithan, G. (1986). Characterization and decoration of the two-dimensional Penrose lattice. *Physical Review B*, *34*(10), 6924.

[**12**] Choy, T. C. (1985). Density of states for a two-dimensional Penrose lattice: Evidence of a strong Van-Hove singularity. *Physical review letters*, *55*(26), 2915.

[13] You, J. Q., Nori, F., & Lam, C. H. (1994, January). Electronic Density of States for Penrose Tilings and Vicsek Fractal. In *Materials Science Forum* (Vol. 150, pp. 435-444). Trans Tech Publications Ltd.

Chapter 15

BLUE LUMINOUS VARIABLES

E. Nihal ERCAN[1]

1 Prof. Dr., Boğaziçi University, Physics Department

History:

Blue Luminous Variables (LBVs) are some of the brightest stars of the universe. They have unstable luminosities with varying high magnitudes and have a violent mass loss. They are massive, hot, and rare stars.

Till the 80s we did not have so much observational or theoretical research about them. Observations began to increase after the 80s but theoretical works about LBVs are not sufficient to explain some processes of LBVs such as instability (1).

The first LBVs were realized by astronomers P Cygni and Eta Carinae. We have known them since 1600 but they were not classified as LBV stars since LBV was not a class of stars till 1984. Between 1600 and 1800, astronomers observed that Eta Carinae varied between limits of second and fourth magnitude. After 1820 it began to vary rapidly. Then it became one of the brightest stars in the late 1830s. It had magnitudes between +1 and -1 for the next 20 years. It was called "fitfully variable" and was described as "sudden flashes and relapses" by John Herschel (2). Its total luminosity output was as large as a supernova during the period in which violent eruptions occurred. After this period the luminosity decreased to the eighth magnitude. Then the brightness began to increase again after 1900. Astronomers found some evidence from some outlying debris that this fading and shining loop had occurred before(2).

The other important historical example is P Cygni. P Cygni was observed as a third-magnitude star suddenly in 1600. As we mentioned before these sudden changes are the main characteristic property of LBVs. I want to talk about them like a story because of their varying character: Once upon a time there was a very bright star, after a blink, it turned into a faded star after another blink it has been a bright star again and it has lived varying like this until its death. Anyway, It began to fade to the fifth magnitude in 1655. Any remarkable change did not occur until 1700 but its brightness increased slowly till that time (de Groot 1988; de Groot and Lamers 1992)(3). P Cygni is not just famous because of this property. Also, it has distinct emission line profiles that are interesting as their variability(4).

Another LBV in the Large Magellanic Cloud, S Doradus, has been known since 1897. The same varying brightness has been observed for S Doradus(28). S Doradus is one of the brightest stars we know with nearly -8.9 absolute magnitude which is nearly a million times brighter than our sun(29). But despite their similarities, these three stars have not been seen as the same type of stars until the late mid-20th century.

The first three variable stars which were observed in external galaxies; variables 1, 2, and 3 in the Triangulum Galaxy(M33), were studied by John

Charles Duncan in 1922. Then in 1926, Edwin Hubble observed variables A, B, and C in M33. In 1929 he observed some variables in M31. Then Alan Sandage and Edwin Hubble studied Var A, Var B, Var C, and Var 2 in M33 and Var 1 9 in M31 in very detail in 1953. After their elaborated study Var 1 and Var 3 were excluded from the group of variable stars that they studied. Var 1 was too faint from others and Var 3 was a Cepheid Variable. These stars were some of the brightest stars in M31 and M33 and they were irregular variables. Hubble and Sandage also noted that S Doradus may be in the same class as these stars (Because of this the class will be named S Doradus Variables in 1974, this name contained P Cygni, S Doradus, η Carinae, and the Hubble-Sandage variables.)(5). These stars were called Hubble Sandage variables after their work.

Var 83 in M33; AE Andromeda, AF Andromeda, Var 15, and Var A-1 in M31 were added to this class of variables in the 1970s. Studies showed that all these stars (, η Carinae, P Cygni, Hubble–Sandage variables, S Doradus variables, and other similar) are located in the upper region of the HR diagram, known as the S Doradus instability strip. They had high mass loss and characteristics in common. They had similar "UV measurements of mass loss, infrared observations of circumstellar material, models of interior evolution, plus observations of very luminous stars in nearby galaxies"(6). They have been mentioned as luminous blue variables in some papers. At that time it was just a description that described them well but was not strong enough since being blue and luminous is not true for all LBVs(7). It was not a formal name but people had begun to get used to this name(8). Roberta Humphreys studied these eight stars and she called them Blue Luminous Variables in her study in 1978. This name became a formal name for a star class that contains, η Carinae, P Cygni, Hubble–Sandage variables, S Doradus variables, and other similar stars in 1984 in a presentation by Peter Conti at the IAU symposium.

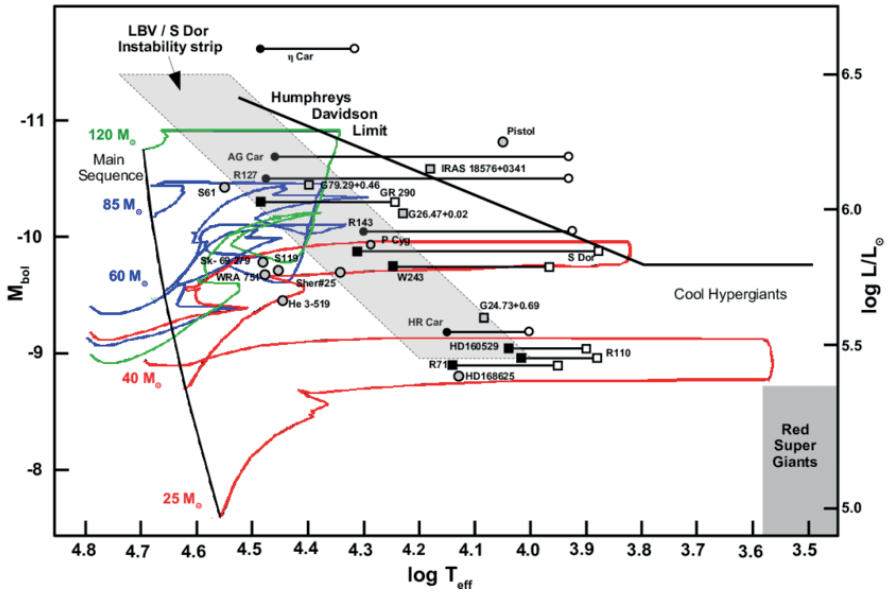

Red lines indicate the least massive stars, blue for intermediate ones, and green for massive ones. See reference (9)

(https://www.researchgate.net/figure/HRD-with-Galactic-and-LMC-LBVs-and-LBV-candidates-Circles-are-used-for-LBVs-with-an_fig2_344176040)

General Properties:

Basically, an LBV is a hot, massive, luminous, and unstable star. But this description is not sufficient since there are lots of stars that show this character. The difference that helps us to distinguish a star as an LBV is its instability, an LBV "exhibits a particular type of instability"(10). We will talk about seven properties of an LBV star: 1. Luminosity, 2. Photometric Variability, 3. Spectra, 4. Characteristic Temperatures, 5. Mass-Loss Rates, 6. Ejecta and Circumstellar Material, 7. Total Mass Ejected. (I took these subtitles' names the same as the names from Humphreys and Davidson's article(10) because I thought that it was the clearest way .)

1. Luminosity:

They have very high luminosity values, the least luminous ones have 25.10^4 L0 (I could not write the luminosity of the Sun the way it is written so I will use L0 for it)with absolute bolometric magnitudes are nearly between -8, and-9 and the most luminous ones have 10^6 L0 with absolute bolometric magnitudes brighter than -9.5. With these luminosities, we can see that they

are located in the upper regions (near the top) of the HR diagram. And we can say that "they are too luminous to become red supergiants" (10).

The most luminous ones "are close to "The Eddington limit" (11), which is the upper limit to the mass of a star and if a star exceeds this mass limit the luminosity would be so high that it would blow off the outer layers of the star (12). So for a stable atmosphere luminosity/mass ratio must not exceed this limit.

Y = (k.L) / (4.pi.c.G.M) (k: opacity per unit mass, L: luminosity, c: speed of light, G: gravitational constant, M: mass of the star) See reference: (11)

The Y value is the ratio of outward radiation and inward gravity force in a hot star's photosphere. And this Y value is our luminosity/mass limit. Since LBVs are close to this limit we can say that radiation pressure reduces their stability.

2. Photometric Variability:

Their photometric variations have a wide range of amplitudes and time scales. (11)

When we say variation it indicates visual wavelengths and fluctuations that it represents mostly in apparent temperature, not luminosity. We can look at them under 4 subtitles: Giant eruptions, eruptions, small oscillations, and microvariations.

Giant Eruptions: They are sudden ejections of large amounts of mass and they increase the bolometric luminosity. Change in visual magnitude is larger than 2 mag. We can give Eta Carinae's outburst from 1837 to 1860 as an example. Its luminosity increased by 2 magnitudes and its visual magnitude increased by 3-5 mag (11). P Cygni in the 1600s, V 12 in NGC 2403 (Tammann and Sandage 1968), and SN 1961V in NGC 1058 (Goodrich et al. 1989) can be given as other examples (11). After these giant eruptions, stars can stay stable or can fade quickly. There is no certain time scale for giant eruptions since there are few of them. But it is possible that their frequencies can be a few or thousand years.

Eruptions: they occur in several months and brightness can increase up to two magnitudes during this process. The time scale for eruptions is between 10 and 40 years and visual magnitude changes by 1-2 mag on this scale. During this time, small variations occur also. When brightness reaches max value the atmosphere is expanded so much. So during the usual eruption, the bolometric magnitude stays the same. S Dor and R 127 in the LMC, AG Car in our galaxy, plus some of the LBVs in M31 and M33 (Hubble and Sandage 1953)(11) can be given as an example of this type.

Small Oscillations: brightness changes by half a magnitude and their time scales are very short, several months to a few years.

Microvariations: visual magnitude increases less than 0.1 mag. These have been reported for HR and AG Carinae but they also occur in normal supergiants (11). Alpha-Cygni has microvariations too, it is estimated that they occur due to nonradial gravity mode pulsation (26)(25, I took it from 30 but 31 is the original reference of it.)

3. Spectra:

They have emission lines of H, He I, and Fe II and their spectra show P Cygni profiles (we said that LBVs are also called S Doradus, actually, the first LBV that is classified as a variable star is P Cygni so LBVs could be called as P Cygni. But because P Cygni Profiles may cause confusion, they did not use this name)(13). At their minimum visual, LBVs show H and He I lines in their spectrum like a hot supergiant and Fe II is strongest for many of them(11). "But some LBVs at minimum also resemble the Of/WN9 stars (Walbom 1977; Bohannan and Walborn 1989). R 127 was one of the original Of/WN9 stars and AG Car and HDE 269582 are now considered members of this class at minimum light."(11). At maximum visual, they have a more expanded atmosphere, and their spectrum is more like A or F type of cool supergiant. Fe II line gets weaker and higher resolution we can still observe P Cygni profiles.

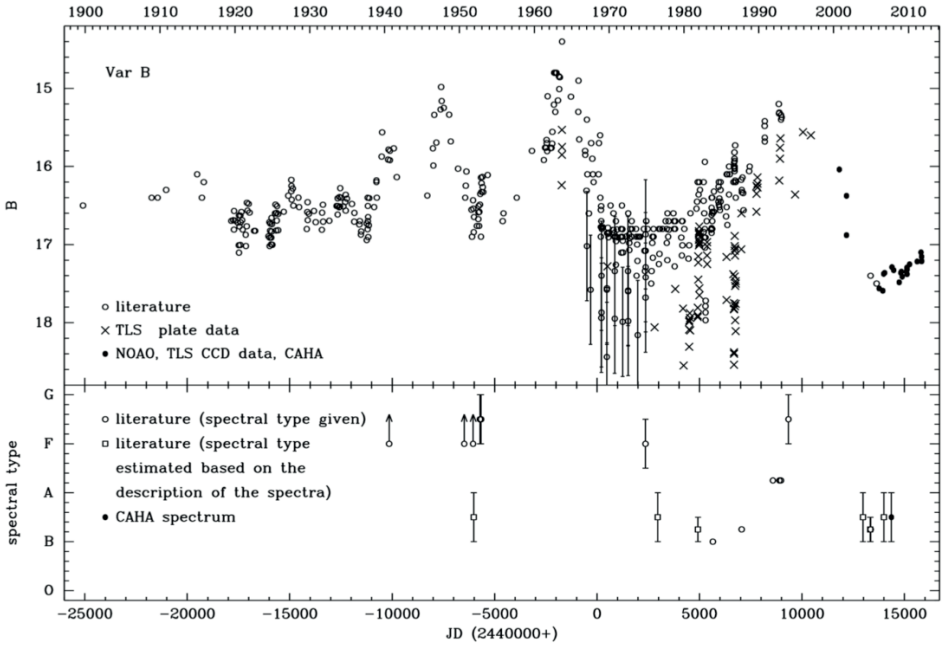

A figure from Burggraf (14)

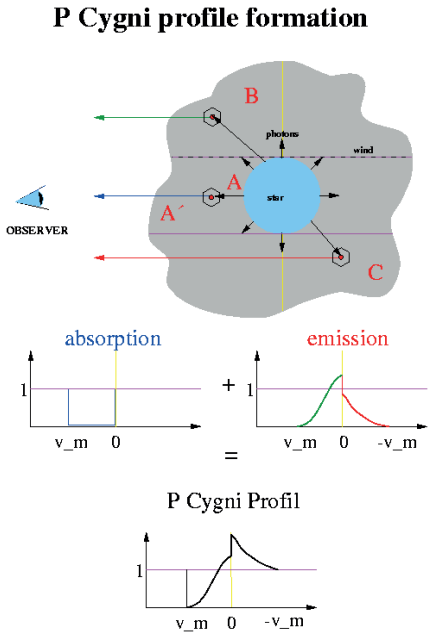

An illustration to understand P Cygni Profiles better (30)

(http://www.ifa.hawaii.edu/users/kud/windsfromhotstars/hotwinds.html)

Species	Wavelength	v_r	$v_e \sin i$	
			FT	PF
He I	3926.54	165	116	101
He I	4009.26	191	88	122
He I	4026.27	157	97	113
He I	4120.90	159	78	91
He I	4143.75	169	103	105
He I	4387.93	169	76	93
He I	4437.55	179	–	–
He I	4471.58	158	88	88
He I	4713.24	175	96	60
He I	4921.93	151	–	–
He I	5047.74	168	–	–
C II	4267.15	166	86	87
Si III	4552.62	162	106	97
Si III	4567.84	174	–	–
Si III	4574.76	172	–	–

Radial and projected rational velocity (km/s) of He I line spectra, See reference: (27)

4. Characteristic Temperatures:

If we try to give average numbers for the least and the most luminous ones, the least luminous ones have surface temperatures around 10000 K and

the most luminous ones are around 25000 K. These values depend on which period of LBS is on.

At a visual minimum, they have surface temperatures between 12000 and 30000 K so they are hot. At visual maximum, their temperatures are nearly between 7000 and 8000 K so they are cooler. This stage is called " eruptive state". The photospheric layers are more diffusing during this eruptive state. When it is so much diffusing, the effecting temperature relation between luminosity and radius becomes invalid. Because they do not have a unique radius during this eruption phase(15). Since we do not have a clear relation, the effective temperature becomes less meaningful for an LBV eruption. Some apparent temperature (Tapp) that "is defined in terms of the emergent spectrum itself"(15) is used instead of effective temperature to be more clear.

5. Mass Loss Rates:

As we mentioned before they have a very high mass loss rate. The average mass loss rate of LBVs is between $10^{(-5)}$ and $10^{(-4)}$ (Mass of sun/year) as mentioned in (15). This value is way more large (10-100 times) than the mass-loss rate of stars that are in the same luminosity range. These mass loss rates are not observed directly. They are calculated from mostly a spherical model that we build by observations.

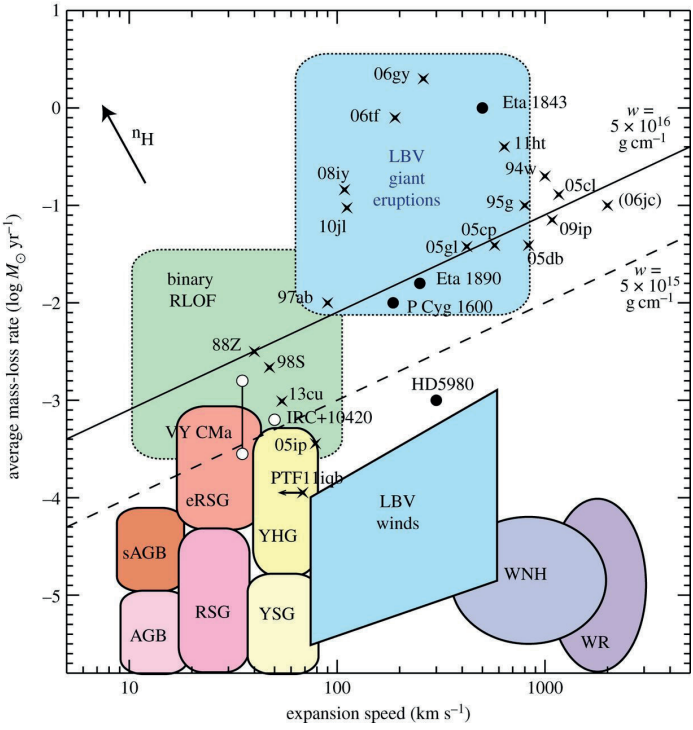

See reference: (16)

6. Ejecta and Circumstellar Material:

"Most LBVs show some evidence for an excess of infrared radiation and circumstellar ejecta"(15). And this infrared exceed is very common for LBVs. This happens due to free-bound and free-free emissions (Humphreys et al. 1984; Leitherer et al. 1985). Due to circumstellar dust, longer wavelengths can be observed too (McGregor et al. 1988)(15).

Ejectas can be seen as different shapes, mostly they are seen as circumstellar shells or ring nebula. "Some examples are AG Car (Thackeray 1977; Stahl 1987), He 3-519 (Stahl 1987), R 127 (Stahl 1987; Clampin et al. 1993), and HR Car (Hutsemekers and Von Drom 1991)"(15). These small nebulae may be formed by slow and fast wind interaction during the S Doradus cycle since the giant ones are the result of eruptions (17). But some of them can be very clear in some extraordinary examples like Eta Carinae.

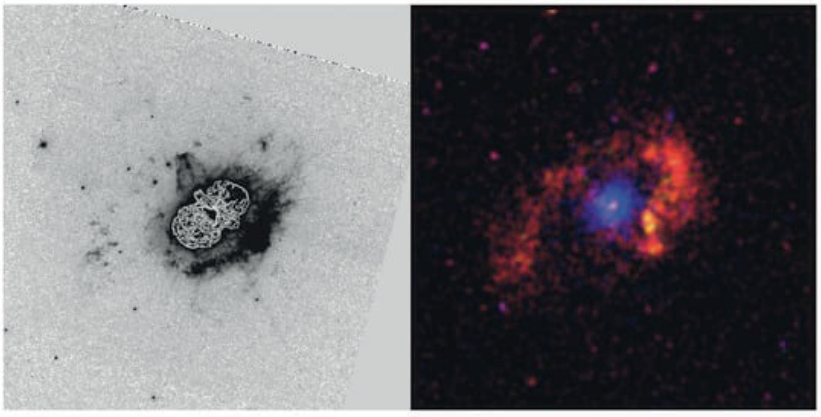

The nebula around η Carinae in the optical and X-ray. **Left**: An optical F658N HST image in greyscale, the Homunculus nebula additionally marked in contour to distinguish it from the outer ejecta, shown only in greyscale (18) **Right**: A CHANDRA Xray image with colour-coded energy regimes(19). (36)

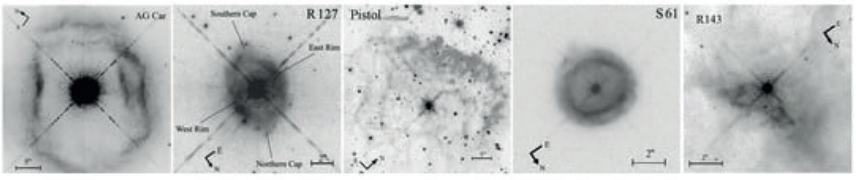

HST images of LBV nebulae sorted by morphology: hourglass AG Car (32), R 127 with bipolar attachments, weakly bipolar He 3-519 (33), spherical S 61 (34), and last in row irregular R 143 (3). (34, I took these images and explanations from this source)

7. Total Mass Loss:

To find out the mass lost of the LBV stage we need duration and averaged mass loss rate since these values are changed from one LBV to another LBV. LBVs that have more violent eruptions like P Cygni and Eta Carinae have a larger total mass loss. For example, the famous 1840s outburst of Eta Carinae probably caused 2-3 M0 (mass of the sun) mass loss. This shows us it the mass loss rate is way larger than the values that we mentioned on the mass loss rate. It is nearly $10^{(-3)}$ (M0/year), see reference (20) We can say that since they are very massive stars, their total mass loss is larger.

Evolution of LBVs:

The duration of the LBV stage is shorter than other massive stars, roughly 25000 years (21). Theoretically, a star must be more massive than 50 M0 can turn into an LBV but we observed that there are LBVs that are less massive (21). We can see two dense areas of LBVs on the HR diagram. The first one contains brighter and hotter LBVs like AG Car, R 127, S 61, P Cyg, WRA 751, and the second one contains less bright and cooler LBVs like HR Car, R 71, HD 160529 (21).

In 1979 Humphreys and Davidson suggested that if stars with larger mass than 40 M0 in the post-main sequence stage encounter a limit to their stability this may cause a period of very high mass loss that is called as LBV phase. (24).

After the LBV stage, a star turns into a Wolf Rayet or a supernova. This evolution depends on the LBV's mass and mass loss rate. (22)

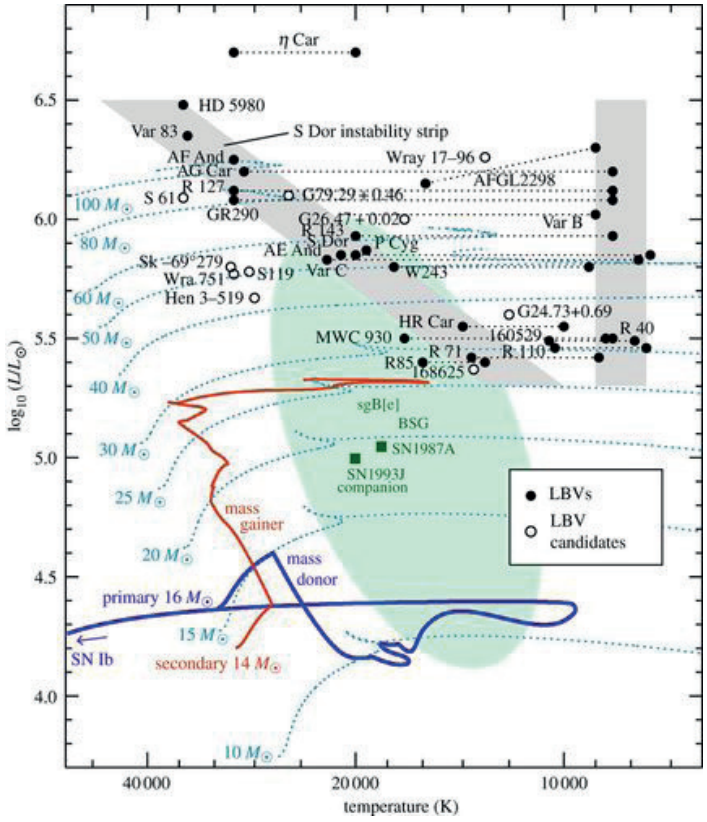

Evolution paths of some LBV models. " (Nathan Smith, 2017, Luminous blue variables and the fates of very massive stars, figure) See reference:(23)

Conclusion:

LBVs are some of the brightest stars (not all of LBV) with unstable characters. Violent and sudden eruptions occur sometimes on them. These eruptions seem as the main reason for sudden and large brightness changes. The magnitude increases then decreases then increases and this goes like this. It repeats this increase-decrease loop but it does not have a certain period. They have peculiar spectroscopic variability (25). We do not have a detailed theoretical model to explain this phenomenon. Most of our knowledge about them comes from observations and basic approximate models. So LBVs are moody, massive, gorgeous stars in the universe. Theoretical studies are needed to explain all their observational properties in a better way.

I particularly want to thank Bedirhan Alkan, one of my undergraduate students, who helped me to prepare this manuscript.

REFERENCES:

1. Humphreys RM, Davidson K. 1994, The luminous blue variables: astrophysical geysers. **Publ. Astron. Soc. Pac.** 106, p.1.
2. Humphreys RM, Davidson K. 1994, The luminous blue variables: astrophysical geysers. **Publ. Astron. Soc. Pac.** 106, p.1.
3. Humphreys RM, Davidson K. 1994, The luminous blue variables: astrophysical geysers. **Publ. Astron. Soc. Pac.** 106, p.2.
4. Humphreys RM, Davidson K. 1994, The luminous blue variables: astrophysical geysers. **Publ. Astron. Soc. Pac.** 106, p.2.
5. https://en.wikipedia.org/wiki/Luminous_blue_variable
6. Humphreys RM, Davidson K. 1994, The luminous blue variables: astrophysical geysers. **Publ. Astron. Soc. Pac.** 106, p.2.
7. Weis, Kerstin, Dominik J. Bomans. 2020. Luminous Blue Variables, *Galaxies* 8, no. 1, p.3
8. https://en.wikipedia.org/wiki/Luminous_blue_variable.
9. Weis, Kerstin, Dominik J. Bomans. 2020. Luminous Blue Variables, *Galaxies* 8, no. 1, p.6.
10. Humphreys RM, Davidson K. 1994, The luminous blue variables: astrophysical geysers. **Publ. Astron. Soc. Pac.** 106, p.2.
11. Humphreys RM, Davidson K. 1994, The luminous blue variables: astrophysical geysers. **Publ. Astron. Soc. Pac.** 106, p.3.
12. https://en.wikipedia.org/wiki/Luminous_blue_variable
13. Burggraf, B. LBVs in M33: Variability and Evolutionary State. Ph.D. Thesis, Ruhr University Bochum, Bochum, Germany, 2015.Weis, Kerstin, Dominik J. Bomans. 2020. Luminous Blue Variables, *Galaxies* 8, no. 1, p.7.
14. Humphreys RM, Davidson K. 1994, The luminous blue variables: astrophysical geysers. **Publ. Astron. Soc. Pac.** 106, p.4.
15. Smith N. 2014Mass loss: its effect on the evolution and fate of high-mass stars. **Annu. Rev. Astron. Astrophys**. 52, 487–528.
16. Weis, Kerstin, Dominik J. Bomans. 2020. Luminous Blue Variables, *Galaxies* 8, no. 1, p.7.
17. Weis, K. The outer ejecta of η Carinae. In *The Fate of the Most Massive Stars*; Astronomical Society of the Pacific Conference Series; Humphreys, R., Stanek, K., Eds.; Astronomical Society of the Pacific: San Francisco, CA, USA, 2005; Volume 332, p. 275.
18. Weis, K.; Corcoran, M.F.; Davidson, K. On the X-ray Emission of η Carinae's Outer Ejecta. In *The High Energy Universe at Sharp Focus: Chandra Science*;

Astronomical Society of the Pacific Conference Series; Schlegel, E.M., Vrtilek, S.D., Eds.; Astronomical Society of the Pacific: San Francisco, CA, USA, 2002; Volume 262, p. 275.

19. Humphreys RM, Davidson K. 1994, The luminous blue variables: astrophysical geysers. **Publ. Astron. Soc. Pac.** 106, p.5
20. Weis, Kerstin, Dominik J. Bomans. 2020. Luminous Blue Variables, *Galaxies* 8, no. 1, p.5.
21. Weis, Kerstin, Dominik J. Bomans. 2020. Luminous Blue Variables, *Galaxies* 8, no. 1, p.6.
22. Nathan Smith, 2017, Luminous blue variables and the fates of very massive stars, figure 3 and its explanation.
23. Humphreys RM, Davidson K. 1994, The luminous blue variables: astrophysical geysers. **Publ. Astron. Soc. Pac.** 106, p.15.
24. V. M. Kalari, J. S. Vink, P. L. Dufton and M. Fraser, 2018, How common is LBV S Doradus variablility at low metallicity?, A&A, 618 A17, p.1.
25. Lefever, K., Puls, J., & Aerts, C. 2007, A&A, 463, 1093.
26. V. M. Kalari, J. S. Vink, P. L. Dufton and M. Fraser, 2018, How common is LBV S Doradus variablility at low metallicity?, A&A, 618 A17, p.7.
27. H, Shapley, 1925, Harvard College Observatory, Bulletin 814, p.1.
28. Weis, Kerstin, Dominik J. Bomans. 2020. Luminous Blue Variables, *Galaxies* 8, no. 1, fig. 4 and 6.
29. Weis, K. Gone with the wind: Nebulae around LBVs. Bulletin de la Societe Royale des Sciences de Liege 2011,80, 440–444.
30. Weis, K.; Duschl, W.J.; Bomans, D.J. An outflow from the nebula around the LBV candidate S 119. A&A 2003, 398, 1041–1048.
31. Weis, K. On the structure and kinematics of nebulae around LBVs and LBV candidates in the LMC. A&A 2003, 408, 205–229.
32. https://www.britannica.com/science/Eddington-mass-limit
33. https://en.wikipedia.org/wiki/S_Doradus
34. http://www.ifa.hawaii.edu/users/kud/windsfromhotstars/hotwinds.html

*Pickering, Edward C. (1905). "Second supplement to Catalogue of Variable Stars". Annals of Harvard College Observatory. (I did not use this catalog directly but some of the sources that i used take stars from this catalog)

Chapter 16

INVESTIGATING THE ELECTRONIC STRUCTURES OF CARBON NANOTUBES THROUGH DENSITY FUNCTIONAL THEORY

Veysel ÇELİK[1]

1 Siirt University, Faculty of Education, Department of Mathematics and Science Education, veysel3@gmail.com, ORCID No: 0000-0001-5020-8422

1. INTRODUCTION

Graphene is a monolayer of carbon atoms that are organized in a hexagonal lattice structure, has captivated the scientific community due to its remarkable electronic, thermal, and mechanical properties. This two-dimensional material, first isolated in 2004 by Andre Geim and Konstantin Novoselov, has been heralded for its potential in various applications, ranging from electronics to materials science, owing to its high electron mobility, strength, and transparency (Novoselov et al., 2004). Transitioning from two-dimensional graphene, Carbon Nanotubes (CNTs) are cylindrical nanostructures derived from rolled graphene sheets, maintaining many of the extraordinary properties of graphene while introducing new characteristics due to their altered geometry. CNTs can be categorized into Single-Walled Carbon Nanotubes (SWCNTs) and Multi-Walled Carbon Nanotubes (MWCNTs), each with distinct properties and applications in nanotechnology, materials science, and even in the medical field (Iijima, 1991).

Carbon nanotubes have swiftly become a focal point of robust global interest, owing to their potential to showcase unique physical properties that could permeate numerous scientific and technological domains, such as ultra-durable composites and nanoelectronics (Dresselhaus et al., 1996; Yakobson and Smalley, 1997; Dekker, 1999). The investigations have unveiled that these nanotubes, being the stiffest material known to date (Treacy et al., 1996; Wong et al., 1997), exhibit elastic buckling rather than fracturing when subjected to substantial bending or compressive strains (Wong et al., 1997; Yakobson et al., 1996). This specific mechanical attribute distinctly underscores their significant potential in the realm of advanced composites. Despite this, we posit that the extraordinary electronic properties of carbon nanotubes present not only the most intriguing intellectual challenges but also immense potential for innovative applications. Remarkably, initial theoretical calculations indicated that SWNTs could manifest either metallic or semiconducting characteristics, determined solely by their diameter and helicity (Hamada et al., 1992; Mintmire et al., 1992; Saito et al., 1992). Furthermore, this capability to exhibit fundamentally divergent electronic properties without altering local bonding has been experimentally verified through atomically resolved scanning tunneling microscopy (STM) measurements (Wilder et al., 1998; Odom et al., 1998), differentiating nanotubes from other nanowire materials (Lieber, 1998; Hu et al., 1999).

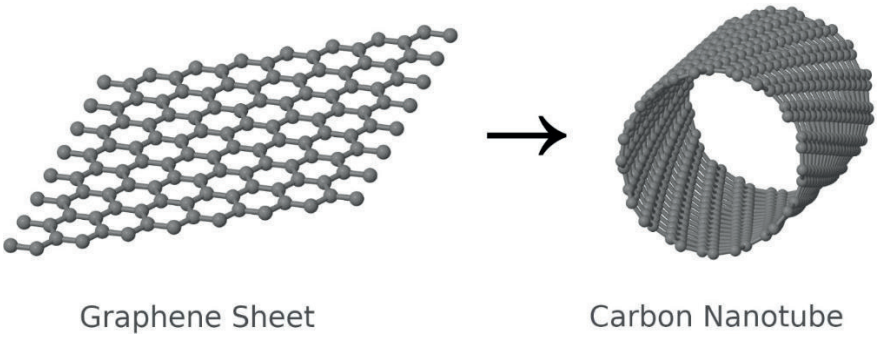

Figure 1: Carbon nanotubes are obtained by rolling graphene sheets.

The properties of SWCNTs are significantly influenced by their chiral indices, denoted (n, m), which describe how the graphene sheet is rolled to form the nanotube (Figure 1). The chiral indices not only determine the nanotube's diameter but also dictate its electronic properties, categorizing it as either metallic or semiconducting. The variation in electronic properties based on chiral indices has been a focal point in research, as it allows for the tailoring of SWCNTs for specific applications in nanodevices, sensors, and more (Saito et al., 1998).

Density Functional Theory (DFT), a method of quantum mechanics, plays a pivotal role in investigating the electronic properties of materials like graphene and CNTs. DFT allows researchers to study the electronic structure, enabling the prediction of material properties, such as their conductivity, reactivity, and stability. Particularly for materials like SWCNTs, where electronic properties are paramount and can be manipulated for various applications, DFT provides crucial insights that bridge theoretical predictions with experimental endeavors (Hohenberg and Kohn, 1964). In this book chapter, we will examine an in-depth investigation of the electronic properties of SWCNTs via DFT, explore how chiral indices affect these properties, and describe the potential applications and implications of these nanomaterials in technology and materials science.

2. DENSITY FUNCTIONAL THEORY (DFT) METHODOLOGY

The DFT is a widely employed quantum mechanical computational approach utilized in the fields of physics and chemistry to examine the electronic configuration of complex systems comprising several interacting particles. This method is particularly valuable In order to investigate the electronic structure of atoms, molecules, and condensed phases. The Hohenberg-Kohn theorem is the underlying premise of DFT, asserting that the electron density

of a many-electron system uniquely determines its ground state features. The electron density, in turn, minimizes a functional (a function of a function) of the total energy. Mathematically, the total energy E can be expressed as a functional of the electron density $\rho(r)$:

$$E[\rho(r)] = T[\rho(r)] + V_{ee}[\rho(r)] + V_{ne}[\rho(r)] + V_{nn}$$

Here, $T[\rho(r)]$ is the kinetic energy functional, $V_{ee}[\rho(r)]$ is the electron-electron interaction energy functional, $V_{ne}[\rho(r)]$ is the nuclear-electron interaction energy, and V_{nn} is the nuclear-nuclear interaction energy. The Kohn-Sham (KS) equations, the invention of Walter Kohn and Lu Jeu Sham, provide a practical method for applying DFT. The KS approach is characterized by the introduction of a theoretical framework wherein a set of non-interacting electrons is employed, possessing an electron density that is equivalent to that of the actual interacting system. The KS equations can be written as:

$$\left[-\frac{1}{2}\nabla^2 + V_{eff}(r)\right]\psi_i(r) = \varepsilon_i\psi_i(r)$$

Where $\psi_i(r)$ are the Kohn-Sham orbitals, ε_i are the corresponding eigenvalues, and V_{eff}) is the effective potential, which includes the external potential $V_{ext}(r)$ and the potential due to the electron-electron interactions, which is composed of the classical electrostatic (Hartree) potential and the exchange-correlation potential $V_{xc}(r)$. Mathematically,

$$V_{eff}(r) = V_{ext}(r) + V_H[\rho(r)] + V_{xc}[\rho(r)]$$

Here,$V_H[\rho(r)]$ is the Hartree potential, and $V_{xc}[\rho(r)]$ is the exchange-correlation potential, which encapsulates the complex quantum mechanical interactions between electrons. The exact form of $V_{xc}[\rho(r)]$ is unknown and is typically approximated in practical DFT calculations. The DFT and the Kohn-Sham approach provide a powerful and widely used framework for studying electronic systems, enabling the calculation of various properties of atoms, molecules, and solids with reasonable computational cost and often with high accuracy, provided that appropriate exchange-correlation functionals are employed.

3. EFFECTIVE MASS

The effective mass m^* is derived from the curvature of the electron energy bands in the momentum space, which are described by the electron's dispersion relation $E(k)$, where E is the energy and k is the wave vector. The

effective mass can be mathematically described as the second derivative of energy relative to wave vector:

$$\frac{1}{m^*} = \frac{1}{\hbar^2}\frac{d^2E}{dk^2}$$

where $\hbar$ is the reduced Planck's constant. This relation implies that the effective mass is inversely related to the curvature of the energy band: a higher curvature corresponds to a lower effective mass and vice versa. It's crucial to note that the effective mass can be direction-dependent (anisotropic) and can even become negative in certain regions of the band structure, influencing the carrier dynamics in semiconductor materials and devices.

4. DIRAC CONE AND THE GRAPHENE

The Dirac cone is a concept frequently encountered in solid-state physics and material science, particularly describing the electronic properties of two-dimensional materials like graphene. Graphene, forming a single layer of carbon atoms, exhibits peculiar and fascinating electronic properties. When visualizing the energy-momentum relationship of electrons in the band structure of graphene, two bands appear in the shape of a Dirac cone (an upper and a lower band). These bands touch each other at the Dirac point, often referred to as K and K' points. Here, the electronic properties of graphene manifest similarly to those of free relativistic particles. This unique concept is named after the theoretical physicist Paul Dirac, who formulated the Dirac equation to describe the relativistic motion of electrons. Electrons in graphene behave as Dirac fermions with zero effective mass, due to the unique electronic structure of the material. Mathematically, the Dirac cone is expressed with the following formula:

$$E(k) = \pm v_F \hbar |k|$$

Where,

- $E(k)$: Energy,
- v_F: Fermi velocity, assessed to be approximately 10^6 m/s in graphene,
- $\hbar$: Reduced Planck's constant ($\hbar/2\,\pi$), where h is Planck's constant,
- k: Wave vector,
- $\pm$ symbol: Indicates that the energy is for both electrons (positive) and holes (negative).

This particular band structure leads to unique properties of graphene, such as high electron mobility and thermal conductivity. The Dirac cone and

associated phenomena have potential applications in nanotechnology and next-generation electronic devices, thus research on this topic remains a significant focus for scientists and engineers.

5. CHIRAL INDICES IN CARBON NANOTUBES

The *chiral index* in the context of CNTs is represented as a pair of integers (*n*,*m*) and is vital for denoting the atomic structure and symmetry of the nanotube. The concept elucidates how a graphene sheet is envisaged to be rolled up to create the nanotube. This numeric pair gives rise to different types of CNTs as follows:

1. **Armchair (n=m):** When *n* equals *m*, we obtain an armchair nanotube, recognized by a characteristic pattern akin to the armrests of an armchair.
2. **Zigzag (m=0):** When *m* equals 0, the nanotube is called a "zigzag" nanotube.
3. **Chiral (otherwise or n≠m):** Chiral nanotubes emerge when the nanotube is neither armchair nor zigzag. Here, the hexagons portray a distinct tilt, spiraling or forming a helical pattern along the tube axis.

Chiral index is intricately tied to the electronic properties of the nanotube. Typically, armchair nanotubes manifest metallic properties, while zigzag and chiral nanotubes can either be metallic or semiconducting, contingent on the specific values of (*n*,*m*).

6. COMPUTATIONAL DETAILS

The SWCNTs of various chiralities were studied to explore their electronic properties. Chirality was defined by the (n, m) indices, with several representative structures chosen to offer a broad view of the property variations in these nanostructures. All nanotubes were optimized to determine their equilibrium geometries and minimize the total energy. The periodic boundary conditions were applied along the tube axis, while sufficient vacuum was ensured in the perpendicular directions to minimize interactions between the periodic images. The Vienna Ab initio Simulation Package (VASP) was utilized for conducting all electronic structure computations. (Kresse and Hafner, 1993; Kresse and Joubert, 1999). Within the Generalized Gradient Approximation (GGA), the exchange-correlation functional was described., employing the Perdew-Burke-Ernzerhof (PBE) functional (Perdew et al., 1996). The projector-augmented wave (PAW) method is a computational technique used in electronic structure calculations (Blöchl, 1994; Kresse and Furthmüller, 1996). In the calculations in this study, a plane-wave basis set with a kinetic energy cutoff of 520 eV was used, and using a Monkhorst-Pack k-point mesh, the Brillouin zone was sampled. (Monkhorst and Pack, 1976)

with a resolution approximately equal to $2\pi \times 0.03$ Å^{-1}. For each SWCNT, the geometry was optimized until the forces on each atom were below 0.01 eV/Å. During geometry optimization, the unit cell dimensions along the tube axis were allowed to relax, while maintaining the tube symmetry. For the examination of the electronic properties, band structure calculations were performed. The Kohn-Sham eigenvalues were computed along a high-symmetry path in the first Brillouin zone, which is suitable for cylindrical structures.

7. ELECTRONIC STRUCTURES

7.1 Graphene: 2D Material

Graphene can be defined as a monolayer of carbon atoms that are organized in a two-dimensional lattice resembling a honeycomb structure. Figure 2 shows the crystal structure and bilayer structure of graphene in certain sizes. The basic structural unit of diverse carbon allotropes, such as graphite, carbon nanotubes, and fullerenes, is known as the basic structural element. As mentioned before, graphene exhibits remarkable physical properties that have captivated scientists and engineers since its isolation in 2004 by physicists Andre Geim and Konstantin Novoselov, work for which they were awarded the Nobel Prize in Physics in 2010.

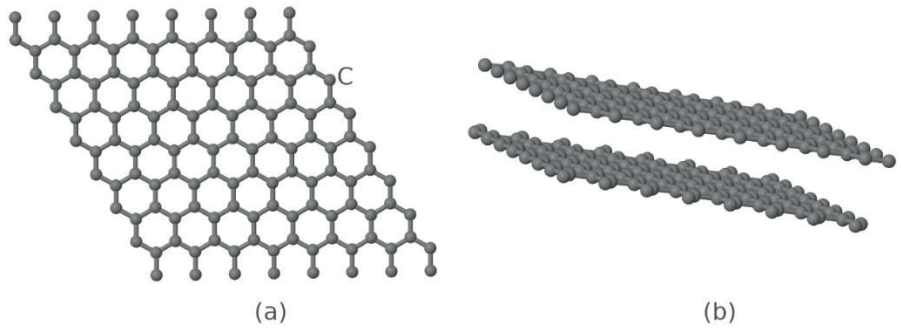

Figure 2: Two types of graphene structures. Here (a) shows single layer graphene, (b) shows bilayer graphene

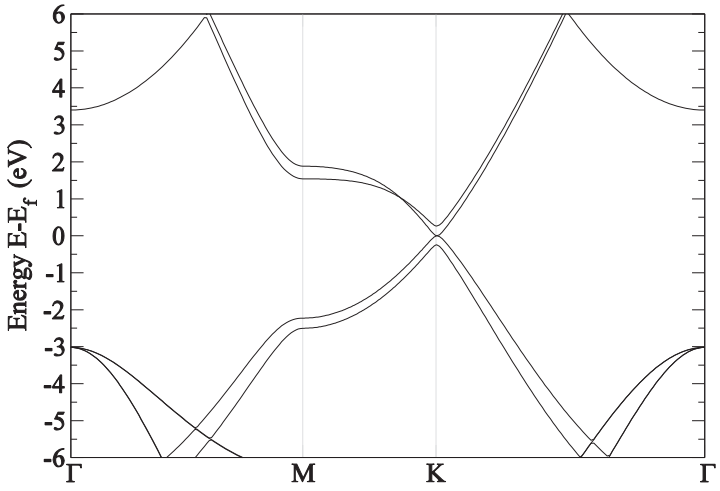

Figure 3: Electronic band structure obtained for graphene sheet.

Some of the notable properties of graphene include:

- **Strength:** It is incredibly strong for its weight, being about 200 times stronger than steel, making it one of the strongest materials known.
- **Conductivity:** Graphene is highly conductive, both thermally and electrically. Its electrons have extremely high mobility, which means they can move through the material very quickly, even at room temperature.
- **Transparency:** Despite being very dense, it is also transparent, absorbing only 2.3% of reflecting light, which is quite remarkable for a material that is just one atom thick (Nair et al., 2008).
- **Flexibility:** It is also extremely flexible and can be bent, twisted, and stretched without damage.

The distinctive characteristics of these qualities contribute to a diverse array of possible applications, such as in the development of transparent conductive films, nanocomposite materials, energy storage systems, and various electronic components. For instance, it could be used in the creation of ultra-fast transistors, improved solar cells, new types of light sources, and flexible electronics. Moreover, due to its high surface area (around), It is also under consideration for use in various applications like supercapacitors and batteries (Xia et al., 2009; Kim et al., 2014). Graphene also poses interesting phenomena in quantum physics, such as quantum anomalous Hall effect and the appearance of massless Dirac fermions, making it a rich platform for scientific research.

In the study in this book chapter, the band structure of the graphene layer was calculated to better understand its electronic structure. The graph of the calculated band structure is shown in Figure 3. Near the Fermi energy, at point K, we observe a linear crossing (Dirac cone), pointing to massless Dirac fermions, a known feature of graphene. This crossing is the reason why graphene has high mobility and unique electronic properties. Also, we can observe that there is no energy band gap in this graph. This indicates that graphene is not a semiconductor, but actually a zero band gap semiconductor (or sometimes referred to as metallic). Such a band structure lays the foundation for many of graphene's unique properties, such as ultra-high electron mobility, the ambipolar electric field effect, and the anomalous quantum Hall effect.

7.2 Carbon Nanotubes

The electrical band structure of armchair nanotubes with varying (n,n) indices is depicted in Figure 4. Armchair CNTs usually have metallic properties. This means that armchair CNTs do not have an energy band gap. In this study, the values of the obtained band gaps are listed in Table 1. Compared to the others in Table 1, the structure with the widest band gap is (7,7). However, the narrowest band gap occurs in the (9,9) structure. In general, the value of the band gaps in the armchair structure is very close to zero. Here, the conduction band minimum (CBM) and the valence band maximum (VBM) do not overlap but almost touch each other. Figure 5 shows the band structures obtained for various armchair structures. In graphene's band structure, there is a special energy distribution called the Dirac cone around the Fermi level. This energy distribution is preserved in armchair CNTs. Table 1 also lists the effective masses obtained for the electron and hole using the parabolic fitting method of band edges in the calculations. The effective mass values for both electron and hole are quite low. This means that electrons can move at high speeds and have high electron mobility. Metallic armchair CNTs can exhibit quantum resistance under certain conditions. This means that the resistance of the CNT takes a certain minimum value, and this resistance is determined by the fundamental rules of quantum mechanics. As mentioned earlier, armchair CNTs have high electron mobility. This makes them an ideal material for electronic circuits, especially in high-frequency applications. These band structure characteristics of armchair CNTs make them very attractive for nanoscale electronic applications. However, challenges in the production process and issues like purity may limit the large-scale applications of these nanotubes.

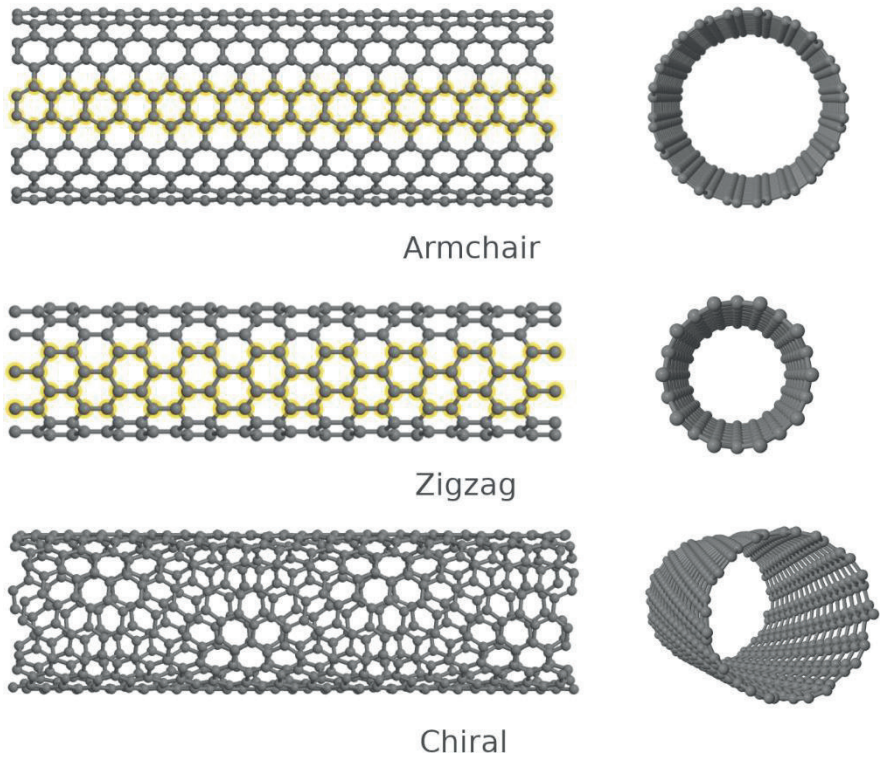

Figure 4: 3D models of armchair, zigzag and chiral nanotubes.

The figure 4 shows the general structure of three types of single-walled graphene nanotubes. In zigzag nanotubes, carbon atoms are arranged in a straight line along the tube. This structure can be metallic or semiconductor, depending on the diameter and number of helices of the nanotube. The index of zigzag graphene nanotubes is usually expressed as (n,0). Here "n" represents the number of coils of the tube. Depending on this "n" value, the electronic band structure of zigzag graphene nanotubes changes. If the value "n" is a multiple of 3 (i.e. n = 3m, m is an integer), the zigzag nanotube shows metallic properties. For such nanotubes the band gap is zero, meaning there is no difference in energy between the conducting and insulating bands. If the "n" value is not a multiple of 3, the zigzag nanotube shows semiconductor properties. For such nanotubes, the band gap is non-zero and this value varies depending on the value of "n" and the diameter of the nanotube.

The figure 6 shows the band structures obtained for zigzag nanotubes according to different indices. The data obtained from band structure calculations are listed in Table 2. According to the data obtained, the structures

(3,0), (4,0), (5,0) and (6,0) are metallic in character. For these structures, the metallicity does not depend on the n index being a multiple of 3. When the value of the n index is increased, the structure acquires a semiconductor character after (7,0). Although the value of the band gap increases in proportion to the increase in the value of n, the situation changes in the (9,0) structure and a sudden narrowing of the band gap is observed. This situation supports the knowledge that metallic character occurs when the n index value is a multiple of 3. Among the structures (7,0), (8,0), (9,0) and (10,0), the only structure whose n value is a multiple of 3 is the (9,0) structure. When the effective masses in Table 2 are compared, the lowest value was obtained in the structure (9.0). However, in wide band gap structures, (10,0) has the lowest effective mass value. This indicates that the (10,0) structure may be a semiconductor with high carrier mobility.

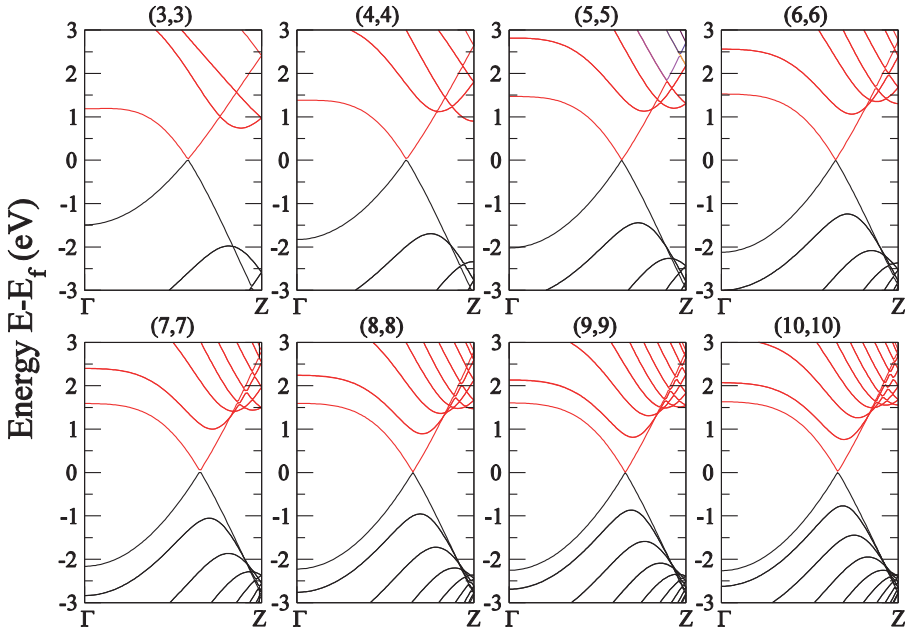

Figure 6: Band structures obtained for armchair nanotubes with different indexes.

Table 1: Data obtained from the band structure of armchair nanotubes with different indexes. E_g represents the band gap and its unit is eV. The m_e and m_h represent the effective mass of electron and hole, respectively. Effective mass values are given in terms of the rest mass of an electron.

Armchair	E_g (eV)	m_e	m_h
(3,3)	0.032	0.042	0.041
(4,4)	0.039	0.037	0.039
(5,5)	0.007	0.034	0.035
(6,6)	0.009	0.034	0.034
(7,7)	0.062	0.036	0.036
(8,8)	0.017	0.033	0.033
(9,9)	0.003	0.032	0.033
(10,10)	0.032	0.033	0.034

Based on the acquired data, the "n" value coupling emerges as a pivotal factor in pinpointing the potential of zigzag graphene nanotubes within electronic applications. For instance, metallic zigzag nanotubes, with their inherent electrical conductivity, might be aptly suited for applications demanding specific conductivity requirements. Conversely, semiconductor zigzag nanotubes, owing to their distinct properties, may offer optimal performance in semiconductor devices, such as transistors, by potentially enabling more efficient charge carrier management

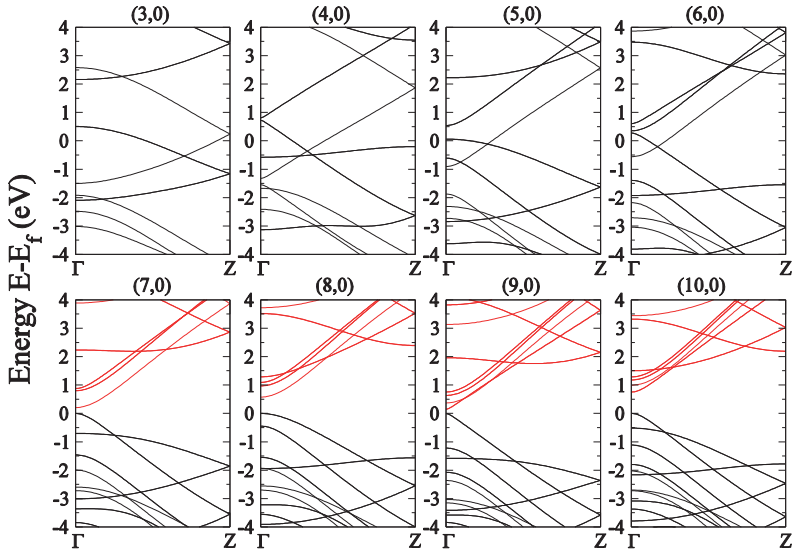

Figure 7: Band structures obtained for zigzag nanotubes with different indexes.

Table 2: Data obtained from the band structure of zigzag nanotubes with different indexes. E_g represents the band gap and its unit is eV. The m_e and m_h represent the effective mass of electron and hole, respectively. Effective mass values are given in terms of the rest mass of an electron.

Zigzag	E_g (eV)	m_e	m_h
(3,0)	Metallic	-	-
(4,0)	Metallic	-	-
(5,0)	Metallic	-	-
(6,0)	Metallic	-	-
(7,0)	0.206	0.162	0.092
(8,0)	0.576	0.165	0.284
(9,0)	0.146	0.030	0.031
(10,0)	0.751	0.080	0.081

Figure 8 shows the band structures obtained by calculations for structures with three different chiral indices. As can be seen from the graphs, there are significant differences in the energy band structure of each chiral nanotube structure. The energy levels shown in red indicate the conduction band, which is empty energy levels. The Fermi energy level occurs above the filled valence band shown in black. In all structures the electronic character is semiconductor.

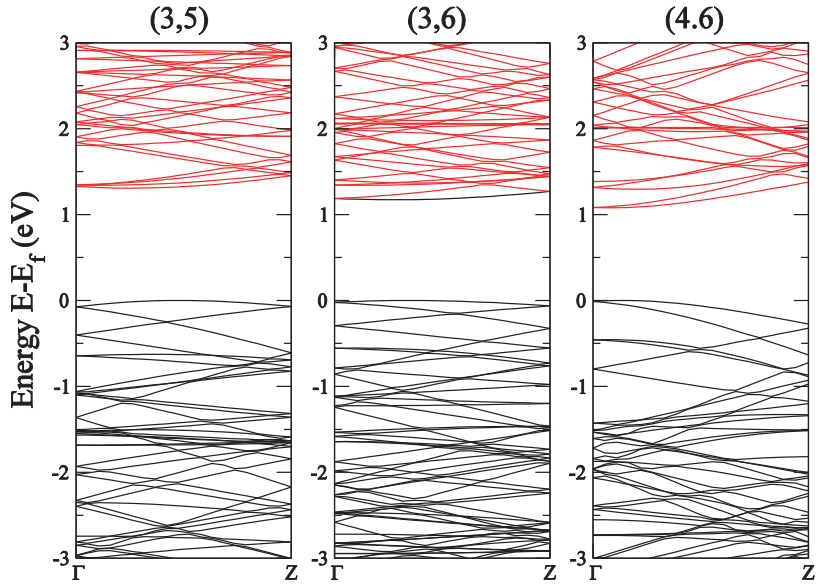

Figure 8: Band structures obtained for chiral nanotubes with different indexes.

Table 3: Data obtained from the band structure of chiral nanotubes with different indexes. E_g represents the band gap and its unit is eV. The m_e and m_h represent the effective mass of electron and hole, respectively. Effective mass values are given in terms of the rest mass of an electron.

Chiral	**E_g (eV)**	Transition	m_e	m_h
(3,4)	1.308	Indirect	0.186	0.187
(3,5)	1.173	Indirect	0.220	0.263
(4,6)	1.079	Indirect	0.229	0.181

Table 3 lists the data obtained from the electronic band structure. Looking at the table, it can be seen that the band gap values (E_g) of these nanotubes are 1.308 eV, 1.173 eV and 1.079 eV for the chiral indices (3.4), (3.5) and (4.6), respectively. This shows that the band gap value decreases depending on the chiral index of the nanotube. However, a more in-depth examination is required to determine exactly what causes these differences. We also see that the nature of the transition for all nanotubes is indirect. Indirect transition means that the VBM and the CBM are not of the same momentum (k-value). This means that such semiconductors may be less sensitive to optical excitations. There are some differences between the effective mass values of electron m_e and hole m_h. These values can have a significant impact on the carrier mobility and other electronic properties of the semiconductor. The (3,4) has the lowest effective mass value. According to the obtained data, the electronic properties of chiral carbon nanotubes can vary significantly depending on the chiral index. This work demonstrates the effect of nanotube chirality on the band gap, transition nature, and carrier masses. These findings provide important information on how chiral carbon nanotubes can be optimized for electronics and optoelectronics applications.

8. CONCLUSION

This chapter provided an in-depth exploration of the electronic properties of several carbon allotropes, specifically focusing on graphene and various structures of carbon nanotubes (CNTs). The presented comprehensive analyses elucidate the intrinsic electronic characteristics, offering insights into their potential and limitations in numerous applications.

Graphene, with its remarkable properties like exceptional strength, high conductivity, transparency, and flexibility, holds promise for various applications ranging from transparent conductive films to energy storage and several electronic components. Its distinctive band structure, especially the Dirac cone observed near the Fermi energy, underpins its high electron mobility and several other unique electronic properties.

Similarly, carbon nanotubes (CNTs) reveal diverse electronic properties heavily dependent on their structural configurations. Armchair CNTs, in

general, demonstrate metallic properties, with electronic band structures and effective mass values conducive to high-speed and high-mobility electronic applications, though production challenges may stymie large-scale applications. Zigzag CNTs illustrate the crucial role of structural parameters, such as the index "n" in dictating their electronic properties, thereby offering a pathway to engineer nanotubes for specific electronic roles, whether metallic or semiconducting, by judicious selection of structural parameters. Lastly, chiral CNTs exhibit a broad spectrum of semiconductor properties that hinge on their chiral indices, accentuating the importance of understanding and optimizing chirality to tailor CNTs for particular applications in electronics and optoelectronics.

In essence, the tailored electronic properties emerging from the specific structural configurations of graphene and CNTs spotlight the vast potential and versatility these carbon-based materials extend to the realm of electronics. Through a deepened understanding and subsequent optimization of these properties, researchers and engineers can further push the boundaries, crafting novel, efficient, and perhaps more sustainable electronic devices in the future. Nevertheless, challenges related to the scalability, purity, and production processes of these materials remain to be addressed comprehensively to translate the promising laboratory-scale results to real-world applications.

In pursuit of materializing the promising applications of these carbon allotropes, future studies and developments must be steered towards ameliorating production methodologies, ensuring reproducibility, and exploring viable strategies for seamlessly integrating these materials into existing and emerging technologies.

REFERENCES

Blöchl, P. E. (1994). Projector augmented-wave method. *Phys. Rev. B*, 50:17953–17979.

Dekker, C. (1999). Carbon Nanotubes as Molecular Quantum Wires. *Physics Today*, 52(5):22–28.

Dresselhaus, M., Dresselhaus, G., and Eklund, P. (1996). Chapter 1 - historical introduction. In Dresselhaus, M., Dresselhaus, G., and Eklund, P., editors, *Science of Fullerenes and Carbon Nanotubes*, pages 1–14. Academic Press, San Diego.

Hamada, N., Sawada, S.-i., and Oshiyama, A. (1992). New one-dimensional conductors: Graphitic microtubules. *Phys. Rev. Lett.*, 68:1579–1581.

Hohenberg, P. and Kohn, W. (1964). Inhomogeneous electron gas. *Physical review*, 136(3B):B864.

Hu, J., Odom, T. W., and Lieber, C. M. (1999). Chemistry and physics in one dimension:synthesis and properties of nanowires and nanotubes. *Accounts of Chemical Research*, 32(5):435–445.

Iijima, S. (1991). Helical microtubules of graphitic carbon. *Nature*, 354(6348):56–58.

Kim, H., Park, K.-Y., Hong, J., and Kang, K. (2014). All-graphene-battery: bridging the gap between supercapacitors and lithium ion batteries. *Scientific Reports*, 4(1):5278.

Kresse, G. and Furthmüller, J. (1996). Efficient iterative schemes for *ab initio* total-energy calculations using a plane-wave basis set. *Phys. Rev. B*, 54:11169–11186.

Kresse, G. and Hafner, J. (1993). *Ab initio* molecular dynamics for liquid metals. *Phys. Rev. B*, 47:558–561.

Kresse, G. and Joubert, D. (1999). From ultrasoft pseudopotentials to the projector augmented-wave method. *Phys. Rev. B*, 59:1758–1775.

Lieber, C. M. (1998). One-dimensional nanostructures: Chemistry, physics i& applications. *Solid State Communications*, 107(11):607–616.

Mintmire, J. W., Dunlap, B. I., and White, C. T. (1992). Are fullerene tubules metallic? *Phys. Rev. Lett.*, 68:631–634.

Monkhorst, H. J. and Pack, J. D. (1976). Special points for brillouin-zone integrations. *Phys. Rev. B*, 13:5188–5192.

Nair, R. R., Blake, P., Grigorenko, A. N., Novoselov, K. S., Booth, T. J., Stauber, T., Peres, N. M. R., and Geim, A. K. (2008). Fine structure constant defines visual transparency of graphene. *Science*, 320(5881):1308–1308.

Novoselov, K. S., Geim, A. K., Morozov, S. V., Jiang, D., Zhang, Y., Dubonos, S. V., et al. (2004). Electric field effect in atomically thin carbon films. *Science*, 306(5696):666–669.

Odom, T. W., Huang, J.-L., Kim, P., and Lieber, C. M. (1998). Atomic structure and electronic properties of single-walled carbon nanotubes. *Nature*, 391(6662):62–64.

Perdew, J. P., Burke, K., and Ernzerhof, M. (1996). Generalized gradient approximation made simple. *Phys. Rev. Lett.*, 77:3865–3868.

Saito, R., Dresselhaus, G., and Dresselhaus, M. S. (1998). *Physical properties of carbon nanotubes*. Imperial College Press.

Saito, R., Fujita, M., Dresselhaus, G., and Dresselhaus, M. S. (1992). Electronic structure of chiral graphene tubules. *Applied Physics Letters*, 60(18):2204–2206.

Treacy, M. M. J., Ebbesen, T. W., and Gibson, J. M. (1996). Exceptionally high young's modulus observed for individual carbon nanotubes. *Nature*, 381(6584):678–680.

Wilder, J. W. G., Venema, L. C., Rinzler, A. G., Smalley, R. E., and Dekker, C. (1998). Electronic structure of atomically resolved carbon nanotubes. *Nature*, 391(6662):59–62.

Wong, E. W., Sheehan, P. E., and Lieber, C. M. (1997). Nanobeam mechanics: Elasticity, strength, and toughness of nanorods and nanotubes. *Science*, 277(5334):1971–1975.

Xia, J., Chen, F., Li, J., and Tao, N. (2009). Measurement of the quantum capacitance of graphene. *Nature Nanotechnology*, 4(8):505–509.

Yakobson, B. I., Brabec, C. J., and Bernholc, J. (1996). Nanomechanics of carbon tubes: Instabilities beyond linear response. *Phys. Rev. Lett.*, 76:2511–2514.

Yakobson, B. I. and Smalley, R. E. (1997). Fullerene nanotubes: $C_{1,000,000}$ and beyond: Some unusual new molecules—long, hollow fibers with tantalizing electronic and mechanical properties—have joined diamonds and graphite in the carbon family. *American Scientist*, 85(4):324–337. Full publication date: JULY-AUGUST 1997.

Chapter 17

ON EIGENFUNCTIONS OF THE STURM-LIOUVILLE PROBLEMS WITH BOUNDARY CONDITIONS RATIONALLY DEPENDENT ON THE EIGENPARAMETER

Ayşe KABATAŞ[1]

1 Asst. Prof. Dr.; Karadeniz Technical University, Science Faculty, Department of Mathematics. akabatas@ktu.edu.tr ORCID No: 0000-0003-3273-3666

INTRODUCTION

The second-order linear ordinary differential equation on the real interval I is of the form

$$a_0(x)y'' + a_1(x)y' + a_2(x)y = f(x) \tag{1}$$

where the coefficients $a_0(x), a_1(x)$ and $a_2(x)$ are sufficiently regular. When $f(x) = 0$ on I, the equation is called *homogeneous*, otherwise it is *nonhomogeneous*.

If the function $a_0(x)$ does not vanish at any point on I, the equation (1) may be divided by $a_0(x)$ to give

$$y'' + b(x)y' + c(x)y = g(x) \tag{2}$$

where $b(x) = a_1(x)/a_0(x), c(x) = a_2(x)/a_0(x)$ and $g(x) = f(x)/a_0(x)$.

With $I = [x_0, x_1]$, the solutions of the equation (2) may be subjected to boundary conditions at x_0 and x_1. These boundary conditions can be generalized by the pair of equations

$$\alpha_1 y(x_0) + \alpha_2 y'(x_0) + \alpha_3 y(x_1) + \alpha_4 y'(x_1) = \zeta, \tag{3}$$

$$\beta_1 y(x_1) + \beta_2 y'(x_1) + \beta_3 y(x_0) + \beta_4 y'(x_0) = \varrho \tag{4}$$

where ζ, ϱ, α_i and β_i $(i = 1,2,3,4)$ are constants. Besides, $\sum_{i=1}^{4}|\alpha_i| > 0$ and $\sum_{i=1}^{4}|\beta_i| > 0$, that is, such that not all the α_i or β_i are zeros (Al-Gwaiz, 2008). The problem (2)-(4) is called a *boundary value problem*. The boundary conditions (3) and (4) are called *homogeneous* if $\zeta = \varrho = 0$ and *seperated* if $\alpha_3 = \alpha_4 = \beta_3 = \beta_4 = 0$.

We are interested in the eigenvalue problem, which is slightly modified notation of (2),

$$\frac{d^2y}{dx^2} + b(x)\frac{dy}{dx} + [c(x) + \lambda d(x)]y = 0 \tag{5}$$

where λ is a real spectral parameter independent of x to be determined by the boundary conditions. Let introduce the integrating factor $p(x)$ by

$$p(x) = exp\left(\int b(x)dx\right).$$

Multiplying the equation (5) by $p(x)$, we obtain

$$\frac{d}{dx}\left[p(x)\frac{dy}{dx}\right] + [q(x) + \lambda r(x)]y = 0 \tag{6}$$

where $q(x) = p(x)c(x)$ and $r(x) = p(x)d(x)$. This equation is known as the *Sturm-Liouville equation*. If $p(x) = r(x) = -1$, the equation (6) can be written

$$-y'' + q(x)y = \lambda y. \tag{7}$$

In this chapter, we will handle the Sturm-Liouville equation (7) under the boundary conditions rationally dependent on the spectral parameter.

Sturm-Liouville problems are boundary value problems that naturally arise when solving certain partial differential equation problems, which often describe the oscillation of pendula, vibrations, resonances or waves, using a seperation of variables method. A solution to such a problem is the function that satisfies the given problem - both the differential equation and the boundary conditions. Here, the spectral parameter may appear only in the equation itself or in both the equation and the boundary conditions. Classical problems for Sturm-Liouville operators without λ under the boundary conditions have been studied fairly completely (Başkaya, 2020; Başkaya, 2021b; Coşkun et al., 2019; Kabataş, 2022a; Kabataş, 2022b; Titchmarsh, 1962; Zettl, 2010). There are only a rather limited number of papers on differential operators with boundary conditions dependent on the spectral parameter (Başkaya, 2018a; Başkaya, 2018b; Başkaya, 2018c; Başkaya, 2021a, Binding et al., 2004; Coşkun and Başkaya, 2018; Coşkun and Kabataş, 2016; Coşkun et al., 2017; Kabataş, 2023).

Consider the Sturm-Liouville problem

$$y'' + [\lambda - q(x)]y = 0 \tag{8}$$

$$y(0)cos\theta = y'(0)sin\theta, \quad \theta \in [0, \pi), \tag{9}$$

$$\frac{y'}{y}(1) = s(\lambda) \tag{10}$$

on the finite interval $[0,1]$. We define

$$s(\lambda) = \frac{m(\lambda)}{v(\lambda)} \tag{11}$$

where m and v are polynomials with real coefficients and no common zeros. When $\theta = 0$, the boundary condition (9) is taken as $y(0) = 0$ and when $s(\lambda) = \infty$, (11) is accepted as $y(1) = 0$. In addition, if $deg(m) \leq deg(v) = M$, let $m(\lambda) = A_M\lambda^M + \ldots + A_0$ where $A_M \in \mathbb{R}$ (it may be zero) and assume that v is monic; while if $M = deg(m) > deg(v)$, let $v(\lambda) = A_{M-1}\lambda^{M-1} + \ldots + A_0$ where $A_{M-1} \in \mathbb{R}$ (it may be zero) and assume that m is monic.

We shall subsequently refer to q as the potential and we will assume that $q(x)$ is a real-valued L_1-function on the interval [0,1]. Also, $q(x)$ has a mean value zero, i. e., $\int_0^1 q(t)dt = 0$. Here, we determine asymptotic estimates for the non-trivial solutions of the Sturm-Liouville problem (8)-(10) under these conditions.

The values of the parameter λ for which the problem (8)-(10) has non-zero solutions are called *eigenvalues*. The corresponding non-trivial solutions are called *eigenfunctions* (Freiling and Yurko, 2008). In (Binding et al., 2004), it was shown that the eigenvalues of the problem (8)-(10) satisfy as $n \to \infty$

(i) for $\theta \neq 0,\ deg(m) \leq deg(v) = M$

$$\lambda_n = (n - M)^2\pi^2 + 2cot\alpha - 2A_m + o(n^{-1}), \tag{12}$$

(ii) for $\theta = 0, deg(m) \leq deg(v) = M$

$$\lambda_n = (n + \frac{1}{2} - M)^2\pi^2 - 2A_M + o(n^{-1}), \tag{13}$$

(iii) for $\theta \neq 0, M = deg(m) > deg(v)$

$$\lambda_n = \left(n + \frac{1}{2} - M\right)^2 \pi^2 + 2cot\alpha + 2A_{M-1} + o(n^{-1}), \tag{14}$$

(iv) for $\theta = 0, M = deg(m) > deg(v)$

$$\lambda_n = (n + 1 - M)^2\pi^2 + 2A_{M-1} + o(n^{-1}). \tag{15}$$

All eigenvalues are algebraically simple and real for large n.

Throughout the chapter, we examine the eigenfunctions corresponding to λ_n s given by (12)-(15).

ASYMPTOTIC APPROXIMATIONS FOR THE EIGENFUNCTIONS

As similar to the (Harris, 1997), we define a complex valued solution, $u(x,\lambda)$, of the equation (8). If $w(x,\lambda)=\frac{u\prime(x,\lambda)}{u(x,\lambda)}$ transform is applied to (8), we have the Riccati equation

$$w' = -\lambda + q - w^2. \tag{16}$$

We set

$$S(x,\lambda) := Re\{w(x,\lambda)\}, T(x,\lambda) := Im\{w(x,\lambda)\}. \tag{17}$$

where $w(x,\lambda)$ is a complex-valued solution of (16). It is given in (Harris, 1997) that any non-trivial real-valued solution, z, of (8) can be expressed as

$$z(x,\lambda) = c_1 \exp\left(\int_0^x S\,(t,\lambda)dt\right)\cos\left\{c_2 + \int_0^x T\,(t,\lambda)dt\right\} \tag{18}$$

with

$$z'(x,\lambda) = c_1 \mathrm{S(x,\lambda)}\exp\left(\int_0^x S\,(t,\lambda)dt\right)\cos\left\{c_2 + \int_0^x T\,(t,\lambda)dt\right\} \\ -c_1 T(x,\lambda)\exp\left(\int_0^x S\,(t,\lambda)dt\right)\sin\{c_2 + \int_0^x T\,(t,\lambda)dt\}. \tag{19}$$

In order to determine the asymptotic approximations, we now define two solutions, $\mathcal{H}(x,\lambda)$ and $\mathcal{F}(x,\lambda)$, of (8) satisfying the following initial conditions

$$\mathcal{H}(0,\lambda) = sin\theta,\ \mathcal{H}'(0,\lambda) = cos\theta \tag{20}$$

and

$$\mathcal{F}(1,\lambda) = v(\lambda), \mathcal{F}'(1,\lambda) = m(\lambda). \tag{21}$$

Theorem 1. Let $\mathcal{H}(x,\lambda)$ be the solution of (8) satisfying (20). Then,

(i) for $\theta \neq 0$

$$\mathcal{H}(x,\lambda) = \frac{sin\theta}{cos[tan^{-1}\gamma(\lambda)]} exp\left(\int_0^x S(t,\lambda)dt\right)$$
$$\times cos\left[tan^{-1}\gamma(\lambda) + \int_0^x T(t,\lambda)dt\right] \quad (22)$$

where

$$\gamma(\lambda) = \frac{S(0,\lambda) - cot\theta}{T(0,\lambda)}. \quad (23)$$

(ii) for $\theta = 0$

$$\mathcal{H}(x,\lambda) = \frac{1}{T(0,\lambda)}\, exp\left(\int_0^x S(t,\lambda)dt\right) sin\left(\int_0^x T(t,\lambda)dt\right). \quad (24)$$

Proof. *(i)* If $\theta \neq 0$, from (18), (19) and (20) we have

$$\mathcal{H}(0,\lambda) = c_1 \cos c_2 = sin\theta, \quad (25)$$

$$\mathcal{H}'(0,\lambda) = c_1 S(0,\lambda)\cos c_2 - c_1 T(0,\lambda)\sin c_2 = cos\theta. \quad (26)$$

By (25),

$$c_1 = \frac{sin\theta}{\cos c_2} \quad (27)$$

and from (23), (26), (27)

$$c_2 = \tan^{-1}\gamma(\lambda). \quad (28)$$

The proof is completed by substituting the values (27) and (28) into (18).
(ii) If $\theta = 0$, instead of the initial condition (20) we take

$$\mathcal{H}(0,\lambda) = 0,\ \mathcal{H}'(0,\lambda) = 1. \quad (29)$$

So, from (18), (19) and (29) it is obtained that

$$\mathcal{H}(0,\lambda) = c_1 \cos c_2 = 0,$$

$$\mathcal{H}'(0,\lambda) = c_1 S(0,\lambda)\cos c_2 - c_1 T(0,\lambda)\sin c_2 = 1.$$

These two equalities give

$$c_1 = -\frac{1}{T(0,\lambda)}\,, c_2 = \frac{\pi}{2}. \tag{30}$$

Substituting (30) into (18) proves the theorem.

Theorem 2. Let $\mathcal{F}(x,\lambda)$ be the solution of (8) satisfying (21). Then,

(i) for $deg(m) \le deg(v) = M$

$$\mathcal{F}(x,\lambda) = \frac{v(\lambda)}{cos[tan^{-1}\sigma(\lambda)]} exp\left(-\int_x^1 S(t,\lambda)dt\right)$$

$$\times cos\left[tan^{-1}\sigma(\lambda) - \int_x^1 T(t,\lambda)dt\right] \tag{31}$$

where

$$\sigma(\lambda) = \frac{S(1,\lambda)}{T(1,\lambda)} - \frac{m(\lambda)}{v(\lambda)T(1,\lambda)}. \tag{32}$$

(ii) for $deg(v) < deg(m) = M$

$$\mathcal{F}(x,\lambda) = \frac{v(\lambda)}{cos[cot^{-1}\Gamma(\lambda)]} exp\left(-\int_x^1 S(t,\lambda)dt\right)$$

$$\times cos\left[cot^{-1}\Gamma(\lambda) - \int_x^1 T(t,\lambda)dt\right] \tag{33}$$

where

$$\Gamma(\lambda) = \frac{v(\lambda)T(1,\lambda)}{v(\lambda)S(1,\lambda) - m(\lambda)}. \tag{34}$$

Proof. *(i)* If $deg(m) \le deg(v) = M$, by using (18), (19) and (21) we get

$$\mathcal{F}(1,\lambda) = c_1 \exp\left(\int_0^1 S\,(t,\lambda)dt\right)\cos\left[c_2 + \int_0^1 T\,(t,\lambda)dt\right] = \mathrm{v}(\lambda), \tag{35}$$

$$\mathcal{F}'(1,\lambda) = c_1 S(1,\lambda)\exp\left(\int_0^1 S(t,\lambda)dt\right)\cos\left[c_2 + \int_0^1 T(t,\lambda)dt\right]$$

$$-c_1 T(1,\lambda)\exp\left(\int_0^1 S(t,\lambda)dt\right)\sin\left[c_2 + \int_0^1 T(t,\lambda)dt\right] = m(\lambda) \quad (36)$$

Thus, we obtain from (35)

$$c_1 = \frac{\mathrm{v}(\lambda)}{\exp\left(\int_0^1 S(t,\lambda)dt\right)\cos\left[c_2 + \int_0^1 T(t,\lambda)dt\right]}$$

and from (36)

$$c_2 = \tan^{-1}\sigma(\lambda) - \int_0^1 T(t,\lambda)dt.$$

For the proof, these values of c_1 and c_2 are used in (18).

The proof of (ii) is similar.

Now we investigate asymptotic approximations for the solutions, $\mathcal{H}(x,\lambda)$ and $\mathcal{F}(x,\lambda)$, of (8) satisfying initial conditions (20) and (21), respectively. For this reason, we need the asymptotic estimates of $S(x,\lambda)$ and $T(x,\lambda)$ given by (17). We seek a solution of the Riccati equation (16) as

$$w(x,\lambda) := i\sqrt{\lambda} + \sum_{k=1}^{\infty} w_k(x,\lambda)$$

where $\lim_{x\to\infty} v_k(x,\lambda) = 0$ for $k = 1,2,\ldots$ (Harris, 1997). Choose w_k so that

$$\begin{aligned} w'_1 + 2i\sqrt{\lambda}w_1 &= q, \\ w'_2 + 2i\sqrt{\lambda}w_2 &= -w_1^2, \\ w'_k + 2i\sqrt{\lambda}w_k &= -\left(w_{k-1}^2 + 2w_{k-1}\sum_{l=1}^{k-2} w_l\right), k \geq 3. \end{aligned}$$

Then, solutions of above equations will be

$$w_1(x,\lambda) = -e^{-2i\sqrt{\lambda}x}\int_x^1 e^{2i\sqrt{\lambda}t}\, q(t)dt,$$

$$w_2(x,\lambda) = e^{-2i\sqrt{\lambda}x}\int_x^1 e^{2i\sqrt{\lambda}t}\, w_1^2(t,\lambda)dt,$$

and for $k \geq 3$

$$w_k(x,\lambda) = e^{-2i\sqrt{\lambda}x}\int_x^1 e^{2i\sqrt{\lambda}t}\left[w_{k-1}^2 + 2w_{k-1}\sum_{l=1}^{k-2} w_l\right]dt.$$

It is shown by Harris (1997) that the series $\sum_{k=1}^{\infty} w_k(x,\lambda)$ and $\sum_{k=1}^{\infty} w'_k(x,\lambda)$ are uniformly absolutely convergent for all $\lambda \geq \lambda_0$. Hence, the series $i\sqrt{\lambda} + \sum_{k=1}^{\infty} w_k(x,\lambda)$ is a solution of (16) and from (17) it is obvious that

$$S(x,\lambda) = Re\sum_{k=1}^{\infty} w_k(x,\lambda), \tag{37}$$

$$T(x,\lambda) = \sqrt{\lambda} + Im\sum_{k=1}^{\infty} w_k(x,\lambda) \tag{38}$$

With a view to finding the asymptotic formulae, we suppose that there exist functions $A(x)$ and $\eta(\lambda)$ so that

$$\left|\int_x^1 e^{2i\sqrt{\lambda}t}\, q(t)dt\right| \leq A(x)\eta(\lambda), \quad x \in [0,1]$$

where

(i) $A(x) := \int_x^1 |q(t)|\, dt$ is decreasing function of x,
(ii) $\eta(\lambda) \to 0$ as $\lambda \to \infty$
(iii) $A(x) \in L^1[0,1]$.

The existence of these functions are established in (Harris, 1997). We define $F(x,\lambda)$ for completeness as follows:

$$F(x,\lambda) := \begin{cases} \dfrac{\left|\int_x^1 e^{2i\sqrt{\lambda}t}\, q(t)dt\right|}{\int_x^1 |q(t)|\, dt}, & \text{if} \int_x^1 |q(t)|\, dt \neq 0, \\ 0, \qquad \text{if} \quad \int_x^1 |q(t)|\, dt = 0 \end{cases}$$

and we set $\eta(\lambda) := sup_{0\le x\le 1} F(x,\lambda)$ ($0 \le F(x,\lambda) \le 1$). So, $\eta(\lambda)$ is well-defined and goes to zero as $\lambda \to \infty$ (Harris, 1997).

As a result of these, the asymptotic approximations for $S(x,\lambda)$ and $T(x,\lambda)$ are given by Coşkun and Başkaya (2010) as follows

$$S(x,\lambda) = -\sin\left(2\sqrt{\lambda}x + \xi_x\right) + O\left(\eta^2(\lambda)\right) \tag{39}$$

and

$$T(x,\lambda) = \sqrt{\lambda} - \cos\left(2\sqrt{\lambda}x + \xi_x\right) + O\left(\eta^2(\lambda)\right) \tag{40}$$

where

$$\sin\xi_x := \int_x^1 q\,(t)\cos(2\sqrt{\lambda}t)dt,$$

$$\cos\xi_x := \int_x^1 q\,(t)\sin(2\sqrt{\lambda}t)dt.$$

Also, it is determined in (Coşkun and Kabataş, 2013) that

$$\int_0^x S\,(t,\lambda)dt = \frac{1}{2\sqrt{\lambda}}\left\{\cos\left(2\sqrt{\lambda}x + \xi_x\right) - \cos\xi_0\right\} + O\left(\frac{\eta^2(\lambda)}{\sqrt{\lambda}}\right), \tag{41}$$

$$\int_0^x T\,(t,\lambda)dt = \sqrt{\lambda}x - \frac{1}{2\sqrt{\lambda}}\left\{\sin\left(2\sqrt{\lambda}x + \xi_x\right) - \sin\xi_0 + \int_0^x q\,(t)dt\right\}$$

$$+O\left(\frac{\eta^2(\lambda)}{\sqrt{\lambda}}\right), \tag{42}$$

$$\int_x^1 S\,(t,\lambda)dt = -\frac{1}{2\sqrt{\lambda}}cos(2\sqrt{\lambda}x + \xi_x) + O(\frac{\eta^2(\lambda)}{\sqrt{\lambda}}), \tag{43}$$

$$\int_x^1 T(t,\lambda)dt = \sqrt{\lambda}(1-x) + \frac{1}{2\sqrt{\lambda}}\left[sin\left(2\sqrt{\lambda}x + \xi_x\right) - \int_x^1 q(t)dt\right]$$

$$+O(\tfrac{\eta^2(\lambda)}{\sqrt{\lambda}}). \quad (44)$$

By using all this, we have the following results.

Theorem 3. For the solutions of (8) having the initial conditions (20), we obtain as $\lambda \to \infty$

(i) for $\theta \neq 0$

$$\mathcal{H}(x,\lambda) = sin\theta cos(\sqrt{\lambda}x) + \frac{sin\theta}{\sqrt{\lambda}}\left[cot\theta + \frac{1}{2}\int_0^x q(t)dt\right]sin(\sqrt{\lambda}x)$$

$$+O\left(\tfrac{\eta(\lambda)}{\sqrt{\lambda}}\right), \quad (45)$$

(ii) for $\theta = 0$

$$\mathcal{H}(x,\lambda) = \tfrac{sin(\sqrt{\lambda}x)}{\sqrt{\lambda}} - \tfrac{1}{2\lambda}\left(\int_0^x q(t)dt\right)cos(\sqrt{\lambda}x) + O(\tfrac{\eta(\lambda)}{\lambda}). \quad (46)$$

Proof. *(i)* For $\theta \neq 0$, we evaluate the terms in (22) as $\lambda \to \infty$. Firstly, substituting (39) and (40) into $\gamma(\lambda)$ given by (23) and using series expansion method one obtains

$$\gamma(\lambda) = \tfrac{-cot\theta + O(\eta(\lambda))}{\sqrt{\lambda}\left[1+O(\frac{\eta(\lambda)}{\sqrt{\lambda}})\right]} = -\tfrac{cot\theta}{\sqrt{\lambda}} + O(\tfrac{\eta(\lambda)}{\sqrt{\lambda}}). \quad (47)$$

From (47) together with inverse trigonometric series we have

$$tan^{-1}\gamma(\lambda) = -\tfrac{cot\theta}{\sqrt{\lambda}} + O(\tfrac{\eta(\lambda)}{\sqrt{\lambda}}).$$

The last equality gives

$$cos[tan^{-1}\gamma(\lambda)] = 1 - \tfrac{cot^2\theta}{2\lambda} + O(\tfrac{\eta(\lambda)}{\lambda}), \quad (48)$$

$$sin[tan^{-1}\gamma(\lambda)] = -\frac{cot\theta}{\sqrt{\lambda}} + O(\frac{\eta(\lambda)}{\sqrt{\lambda}}), \tag{49}$$

$$\frac{sin\theta}{cos[tan^{-1}\gamma(\lambda)]} = sin\theta + \frac{cot^2\theta}{2\lambda sin\theta} + O(\frac{\eta(\lambda)}{\lambda}). \tag{50}$$

Using trigonometric expansions together with (41), (42), (48) and (49) one obtains

$$cos\left[tan^{-1}\gamma(\lambda) + \int_0^x T(t,\lambda)dt\right] = cos(\sqrt{\lambda}x) + \frac{1}{\sqrt{\lambda}} \times \left[cot\theta + \tfrac{1}{2}\int_0^x q(t)dt\right] sin(\sqrt{\lambda}x) + O(\tfrac{\eta(\lambda)}{\sqrt{\lambda}}). \tag{51}$$

Finally, substitution (41), (50) and (51) into (22) proves (45).
(ii) For $\theta = 0$, similar to the proof above we shall evaluate the terms in (24). From (40)

$$\frac{1}{T(0,\lambda)} = \frac{1}{\sqrt{\lambda}}\left[1 + O(\tfrac{\eta(\lambda)}{\sqrt{\lambda}})\right] = \frac{1}{\sqrt{\lambda}} + O(\tfrac{\eta(\lambda)}{\lambda}). \tag{52}$$

So, replacing (41),(42) and (52) into (24) gives (46).
Theorem 4. For the solutions of (8) having the initial conditions (21), we obtain as $\lambda \to \infty$

(i) for $deg(m) \le deg(v) = M$

$$\mathcal{F}(x,\lambda) = \lambda^M cos[\sqrt{\lambda}(1-x)] + \lambda^{M-\frac{1}{2}}\left[\frac{1}{2}\left(\int_x^1 q(t)dt\right) - A_M\right] \times sin[\sqrt{\lambda}(1-x)] + O(\lambda^{M-\frac{1}{2}}\eta(\lambda)), \tag{53}$$

(ii) for $deg(v) < deg(m) = M$

$$\mathcal{F}(x,\lambda) = -\lambda^{M-\frac{1}{2}} sin[\sqrt{\lambda}(1-x)] + \lambda^{M-1}\left[\frac{1}{2}\left(\int_x^1 q(t)dt\right) + A_{M-1}\right] \times cos[\sqrt{\lambda}(1-x)] + O(\lambda^{M-1}\eta(\lambda)). \tag{54}$$

Proof. *(i)* If $deg(m) \leq deg(v) = M$, for the functions $m(\lambda)$ and $v(\lambda)$ we can write asymptotically that

$$m(\lambda) = A_M\lambda^M + O(\lambda^{M-1}),\ v(\lambda) = \lambda^M + O(\lambda^{M-1}). \quad (55)$$

Now, we treat the terms in (31) as $\lambda \to \infty$. From (37) and (38), it is clear that

$$S(1,\lambda) = 0, T(1,\lambda) = \sqrt{\lambda}. \quad (56)$$

So, by (55) and (56) the function $\sigma(\lambda)$ given by (32) will be equal to

$$\sigma(\lambda) = -\frac{A_M\lambda^M + O(\lambda^{M-1})}{\lambda^{M+\frac{1}{2}}\left[1+O(\frac{1}{\lambda})\right]} = -\frac{A_M}{\sqrt{\lambda}} + O(\frac{1}{\sqrt{\lambda^3}}). \quad (57)$$

By (57) one obtains

$$tan^{-1}\sigma(\lambda) = -\frac{A_M}{\sqrt{\lambda}} + O(\frac{1}{\sqrt{\lambda^3}}). \quad (58)$$

From (58)

$$cos[tan^{-1}\sigma(\lambda)] = 1 - \frac{A_M^2}{2\lambda} + O(\frac{1}{\lambda^2}), \quad (59)$$

$$sin[tan^{-1}\sigma(\lambda)] = -\frac{A_M}{\sqrt{\lambda}} + O(\frac{1}{\sqrt{\lambda^3}}), \quad (60)$$

$$\frac{v(\lambda)}{cos[tan^{-1}\sigma(\lambda)]} = \lambda^M + O(\lambda^{M-1}). \quad (61)$$

And, by using (44), (59) and (60) we have

$$cos\left[tan^{-1}\sigma(\lambda) - \int_x^1 T(t,\lambda)dt\right] = cos\left[\sqrt{\lambda}(1-x)\right] + \frac{1}{\sqrt{\lambda}}$$

$$\times\left[\frac{1}{2}\left(\int_x^1 q(t)dt\right) - A_M\right] sin\left[\sqrt{\lambda}(1-x)\right] + O(\frac{\eta(\lambda)}{\sqrt{\lambda}}). \quad (62)$$

Eventually, replacement (43), (61) and (62) into (31) proves the approximate solution (53).

(ii) If $deg(v) < deg(m) = M$, the functions $m(\lambda)$ and $v(\lambda)$ can be written asymptotically that

$$m(\lambda) = \lambda^M + O(\lambda^{M-1}),\ v(\lambda) = A_{M-1}\lambda^{M-1} + O(\lambda^{M-2}). \quad (63)$$

For the proof, the terms in (33) are evaluated as $\lambda \to \infty$. Firstly, we calculate $\Gamma(\lambda)$ given by (34) by using (56) and (63) as follows

$$\Gamma(\lambda) = -\frac{\sqrt{\lambda}[A_{M-1}\lambda^{M-1}+O(\lambda^{M-2})]}{\lambda^M\left[1+O(\frac{1}{\lambda})\right]} = -\frac{A_{M-1}}{\sqrt{\lambda}} + O(\frac{1}{\sqrt{\lambda^3}}).$$

This gives

$$cot^{-1}\Gamma(\lambda) = \frac{\pi}{2} + \frac{A_{M-1}}{\sqrt{\lambda}} + O(\frac{1}{\sqrt{\lambda^3}}).$$

Thus,

$$cos[cot^{-1}\Gamma(\lambda)] = -sin\left[\frac{A_{M-1}}{\sqrt{\lambda}} + O(\frac{1}{\sqrt{\lambda^3}})\right] = -\frac{A_{M-1}}{\sqrt{\lambda}} + O(\frac{1}{\sqrt{\lambda^3}}), \quad (64)$$

$$sin[cot^{-1}\Gamma(\lambda)] = cos\left[\frac{A_{M-1}}{\sqrt{\lambda}} + O(\frac{1}{\sqrt{\lambda^3}})\right] = 1 - \frac{A_{M-1}^2}{2\lambda} + O(\frac{1}{\lambda^2}), \quad (65)$$

$$\frac{v(\lambda)}{cos[cot^{-1}\Gamma(\lambda)]} = -\lambda^{M-\frac{1}{2}} + O(\lambda^{M-\frac{3}{2}}). \quad (66)$$

By (44), (64) and (65) together with trigonometric expansions, it is obtained that

$$cos\left[cot^{-1}\Gamma(\lambda) - \int_x^1 T(t,\lambda)dt\right] = sin\left[\sqrt{\lambda}(1-x)\right] - \frac{1}{\sqrt{\lambda}}$$
$$\times\left[\frac{1}{2}\left(\int_x^1 q(t)dt\right) + A_{M-1}\right]cos\left[\sqrt{\lambda}(1-x)\right] + O(\frac{\eta(\lambda)}{\sqrt{\lambda}}). \quad (67)$$

Substituting (43), (66) and (67) into (33) proves the second estimate (54) of the theorem.

Now, we will give the approximations for the eigenfunctions of the problem (8)-(10).

Theorem 5. The asymptotic formulae for the eigenfunctions of (8) and (20) satisfy as $n \to \infty$

(i) for $\theta \neq 0,\ deg(m) \leq deg(v) = M$

$$\mathcal{H}(x,n) = sin\theta cos[(n-M)\pi x] + \frac{sin\theta}{(n-M)\pi}\left[cot\theta + \frac{1}{2}\int_0^x q(t)dt\right]$$

$$\times sin[(n-M)\pi x] + O(\tfrac{\eta(n)}{n}),$$

(ii) for $\theta \neq 0, M = deg(m) > deg(v)$

$$\mathcal{H}(x,n) = sin\theta cos\left[(n+\frac{1}{2}-M)\pi x\right] + \frac{sin\theta}{(n+\frac{1}{2}-M)\pi}$$

$$\times \left[cot\theta + \tfrac{1}{2}\textstyle\int_0^x q(t)dt\right] sin\left[(n+\tfrac{1}{2}-M)\pi x\right] + O(\tfrac{\eta(n)}{n}),$$

(iii) for $\theta = 0,\ deg(m) \leq deg(v) = M$

$$\mathcal{H}(x,n) = \frac{sin\left[(n+\frac{1}{2}-M)\pi x)\right]}{(n+\frac{1}{2}-M)\pi} - \frac{1}{2(n+\frac{1}{2}-M)^2\pi^2}\left(\int_0^x q(t)dt\right)$$

$$\times cos\left[(n+\tfrac{1}{2}-M)\pi x)\right] + O(\tfrac{\eta(n)}{n^2}),$$

(iv) for $\theta = 0, M = deg(m) > deg(v)$

$$\mathcal{H}(x,n) = \frac{sin[(n+1-M)\pi x)]}{(n+1-M)\pi} - \frac{1}{2(n+1-M)^2\pi^2}\left(\int_0^x q(t)dt\right)$$

$$\times cos[(n+1-M)\pi x)] + O(\tfrac{\eta(n)}{n^2}).$$

Theorem 6. The asymptotic formulae for the eigenfunctions of (8) and (21) satisfy as $n \to \infty$

(i) for $\theta \neq 0,\ deg(m) \leq deg(v) = M$

$$\mathcal{F}(x,n) = [(n-M)\pi]^{2M} cos[(n-M)(1-x)\pi] + [(n-M)\pi]^{2M-1}$$

$$\times \left[\frac{1}{2}\left(\int_x^1 q(t)dt\right) - A_M\right] sin[(n-M)(1-x)\pi]$$

$$+O(n^{2M-1}\eta(n)),$$

(ii) for $\theta = 0,\ deg(m) \leq deg(v) = M$

$$\mathcal{F}(x,n) = \left[(n+\frac{1}{2}-M)\pi\right]^{2M} cos\left[(n+\frac{1}{2}-M)(1-x)\pi\right]$$

$$+\left[(n+\frac{1}{2}-M)\pi\right]^{2M-1}\left[\frac{1}{2}\left(\int_x^1 q(t)dt\right) - A_M\right]$$

$$\times sin\left[(n+\tfrac{1}{2}-M)(1-x)\pi\right] + O(n^{2M-1}\eta(n)),$$

(iii) for $\theta \neq 0, M = deg(m) > deg(v)$

$$\mathcal{F}(x,n) = -\left[(n+\frac{1}{2}-M)\pi\right]^{2M-1} sin\left[(n+\frac{1}{2}-M)(1-x)\pi\right]$$

$$+\left[(n+\frac{1}{2}-M)\pi\right]^{2M-2}\left[\frac{1}{2}\left(\int_x^1 q(t)dt\right) + A_{M-1}\right]$$

$$\times cos\left[(n+\tfrac{1}{2}-M)(1-x)\pi\right] + O(n^{2M-2}\eta(n)),$$

(iv) for $\theta = 0, M = deg(m) > deg(v)$

$$\mathcal{F}(x,n) = -[(n+1-M)\pi]^{2M-1} sin[(n+1-M)(1-x)\pi]$$

$$+[(n+1-M)\pi]^{2M-2}\left[\frac{1}{2}\left(\int_x^1 q(t)dt\right) + A_{M-1}\right]$$

$$\times cos[(n+1-M)(1-x)\pi] + O(n^{2M-2}\eta(n)).$$

To prove Theorem 5 and Theorem 6, we replace the eigenvalues (12)-(15) in the results of Theorem 3 and Theorem 4.

REFERENCES

Al-Gwaiz, M. A. (2008). Sturm-Liouville Theory and its Applications. London: Springer-Verlag.

Başkaya, E. (2018a). Asymptotics of eigenvalues for Sturm-Liouville problem including eigenparameter-dependent boundary conditions with integrable potential. New Trends in Mathematical Sciences, 6(3), 39-47.

Başkaya, E. (2018b). Asymptotics of eigenvalues for Sturm-Liouville problem including quadratic eigenvalue in the boundary condition. New Trends in Mathematical Sciences, 6(3), 76-82.

Başkaya, E. (2018c). Asymptotics of eigenvalues for Sturm-Liouville problem with eigenparameter dependent-boundary conditions. New Trends in Mathematical Sciences, 6(2), 247-257.

Baskaya, E. (2020). Periodic and semi-periodic eigenvalues of Hill's equation with symmetric double well potential. TWMS Journal of Applied and Engineering Mathematics, 10(2), 346-352.

Başkaya, E. (2021a). Asymptotic eigenvalues of regular Sturm-Liouville problems with spectral parameter-dependent boundary conditions and symmetric single well potential. Turkish Journal of Mathematics and Computer Science, 13(1), 44-50.

Başkaya, E. (2021b). On the gaps of Neumann eigenvalues for Hill's equation with symmetric double well potential. Tbilisi Mathematical Journal, 8, 139-145.

Binding, P. A., Browne, P. J., and Watson, B. A. (2004). Equivalance of inverse Sturm-Liouville problems with boundary conditions rationally dependent on the eigenparameter. Journal of Mathematical Analysis and Applications, 291, 246-261.

Coşkun, H., and Başkaya, E. (2010). Asymptotics of eigenvalues of regular Sturm-Liouville problems with eigenvalue parameter in the boundary condition for integrable potential. Mathematica Scandinavica, 107(2), 209-223.

Coşkun, H., and Başkaya, E. (2018). Asymptotics of eigenvalues for Sturm-Liouville problem with eigenvalue in the boundary condition for differentiable potential. Annals of Pure and Applied Mathematics, 16(1), 7-19.

Coşkun, H., Başkaya E., and Kabataş, A. (2019). Instability intervals for Hill's equation with symmetric single well potential. Ukrainian Mathematical Journal, 71(6), 977-983.

Coşkun, H., and Kabataş, A. (2013). Asymptotic approximations of eigenfunctions for regular Sturm-Liouville problems with eigenvalue parameter in the boundary condition for integrable potential, Mathematica Scandinavica, 113(1), 143-160.

Coşkun, H., and Kabataş, A. (2016). Green's function of regular Sturm-Liouville problem having eigenparameter in one boundary condition. Turkish Journal of Mathematics and Computer Sciences, 4, 1-9.

Coşkun, H., Kabataş, A., and Başkaya. E. (2017). On Green's function for boundary value problem with eigenvalue dependent quadratic boundary condition. Boundary Value Problems. Article number:71.

Freiling, G., and Yurko, V. (2008). Inverse Sturm-Liouville Problems and Their Applications. New York: Nova Science Publishers.

Harris, B. (1997). The form of the spectral functions associated with Sturm-Liouville problems with continuous spectrum. Mathematika, 44(1), 149-161.

Kabataş, A. (2022a). Eigenfunction and Green's function asymptotics for Hill's equation with symmetric single well potential. Ukrainian Mathematical Journal, 74(2), 218-231.

Kabataş, A. (2022b). On eigenfunctions of Hill's equation with symmetric double well potential. Communications Faculty of Sciences University of Ankara Series A1 Mathematics and Statistics, 71(3), 634-649.

Kabataş, A. (2023). One boundary value problem including a spectral parameter in all boundary conditions. Opuscula Mathematica, 43(5), 651-661.

Titchmarsh, E. C. (1962). Eigenfunction Expansions Associated with Second Order Differential Equations, Part I-II. Oxford: Clarendon Press.

Zettl, A. (2010). Sturm-Liouville Theory. United States of America: American Mathematical Society.

Chapter 18

PULSE POSITION MODULATION TRANSMISSION SCHEMES IN VISIBLE LIGHT COMMUNICATION SYSTEMS

Methmet SÖNMEZ[1]

1 Doç. Dr., Osmaniye Korkut Ata Üniversitesi, Mühendislik Fakültesi, Elektrik-Elektronik Mühendisliği Bölümü

1. Introduction

In the future, there will be an increasing demand for sharing of big data applications, such as transmission of voice, image and video over wireless communication systems (Sreedeviet al., 2022; Stergiou and Psannis, 2022). The efficiency of power consumption is a crucial issue to ensure the long battery life for wireless communication devices which supports the transmission of these data packets (Khanh et al., 2022; Sun et al., 2016). Addition to this, it is expected that next generation mobile systems such as 6G (Sixth Generation) will expand the transmission circle (Sejan et al., 2022; Tong et al., 2023).

With continuing efforts from academia and industry, it is expected the wireless communication systems will provide the sharing of enormous data in the near future (Chowdhuryet al., 2019). Therefore, the visible light communication technology is emerging as one promising candidate to aid to Radio Frequency communication systems (Nor, 2021). The visible light communication systems use a Light Emitted Diode (LED) at the transmitter side while it employs a photo-detector at the receiver side. Therefore, this communication system uses visible light scattered from LED to carry the data signal.

In the literature, many papers related to visible light communication have taken into account several challenges, including inter-symbol interference (ISI) (Shi et al., 2023), indoor localization (Sen et al., 2023), dimming support (Saengudomlert and Buddhacharya, 2023), and high data rate (Younus, et al., 2023). To solve many problems related to inter-symbol interference, some papers have proposed equalization based algorithms (Bostanoglu et al., 2023; Jin et al., 2023; Yang et al., 2023). Proposed algorithms prevent the ISI and allows high data rate for visible light communication systems. The machine learning algorithms have been much attached attention to estimate the location of mobile user in indoor communication systems (Abdalmajeed et al., 2023; Long et al., 2023; Sejan et al., 2023). Specifically, the machine learning techniques are widely used in detection threshold (Ayten and Sönmez, 2021), modulation classification (Ağır and Sönmez, 2023), channel modelling (Turan and Coleri, 2021), location tracking (Danys et al., 2022), and high speed systems (Chi et al., 2020).

Both the providing of power efficiency and the expanding of transmission distance at the same time are observed as important challenges in wireless communication systems since BER performance of communication systems is affected by both parameters (Din and Kim, 2014; Rehmanet al., 2019; Wang et

al., 2016). The modulation scheme used in the optical wireless communication systems is one of the leading solution of above mentioned challenges. Hence, it can be asserted that it has been proposed the many modulation schemes to facilitate the data transmission for visible light communication systems (Gancarz et al., 2015). One of the most used schemes is PPM (Pulse Position Modulation) transmission method. This scheme is employed according to position of filled slot. In literature, PPM is improved by integrating PWM (Pulse Width Modulation) scheme to ensure dimming support. For instance, the VPPM (Variable Pulse Position Modulation) scheme has been proposed to provide both a dimmable system by controlling LED light and data transmission at the same time (Lee and Park, 2011; Raj et al., 2021).

Several PPM based transmission methods were proposed for optical communication scheme before VLC became a popular wireless optical system. Therefore, these modulation schemes have been investigated in terms of bandwidth efficiency, power consumption, data transmission performance for optical systems by several researchers. One of these schemes is Overlapping PPM (OPPM) technique. In the literature, CDMA (Code Division Multiplexing Access) method is integrated OPPM to enhance the transmission performance (Farghal et al., 2014). Another transmission method can be given as Multilevel PPM (MPPM) scheme that is suggested to improve the bandwidth utilization efficiency (Nguyen and Lampe, 2010).

Addition to bandwidth and energy efficiencies enhancement of PPM, PPM transmission method has been investigated in terms of shorting of codeword number. The first of these enhancements was actualized when proposed the Shorten PPM (SPPM) scheme (Sui and Zhou, 2009). This scheme decreases the codeword of traditional PPM by adding a MSB (Most Significant Bit) that is detected by using a threshold level. Secondly, it has been further reduced the codeword of shorten PPM by improving Offset PPM scheme (Sibley, 2011). The slot level of Offset PPM is detected by using a threshold level that must be variable to support the user mobility condition in indoor communication systems. It is the most significant disadvantage for detecting of this type signal.

In this article, it has been represented transmitter and receiver algorithms for visible light communication systems. Addition to this, LoS (Line of Sight) and NLoS (Non LoS) optical channel models are addressed to observe distribution of optical signal by considering direct and non-direct paths in indoor media. Moreover, it is reported modulation techniques based on Pulse Position

Modulation. Specifically, PPM and dimming supporting PPM transmission schemes are given in the article.

2. Visible Light Communication

Visible light communication systems are becoming a strong candidate for indoor usage. However, it must be solved the many challenges that limit their use applicability. Although lighting technology has been improved very well, it is very formidable period for low cost manufacturing of lighting based devices to support high data rate. Specifically, LED nonlinearity has been addressed from many researchers due to inter symbol interference. Therefore, visible light communication systems are expected both high data rate and economical usage. In this section, we give a report to insight visible light communication systems in terms of transmitter and receiver units. In Figure 1, a block diagram is illustrated for visible light communication system.

To obtain suitable signal for modulator stage, a Tx Data which will be transmitted signal is applied for encoder block. Then, modulated signal is generated at modulator stage by using encoding signal. To obstruct the inter-symbol interference and prevent the LED nonlinearity, pre-equalization algorithm can be implemented on VLC system (Chi et al., 2018). Thanks to pre-equalization, data rate can be increased by reducing the ISI. At the end stage of transmitter, LED array is keying by taking account modulation type and target dimming level. Therefore, it considered that the modulated signal is applied a LED driver circuit at the transmitter side.

At the receiver side, the light is detected by photo-detector. Detected light generates a current signal at the pins of photo-detector since photo-detector is current-based sensor. It can be used a Transimpedance Amplifier to convert the current to voltage signal (Pham et al., 2017). Thanks to an amplifier, the signal with low amplitude at output of transimpedance can be amplified to obtain a workable signal. Then, received signal is passed through demodulation process to acquire data signal.

The path between LED array and photo-diode can be defined as LoS and NLoS. Direct path is very basic model since reflecting signal is ignored in this channel model. Reflecting signal causes ISI since it is considered a phase difference between direct signal and reflecting signal. Addition to this, it can be observed a phase difference between reflected signals. Therefore, this causes ISI case that prevents high data transfer.

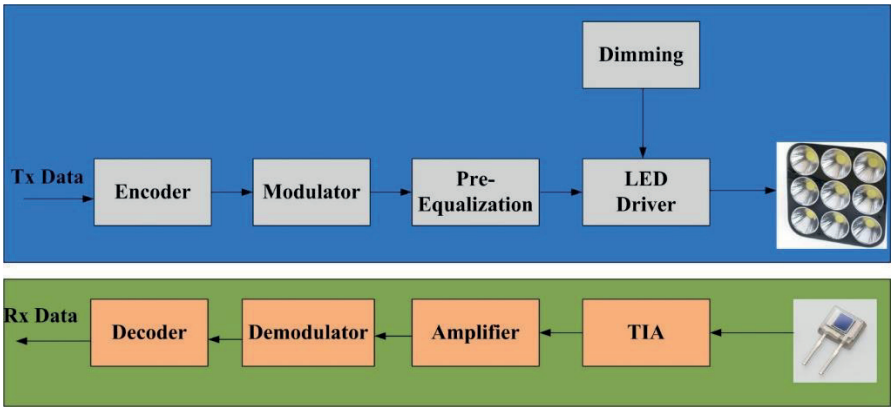

Figure 1. VLC Block Scheme

One of the most important parameters of a VLC channel is the Channel DC (Direct Current) gain since it acts as a coefficient between transmitter and receiver powers. Thus, it can be considered that DC gain can be an attenuation indicator. The optical power received Pr can be given as follows:

$$P_r = H(0)P_t \tag{1}$$

where, Pt and Pr can be defined as transmitted power, channel DC gain, respectively (Komine and Nakagawa, 2004). Additionally, the channel DC gain can be defined as follows:

$$H(0) = \begin{cases} \dfrac{(m+1)A_r}{2\pi D_k^2}\cos^m(\varphi)T_s(\psi)g(\psi)\cos(\psi), & 0 \le \psi \le \Psi_c \\ 0 \qquad\qquad\qquad\qquad , & \psi > \Psi_c \end{cases} \tag{2}$$

where, D_k can be depicted as distance between VLC AP and mobile user. Moreover, Ar is the surface area of the photodiode, and m introduces the order of Lambertian emission. Ts and g can be presented as the gain of optical filter and the optical concentrator of gain, respectively. Finally, ψ and φ are observe the angle of incidence and the angle of irradiance, respectively (Qiu et al., 2016). The received signal can be explained by (Singh et al., 2019),

$$s(t) = RH(0)P_tM_If(t) + n(t) \tag{3}$$

The NLoS condition can be defined by taking into account reflecting signal. Addition, this signal cause ISI as mentioned above. The received optical power for LoS and NLoS models can be given as (Komine and Nakagawa, 2004; Qiu et al., 2016),

$$P_r = \sum^{NLED} \left\{ P_t H(0) + \int_{wall} P_t dH_{ref}(0) \right\} \quad (4)$$

where, $dH_{ref}(0)$ represents reflected path gain. From Equation (4), it is shown that reflecting signals can interfere the reflecting signal.

3. Modulation Techniques

In visible light communication systems, several modulation schemes have been improved to provide the data transfer among the users. Some of these transmission schemes are based on position method while some techniques aid the data transfer by using amplitude keying method. It is considered that these transmission types have advantages over each other. On-Off Keying (OOK) transmission method, which is one of the amplitude keying methods, has better performance in terms of bandwidth efficiency compared with Pulse Position Modulation (Lee and Park, 2011). It is the most important advantage for OOK scheme.

Visible Light Communication systems have been improved to serve the indoor users hence, these systems must assure some crucial conditions, including mobile user condition (Sönmez, 2020), ambient light effect (Pham et al., 2017). When compared to position based modulation scheme, amplitude keying transmission schemes such as PAM needs estimation and rejection algorithms to support mentioned conditions.

Table 1. Codewords for enormous PPM-based modulation schemes

Data Bits	Standard PPM (8-PPM)	Offset PPM	SPPM	Standard OPPM	Wrapped OPPM	$\left(\frac{5}{2}\right)$MPPM
000	10000000	0000	00001	1110000000	11100000	11000
001	01000000	0001	00010	0111000000	01110000	10100
010	00100000	0010	00100	0011100000	00111000	10010
011	00010000	0100	01000	0001110000	00011100	10001
100	00001000	1000	10001	0000111000	00001110	01100
101	00000100	1001	10010	0000011100	00000111	01010
110	00000010	1010	10100	0000001110	10000011	01001
111	00000001	1100	11000	0000000111	11000001	00110

In Table 1, a codeword table is given to compare the slot number of PPM based modulation schemes. According to table, it is demonstrated that the standard PPM have the larger slot size than that of other schemes. The standard OPPM scheme increases the length of filled slot while wrapped OPPM is

decreasing the number of slots. The Offset PPM has minimum slot number when compared to other schemes.

3.1 PPM Transmission Scheme

In this section, we give a basic transmission and very popular scheme for visible light communication systems. The scheme has been studied in various aspects since the beginning of optical communication systems. For a few decades, PPM transmission scheme has been investigated in visible light communication systems.

PPM signal can be achieved by taking into account location of filled slot in symbol period. After transmitted data signal is converted to decimal value, the filled slot is shifted from first slot to target slot up to decimal value of data signal. Hence, OOK transmission scheme gives better performance in terms of bandwidth efficiency than that of PPM scheme. However, the symbol time can be expanded to improve the bandwidth efficiency of PPM scheme by increasing the bit number in a symbol. Therefore, an expression can be given as L-PPM technique. If the bit number in one symbol is represented as M, L is equal to 2^M (Ghassemlooy et al., 2019). The M can be referred to as bit resolution. The slot time can be given follow as:

$$T_{slot} = \frac{T_b M}{L} \tag{4}$$

where, T_{slot} and T_b is defined as slot time and bit period. Addition to this, a symbol period T_s is equal to $T_b M$. According to equation 1, the slot time is decreasing while M is increasing. Hence, inter-slot interference is one of the most significant disadvantages for PPM transmission scheme.

It is given waveform for 2, 4, 8, and 16-PPM transmission schemes in Figure 2 a, b, c, and d, respectively. According to figure, modulation order is increasing while symbol period is expanding. Therefore, it can be considered that L-PPM signal with higher modulation order has superior in terms of bandwidth efficiency than that of L-PPM signal with lower modulation order.

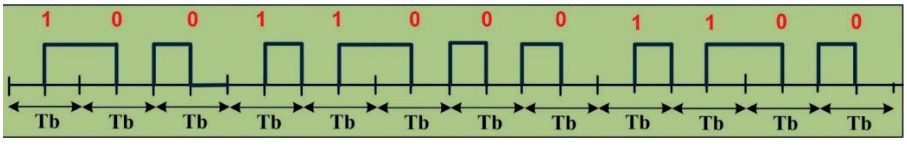

(a)

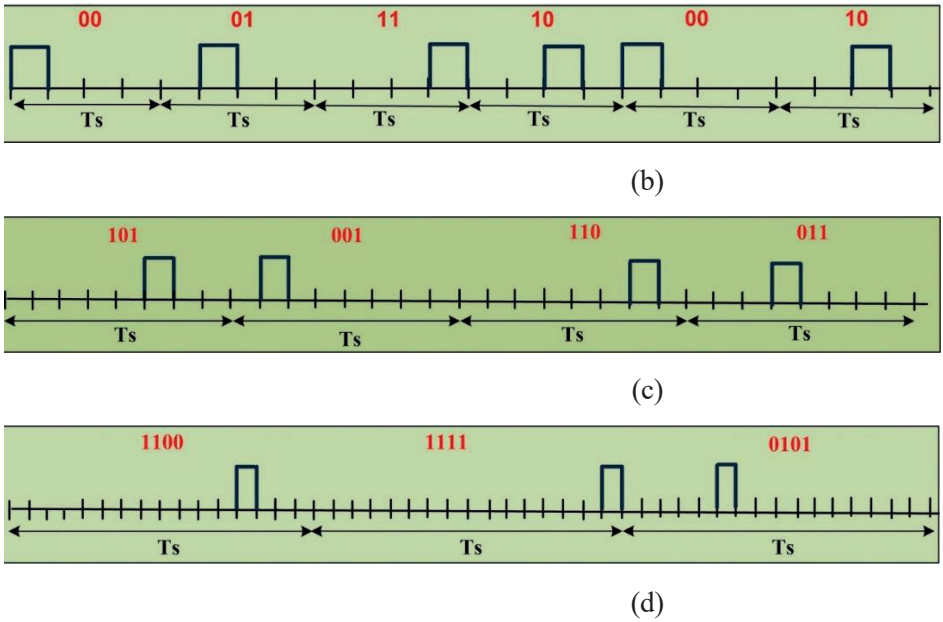

Figure 2. L-PPM transmission scheme

3.2 VPPM

In this section, we give a theoretical framework of the VPPM scheme to observe the physical structure of proposed image transmission systems. The VPPM scheme, which is a type of 2-PPM scheme, aims to control LED dimming level to ensure a dimmable communication system. Also, it is based on binary data transmission method like 2-PPM scheme. The difference between both techniques is the duration of filled or empty slot within a data transmission period. A VPPM signal can be given as shown in Fig. 3.

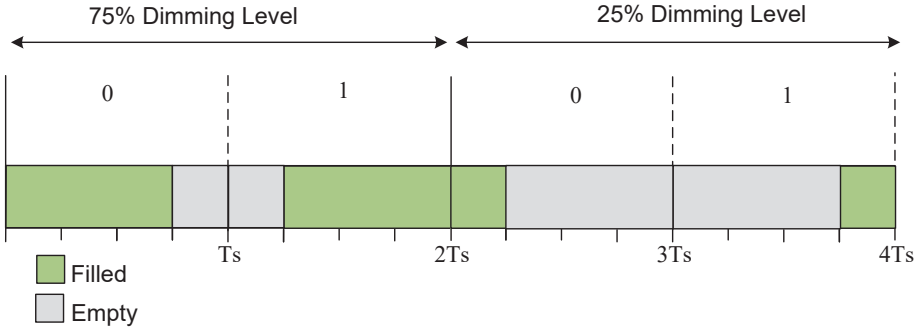

Figure 3. VPPM Signal Waveform

In the Fig. 3, a signal waveform is given to observe the changing of VPPM signal versus time. As shown in the figure, it is used two forms of dimming

level to present the transmitted data bits. If data transmission duration can be referred to Ts, the rate of filled slot to Ts at the dimming level of 75% The OOK signal is given to observe the relationship between data bits and PPM signal.

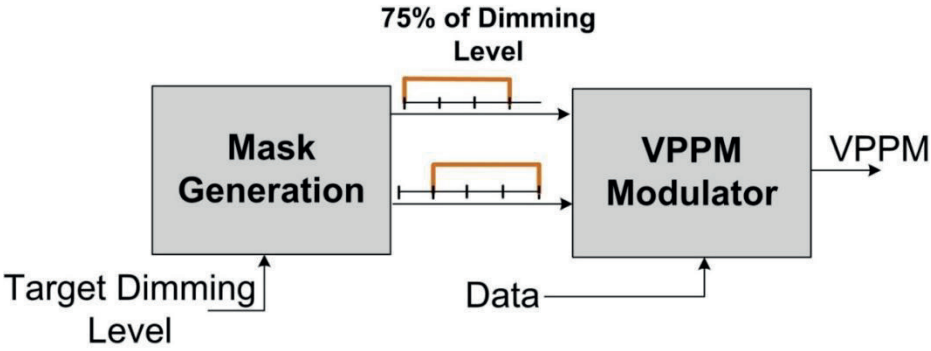

Figure 4. A VPPM Modulator

In Figure 4, it is demonstrated a VPPM modulator block scheme that consists of a mask generation unit that adjusts target dimming level of LED. When compared to traditional PPM signal, VPPM signal has variable duty cycle to support the variable LED brightness. One of the most important disadvantages is that receiver must know the target dimming level that is adjusted at the transmitter side because the dimming level adjusted in transmitter side must be used at demodulation stage. If matching dimming level don't used at receiver side, Bit Error Rate (BER) performance of VPPM scheme will decrease. Therefore, the transceiver performance is affected from mismatching dimming condition.

The Figure 5 illustrates an experimental VPPM signal that is generated by using Filed Programmable Gate Arrays (FPGA) board. The frequency of modulated signal is 500KHz. The 10% of dimming level is adjusted for VPPM signal. The time distance between Cursor A and Cursor B is 50ns as shown in Figure 5a and b. Therefore, it is shown that 10% of dimming can be provided. In the figure, the blue line observes the data bit while yellow line represents the VPPM signal. The experimental result given in Figure 5c investigates duty cycle of VPPM signal for 0 data bit compared with previous results. Moreover, Figure 5d is expanding the oscilloscope screen to observe changing of VPPM signal versus data bit. In Figure 5e, yellow signal is generated at output of optical receiver circuit while blue line is VPPM signal applied to LED driver. It is shown from experimental results that the received signal has affected from noise. It can be considered that the BER performance is decreasing while the distance between receiver and transmitter is increasing.

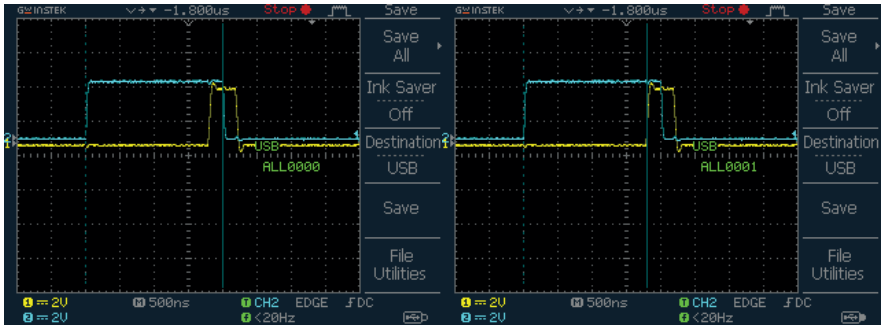

(a) (b)

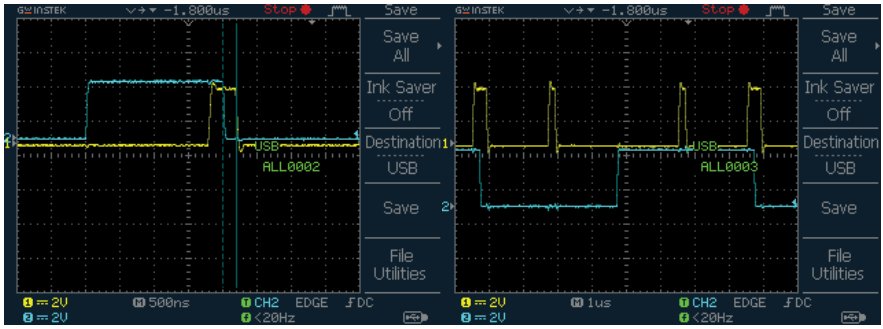

(c) (d)

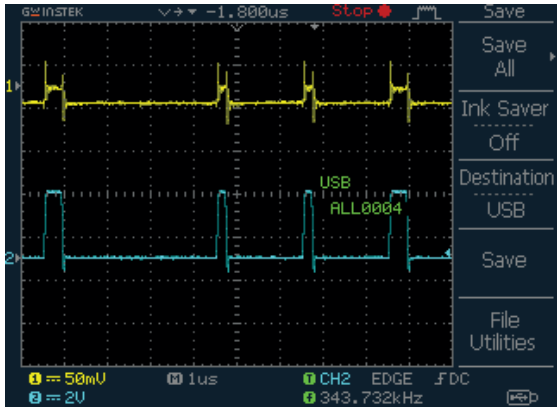

(e)

Figure 5. VPPM Signal at 10% of dimming level

4 Conclusion

Wireless optical communication systems have been investigated in terms of transmission performance for a long time. Visible Light Communication technology which is one of optical communication systems has become as a candidate to solve some challenges in optical systems and aid the Radio Frequency (RF) communication systems. Although many modulation schemes have been proposed for visible light communication systems, PPM transmission scheme is one of leading methods due to its low complexity. In this chapter, we give a theoretical study for both visible light communication systems and PPM based modulation schemes. Specifically, it has been investigated L-PPM and VPPM transmission schemes. Additionally, a FPGA based experimental study is given for waveform of VPPM signal. The oscilloscope results have been observed changing of VPPM signal versus data bit while the modulated signal is evaluated at 500KHz of frequency. In future, FPGA-based VLC system can be studied by considering L-PPM transmission scheme.

REFERENCES

Abdalmajeed, A. M. M., Mahmoud, M., El-Fikky, A. E.-R. A., Fayed, H. A., & Aly, M. H. (2023). Improved indoor visible light positioning system using machine learning. *Optical and Quantum Electronics*, *55*(3), 209.

Ağır, T. T., & Sönmez, M. (2023). The modulation classification methods in PPM–VLC systems. *Optical and Quantum Electronics*, *55*(3), 223. https://doi.org/10.1007/s11082-022-04520-y

Ayten, K., & Sönmez, M. (2021). Threshold detection and slot clustering algorithms in DPIM-VLC systems. *Optik*, *248*, 168085.

Bostanoglu, M., Dalveren, Y., Catak, F. O., & Kara, A. (2023). Modelling and Design of Pre-Equalizers for a Fully Operational Visible Light Communication System. *Sensors*, *23*(12), 5584.

Chi, N., Zhou, Y., Liang, S., Wang, F., Li, J., & Wang, Y. (2018). Enabling Technologies for High-Speed Visible Light Communication Employing CAP Modulation. *Journal of Lightwave Technology*, *36*(2), 510-518.

Chi, N., Zhou, Y., Wei, Y., & Hu, F. (2020). Visible Light Communication in 6G: Advances, Challenges, and Prospects. *IEEE Vehicular Technology Magazine*, *15*(4), 93-102.

Chowdhury, M. Z., Shahjalal, M., Hasan, M. K., & Jang, Y. M. (2019). The Role of Optical Wireless Communication Technologies in 5G/6G and IoT Solutions: Prospects, Directions, and Challenges. *Applied Sciences*, *9*(20), 4367.

Danys, L., Zolotova, I., Romero, D., Papcun, P., Kajati, E., Jaros, R., … Martinek, R. (2022). Visible Light Communication and localization: A study on tracking solutions for Industry 4.0 and the Operator 4.0. *Journal of Manufacturing Systems*, *64*, 535-545.

Din, I., & Kim, H. (2014). Energy-Efficient Brightness Control and Data Transmission for Visible Light Communication. *IEEE Photonics Technology Letters*, *26*(8), 781-784.

Farghal, A. E., Shalaby, H. M. H., & Kawasaki, Z. (2014). Performance Analysis of Multirate Multiservice Optical CDMA Networks Adopting Overlapping PPM Signaling. *Journal of Lightwave Technology*, *32*(15), 2649-2658.

Gancarz, J. E., Elgala, H., & Little, T. D. C. (2015). Overlapping PPM for band-limited visible light communication and dimming. *Journal of Solid State Lighting*, *2*(1), 3.

Ghassemlooy, Z., Popoola, W., & Rajbhandari, S. (2019). *Optical Wireless Communications: System and Channel Modelling with MATLAB®, Second Edition*. CRC Press.

Jin, Z., Yan, L., Zhu, S., Cui, X., & Tian, P. (2023). 10-Gbps visible light communication in a 10-m free space based on violet series-biased micro-LED array and distance adaptive pre-equalization. *Optics Letters*, *48*(8), 2026-2029.

Khanh, Q. V., Hoai, N. V., Manh, L. D., Le, A. N., & Jeon, G. (2022). Wireless Communication Technologies for IoT in 5G: Vision, Applications, and Challenges. *Wireless Communications and Mobile Computing*, *2022*, e3229294.

Komine, T., & Nakagawa, M. (2004). Fundamental analysis for visible-light communication system using LED lights. *IEEE Transactions on Consumer Electronics*, *50*(1), 100-107.

Lee, K., & Park, H. (2011). Modulations for Visible Light Communications With Dimming Control. *IEEE Photonics Technology Letters*, *23*(16), 1136-1138.

Long, Q., Zhang, J., Cao, L., & Wang, W. (2023). Indoor Visible Light Positioning System Based on Point Classification Using Artificial Intelligence Algorithms. *Sensors*, *23*(11), 5224.

Nguyen, T. T., & Lampe, L. (2010). Coded multipulse pulse-position modulation for free-space optical communications. *IEEE Transactions on Communications*, *58*(4), 1036-1041.

Nor, A. M. (2021). Access point selection in beyond 5G hybrid MmWave/Wi-Fi/Li-Fi network. *Physical Communication*, *46*, 101299.

Pham, Q. N., Rachim, V. P., An, J., & Chung, W.-Y. (2017). Ambient Light Rejection Using a Novel Average Voltage Tracking in Visible Light Communication System. *Applied Sciences*, *7*(7), 670.

Qiu, Y., Chen, H.-H., & Meng, W.-X. (2016). Channel modeling for visible light communications—A survey. *Wireless Communications and Mobile Computing*, *16*(14), 2016-2034.

Raj, R., Jaiswal, S., & Dixit, A. (2021). Dimming-Based Modulation Schemes for Visible Light Communication: Spectral Analysis and ISI Mitigation. *IEEE Open Journal of the Communications Society*, *2*, 1777-1798.

Rehman, S. U., Ullah, S., Chong, P. H. J., Yongchareon, S., & Komosny, D. (2019). Visible Light Communication: A System Perspective—Overview and Challenges. *Sensors*, *19*(5), 1153.

Saengudomlert, P., & Buddhacharya, S. (2023). Unipolar GFDM with Dimming Support for Visible Light Communications. *IEEE Transactions on Wireless Communications*, 1-1.

Sejan, M. A. S., Rahman, M. H., Aziz, M. A., Kim, D.-S., You, Y.-H., & Song, H.-K. (2023). A Comprehensive Survey on MIMO Visible Light Communication: Current Research, Machine Learning and Future Trends. *Sensors*, *23*(2), 739.

Sejan, M. A. S., Rahman, M. H., Shin, B.-S., Oh, J.-H., You, Y.-H., & Song, H.-K. (2022). Machine Learning for Intelligent-Reflecting-Surface-Based Wireless Communication towards 6G: A Review. *Sensors*, *22*(14), 5405.

Sen, U., Yesilirmak, Y. E., Bayman, I. O., Arsan, T., Panayirci, E., & Stevens, N. (2023). 3D indoor positioning with spatial modulation for visible light communications. *Optics Communications*, *529*, 129091.

Shi, J., Wei, Y., Luo, Z., Li, Z., Shen, C., Zhang, J., & Chi, N. (2023). 8.8 Gbps PAM-4 visible light communication link using an external modulator and a neural network equalizer. *Optics Letters*, *48*(20), 5193-5196.

Sibley, M. J. N. (2011). Analysis of offset pulse position modulation – a novel reduced bandwidth coding scheme. *IET Optoelectronics*, *5*(4), 144-150.

Singh, A., Srivastava, A., Bohara, V. A., & Rao, G. S. V. R. K. (2019). Performance of hybrid cellular-VLC link for indoor environments under dynamic user movement. *Physical Communication*, *36*, 100816.

Sönmez, M. (2020). Artificial neural network-based threshold detection for OOK-VLC Systems. *Optics Communications*, *460*, 125107.

Sreedevi, A. G., Nitya Harshitha, T., Sugumaran, V., & Shankar, P. (2022). Application of cognitive computing in healthcare, cybersecurity, big data and IoT: A literature review. *Information Processing & Management*, *59*(2), 102888.

Stergiou, C. L., & Psannis, K. E. (2022). Digital Twin Intelligent System for Industrial IoT-based Big Data Management and Analysis in Cloud. *Virtual Reality & Intelligent Hardware*, *4*(4), 279-291.

Sui, M., & Zhou, Z. (2009). The Modified PPM Modulation for Underwater Wireless Optical Communication. *2009 International Conference on Communication Software and Networks*, 173-177. Macau: IEEE.

Sun, Y., Ng, D. W. K., Zhu, J., & Schober, R. (2016). Multi-Objective Optimization for Robust Power Efficient and Secure Full-Duplex Wireless Communication Systems. *IEEE Transactions on Wireless Communications*, *15*(8), 5511-5526.

Tong, Y., Tang, P., Zhang, J., Liu, S., Yin, Y., Liu, B., & Xia, L. (2023). Channel Characteristics and Link Adaption for Visible Light Communication in an Industrial Scenario. *Sensors*, *23*(7), 3442.

Turan, B., & Coleri, S. (2021). Machine Learning Based Channel Modeling for Vehicular Visible Light Communication. *IEEE Transactions on Vehicular Technology*, *70*(10), 9659-9672.

Wang, C., Yu, H.-Y., & Zhu, Y.-J. (2016). A Long Distance Underwater Visible Light Communication System With Single Photon Avalanche Diode. *IEEE Photonics Journal*, *8*(5), 1-11.

Yang, C., Han, D., Zhang, M., Wang, L., Jia, P., Jiang, X., & Huang, X. (2023). Visible light communication-channel-adaptive digital pre-equalization scheme based on a deep learning model. *Optical Engineering*, *62*(1), 018101.

Younus, S. H., Al-Hameed, A. A., & Elmirghani, J. M. H. (2023). Multi-user High Data Rate Indoor VLC Systems. *IETE Journal of Research*, *69*(2), 1056-1069.

Chapter 19

A REVIEW ON BIOLOGICAL ACTIVITIES AND CHEMICAL CONTENTS OF BLACKBERRY

İmran Uysal[1], Alpaslan Dayangaç[2], Nuh Korkmaz[3]
Mustafa Sevindik[3], Hasan Akgül[4]

1 Osmaniye Korkut Ata University, Bahçe Vocational School, Department of Food Processing, Osmaniye, Turkey
2 Osmaniye Korkut Ata University, Faculty of Health Sciences Department of Nutrition and Dietics, Osmaniye, Turkey
3 Osmaniye Korkut Ata University, Science and Literature Faculty, Department of Biology, Osmaniye, Turkey.
4 Akdeniz University, Science Faculty, Department of Biology, Antalya, Turkey

Introduction

Since ancient times, people have been using many natural products for different purposes. Natural products have been widely used, especially in the treatment of diseases. The place of plants among natural products is very important (Mohammed et al., 2020b). Plants are used by people for many purposes such as food, medicine, shelter and heating (Mohammed et al., 2022). Plants that stand out with their nutritional properties are indispensable in diet lists in terms of vitamins, minerals and nutrients (Sevindik et al., 2017). In addition to their food properties, plants are also very important from a medicinal point of view (Mohammed et al., 2020a; Korkmaz et al., 2021). Many studies have reported that plants have many biological activities such as antioxidant, anticancer, antiproliferative, anti-inflammatory, hepatoprotective, DNA protective, antiallergic (Mohammed et al., 2018; Pehlivan et al., 2018; Mohammed et al., 2019; Mohammed et al. ., 2021; Comlekcioğlu et al., 2022; Unal et al., 2022; Kalkan et al., 2023; Sevindik et al., 2023a; Uysal et al., 2023). In this context, determining the biological activities of plants is very important. In our study, the biological activities of Rubus fruticosus L. reported in the literature were compiled.

R. fruticosus is known as "blackberry". It is in the Rosaceae family. R. fruticosus plant is distributed in Asia, South and North America, Oceania and Europe. R. fruticosus grows up to 9 m, has 5 or 7 palmate leaves, and its upper part is dark green and its lower part is light green. It tolerates poor soils and spreads easily in barren lands, ditches and empty lands. The diameter of the flowers varies between 2 and 3 cm and they are white or pink in color. As the fruit matures, its color changes from green to red and black, its diameter is 1-3 cm and its root length is up to 1 m (Blamey and Grey-Wilson, 1989; Parsons and Cuthbertson, 2001; Evans et al., 2007; Clark et al. , 2013; Verma et al., 2014).

Usage areas

When using R. fruticosus, leaves, roots and fruit parts are generally preferred. When we look at its usage areas, in ancient times, its stems and leaves were used to ease difficulties during birth and heal wounds. It has been reported to be used against respiratory disorders, mouth ulcer treatment, skin problems, dysentery, gargling, anemia problems, menstrual conditions, sore throat, asthma, diarrhea treatment, fungal diseases, gingivitis, oral thrush treatment, diuretic, cystitis and hemorrhoids (Rios et al., 1987; Guarrera, 2003; Viegi et al., 2003; Zabihullah et al., 2006; Leonti et al., 2009; Grieve, 2013; Rasheed et al., 2017).

Biological activities

Plants contain many biologically active compounds. Thanks to these bioactive compounds, it has many biological activities (Mohammed et al., 2023a). It was observed that methanol, ethanol, acetone, acetonitrile, water, ethyl acetate, pomace extract, crude methanol, hexane, chloroform, essential oil, polyphenolic extract, and petroleum ether extracts were used in in vitro and in vivo biological activity studies of R. fruticosus. R. fruticosus biological activity study is shown in table 1.

Table 1. Biological activity of Rubus fruticosus

Plant species	**Biological activity**	**Extraction**	**Geographic regions**	**References**
Rubus fruticosus L.	Antioxidant, antiinflammatory, antidiabetic, anticholinesterase, antiproliferative, antihelmintic, antimicrobial, cytotoxic, antıtumor, DNA damage protective	Methanol, ethanol, acetone, acetonitrile, water, ethyl acetate, pomace extract, crude methanol, hexane, chloroform, hydro alcoholic, essential oil, polyphenolic extract, aqueous, distilled water, petroleum ether	Romania, South Korea, Mexico, Italy, Hungary, Turkey, Morocco, Serbia, Pakistan, Oman, Iran, India	(Yilmaz et al., 2009; Rajeswari et al., 2010; Riaz et al., 2011; Abaci et al., 2013; Ali et al., 2013; Radovanović et al., 2013; Yiğit and Yiğit, 2014; Ryu et al., 2016; Četojević-Simin et al., 2017; Koczka et al., 2018; Monforte et al., 2018; Zafra-Rojas et al., 2018; Jazić et al., 2019; Zafra-Rojas et al., 2020; Weli et al., 2020; Cadi et al., 2021; Akyüz et al., 2022; Albert et al., 2022; Barbieri et al., 2022; Takcı et al., 2022)

Antioxidant activity

Antioxidant compounds play a role in suppressing oxidant compounds. While oxidant compounds are not harmful at low levels, they can be quite harmful as their levels increase (Krupodorova and Sevindik, 2020). The antioxidant defense system comes into play in suppressing oxidant compounds (Bal et al., 2019). Oxidative stress occurs when the antioxidant defense system is inadequate. As a result of oxidative stress, many serious diseases such as Alzheimer's, Parkinson's, multiple sclerosis, cancer, and cardiological disorders

can occur (Selamoglu et al., 2020; Eraslan et al., 2021; Saridogan et al., 2021). Supplementary antioxidants play an important role in suppressing oxidative stress (Akgül et al., 2022). In this study, antioxidant activity findings of *R. fruticosus* reported in the literature were compiled. In this context, in a study conducted in Romania, the antioxidant status of *R. fruticosus* was analyzed according to DPPH and FRAP test results using different solvents such as methanol, ethanol, acetone and acetonitrile. As a result of the study, it was reported that the DPPH effect percentage was 47.2017-76.4078% and the FRAP results were 1682.22-3547.68 mg AAE/100 g DW and 228.11-481.06 mg AAE/100 g FW (Albert et al., 2022). In a study conducted in South Korea, the antioxidant status of ethanol extract obtained from *R. fruticosus* was investigated by using the DPPH test. As a result of the study, it was reported that the DPPH radical scavenging activity of all blackberry lines increased as the fruits ripened (Ryu et al., 2016). In a study conducted in Mexico, the antioxidant properties of the extract obtained from *R. fruticosus* were investigated using ABTS and FRAP tests. As a result of the study, it was reported that the ABTS value was 5,422.38 mg AAE/100 g DM and the FRAP value was 12511.44 µmol Fe(II)/100 g DM (Zafra-Rojas et al., 2020). In a study conducted in Italy, the antioxidant properties of ethanol extract obtained from *R. fruticosus* were examined using different tests. As a result of the study, it was reported that the DPPH value was 4,147.194 mg trolox equivalent [TE]/100 mL and the ferric reducing antioxidant power activity was 2,177.830 mg TE/100 mL. It was also reported that the oxygen radical absorbance activity was 95,377.674 µmol TE/100 mL juice and the β-carotene bleaching activity was 72% (Monforte et al., 2018). In a study conducted in Hungary, the antioxidant status of the extract obtained from *R. fruticosus* sample was analyzed. As a result of the study, it was reported that the best FRAP test value in the leaf was between 50-60 µmol AA g^{-1} and the best FRAP test value in the fruit was between 150-200 µmol AA g^{-1} (Koczka et al., 2018). In a study conducted in Turkey, it was reported that the antioxidant percentage of the methanol extract obtained from *R. fruticosus* sample was 72.1-89.4% and the EC50 value was 5.8-8.7 mg (Yilmaz et al., 2009). In a study conducted in Morocco, it was reported that the LC50 value of ethyl acetate extract obtained from *R. fruticosus* was 2.5 mg/mL (Cadi et al., 2021). In another study conducted in Turkey, the antioxidant status of ethanol and water extract obtained from *R. fruticosus* was investigated. As a result of the study, it was reported that the DPPH value was 0.01-0.06 mg/mL and the ABTS value was 0.002-0.028 mg/mL (Akyüz et al., 2022). In another study conducted in Mexico, the antioxidant status of methanol and acetone extract obtained from *R. fruticosus* was investigated using DPPH, FRAP and ABTS tests. The values of the tests used as a result of the study are respectively; It was reported to be 13656.27 µmol TE/100 g db, 12511.44 µmol Fe(II)/100 g db, and 5422.38 mg AAE/100 g db (Zafra-Rojas et al., 2018). In a study conducted in Serbia, the antioxidant status of pomace extract obtained

from *R. fruticosus* was investigated using DPPH, ABTS and OH tests. LC50 values of the tests used as a result of the study are respectively; It was reported to be 127.76 µg mL^{-1}, 26.53 µg mL^{-1} and 168.62 µg mL^{-1} (Jazić et al., 2019). In a study conducted in Serbia, the antioxidant property of the polyphenolic extract obtained from *R. fruticosus* was analyzed using the DPPH test. As a result of the study, it was reported that the LC50 value varied between 22.19 and 31.18 mL g^{-1} (Radovanović et al., 2013). In another study conducted in Serbia, it was reported that the DPPH effect value of the extract obtained from *R. fruticosus* was 2.12 mmol TEAC g^{-1} (Četojević-Simin et al., 2017). In another study in Turkey, it was reported that the DPPH value range of methanol and distilled water extract obtained from *R. fruticosus* was 48.85-89.60% (Takcı et al., 2022).

Antimicrobial activity

Microorganisms have positive or negative effects on many living things (Baba et al., 2020). In recent years, many diseases are of microorganism origin (Mohammed et al., 2023b). The increase in the number of resistant microorganisms, especially due to unconscious use of antibiotic drugs, has gradually reduced the effectiveness of the antimicrobial drugs used (Bal et al., 2017; Islek et al., 2021; Sevindik et al., 2023b). In this context, the discovery of new antimicrobial drugs has become inevitable. Plants are a very important source of antimicrobial drugs. In this study, the activities of *R. fruticosus* against microorganisms reported in the literature were compiled. In a study conducted in Oman, the antimicrobial status of hexane, chloroform, ethyl acetate and hydro alcoholic extract obtained from *R. fruticosus* by agar diffusion method was investigated against two gram-positive *Enterococcus faecalis* and *Staphylococcus aureus* and two gram-negative *Escherichia coli* and *Haemophilus influenza* bacterial strains. As a result of the study, it was reported that the total number of extracts showed moderate to strong antibacterial activity against gram (+ and -), and while the best activity was discovered in hydroalcoholic among all extracts, the inhibition zone of the strains used was in the range of 6–11 mm (Weli et al., 2020). In a study conducted in Pakistan, the antimicrobial status of crude methanolic extract obtained from R. fruticosus against *Escherichia coli, Salmonella typhi, Streptococcus aureus, Proteus mirabilis, Micrococcus luteus, Citrobacter, Bacillus subtilis, Pseudomonas aeruginosa, Aspergilus parasiticus*, *Aspergilus niger, Yersinia aldovae, Candida albicans, Aspergillus effusus, Fusarium solani*, *Macrophomina phaseolina, Saccharomyces cerevisiae* and *Trichophyton rubrum* was analyzed. As a result of the study, it was reported that the root extract had a MIC value of 20 µg against all tested bacterial strains and had no significant effect against fungi (Riaz et al., 2011). In a study conducted in Italy, the antimicrobial status of essential oil obtained from R. fruticosus against *Listeria monocytogenes* was investigated. As a result of the study, it was reported that 0.08 versus 0.09 ((log CFU/mL)/ hour in control) but significantly reduced the final cell load (7.33 versus

8.92 log CFU/mL) (Barbieri et al., 2022). In a study conducted in Serbia, the minimum inhibitory amount (MIC) and minimum bactericidal concentration (MBC) status of the polyphenolic extract obtained from *R. fruticosus* against *Clostridium perfringens, Bacillus subtilis, Listeria innocua, Staphylococcus aureus, Sarcina lutea*, *Micrococcus flavus, Escherichia coli, Pseudomonas aeruginosa, Salmonella enteritidis*, *Shigella sonnei, Klebsiella pneumoniae* and *Proteus vulgaris* strains were analyzed by the liquid microdilution method. As a result of the study, it was reported that the MIC value range varied between 62.5-500 μg mL^{-1} and the MBC value range varied between 62.5-500 μg mL^{-1} (Radovanović et al., 2013). In a study conducted in Turkey, the antimicrobial status of methanol and water extract obtained from *R. fruticosus* was investigated against *Enterobacter aerogenes*, *Escherichia coli, Proteus mirabilis, Pseudomonas aeruginosa* and *Staphylococcus* aureus by disc-diffusion method. As a result of the study, it was reported that methanol and aqueous extracts of blackberry fruits had the highest antibacterial activity against *S. aureus*, with an inhibition zone of 20 mm and a MIC value of 0.312 mg/mL (Yiğit and Yiğit, 2014). In a study conducted in Iran, the effect of aqueous and ethanolic extract obtained from R. fruticosus on *Helicobacter pylori* was investigated. As a result of the study, it was reported that the MIC value range was 400-450 μg mL^{-1} (Abaci et al., 2013). In another study conducted in Serbia, it was reported that the MIC value range of the extract obtained from *R. fruticosus* was 0.39-25 mg mL^{-1} and the MBC/MFC value range was 0.78-25 mg mL^{-1} against all strains used (Četojević-Simin et al., 2017). In another study in Turkey, it was reported that the inhibition zone value range of methanol and distilled water extract obtained from *R. fruticosus* against *Klebsiella* spp., *Proteus* spp., *Pseudomonas* spp., *Escherichia coli*, and *Staphylococcus aureus* strains was 6.50-12.00 mm (Takcı et al., 2022). In a study conducted in India, the antimicrobial status of petroleum ether, chloroform, ethyl acetate, ethanol and water extract obtained from *R. fruticosus* against *Staphylococcus aureus, Bacillus subtilis, Aspergillus niger* and *Penicillium* sp. strains was investigated. As a result of the study, it was reported that the inhibition zone range of the strains used was 4-24 mm (Rajeswari et al., 2010).

Other activities

Apart from antioxidant and antimicrobial activities, *R. fruticosus* has been reported to have many different activities. In a study conducted in Italy, the anti-inflammatory status of ethanol extract obtained from *R. fruticosus* was analyzed. As a result of the study, it was reported that it significantly inhibited carrageenan-induced paw edema in rats by 63-71% and had significant anti-inflammatory effects, especially in relation to phenylbutazone 94-96% (Monforte et al., 2018). In another study conducted in Turkey, the inhibitory effects of ethanol and water extract obtained from immature, intermediate and mature *R. fruticosus* samples on acetylcholinesterase

(AChE), butyrylcholinesterase (BChE), α-glucosidase and α-amylase enzyme activities were investigated. As a result of the study, it was reported that the intermediate value of the ethanol extract for antidiabetic was LC50=0.019 mg mL^{-1}, the immature value was LC50=0.021 mg/mL, and the immature value of the water extract was LC50=0.014 mg mL^{-1}. In addition, it has been reported that the intermediate ripe value is LC50 = 0.014 mg $mL^{-1}$and the ripe value is LC50 = 0.136 mg mL^{-1}, and in terms of anticholinesterase, ethanol and water extracts of fruits at different ripeness stages act as very weak inhibitors against AChE and BChE compared to neostigmine and galantamine. (Akyüz et al., 2022). In a study conducted in Serbia, the antiproliferative status of pomace extract obtained from *R. fruticosus* was investigated. As a result of the study, it was reported that the LC50 value of breast adenocarcinoma (MCF7) was 306.68 μg mL^{-1} and the LC50 value of cervix epitheloid carcinoma (Hela) was 315.49 μg mL^{-1} (Jazić et al., 2019). In a study conducted in Pakistan, the antihelmintic status of crude methanol extract obtained from *R. fruticosus* was investigated. In the study, it was reported that the crude methanolic extract showed excellent anthelmintic activity against *Raillietina spiralis* at a concentration of 20 mg mL^{-1} (Ali et al., 2013). In a study conducted in Oman, the cytotoxicity of hexane, chloroform, ethyl acetate and hydro alcoholic extract obtained from *R. fruticosus* against brine shrimp was investigated using the Nauplii method (BSL). As a result of the study, the cytotoxic activity test reported that the hydroalcoholic extract showed maximum toxicity for LC50 = 4.68–6.96 μg mL^{-1}, and the LC50 value range for all extracts was 4.68–6.96 μg mL^{-1} (Weli et al., 2020). In another study conducted in Serbia, it was reported that the extract obtained from the *R. fruticosus* sample had an antitumor effect against the breast adenocarcinoma cell line, with a cell growth inhibiting effect of EC50 = 52.5 – 64.7 μg mL^{-1} and the highest apoptosis increase AI = 12.2 (Četojević-Simin et al., 2017). In another study in Turkey, the DNA damage protective properties of methanol and distilled water extract obtained from *R. fruticosus* were examined. As a result of the study, it was reported that H_2O_2 has an effect against the mutagenicity of UV-photolysis on pBR322 plasmid DNA (Takcı et al., 2022).

Essential oil content

Plants produce many chemical compounds within themselves. With these features, plants are important natural resources (Akgül et al., 2020). In our study, the chemical contents of R. fruticosus were compiled. For essential oil content studies on R. fruticosus species, the aerial, seed and fruit parts of the plant were generally used. The essential oil content of the R. fruticosus species is shown in table 2.

Table 2. Essential oil contents of Rubus fruticosus L.

Geographic regions	Used Parts	Essential oil contents	References
Poland, Italy, Brazil	Aerial, seed, fruit	E)-hept-2-enal (38.3%), (E)-oct-1-en-3-on (2.3%), (E)-oct-1-en-3-ol (5.8%), E,Z)-hepta-2,4-dienal (3.0-10.9%), (E,Z)-deca-2,4-dienal (4.8-20.8%), (E)-dec-2-enal (1.7-9.5%),E,E)-deca-2,4-dienal (6.9-42.1%), linalool (0.79-4.13%), α-terpineol (3.05%), β-citronellol (4.61%), geraniol (13.67%), β-Ionone (3.68%), α-farnesene (2.01%), olivetol (3.02%), dodecanoic acid (3.11%), hexadecanal (3.27%), tetradecanal (2.18%), phytol (4.87%), methyl ethyl ketone (3.65%), heptane (3.58%), hexanal (2.05%), heptanal (4.55%), 2-heptanol (3.24%), limonene (63.26%)	(Jacques eet al., 2014; Wajs-Bonikowska et al., 2017; Barbieri et al., 2022)

It has been reported that *R. fruticosus* contains E)-hept-2-enal (38.3%), (E)-oct-1-en-3-one (2.3%), (E)-oct-1-en-3-ol (5.8%), E ,Z)-hepta-2,4-dienal (3.0-10.9%), (E,Z)-deca-2,4-dienal (4.8-20.8%), (E)-dec-2-enal (1.7-9.5%),E,E)-deca-2,4-dienal (6.9-42.1%), linalool (0.79-4.13%), α-terpineol (3.05%), β-citronellol (4.61%), geraniol (13.67%) %), β-Ionone (3.68%), α-farnesene (2.01%), olivetol (3.02%), dodecanoic acid (3.11%), hexadecanal (3.27%), tetradecanal (2.18%), phytol (4.87%), methyl ethyl ketone (3.65%), heptane (3.58%), hexanal (2.05%), heptanal (4.55%), 2-heptanol (3.24%) and limonene (63.26%) (Jacques et al., 2014; Wajs-Bonikowska et al., 2017; Barbieri et al., 2022).

Conclusion

In this study, the biological activities and chemical contents of the widely consumed *R. fruticosus* reported in the literature were compiled. According to the findings, it is thought that it may be an important natural source in terms of antioxidant and antimicrobial activities. In addition, it is thought to be an important natural source of many bioactive compounds. As a result, it is thought that *R. fruticosus* may be a source that can be used in pharmacological designs.

REFERENCES

Abachi, S., Khademi, F., Fatemi, H., Malekzadeh, F. (2013). Study of antibacterial activity of selected Iranian plant extracts on Helicobacter pylori. IOSR J. Dental Med. Sci, 5, 155-159.

Akgul, H., Korkmaz, N., Dayangaç, A., & Sevindik, M. (2020). Antioxidant potential of endemic Salvia absconditiflora. *Turkish Journal of Agriculture-Food Science and Technology*, *8*(10), 2222-2224.

Akgül, H., Mohammed, F. S., Kına, E., Uysal, İ., Sevindik, M., & Doğan, M. (2022). Total Antioxidant and Oxidant Status and DPPH Free radical activity of Euphorbia eriophora. *Turkish Journal of Agriculture-Food Science and Technology*, *10*(2), 272-275.

Akyüz, M. (2022). The determination of antidiabetic, anticholinesterase and antioxidant properties of ethanol and water extracts of blackberry (Rubus fruticosus L.) fruits at different maturity stages. South African Journal of Botany, 151, 1035-1048.

Albert, C., Codină, G. G., Héjja, M., András, C. D., Chetrariu, A., Dabija, A. (2022). Study of antioxidant activity of garden blackberries (Rubus fruticosus L.) extracts obtained with different extraction solvents. Applied Sciences, 12(8), 4004.

Ali, N., Aleem, U., Ali Shah, S. W., Shah, I., Junaid, M., Ahmed, G., Ghias, M. (2013). Acute toxicity, brine shrimp cytotoxicity, anthelmintic and relaxant potentials of fruits of Rubus fruticosus Agg. BMC complementary and alternative medicine, 13, 1-6.

Baba, H., Sevindik, M., Dogan, M., & Akgül, H. (2020). Antioxidant, antimicrobial activities and heavy metal contents of some Myxomycetes. Fresenius Environmental Bulletin, 29(09), 7840-7846.

Bal, C., Akgul, H., Sevindik, M., Akata, I., & Yumrutas, O. (2017). Determination of the anti-oxidative activities of six mushrooms. Fresenius Envir Bull, 26(10), 6246-6252.

Bal, C., Sevindik, M., Akgul, H., & Selamoglu, Z. (2019). Oxidative stress index and antioxidant capacity of Lepista nuda collected from Gaziantep/Turkey. Sigma Journal of Engineering and Natural Sciences, 37(1), 1-5.

Barbieri, F., Montanari, C., Šimat, V., Skroza, D., Čagalj, M., Smole-Možina, S., Tabanelli, G. (2022). Effects of Rubus fruticosus and Juniperus oxycedrus derivatives on culturability and viability of Listeria monocytogenes. Scientific Reports, 12(1), 13158.

Blamey, M., Grey-Wilson, C. (1989). Illustrated flora of Britain and Northern Europe. Hodder and Stroughton.

Cadi, H. E., Bouzidi, H. E., Selama, G., Ramdan, B., Majdoub, Y. O. E., Alibrando, F., Cacciola, F. (2021). Characterization of Rubus fruticosus L. berries growing wild in Morocco: phytochemical screening, antioxidant activity and chroma-

tography analysis. European Food Research and Technology, 247, 1689-1699.

Četojević-Simin, D. D., Ranitović, A. S., Cvetković, D. D., Markov, S. L., Vinčić, M. N., Đilas, S. M. (2017). Bioactivity of blackberry (Rubus fruticosus L.) pomace: Polyphenol content, radical scavenging, antimicrobial and antitumor activity. Acta periodica technologica, (48), 63-76.

Clark, L. V., Evans, K. J., Jasieniuk, M. (2013). Origins and distribution of invasive Rubus fruticosus L. agg.(Rosaceae) clones in the Western United States. Biological Invasions, 15, 1331-1342.

Comlekcioglu, N., Dağlı, F., Çömlekcioğlu, U., & Aygan, A. (2022). Cornus mas ve Rosa canina Meyvelerinin Antioksidan Kapasitesi ve Bazı Fitokimyasal Özellikleri. Turkish Journal of Agriculture-Food Science and Technology, 10(9), 1724-1731.

Eraslan, E. C., Altuntas, D., Baba, H., Bal, C., Akgül, H., Akata, I., & Sevindik, M. (2021). Some biological activities and element contents of ethanol extract of wild edible mushroom Morchella esculenta. Sigma Journal of Engineering and Natural Sciences, 39(1), 24-28.

Evans, K. J., Symon, D. E., Whalen, M. A., Hosking, J. R., Barker, R. M., Oliver, J. A. (2007). Systematics of the Rubus fruticosus aggregate (Rosaceae) and other exotic Rubus taxa in Australia. Australian Systematic Botany, 20(3), 187-251.

Grieve, M. (2013). A modern herbal (Vol. 2). Courier Corporation.

Guarrera, P. M. (2003). Food medicine and minor nourishment in the folk traditions of Central Italy (Marche, Abruzzo and Latium). Fitoterapia, 74(6), 515-544.

Islek, C., Saridogan, B. G. O., Sevindik, M., & Akata, I. (2021). Biological activities and heavy metal contents of some Pholiota species. Fresenius Environmental Bulletin, 30(6), 6109-6114.

Jacques, A. C., Chaves, F. C., Zambiazi, R. C., Brasil, M. C., Caramão, E. B. (2014). Bioactive and volatile organic compounds in Southern Brazilian blackberry (Rubus fruticosus) fruit cv. Tupy. Food Science and Technology, 34, 636-643.

Jazić, M., Kukrić, Z., Vulić, J., Četojević-Simin, D. (2019). Polyphenolic composition, antioxidant and antiproliferative effects of wild and cultivated blackberries (Rubus fruticosus L.) pomace. International Journal of Food Science & Technology, 54(1), 194-201.

Kalkan, M., Aygan, A., Çömlekçioglu, N., & Çömlekçioğlu, U. (2023). Olea europaea Yapraklarının Bazı Biyoaktif Özelliklerinin Araştırılması, Antimikrobiyal ve Enzim İnhibisyon Etkinliğinin İncelenmesi. Turkish Journal of Agriculture-Food Science and Technology, 11(3), 496-504.

Koczka, N., Stefanovits-Banyai, E., Prokaj, E. (2018). Element composition, total phenolics and antioxidant activity of wild and cultivated blackberry (Rubus fruticosus L.) fruits and leaves during the harvest time. Notulae Botanicae Horti Agrobotanici Cluj-Napoca, 46(2), 563-569.

Korkmaz, N., Dayangaç, A., Sevindik, M. (2021). Antioxidant, antimicrobial and an-

tiproliferative activities of *Galium aparine. J Fac Pharm Ankara*, 45(3), 554-564.

Krupodorova, T., & Sevindik, M. (2020). Antioxidant potential and some mineral contents of wild edible mushroom Ramaria stricta. AgroLife Scientific Journal, 9(1), 186-191.

Leonti, M., Casu, L., Sanna, F., Bonsignore, L. (2009). A comparison of medicinal plant use in Sardinia and Sicily—De Materia Medica revisited?. Journal of ethnopharmacology, 121(2), 255-267.

Mohammed, F. S., Akgul, H., Sevindik, M., & Khaled, B. M. T. (2018). Phenolic content and biological activities of Rhus coriaria var. zebaria. Fresenius Environmental Bulletin, 27(8), 5694-5702.

Mohammed, F. S., Günal, S., Pehlivan, M., Doğan, M., Sevindik, M., & Akgül, H. (2020b). Phenolic content, antioxidant and antimicrobial potential of endemic Ferulago platycarpa. Gazi University Journal of Science, 33(4), 670-677.

Mohammed, F. S., Günal, S., Şabik, A. E., Akgül, H., & Sevindik, M. (2020a). Antioxidant and Antimicrobial activity of Scorzonera papposa collected from Iraq and Turkey. Kahramanmaraş Sütçü İmam Üniversitesi Tarım ve Doğa Dergisi, 23(5), 1114-1118.

Mohammed, F. S., Karakaş, M., Akgül, H., & Sevindik, M. (2019). Medicinal properties of Allium calocephalum collected from Gara Mountain (Iraq). Fresen Environ Bull, 28(10), 7419-7426.

Mohammed, F. S., Pehlivan, M., Sevindik, E., Akgul, H., Sevindik, M., Bozgeyik, I., & Yumrutas, O. (2021). Pharmacological properties of edible Asparagus acutifolius and Asparagus officinalis collected from North Iraq and Turkey (Hatay). Acta Alimentaria, 50(1), 136-143.

Mohammed, F. S., Sevindik, M., & Uysal, I. (2023a). Total phenolic, flavonoid, protein contents and biological activities of wild mustard. Acta Alimentaria, 52(3), 449-457.

Mohammed, F. S., Sevindik, M., Uysal, I., Sevindik, E., & Akgül, H. (2022). A Natural Material for Suppressing the Effects of Oxidative Stress: Biological Activities of Alcea kurdica. Biology Bulletin, 49(Suppl 2), S59-S66.

Mohammed, F. S., Uysal, I., & Sevindik, M. (2023b). A review on antiviral plants effective against different virus types. Prospects in Pharmaceutical Sciences, 21(2), 1-21.

Monforte, M. T., Smeriglio, A., Germanò, M. P., Pergolizzi, S., Circosta, C., Galati, E. M. (2018). Evaluation of antioxidant, antiinflammatory, and gastroprotective properties of Rubus fruticosus L. fruit juice. Phytotherapy Research, 32(7), 1404-1414.

Parsons, W. T., Cuthbertson, E. G. (2001). Noxious weeds of Australia. CSIRO publishing.

Pehlivan, M., Mohammed, F. S., Sevindik, M., & Akgul, H. (2018). Antioxidant and oxidant potential of Rosa canina. *Eurasian Journal of Forest Science*, *6*(4), 22-25.

Radovanović, B. C., Anđelković, S. M., Radovanović, A. B., Anđelković, M. Z. (2013). Antioxidant and antimicrobial activity of polyphenol extracts from wild berry fruits grown in southeast Serbia. Tropical Journal of Pharmaceutical Research, 12(5), 813-819.

Rajeswari, T., Venil, C. K., Sathya, R., Sunitha, K., Umavisalakshi, S. (2010). Antimicrobial and Phytochemical Screening of Rubus fruticosus. Pharmacologyonline, 3, 297-301.

Rasheed, H. U., Nawaz, H., Rehman, R., Mushtaq, A., Rashid, U. (2017). The Blackberry: A Review on its Composition and Chemistry, Uses and Bioavailability and Potential Health Benefits. Int. J. Chem. Biochem. Sci, 11, 120-128.

Riaz, M., Ahmad, M., Rahman, N. (2011). Antimicrobial screening of fruit, leaves, root and stem of Rubus fruticosus. J. Med. Plants Res, 5(24), 5920-5924.

Rios, J. L., Recio, M. C., Villar, A. (1987). Antimicrobial activity of selected plants employed in the Spanish Mediterranean area. Journal of ethnopharmacology, 21(2), 139-152.

Ryu, J., Kwon, S. J., Jo, Y. D., Jin, C. H., Nam, B. M., Lee, S. Y., Kang, S. Y. (2016). Comparison of phytochemicals and antioxidant activity in blackberry (Rubus fruticosus L.) fruits of mutant lines at the different harvest time. Plant Breeding and Biotechnology, 4(2), 242-251.

Saridogan, B. G. O., Islek, C., Baba, H., Akata, I., & Sevindik, M. (2021). Antioxidant antimicrobial oxidant and elements contents of Xylaria polymorpha and X. hypoxylon (Xylariaceae). *Fresenius Envir Bull.* 30(5), 5400-5404.

Selamoglu, Z., Sevindik, M., Bal, C., Ozaltun, B., Sen, İ., & Pasdaran, A. (2020). Antioxidant, antimicrobial and DNA protection activities of phenolic content of Tricholoma virgatum (Fr.) P. Kumm. Biointerface Research in Applied Chemistry, 10 (3), 5500-5506

Sevindik, M., Akgul, H., Pehlivan, M., & Selamoglu, Z. (2017). Determination of therapeutic potential of Mentha longifolia ssp. longifolia. Fresen Environ Bull, 26(7), 4757-4763.

Sevindik, M., Bal, C., Eraslan, E. C., Uysal, I., & Mohammed, F. S. (2023b). Medicinal mushrooms: a comprehensive study on their antiviral potential. Prospects in Pharmaceutical Sciences, 21(2), 42-56.

Sevindik, M., Mohammed, F. S., & Uysal, I. (2023a). Autism: plants with neuro-psychopharmacotherapeutic potential. Prospects in Pharmaceutical Sciences, 21(3), 38-48.

Takcı, H. A. M., Sema, G. E. N. Ç., Yalçın, A., Özdemir, E. (2022). In vitro Antibacterial, Antioxidant and DNA Damage Protective Activity of Blackberry (Rubus fruticosus L.) Root Extracts. International Journal of Life Sciences and Biotechnology, 5(2), 225-234.

Unal, O., Eraslan, E. C., Uysal, I., Mohammed, F. S., Sevindik, M., & Akgul, H. (2022). Biological activities and phenolic contents of Rumex scutatus collected from

Turkey. Fresenius Environmental Bulletin, 31(7), 7341-7346.

Uysal, I., Koçer, O., Mohammed, F.S., Lekesiz, Ö., Doğan, M., Şabik, A.E., Sevindik, E., Gerçeker, F.O., Sevindik, M. (2023). Pharmacological and Nutritional Properties: Genus Salvia. *Adv Pharmacol*, 11(2), 140-155

Verma, R., Gangrade, T., Punasiya, R., Ghulaxe, C. (2014). Rubus fruticosus (blackberry) use as an herbal medicine. Pharmacognosy reviews, 8(16), 101.

Viegi, L., Pieroni, A., Guarrera, P. M., Vangelisti, R. (2003). A review of plants used in folk veterinary medicine in Italy as basis for a databank. Journal of Ethnopharmacology, 89(2-3), 221-244.

Wajs-Bonikowska, A., Stobiecka, A., Bonikowski, R., Krajewska, A., Sikora, M., Kula, J. (2017). A comparative study on composition and antioxidant activities of supercritical carbon dioxide, hexane and ethanol extracts from blackberry (Rubus fruticosus) growing in Poland. Journal of the Science of Food and Agriculture, 97(11), 3576-3583.

Weli, A. M., Al-Saadi, H. S., Al-Fudhaili, R. S., Hossain, A., Putit, Z. B., Jasim, M. K. (2020). Cytotoxic and antimicrobial potential of different leaves extracts of R. fruticosus used traditionally to treat diabetes. Toxicology Reports, 7, 183-187.

Yiğit, D., Yiğit, N. (2014). Antibacterial properties of blackberry (Rubus Fruticosus). Erzincan University Journal of Science and Technology, 7(2), 267-274.

Yilmaz, K. U., Zengin, Y., Ercisli, S., Serce, S., Gunduz, K., Sengul, M., Asma, B. M. (2009). Some selected physico-chemical characteristics of wild and cultivated blackberry fruits (Rubus fruticosus L.) from Turkey. Romanian biotechnological letters, 14(1), 4152-4163.

Zabihullah, Q., Rashid, A., Akhtar, N. (2006). Ethnobotanical survey in kot Manzaray Baba valley Malakand agency, Pakistan. Pak J Plant Sci, 12(2), 115-121.

Zafra-Rojas, Q. Y., González-Martínez, B. E., Cruz-Cansino, N. D. S., López-Cabanillas, M., Suárez-Jacobo, Á., Cervantes-Elizarrarás, A., Ramírez-Moreno, E. (2020). Effect of ultrasound on in vitro bioaccessibility of phenolic compounds and antioxidant capacity of blackberry (Rubus fruticosus) residues cv. Tupy. Plant Foods for Human Nutrition, 75, 608-613.

Zafra-Rojas, Q., Cruz-Cansino, N., Delgadillo-Ramírez, A., Alanís-García, E., Añorve-Morga, J., Quintero-Lira, A., Ramírez-Moreno, E. (2018). Organic acids, antioxidants, and dietary fiber of Mexican blackberry (Rubus fruticosus) residues cv. Tupy. Journal of Food Quality, https://doi.org/10.1155/2018/5950761.